University of Alberta

Fabrication of Graphitic Carbon Nanostructures and Their Electrochemical Applications

by

Rongbing Du

A thesis submitted to the Faculty of Graduate Studies and Research
in partial fulfillment of the requirements for the degree of

Doctor of Philosophy

Department of Chemistry

Spring 2010
Edmonton, Alberta

Examining Committee

Dr. Mark T. McDermott, Chemistry

Dr. D. Jed Harrison, Chemistry

Dr. Jillian M. Buriak, Chemistry

Dr. Richard L. McCreery, Chemistry

Dr. Michael J. Brett, Electrical & Computer Engineering

Dr. Robin L. McCarley, External Examiner, Department of Chemistry, Louisiana State University

Abstract

New methods to fabricate nanometer sized structures will be a major driving force in transforming nanoscience to nanotechnology. There are numerous examples of the incorporation of nanoscale structures or materials enhancing the functionality of a device. Graphitic carbon is a widely used material in electroanalysis due to a number of advantageous properties such as wide potential window, low cost, mechanical stability, and applicability to many common redox systems. In this thesis, the fabrication of nanometer sized graphitic carbon structures is described. These structures were fabricated by using a combination of electron-beam lithography (EBL) and pyrolysis. EBL allows for the precise control of shape, size and location of these carbon nanostructures. The structure and electrochemical reactivity of thin films of the pyrolyzed material is initially examined. The methodology to fabricate nanosized carbon structures and the structural and electrical characterization of the nanostructure is presented.

The nanometer sized carbon structures fabricated in this work are being applied as nanoelectrodes. For nanoband structures, we observe a limiting current plateau which is characteristic of radial diffusion to cylindrical ultramicroelectrodes. Their voltammetric behaviour shows good agreement with classical theoretical predictions. Both carbon film and nanoband electrodes have been used as substrates for metal electrodeposition. The size and morphology of the deposited Au particles depends greatly on the substrate. On the nanoband electrodes, the Au particles exhibit a multi-branched or dendridic morphology. Their size and surface area are much larger than those electrodeposited on the carbon film electrode under the same conditions. The surface enhanced Raman spectroscopy (SERS) properties of the gold deposited on the nanobands was studied. A high enhancement in Raman intensity for a molecular layer on the nanoband supported gold is observed.

Acknowledgements

The accomplishment of this thesis would not have been possible without the encouragement, advice, and assistance from many people who I wish to thank. First and foremost I would like to thank my wife Yunhui. Thank you for your love, encouragement and sacrifices throughout the past eight years. I would never have made it this far without your love and support. A very emotional "thank you" goes to my parents who gave me love and support that I grew up.

I especially want to thank my research advisor, Dr. Mark McDermott, for his scholarly guidance and tremendous advice at all stages in my study and research at University of Alberta. I will always be grateful for the friendly, yet disciplined environment that you nurtured in our research lab and I really appreciated your generosity of providing me the opportunity to fully experience the research practice. Thanks, Boss, for having confidence and trust in me and for positive recommendation that helped me to land my first job. I hope that the McDermott group continues to grow and achieve even greater success in the future. I wish you and your family all the best that life has to offer.

Much sympathy should go to past and present members of the McDermott Group. Most notably, I would like to thank Dr. Mirwais Aktary and Dr. Soloman Ssenyange for training me on electron beam lithography and photolithography. I would also like to thank Ni Yang who helped me to acquire most SERS spectra in Chapter 6. I would like to acknowledge Dr. Hongmei Shan, Dr. Francis Nsiah, Dr. Chris Grant, Dr. Peng Wu, Andrew Smith, Dwayne Shewchuk, Roderick Chisholm and Lars Laurentius for their support and friendship.

I would like to acknowledge Professor Richard McCreery for allowing me to use facilities in his lab. I would also like to thank Professor Michael Brett for allowing me to audit his class of microfabrication. The microfabrication knowledge I learned in your class helps a lot in my later research.

Considerable work for this thesis was conducted in the UofA Nanofab, and thanks go to all the staff of the Nanofab (particularly Stephanie Bozic and Keith Franklin) for their training and assistance throughout. I wish to express my gratitude to all the staff at National Institute for Nanotechnique (NINT). I would also like to thank Dr. Dimitre Karpuzov, Dr. Anqiang He, and Dr. Shihong Xu in Alberta Centre for Surface Engineering and Science (ACSES) for their helps.

Lastly, but not least, I would like to acknowledge my new advisor Dr. Greg Lopinsky for allowing me to finish writing up my thesis and at the same time working in his lab. I appreciate very much your support and the opportunity to perform future research in your lab.

Table of Contents

List of Tables

List of Figures

List of Schemes

List of Abbreviations

3D	three dimensional
AAO	anodic aluminum oxide
APCVD	atmospheric pressure chemical vapor deposition
AFM	atomic force microscopy
BDD	boron-doped diamonds
BSEs	backscattered electrons
CAFM	conductive atomic force microscopy
cm^{-1}	wavenumber
CNTs	carbon nanotubes
CVD	chemical vapor deposition
DI	deionized
DUV	deep ultraviolet light
DNQ	diazonaphthoquinone
eV	electron volt
EBL	electron beam lithography
ECF	electron beam evaporated carbon film
ECP	electrochemical pre-treatment
ECR	electron cyclotron resonance

EGO	electrochemical graphitic oxide
ET	electron transfer
g	gram
GC	glassy carbon
HOPG	highly oriented pyrolytic graphite
μCP	microcontact printing
μL	microliter
mol	mole
M	moles per liter
MT	mass transport
MWCNT	multi-walled carbon nanotubes
MEMS	microelectromechanical systems
NAB	nitroazobenzene
NIL	nanoimprint lithography
nm	nanometer
P8	pyrolyzed SU-8 carbon film
PDMS	polydimethylsiloxane
PAN	polyacrylonitrile
PEB	post exposition baking

PGA	photo acid generator
PMMA	poly(methyl methacrylate)
PPF	pyrolyzed photoresist film
PVD	physical vapor deposition
RIE	reactive ion etching
RMS	root mean square
SAM	self-assembled monolayers
SECM	scanning electrochemical microscopy
SEM	scanning electron microscopy
SERS	surface enhanced Raman spectroscopy
STM	scanning tunneling microscopy
SWCNTS	single walled carbon nanotubes
TEM	transmission electron microscopy
3D	three dimensions
2D	two dimensions
UV	ultraviolet
XPS	X-ray photoelectron spectra

List of Symbols

ξ	the ratio of different diffusion coefficients
ρ	resistivity
Γ	surface density of adsorbed molecules
A	area
cm^{-1}	wavenumber
C	the concentration of electroactive species
D	diffusional coefficient
d_{002}	the interplanar spacing of graphite
E	potential of an electrode versus a reference
ΔE_p	the potential difference between the cathodic and anodic peak
F	charge on one mole of electrons
i	current
I	intensity of Raman signals
g	gram
k^0	heterogeneous electron transfer rate constant
L	length
L_a	the in-plane crystallite size of graphite
L_c	the crystallite size perpendicular to the graphene planes
n	the electron number involved in the electrochemical reaction
r	radius of disk electrodes

R	resistance
R_s	sheet resistance
t	time
w	the width of band electrodes
X_D	diffusion layer thickness
v	linear potential scan rate

Chapter 1. Introduction

The transformation of nanoscience into nanotechnology will rely heavily on both nanomaterial synthesis and nanofabrication. Nanofabrication can be generally divided into two approaches: Bottom-up fabrication and top-down fabrication.[1,2] Bottom-up methods, such as self-assembly and Langmuir-Blodgett etc., generally involve various forms of self-assembly and have been reviewed.[1] Alternatively, top-down lithographic approaches, such as electron-beam lithography (EBL) and nanoimprint lithography, provide arbitary geometrical designs and nanometer-level controllable dimensions.[2] This thesis is concerned mainly with the development of a fabrication methodology for carbon nanostructures using EBL.

The fabrication of electrodes with nanoscopic dimensions is attracting attention in the development of miniature sensors.[3] Compared with conventional macroelectrodes, nanoelectrodes possess advantageous characteristics, such as higher mass transfer efficiency, fast establishment of a steady state current, higher signal-noise ratio, and lower iR drop.[4] Their utilization in nanobiosensors, single cell detection, and single molecule electrochemistry has been reviewed.[4-6]

Both metals and carbon materials can be used for the fabrication of nanoelectrodes with various shapes. Currently, most nanoelectrodes are prepared from noble metals, such as gold and platinum. These metal electrodes, however, have narrower potential window and higher background currents than carbon electrodes, which limits analytes that can be measured and increases the detection limit.[7] In addition, the electrochemical activity of carbon electrodes is often superior to those of noble metals for organic and biological molecules in both aqueous and nonaqueous solutions.[8] Thus, the fabrication and utilization of carbon nanoelectrodes is an interesting research area.

1.1. Carbon allotropes

Carbon materials exist in three main allotropes, such as diamond, graphite, and fullerenes (e.g. buckyballs and carbon nanotubes). All of these different forms of carbon can be used as electrodes. Diamond is composed of tetrahedral bonded carbon atoms which are sp^3 hybridized. Crystalline diamond has a low conductivity due to a wide band gap of > 6 eV.[8] The conductivity of diamond, however, can be greatly increased by doping with boron,[9-11] nitrogen[12] or phosphorus.[13,14] Boron-doped diamond (BDD) is the most commonly used conductive diamond material.[8] Boron is electron-deficient relative to carbon and boron doping leads to p-type conduction in diamond.[11] At sufficiently high boron concentrations, diamond exhibits metallic conductivity at room temperature.[9]

Since the discovery of carbon nanotubes (CNTs) by Iijima in 1991,[15] they have been widely applied in electrochemistry. CNTs can be classified into single-walled carbon nanotubes (SWCNTs) and multi-walled carbon nanotubes (MWCNTs). The structure of SWCNTs consists of a single cylindrical wall of graphene while MWCNTs consist of a number of concentric cylinders. Based on

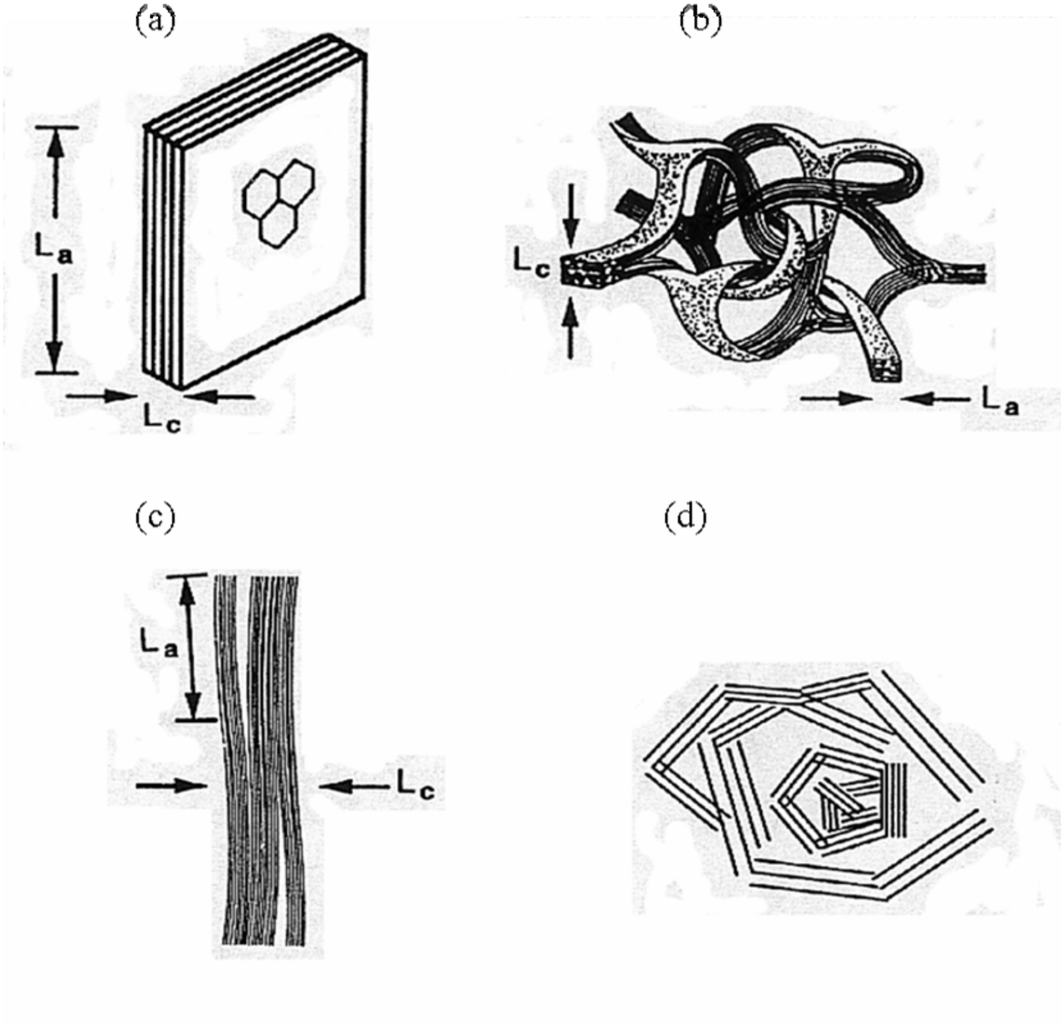

Figure 1.1. Four types of sp^2 carbons. (a) HOPG, (b) GC, (c) carbon fiber, and (d) carbon black (GC structure was originally proposed by Jenkins and Kawamura in reference 30).

their electric properties, carbon nanotubes can be classified into two types: metallic type or semiconducting type. Metallic type CNTs have been widely used in electrochemistry[16-21] while semiconducting CNTs are commonly investigated as biosensors.[22-26]

Graphite is composed of sp^2 hybridized carbon atoms. Graphitic carbons include highly ordered pyrolytic graphite (HOPG), glassy carbon (GC), carbon fibre, pyrolytic carbon, etc. Although all these types of sp^2 carbon share the same carbon-carbon bonding, their morphology and crystallographic properties are different. For example, highly oriented pyrolytical graphite (HOPG) is well known for its highly-ordered surface structure with a significant fraction of basal-plane sites and a small fraction of edge sites. High-surface-area carbon blacks, however, exhibit a surface with predominantly edge sites. Figure 1.1 shows the structures of four widely used sp^2 carbons.

1.2 Structure of graphite

Graphite can be viewed as stacked two-dimensional graphene sheets. The structure of a graphene sheet is consistent with a very large "polyaromatic-like" molecule as shown in Figure 1.2.[27] The carbon-carbon bond length is 1.42 Å within the same basal plane, while the interplanar spacing is 3.35 Å. Different sheets interact through van der Waals' forces. As the strength of van der Waals' forces is not strong, the planes can move with respect to each other.

Three parameters are often used to characterize the dimension of the crystallites of graphite materials. As shown in Figure 1.2, L_a refers to the in-plane crystallite size, L_c is the size perpendicular to the graphene planes and d_{002} is the

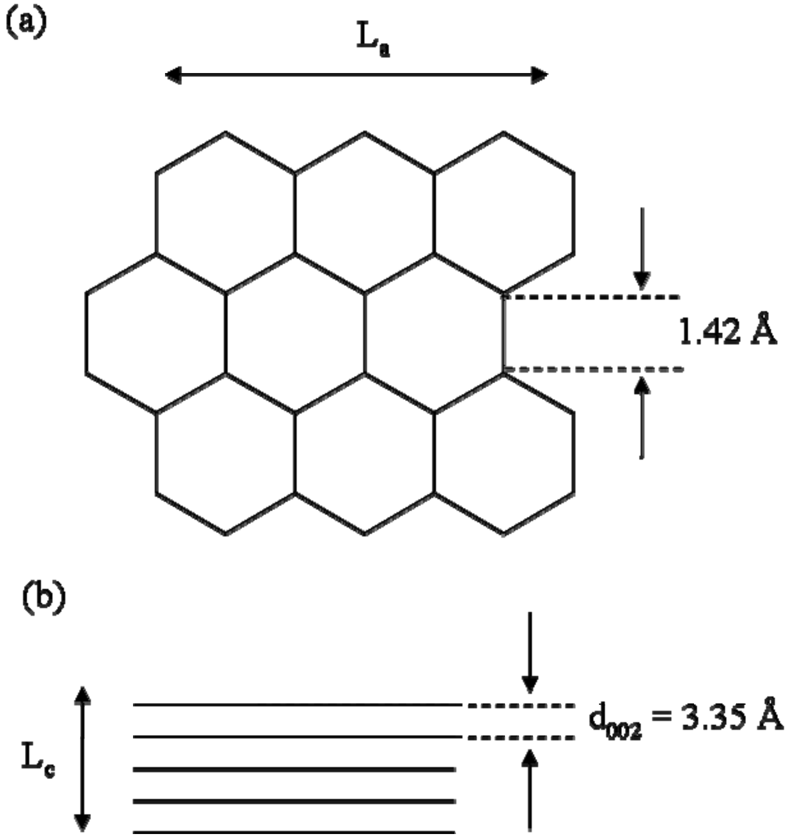

Figure 1.2. Crystallographic structures of graphite. (a) view of a basal plane and (b) view of an edge plane (Figure is adapted from reference 27).

interplanar spacing. These parameters can be obtained by X-ray diffraction and Raman spectroscopy. L_a and L_c values in HOPG and natural single crystal graphite are larger than 1 μm, while L_a and L_c values range from 10 nm to 100 nm in polycrystalline graphites and from 1 nm to 10 nm in carbon blacks.[27]

1.3 Preparation and structure of various graphite materials

Due to the high ash content of natural graphites, most graphitic carbons used in electrochemistry are fabricated from hydrocarbon souces.[28] Depending on the organic precursors and preparation methods employed, graphite materials with various microstructures can be obtained as illustrated in scheme 1.1.[28]

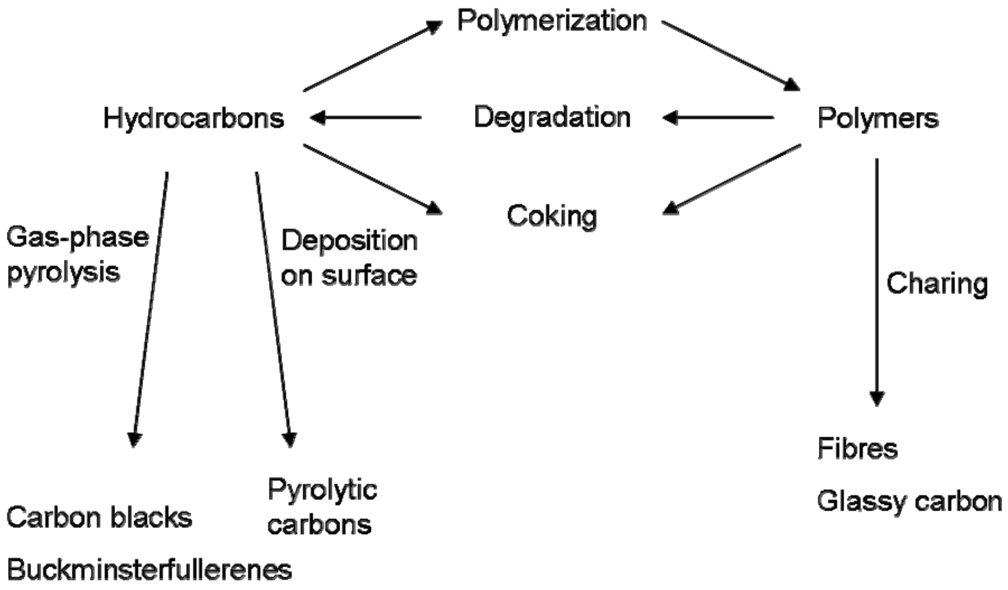

Scheme 1.1. Preparation routes of various graphitic carbons.

HOPG is a widely used model for ordered graphite materials. HOPG is made by high temperature deposition of gaseous hydrocarbons onto a hot surface. At high deposition temperature, significant ordering of carbon atoms parallel to the hot surface occurs (a-axis). After that, high temperature and high pressure along the vertical direction (c-axis) are applied.[27] HOPG has an atomically smooth basal plane. The root-mean-square (RMS) roughness measured by STM is 0.24 nm.[29]

GC is prepared by heating polymeric resins, such as polyacrylonitrile (PAN) or phenol/formaldehyde polymers, to 1000-3000^{o}C in an inert atmosphere.[27] These highly crosslinked polymeric precursors change directly into a form of carbon without a plastic phase.[30] Direct pyrolysis of phenolic resin to GC has been studied previously.[31] The pyrolysis of phenolic resin includes two stages based on the heating temperatures as illustrated in Figure 1.3.[30] At lower temperature, between 350 and 500^{o}C, intermolecular cross-links between hydroxyl groups in phenolic groups and methylene units form with elimination of water, producing aromatic ribbon-like molecules. Further increasing the temperature to more than 500^{o}C, the ribbon molecules interact with each other with the elimination of hydrogen. This graphitization step leads to the formation of GC. Another polymeric source is PAN resin. The pyrolysis process of PAN has been extensively studied.[32-34] Except for a large number of side reactions, the principle chemical process occurs as shown in Figure 1.4.[27] During the high temperature pyrolysis process, the strong C-C bonds in the polymeric molecule do not break. This prevents the formation of extended graphite crystals

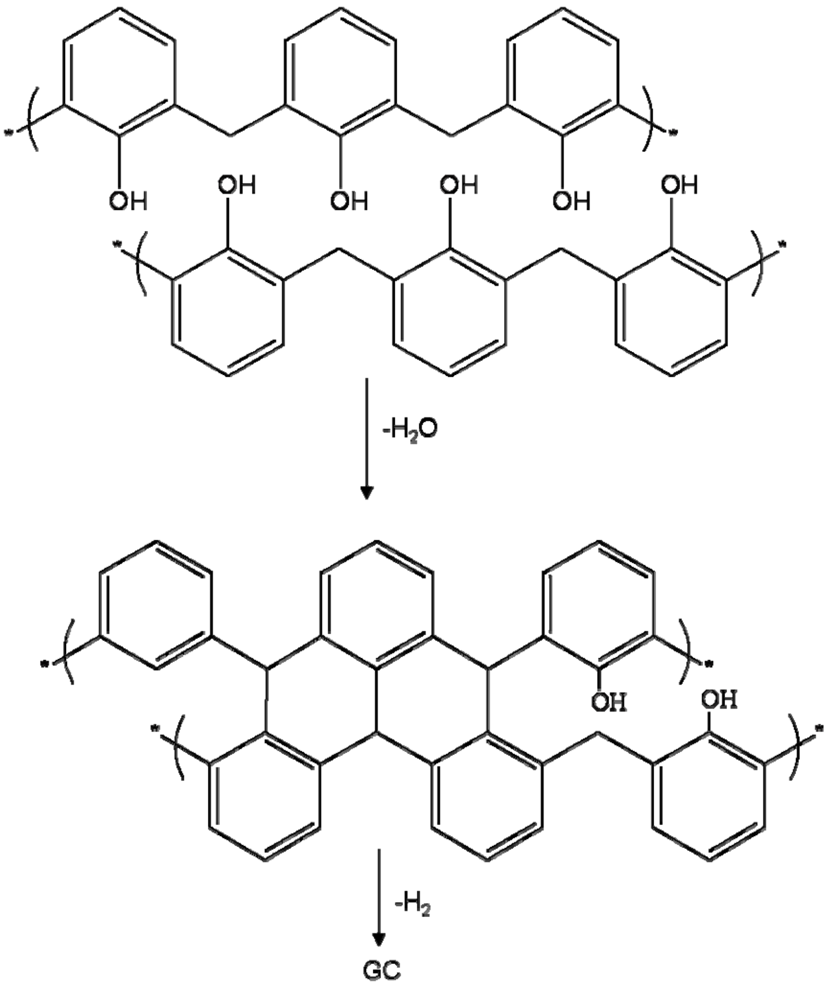

Figure 1.3. Reaction sequence of carbonization from phenolic resins to GC (Figure is adapted from reference 31).

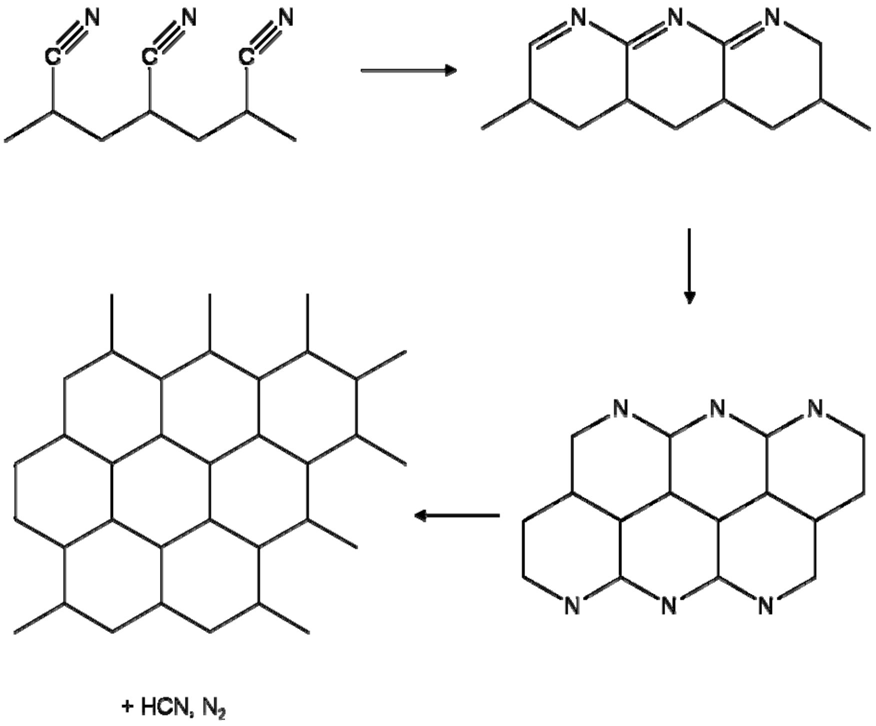

Figure 1.4. Reaction sequence of carbonization from polyacrylonitrile (PAN) to GC (Figure is adapted from reference 27).

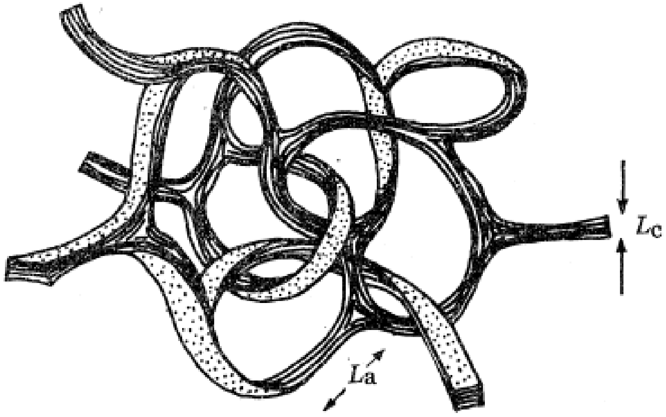

Figure 1.5. Structural model for the network of ribbon stacks in glassy carbon. Reprinted with permission from ref. 30. Copyright 1971 Nature Publishing Group.

and leads to a limited crystalline size (L_a and L_c ranging from 10 to 70 Å).[27] GC does not graphitize to ordered crystals even at a temperature of 3000°C due to the unbroken C-C bonds.[27]

GC is hard and brittle with a slightly lower electrical and thermal conductivity than those of graphites.[30] The final structure of GC is composed of interwoven graphitic ribbons as demonstrated in Figure 1.5.[30] The interwoven structure leads to the mechanical hardness and lower density.[30,35]

Carbon fibers have been extensively used as electrodes for bio-sensors[36-40] and in-vivo monitoring in living tissues.[41] The fabrication method of carbon fibers can be classified into two types: pyrolysis from hydrocarbons or polymeric precursors and catalytic chemical vapour deposition.[27] In order to increase the tensile strength, carbon fibers are generally designed to align the a-axis along the length of the fibers. Although both GC and carbon fibers are fabricated via pyrolysis of polymeric precursors, the difference between GC and carbon fibers is evident. GC is isotropic because there is no preferred orientation introduced by the manufacturing process. Carbon fibers, however, are designed to have a preferred orientation for maximum tensile strength.[27]

Table 1.1. Comparison of physical properties of various graphitic carbons.[8]

	Apparent density (g/cm^3)	d_{002} (Å)	ρ (Ω·cm)	L_a (Å)	L_c (Å)
HOPG, a-axis	2.26	3.354	4×10^{-5}	> 10000	
HOPG, c-axis			0.17		> 10000
Pyrolytic graphite	2.18	3.34		1000	1000
Randomly oriented graphite	1.8	3.35	1×10^{-3}	300	300
Tokai GC-10	1.5	3.49	4.5×10^{-3}	20	10
Tokai GC-20	1.5	3.48	4.2×10^{-3}	25	12
Tokai GC-30	1.5	3.41	3.7×10^{-3}	55	70
Carbon fiber	1.8	3.4	$(5\text{-}20) \times 10^{-3}$	> 100	40
Carbon black (spheron 6)	(1.3-2.0)	3.55		20	13
Evaporated a-C		> 3.4		~10	~10
Pyrolyzed photoresist film (PPF)			0.006		

Carbon blacks have been widely used as catalyst supports for fuel cells.[42] They can be made by burning or thermally decomposing hydrocarbon in the gas phase. The carbon black particle size is very small (300-500 Å) and the surface area is very high (5000 m^2/g).[27]

More recently, pyrolyzed photoresist films (PPF) prepared by pyrolyzing commercially available photoresists have been reported.[43] Photoresist films are spin-coated onto a suitable substrate surface first, and then pyrolyzed at 1000°C in an inert atmosphere. PPF samples exhibit an extremely flat surface (RMS < 0.5 nm).[43] For comparison, the RMS roughness of polished GC and vacuum heat-treated GC disks was found to be 4.1 and 4.5 nm, respectively.[43,44] In addition, PPF samples show a low oxygen/carbon (O/C) atomic ratio due to the pyrolysis process in a reducing atmosphere. A low capacitance of ~8.1 $\mu F/cm^2$ was obtained and a low background current was observed. PPF samples show good electrochemical reactivity which is comparable to that of GC.[43] The comparison of different graphitic carbon electrodes has been described in Table 1.1, which was originally reviewed by McCreery.[8]

1.4 Carbon surface chemistry

1.4.1 Surface oxide functional groups

The surface of graphitic materials contains various fractions of basal and edge plane. Basal plane refers to the atomically ordered hexagonal plane containing the "a-axis", while edge plane is parallel to the "c-axis". As shown in Figure 1.6, the edge plane is not atomically flat and can contain a variety of

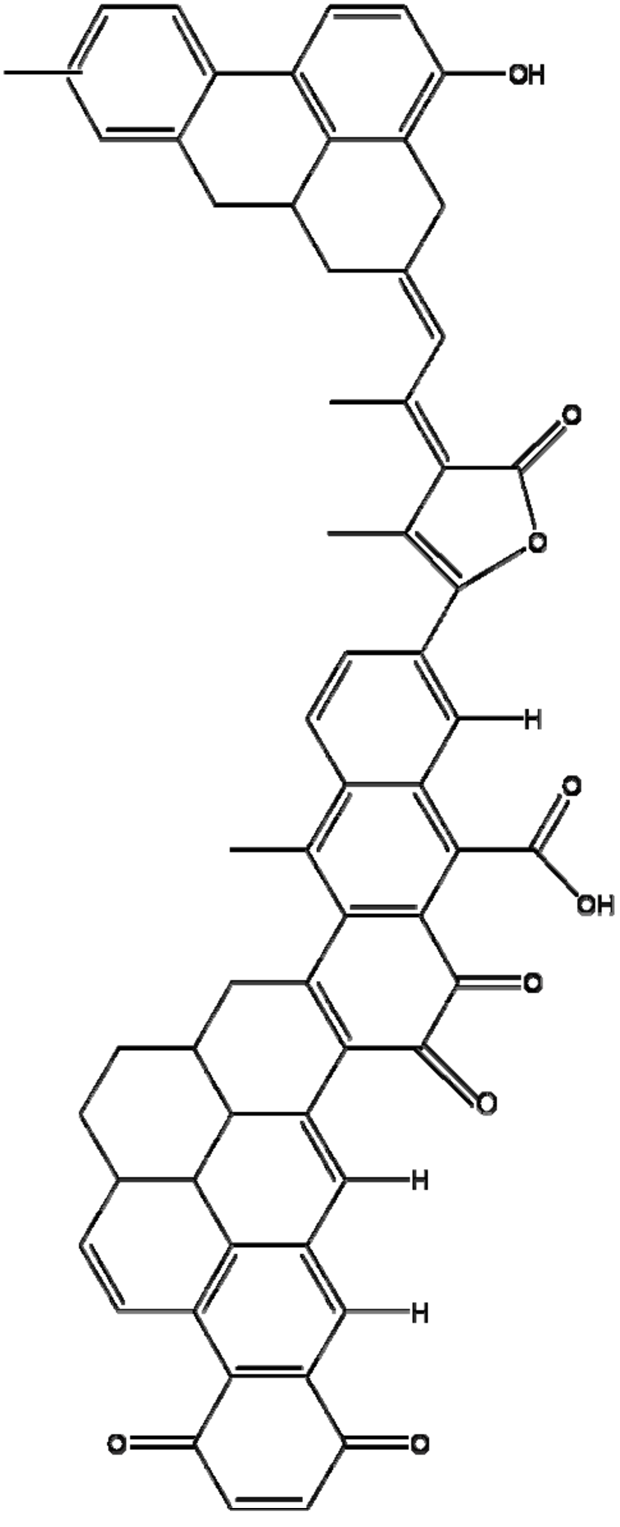

Figure 1.6. Edge plane surface of graphite or the graphene sheets in sp^2 carbon materials.

functional groups.[35] The edge plane shows much higher activity toward electron transfer and adsorption than the basal plane.[45-47]

Graphite surfaces are susceptible to air oxidation due to the thermodynamic stability of carbon–oxygen bonds. The surface oxides on carbon electrodes include carbonyls, phenolic OH, lactones, ethers and carboxylates as illuminated in Figure 1.6. These surface oxide groups are extremely hard to remove. The oxide functional groups, however, can be beneficial with respect to certain redox reactions, such as $Eu^{2+/3+}$, $Fe^{2+/3+}$ and $V^{2+/3+}$, when hydrogen bond or adsorption is involved.[8,47]

1.4.2 Pre-treatment of carbon electrode surface

Pre-treatment or activation of a graphitic carbon electrode is widely employed in electrochemical experiments to increase the electrode reactivity and reproducibility. The final surface structure of graphitic carbon electrodes is affected by the pre-treatment. A variety of techniques and methods have been developed to activate graphitic carbon electrodes, which include polishing, sonication in isopropanol/activated carbon (AC) mixture, electrochemical pre-treatment (ECP), vacuum heat treatment, and laser activation etc.

Polishing, which produces a mirror like surface, has been widely used to clean GC electrodes in electrochemical labs. This procedure includes grinding the “as received” GC with fine grit silicon carbide paper and then polishing in aqueous alumina slurries or diamond paste with particle size from micron to submicron successively. Polishing affects the level of surface oxides at graphitic carbon. A polished surface with a water/alumina slurry has a surface O/C ratio of 7-20%, while the same surface polished at a cyclohexane/alumina slurry gives a surface O/C ratio of 4%.[48]

Sonication in an isopropanol/activated carbon mixture can be used to clean carbon electrodes which can not be polished.[43,49] Active carbon (AC) has a relatively large surface area compared to the electrode surface and impurities on the electrode surface and in the solvent are preferentially adsorbed at the AC surface. This leads to a clean carbon electrode surface and a large increase in electron transfer rate.[43,49]

Electrochemical pre-treatment (ECP) of graphitic carbon electrodes has been widely used to increase electron transfer (ET) rate. This procedure involves application of various potential programs to the carbon electrode in a solution. ECP in acid or neutral solution leads to the formation of a graphitic oxide layer at the electrode surface, which is referred to as electrochemical graphitic oxide (EGO).[50,51] EGO is a nonconductive layer with porous and hydrated structures. The layer thickness can be increased to about a micrometer.[50] About 25% weight of EGO is composed of oxygen.[50]

Carbon surfaces are commonly covered with oxides due to air oxidation. These surface oxides, however, can be removed by vacuum heat treatment.[29,48,52] A low O/C ratio of 1.6 was obtained by vacuum heat treatment of GC electrode at 725^{o}C.[48] Other pre-treatment procedures also include laser activation, which leads to a clean surface by desorbing impurities off the electrode.[53]

1.4.3 Chemically modified carbon electrodes

There have been numerous methods reported to chemically modify the surface of carbon electrodes.[54-58] Relevent to the work in this thesis is the reduction of diazonium salts. Since the introduction by Pinson et al.,[54] electrochemical reduction of diazonium salts at carbon electrodes has been widely used to modify carbon surfaces. The mechanism of this reaction is presented in Scheme 1.2. Aryl radicals are produced via one electron reduction of diazonium salt, which then initiates the formation of a covalent bond to the surface.[59]

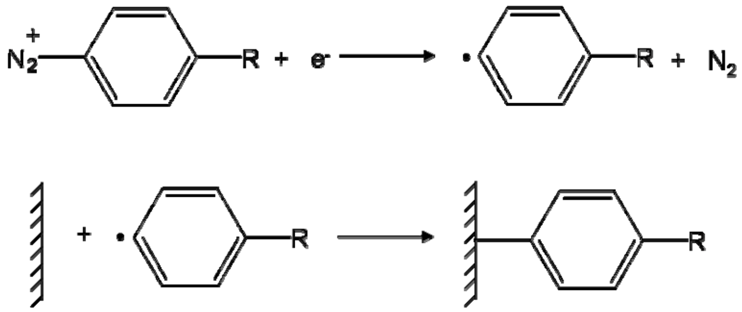

Scheme 1.2. Mechanism of the electrochemical reduction of diazonium salts (Figure is taken from reference 59).

Both monolayer[59] and multilayer organic films[60-62] can be obtained on an electrode surface by the electrochemical reduction of diazonium salts. The mechanism for the formation of organic multilayer on the carbon surface was first proposed by Kariuki et al.[60,61] and later described by Pinson and coworkers[62] as shown in Scheme 1.3. After the generation of aryl radical and subsequent bonding to a carbon surface (R1 + R2 in Scheme 1.3), further transfer of an electron to another diazonium salts produces a new radical. New radicals attack grafted aryl

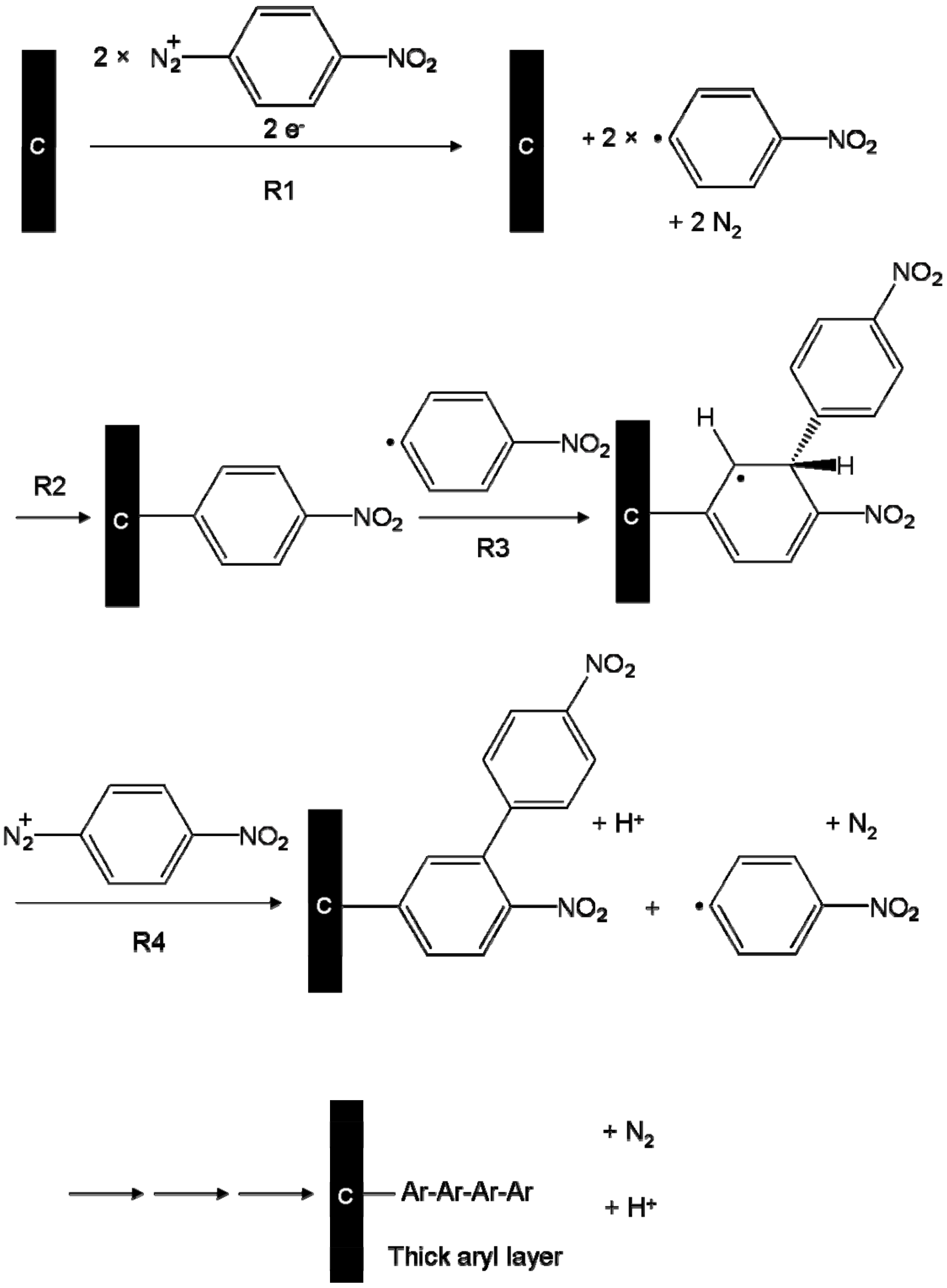

Scheme 1.3. Mechanism of multilayer formation (Figure is taken from reference 62).

groups and produce cyclhexadienyl radicals (R3 in Scheme 1.3). The radicals subsequently lose a hydrogen radical by electron transfer with another nitrophenyl diazonium cation as described by reaction R4. Repeating these reactions would lead to the formation of a thick multilayer on a carbon electrode surface. The reduction method has been successfully applied on a variety of carbon surfaces, including GC,[59] HOPG,[61] and PPF.[63,64]

1.5 Carbon micro- and nanoelectrodes

Since the introduction by Wightman and Fleischmann and their co-workers,[65,66] research and applications of nanoelectrodes have been brought to the forefront by research into low volume electroanalytical sensors. Compared with conventional electrodes, electrodes with micro- or nanometer size have new characteristics: higher mass transfer (MT) efficiency, smaller RC cell time constant, lower iR drop, higher signal-noise ratio, and higher current density. These intriguing properties lead to widespread applications, such as in-vivo measurements of biological cells,[67] electrochemical imaging,[68,69] and electrodeposition.[39]

1.5.1 Linear diffusion and nonlinear diffusion

Three different types of MT, diffusion, convection and migration, can exist in an electrochemical experiment.[70] When the experiment is operating in a quiescent solution with a high concentration of a supporting electrolyte, the mass transport of an electroactive species near the electrode is simplified to the diffusion mode. Diffusion is caused by concentration gradients at the interfacial region between the electrode surface and the bulk solution. When a potential is applied to the electrode, the concentration of electroactive species near the electrode surface will be changed due to the electrochemical reaction. This leads to a concentration gradient between the electrode surface and the bulk solution. The region next to the electrode surface, where the concentrations of electroactive species differ from those in the bulk solution, is referred to as a diffusion layer. The diffusion layer thickness can be estimated by $\sqrt{2Dt}$.[70]

Diffusion can be classified into two modes: linear and nonlinear. Diffusion to a conventional planar electrode surface is commonly linear diffusion, whose flux direction is perpendicular to the planar surface as shown in Figure 1.7 (a). The diffusion current at conventional planar electrodes follows the Contrell equation:

$$i = nFADC\frac{1}{\sqrt{\pi Dt}} \tag{1.1}$$

where D is diffusion coefficient, C is the concentration of electroactive species, and A is electrode area, t is experimental time, and $\sqrt{\pi Dt}$ equals to diffusion layer thickness. The diffusion layer thickness is time-dependent and thus current is also time-dependent (Eqn.1.1).

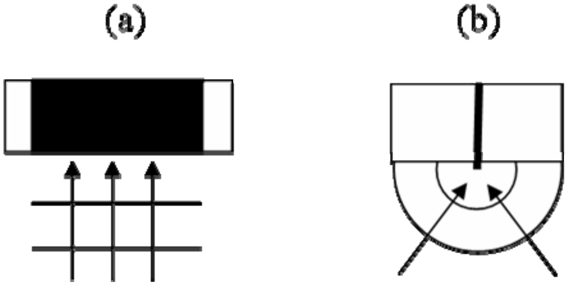

Figure 1.7. Schematic of flux for (a) linear diffusion, (b) nonlinear diffusion.

Similar to conventional planar electrode, oxidation or reduction of electroactive species at a micro- or nanoelectrode surface also generates a concentration gradient between the interface and the bulk solution. However, MT reaches a steady state when the diffusion layer thickness is much larger than the electrode size. This is referred to as nonlinear diffusion. For nonlinear diffusion, as shown in Figure 1.7 (b), the diffusion layer moves further out into the bulk solution as time increases. The area of the diffusion layer boundary also increases and a larger solution volume contributes to the flux at the electrode. The increase in the boundary area compensates for the increase in diffusion layer thickness with time. Thus, the flux of the active species to the electrode surface by diffusion is constantly maintained. For a nanodisk electrode, the steady state diffusion current is independent of time, as described by the following equation.

$$I_{ss} = 4nFDCr \qquad (1.2)$$

where r is the radius of nanodisk electrodes.

1.5.2. Nano-disk or cone electrodes

Nanodisk or cone electrodes can be positioned near small objects, which leads to widespread application for the in-vivo measurements of biological cells.[65,71] The small diameter of a nanodisk electrode also leads to fast establishment of steady state nonlinear diffusion. The limiting current can be expressed by Equation. 1.2.[70]

Nanodisk or nanocone electrodes can be prepared by an etching/insulation method. This method involves two basic processes: first, metal wires or carbon fibers are etched to sharp tips. Second, an insultating layer is coated on the electrode except at the apex of fiber tips, thus providing a very tiny exposed electrode area. Strein and Ewing[72] prepared nanometer sized carbon disk electrodes by flame-etching carbon fibers. A carbon fiber was encapsulated in a glass capillary tube. The protruding tip of carbon fiber was subsequently etched to tip diameters in the range of 100 nm or smaller by passing slowly through an oxygen/methane flame. The tapered tip of carbon fiber was electrochemically coated with a thin poly(oxyphenylene) film for insulation except the very tip of the taper, where the copolymer was removed by either field emission arc or cutting with a scalpel. This fabrication method, however, has limitations. For example, the surface of the electrodes was not very smooth and therefore influenced their electrochemical characteristics.[73] Further more, this method has a low success rate.[72]

Meulemans et al.[74] used a different etching method when preparing an ultra-micro carbon electrode with a tip diameter from 500 nm to 2 μm. Carbon fiber with diameter of 12 μm was electrochemically etched in a sodium nitrite solution by applying a 2-6 V alternating current (AC) signal. The tapered tip of carbon fibers was pushed down inside a capillary tube and subsequently sealed in glass by heating the glass tube with a pulling force. The tube was broken at the extreme tip position. A similar procedure was employed by Wightman and coworkers.[67] They constructed a carbon conical microelectrode with a tip radius in the micro range and used it to monitor the release of catecholamines from biological cells. The electrochemical behavior of etched electrodes did not follow the classic theory but were still suitable for the amperometric measurement.

Chen and Kucernak et al.[38] fabricated carbon nanoelectrodes with an effective radius down to 1 nm by using electrophoretic paint. Carbon fibers were electrochemically etched in a 0.01 M NaOH solution with different voltages, which produced a sharp tapered end structure. An inverted deposition process was specially designed to coat etched carbon fibers with electrophoretic paint. The carbon fiber was immersed in the deposition solution in a tip-up direction. The sharp tip was positioned just to break through the solution surface with the tip apex still in contact with the solution with a very thin meniscus. An advantage of this arrangement is less deposition on the very end of the tip while the insulting film was thick enough to avoid pinholes. Heat treatment was employed and the insulting layer solidified and contracted, which forced the tip of the carbon fiber to protrude. The electrode diameter could be controlled by repeating the electrophoretic painting and heat treatment cycles.[75]

1.5.3 Nanoband electrodes

Nanoband electrodes have a macroscopic length and a nanometer sized width. The nanometer sized width leads to many advantageous properties of nanoelectrodes, while a macroscopic length results in easily measured currents.[76]

The comparison of band electrodes and hemicylindrical electrodes has been reporteded by Wightman and co-workers.[77,78] The limiting current for a potential step experiment at a band electrode of width w at long times can be approximated as the current at a hemicylinder electrode with an effective radius. The relevant equation is

$$I(t) = \frac{2nFDlC\pi}{\ln\left(4Dt/r^2\right)} \tag{1.3}$$

where n is the electron number involved in the electrochemical reaction, F is the Faraday constant, D is the diffusional coefficient, l is the length of nanoband electrode, C is the concentration of electroactive species, t is time, r is the effective radius of the equivalent hemicylinder, for which different calculation methods have been proposed. Wehmeyer et al.[77] suggested the effective radius of $r = w/\pi$, while Szabo et al.[78] indicated that $r = w/4$ was more accurate for the current at longer time. The difference in the current predicted by these two theories, however, was found to be small for nanometer sized band electrodes at long times.[79]

Nanoband electrodes with a width less than 20 nm, however, show different electrochemical behavior.[77] The limiting currents deviate from the prediction of eqn.1.3 due to the effects of the finite size of redox molecules relative to the electrode width and the altered fluid density and viscosity near the electrode surface.[80] White and coworkers[79,80] prepared metal nanoband electrodes with widths ranging from 2 nm to 50 nm. The influence of near surface fluid properties, such as density and viscosity, on the electrochemical properties was investigated. They demonstrated that the assumption of a homogeneous fluid in classical theory is inconsistent with the physical properties of nanoband electrodes.[79] By taking the fluid inhomogeneity into account, the limiting current at nanoelectrode with width less than 30 nm can be estimated by equation 1.4.[79,81]

$$I(t) = 2nFDlC\pi\left\{\frac{\left[\left(1+\frac{r}{z}\right)\ln\left(4Dt/r^2\right)-8\xi\right]}{\left[\left(1+\frac{r}{z}\right)\ln^2\left(4Dt/r^2\right)\right]}\right\} \tag{1.4}$$

where z is the thickness of the interfacial reaction layer at the electrode surface, ξ is the ratio of bulk diffusion coefficient (D_{bulk}) to that near the electrode surface (D_{surf})

Nanoband electrodes can be constructed by sealing thin metal or carbon films, such as foils and deposited films, in insulting materials.[72,77,82,83] As shown in Figure 1.8, the thin film is sandwiched with non-conducting materials, and the nanoband electrode is exposed to solutions by polishing the edge. The electrode width is roughly estimated by the thickness of the conductive film.

McCarley and coworkers[81] fabricated nanoscopic Au band electrodes with widths ranging from 3 to 150 nm. Small-grained, electrically conductive Au films with thickness down to 3 nm were deposited onto silane-modified glass substrates and subsequently insulated on the topside of the Au film with epoxy resin. The film edge was exposed to solution and used as a nanoband electrode. Although the real area of the electrode was much larger than expected, well-behaved cyclic voltammograms were observed.

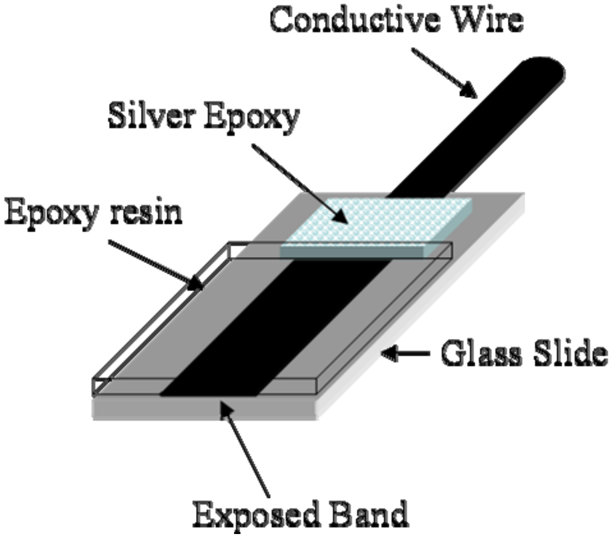

Figure 1.8. Schematic of sandwich type nanoband electrodes.

The fabrication of carbon nanoband electrodes based on ultrathin carbon films has been described by Wang and coworkers.[82] Carbon films with various thicknesses were prepared by carbonization of spin-coated polyacrylonitrile (PAN) films. After sandwiching carbon films between insulting supporters, nanoband electrodes with width from 10 to 90 nm were constructed. Sigmoidal-shaped voltammograms were observed, which agrees with classic theoretical predictions.

A grinding process is commonly required to expose the film edge to solutions. Due to the varying degrees of hardness of the materials used to construct the electrode, overpolishing can cause the epoxy and /or the electrode to become recessed between the harder microscope slides.[77] This will inhibit diffusion of electroactive species to the surface of the electrode and distort the current-voltage relationships.

1.5.4 Carbon nanoelectrode array

The predominant disadvantage of individual nanoelectrodes is their extremely small current which brings great challenges to the measurement equipment. This can be overcome by utilization of nanoelectrode arrays, which integrate many individual nanoelectrodes. Each electrode of an electrode array behaves independently, leading to a signal which can be thousands of times larger than that from a single nanoelectrode.[84] Thus the development of nanoelectrode arrays has attracted increasing interests.

The electrochemical properties of a micro or nanoelectrode array are dependent to the ratio of electrode size (w) to the separation distance (d) and scan rate applied.[85-87] Four different cases of diffusion profiles at a micro or nanoelectrode array are illustrated in Figure 1.9.[87] In the case of very fast scan rates and widely separated electrodes, the diffusion layer thickness, X_D, is much smaller than the microelectrode size as illustrated by Figure 1.9 (a). The diffusion at the electrode surface is governed by linear diffusion. Thus electrode arrays behave like a scaled down macroelectrode and the voltammogram is peak shaped. In the second case, as shown in Figure 1.9 (b), X_D is larger than the electrode size (w) but smaller than separation distance (d). The diffusion at an individual electrode is dominated by the nonlinear diffusion. An electrode array thus produces a sigmoid shaped voltammogram which is independent of the scan rate at low scan rates. The steady state limiting current obtained at an electrode array is equal to the product of the current at an isolated electrode and the total number of electrodes in the array. This ideal electrochemical behavior is desirable for an analytical electrochemist.[86] In the above two cases, the diffusion layer thickness is smaller than the separation distance and thus electrochemical behavior can be considered as a collection of isolated electrodes. In the case of Figure 1.9 (c), the separation distance (d), however, is not large enough to prevent the overlapping of adjacent diffusion layers. As diffusion layers at adjacent electrodes overlap, an individual electrode experiences shielding from neighbors, leading to a decrease of flux density. Such an electrochemical behavior is likely to be avoided for an optimized microelectrode array. In the case of Figure 1.9 (d), X_D far exceeds the separation distance, leading to complete overlap of diffusion layers. The diffusion at the electrode array is governed by linear diffusion. The current response is equal to that of a macroelectrode with the same geometric area. A peak shaped voltammogram thus can be obtained.

(a) Separated diffusion layers (linear diffusion)

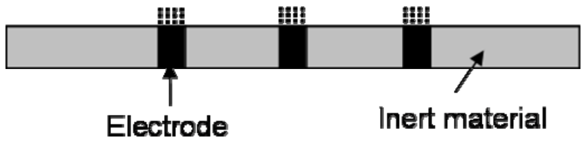

(b) Separated diffusion layers (radial diffusion)

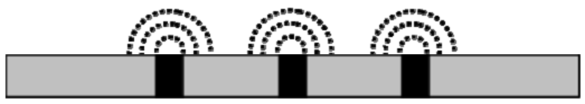

(c) Overlapped diffusion layers

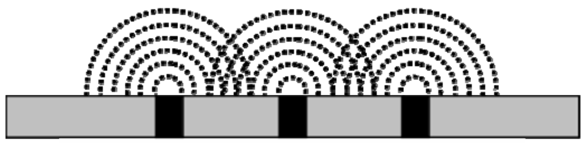

(d) Heavily overlapped diffusion layers (linear diffusion)

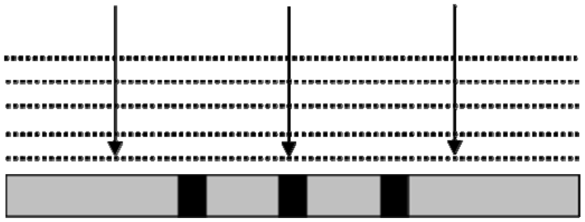

Figure 1.9. Schematic of four cases of diffusion profiles at a micro or nanoelectrode array (Figure is adapted from reference 87).

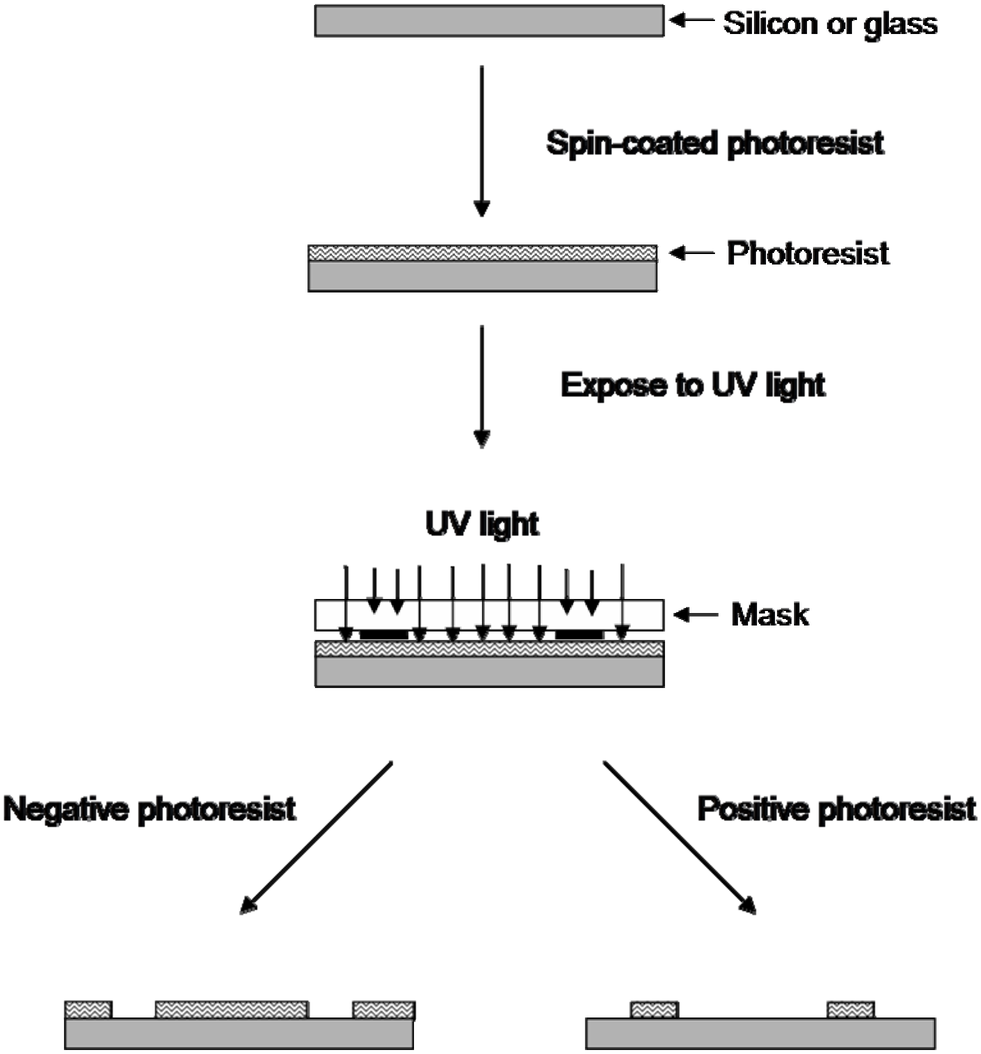

Figure 1.10. Schematic of photolithographic patterning with positive and negative photoresist films.

Nanoelectrode arrays or ensembles can be prepared by various methods and techniques. The reported approaches include template synthesis,[88-92] microphase separation,[93] and block copolymer self-assembling.[94] The template systhesis method has been widely used to construct nanodisk electrode ensembles.[88-92] A porous membrane, such as a polycarbonate membrane or anodic aluminum oxide (AAO) template, was generally used in this method. Gold or platinum metals were electrodeposited into the pores of the porous membranes, which are cylindrical with uniform diameters. The metal nanopillars obtained within the pores were then used as nanoelectrode arrays. These fabrication methods, however, produce nanoelectrode ensembles rather than nanoelectrode arrays, which are supposed to exhibit a controlled individual electrode size and separation distance.

A large fraction of nanoelectrode arrays are prepared by micro- or nanofabrication techniques, which are traditionally used for electronic circuits. The application of lithographic fabrication techniques exhibits advantages of mass production of disposable electrodes with reproducible electrochemical properties. Widely employed micro or nanofabrication processes include lithography, etching, and thin film growth.[95] Photolithography is the most commonly used lithographic technique for the fabrication of microstructures. It is used to transfer the patterns from a photomask to a photoresist film on a substrate surface. Figure 1.10 shows the photolithography process. When positive photoresist is exposed to UV light, the polymer is degraded and is easily washed away using a developer solution. When the negative photoresist is exposed to UV light, the polymer

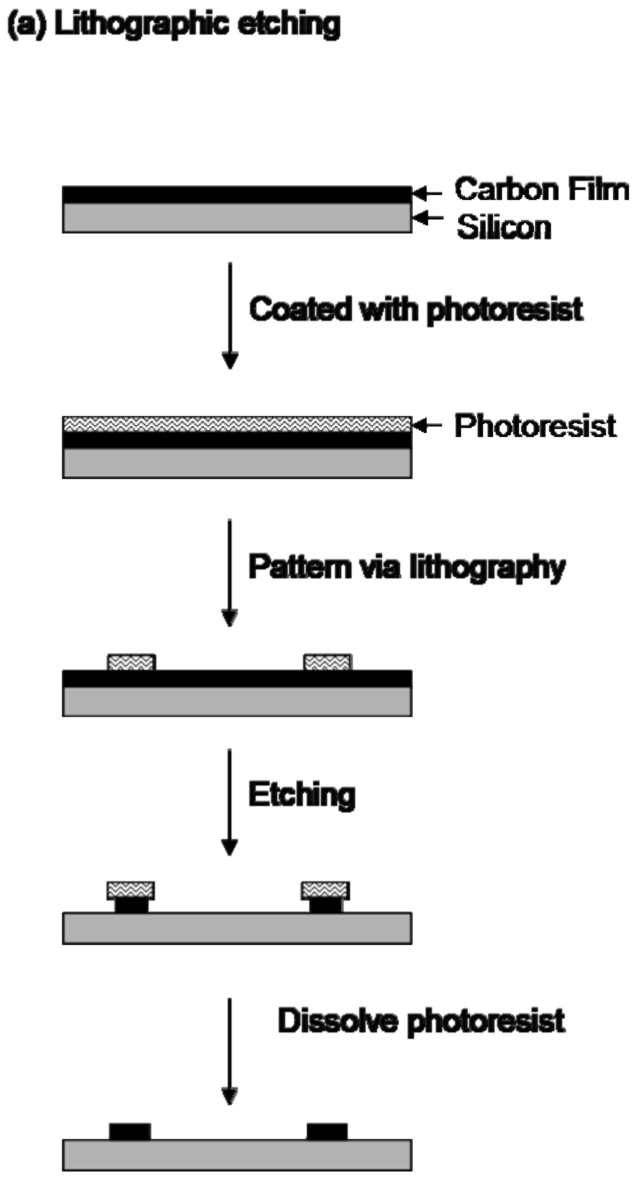
(a) Lithographic etching
Carbon Film
Silicon
Coated with photoresist
Photoresist
Pattern via lithography
Etching
Dissolve photoresist

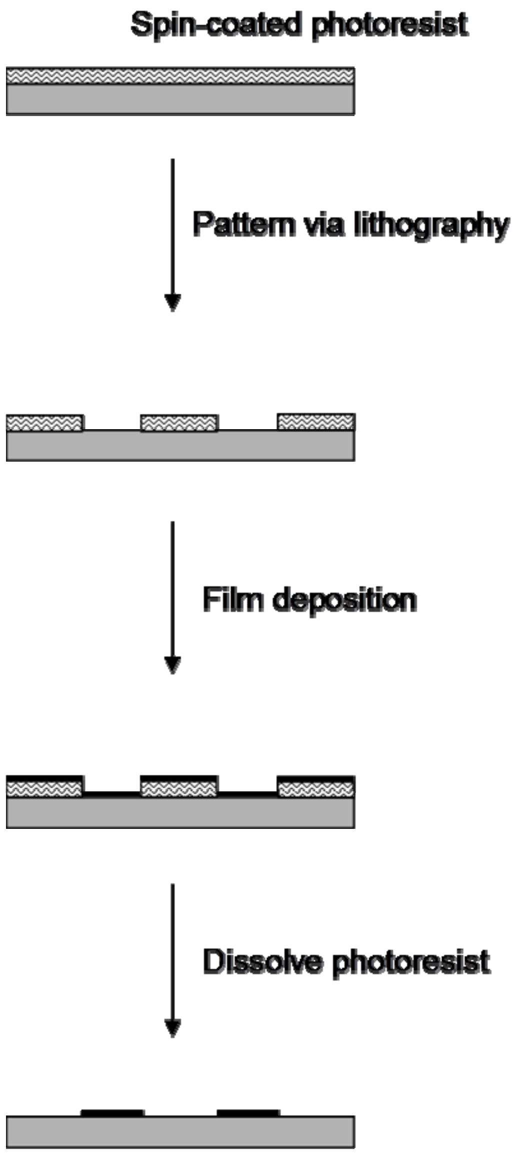

(b) Lithographic deposition

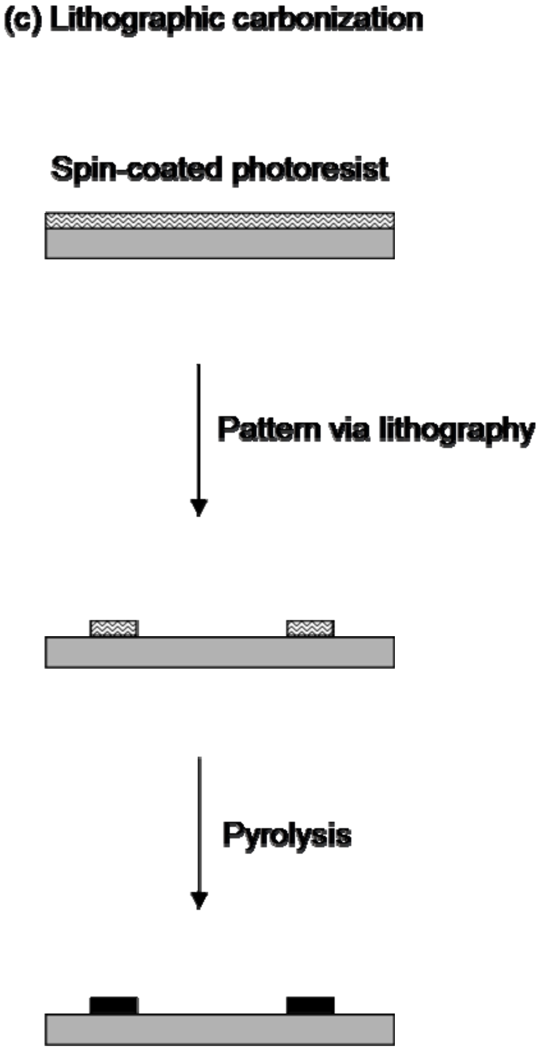

Figure 1.11. Schematic illustration of the processes required for (a) lithographic etching, (b) lithographic deposition and (c) lithographic carbonization.

solution. In both cases, the remaining photoresist acts as a protective mask for the next etching or deposition process. Other widely used lithographic techniques also include electron-beam lithography (EBL)[96] and nanoimprint lithography (NIL).[97] Compared to the photolithography technique, both EBL and NIL can be used to pattern nanoscale structures.

Three different fabrication approaches can be employed to construct nanoelectrode arrays, which are lithographic etching, lithographic deposition and lithographic carbonization respectively. These fabrication methods involve a combination of lithography, etching or lift-off steps. They are illustrated in Figure 1.11 (a), (b) and (c) respectively.

The lithographic etching method involves film deposition, lithographic patterning and subsequent etching steps. McDermott and coworkers reported the fabrication of carbon nanoelectrode arrays via lithographic etching of carbon films.[98] A convenient electrochemical etching procedure was employed in this fabrication process, which involves anodization of the graphitic substrate in basic electrolyte.[98-100] The etching reactions likely involve the adsorption and intercalation of hydroxide anions and result in a breakup of carbon lattice as shown in the following electrochemical reactions.[98]

$$C(s) + OH^- (aq) \rightarrow C(s)OH(ads) + e^-$$

$$C(s) + OH^- (aq) \rightarrow C(s)OH(int)$$

$$4C(s)OH(ads, int) \rightarrow 4\{C\} + 2H_2O + O_2$$

where C(s) implies an intact carbon lattice, C(s)OH(ads) refers to OH groups chemisorbed to the GC surface, C(s)OH(int) corresponds to intercalated OH^-, {C} indicates a carbon material removed from substrate. Carbon electrodes from 660 nm to 30 μm were fabricated by changing the etching time. The nanoband electrode arrays show well behaved cyclic voltammograms.[98]

The fabrication of nanoband electrode arrays with much smaller electrode size have been reported by Nagale et al with a slightly different fabrication procedure.[76,101] The fabrication processes are described in Figure 1.12. Briefly, metal and silicon nitride films were deposited onto a glass slide surface. Then samples were spin coated with photoresist and patterned by photolithography. After developing, etching and removing the organic photoresist residues, Metal film edges were exposed to solutions. The width of the nanoband electrode is equal to the thickness of the metal film.

Lithographic deposition methods involve lithographic patterning, film deposition, and lift-off steps. Different to nanoelectrodes fabricated by the lithographic etching method, whose width can be controlled by etching periods or film thickness, electrode widths fabricated by lithographic deposition are commonly controlled by the lithographic patterning. Thus nanolithographic techniques are ordinarily employed. Ueno et al.[102] constructed nanoelectrode arrays with controlled electrode size and separation spacing by the combination of EBL and lift-off techniques. A similar procedure was also adopted by Blackstock.[103] An array of 50 nm wide carbon wires with a 100 nm gap was fabricated using a standard EBL and subsequently coating with carbon films

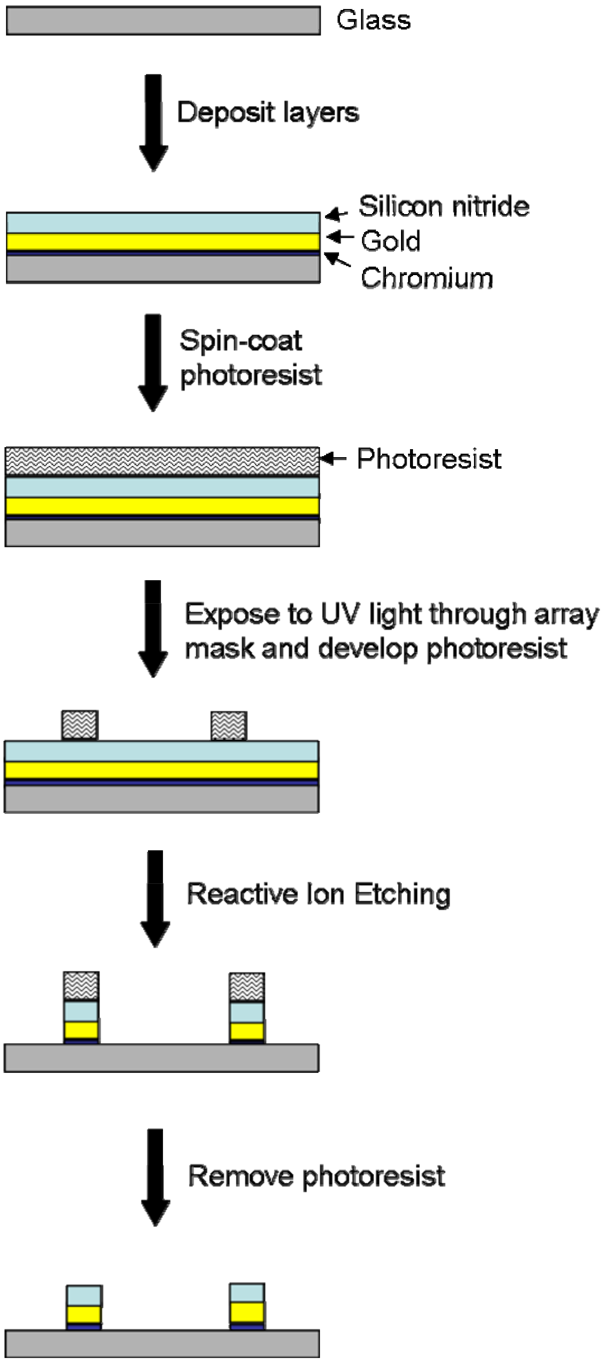

Figure 1.12. Fabrication processes of Au film edge electrode arrays.

by an e-beam evaporator.

Direct lithographic carbonization uses fewer steps and shows advantages of simplicity compared to lithographic etching and lithographic deposition. Direct pyrolysis of patterned polymeric precursor resins by heating under an inert atmosphere has been described by Whitesides and coworkers.[104-106] Structures of various shapes have been successfully fabricated. Kostecki et al. described a procedure to construct carbon microelectrodes consisting of a patterned interdigitated electrode.[107] Photolithography was employed to pattern photoresist layers on a silicon wafer to form the microstructures. The patterned photoresist was then pyrolyzed to carbon. Similarly, Madou and coworkers[108] also described the fabrication of carbon microdisk electrode arrays by the combination of photolithography and pyrolysis. Cylindrical SU-8 posts with various sizes and densities were patterned and created under photolithography and subsequently pyrolyzed under inert atmosphere.

1.5.5. Carbon nanotube based nanoelectrodes

Carbon nanotubes have been widely used as nanoelectrodes. Heller et al.[18,109] reported the application of a single-walled carbon nanotube (SWNT) as a nanoelectrode for electrochemistry. A metallic SWNT was contacted with metal pads on both ends to act as current collectors. An electrochemical window was patterned on PMMA film to expose parts of SWNT to electrolyte solution. Cyclic voltammograms with sigmoid shape at single SWNT electrode were obtained. Campbell et al.[110] also demonstrated electrochemical nanotubular electrodes constructed from single multi-walled carbon nanotube (MWNT). The MWNT was mounted with a sharpened platinum wire electrode. After insulating with electropolymerized phenol and subsequent cutting, a ~150 nm diameter nanodisk electrode was obtained. Similar carbon nanotube electrode, which modified onto carbon fiber electrode surface, was also demonstrated by Chen et al.[36]

Most nanoelectrodes fabricated from carbon nanotubes are electrode arrays. Koehne et al[111] reported the fabrication and characterization of carbon nanotube nanoelectrode arrays. The density and diameter of carbon nanotubes can be roughly controlled by lithography. Similar carbon nanotube electrode arrays have also been demonstrated[16,112] and their applications on bio-sensors were also reported.[17,20]

1.6. Objectives of this thesis

As noted above, carbon materials are very important in electrochemical applications. The incorporation of carbon materials in micro- and nanoscale devices is being widely investigated due to the promise of enhanced functionality. Carbon nanotubes have been widely investigated. However, positioning and addressability of single carbon nanotubes are still challenging. This provides the motivation for the development of new processes to produce nanoscale carbon materials. The objective of this thesis work was to develop the methodology for the fabrication of nanometer sized graphitic carbon structures. A secondary objective was to explore electrochemical and spectroscopic applications of these nanostructures.

Chapter 2 addresses the characterization and the electrochemical reactivity of the material used in the nanofabrication process: pyrolyzed SU-8 photoresist. In chapter 3, attention is focused on the fabrication of conducting, nanometer sized carbon structures and their characterization.

The analytical applications of nanoelectrodes are an expanding area of research. This is due primarily to research into low volume electroanalytical sensors, which have become increasingly relevant as engineers and scientists explore the analytical benefits of miniaturization in electrochemical detection. Chapter 4 describes the fabrication and electrochemical characterization of single carbon nanoband electrode and their arrays.

Chapter 5 reports on Au electrodeposition on carbon film electrodes. The nucleation mechanism and growth process are investigated by both electrochemical methods and SEM. Chapter 6 describes Au deposition on the carbon micro- and nanoband electrodes. Multi-branched Au nanopaticles are obtained and a deposition mechanism is proposed. Their application as surface enhanced Raman spectroscopy (SERS) substrate is also demonstrated.

1.6 References:

1. Ozin, G. A.; Hou, K.; Lotsch, B. V.; Cademartiri, L.; Puzzo, D. P.; Scotognella, F.; Ghadimi, A.; Thomson, J., Nanofabrication by self-assembly. *Materials Today* **2009,** 12, 12-23.
2. Cheng, J. Y.; Ross, C. A.; Smith, H. I.; Thomas, E. L., Templated self-assembly of block copolymers: Top-down helps bottom-up. *Advanced Materials* **2006,** 18, 2505-2521.
3. Wei, D.; Bailey, M. J. A.; Andrew, P.; Ryhanen, T., Electrochemical biosensors at the nanoscale. *Lab on a Chip* **2009,** 9, 2123-2131.
4. Wu, Y. H.; Hu, S. S., Electrochemistry at nanoelectrodes. *Indian Journal of Chemistry Section a-Inorganic Bio-Inorganic Physical Theoretical & Analytical Chemistry* **2005,** 44, 891-898.
5. Arrigan, D. W. M., Nanoelectrodes, nanoelectrode arrays and their applications. *Analyst* **2004,** 129, 1157-1165.
6. Zoski, C. G., Ultramicroelectrodes: Design, fabrication, and characterization. *Electroanalysis* **2002,** 14, 1041-1051.
7. Niwa, O., Electroanalytical chemistry with carbon film electrodes and micro and nano-structured carbon film-based electrodes. *Bulletin of the Chemical Society of Japan* **2005,** 78, 555-571.
8. McCreery, R. L., Advanced carbon electrode materials for molecular electrochemistry. *Chemical Reviews* **2008,** 108, 2646-2687.
9. Landstrass, M. I.; Ravi, K. V., Resistivity of chemical vapor-deposited diamond films. *Applied Physics Letters* **1989,** 55, 975-977.

10. Swain, G. M.; Ramesham, R., The electrochemical activity of boron-doped polycrystalline diamond thin-film electrodes. *Analytical Chemistry* **1993,** 65, 345-351.

11. Kalish, R.; Uzansaguy, C.; Samoiloff, A.; Locher, R.; Koidl, P., Doping of polycrystalline diamond by boron ion-implantation. *Applied Physics Letters* **1994,** 64, 2532-2534.

12. Wood, P.; Wydeven, T.; Tsuji, O., Influence of reactant gas-composition on selected properties of N-doped hydrogenated amorphous-carbon films. *Thin Solid Films* **1995,** 258, 151-158.

13. Veerasamy, V. S.; Amaratunga, G. A. J.; Davis, C. A.; Timbs, A. E.; Milne, W. I.; McKenzie, D. R., N-type doping of highly tetrahedral diamond-like amorphous-carbon. *Journal of Physics-Condensed Matter* **1993,** 5, L169-L174.

14. Bohr, S.; Haubner, R.; Lux, B., Influence of phosphorus addition on diamond CVD. *Diamond and Related Materials* **1995,** 4, 133-144.

15. Ajayan, P. M.; Iijima, S., Smallest carbon nanotube. *Nature* **1992,** 358, 23-23.

16. Dumitrescu, I.; Unwin, P. R.; Wilson, N. R.; Macpherson, J. V., Single-walled carbon nanotube network ultramicroelectrodes. *Analytical Chemistry* **2008,** 80, 3598-3605.

17. Tu, Y.; Lin, Y. H.; Yantasee, W.; Ren, Z. F., Carbon nanotubes based nanoelectrode arrays: Fabrication, evaluation, and application in voltammetric analysis. *Electroanalysis* **2005,** 17, 79-84.

18. Heller, I.; Kong, J.; Heering, H. A.; Williams, K. A.; Lemay, S. G.; Dekker, C., Individual single-walled carbon nanotubes as nanoelectrodes for electrochemistry. *Nano Letters* **2005,** 5, 137-142.

19. Li, J.; Ng, H. T.; Cassell, A.; Fan, W.; Chen, H.; Ye, Q.; Koehne, J.; Han, J.; Meyyappan, M., Carbon nanotube nanoelectrode array for ultrasensitive DNA detection. *Nano Letters* **2003,** 3, 597-602.

20. Koehne, J.; Chen, H.; Li, J.; Cassell, A. M.; Ye, Q.; Ng, H. T.; Han, J.; Meyyappan, M., Ultrasensitive label-free DNA analysis using an electronic chip based on carbon nanotube nanoelectrode arrays. *Nanotechnology* **2003,** 14, 1239-1245.

21. Azamian, B. R.; Davis, J. J.; Coleman, K. S.; Bagshaw, C. B.; Green, M. L. H., Bioelectrochemical single-walled carbon nanotubes. *Journal of the American Chemical Society* **2002,** 124, 12664-12665.

22. Lee, G. J.; Lim, J. E.; Park, J. H.; Choi, S. K.; Hong, S.; Park, H. K., Neurotransmitter detection by enzyme-immobilized CNT-FET. *Current Applied Physics* **2009,** 9, S25-S28.

23. Abe, M.; Murata, K.; Ataka, T.; Matsumoto, K., Comparison of sensitivities of carbon nanotube field-effect transistor biosensors with and without top metal gate. *Journal of Applied Physics* **2008,** 104.

24. Rogers, K. R., Recent advances in biosensor techniques for environmental monitoring. *Analytica Chimica Acta* **2006,** 568, 222-231.

25. Stern, E.; Vacic, A.; Reed, M. A., Semiconducting nanowire field-effect transistor biomolecular sensors. *IEEE Transactions on Electron Devices* **2008,** 55, 3119-3130.

26. Hu, P.; Fasoli, A.; Park, J.; Choi, Y.; Estrela, P.; Maeng, S. L.; Milne, W. I.; Ferrari, A. C., Self-assembled nanotube field-effect transistors for label-free protein biosensors. *Journal of Applied Physics* **2008,** 104.

27. McCreery, R. L., Carbon electrodes: Structural effects on electron transfer kinetics. In *Electroanalytical Chemistry*, Bard, A. J., Ed. New York, 1991; pp 221-374.

28. Pocard, N. L.; Alsmeyer, S. C.; McCreery, R. L.; Neenan, T. X.; Callstrom, M. R., Doped glassy carbon: A new material for electrocatalysis. *Journal of Material Chemistry* **1992,** 2, 771-184.

29. McDermott, M. T.; McDermott, C. A.; McCreery, R. L., Scanning tunneling microscopy of carbon surfaces - relationships between electrode-kinetics, capacitance, and morphology for glassy-carbon electrodes. *Analytical Chemistry* **1993,** 65, 937-944.

30. Jenkins, G. M.; Kawamura, K., Structure of glassy carbon. *Nature* **1971,** 231, 175-179.

31. Jenkins, G. M.; Kawamura, K.; Ban, L. L., Formation and structure of polymeric carbons. *Proceedings of the Royal Society of London Series a-Mathematical and Physical Sciences* **1972,** 327, 501-506.

32. Renschler, C. L.; Sylwester, A. P.; Salgado, L. V., Carbon-films from polyacrylonitrile. *Journal of Materials Research* **1989,** 4, 452-457.

33. Chung, T. C.; Schlesinger, Y.; Etemad, S.; Macdiarmid, A. G.; Heeger, A. J., Optical studies of pyrolyzed polyacrylonitrile. *Journal of Polymer Science Part B-Polymer Physics* **1984,** 22, 1239-1246.

34. Renschler, C. L.; Sylwester, A. P., Conductive, spin-cast carbon-films from polyacrylonitrile. *Applied Physics Letters* **1987,** 50, 1420-1422.

35. Kinoshita, K., *Carbon: Electrochemical and physicochemical properties*. Wiley: New York, 1988.

36. Chen, R. S.; Huang, W. H.; Tong, H.; Wang, Z. L.; Cheng, J. K., Carbon fiber nanoelectrodes modified by single-walled carbon nanotubes. *Analytical Chemistry* **2003,** 75, 6341-6345.

37. Chen, S. L.; Kucernak, A., The voltammetric response of nanometer-sized carbon electrodes. *Journal of Physical Chemistry B* **2002,** 106, 9396-9404.

38. Chen, S. L.; Kucernak, A., Fabrication of carbon microelectrodes with an effective radius of 1 nm. *Electrochemistry Communications* **2002,** 4, 80-85.

39. Chen, S. L.; Kucernak, A., Electrodeposition of platinum on nanometer-sized carbon electrodes. *Journal of Physical Chemistry B* **2003,** 107, 8392-8402.

40. Fei, J. J.; Wu, K. B.; Wang, F.; Hu, S. S., Glucose nanosensors based on redox polymer/glucose oxidase modified carbon fiber nanoelectrodes. *Talanta* **2005,** 65, 918-924.

41. Wu, W. Z.; Huang, W. H.; Wang, W.; Wang, Z. L.; Cheng, J. K.; Xu, T.; Zhang, R. Y.; Chen, Y.; Liut, J., Monitoring dopamine release from single

living vesicles with nanoelectrodes. *Journal of the American Chemical Society* **2005,** 127, 8914-8915.

42. Bron, M., Carbon black supported gold nanoparticles for oxygen electroreduction in acidic electrolyte solution. *Journal of Electroanalytical Chemistry* **2008,** 624, 64-68.

43. Ranganathan, S.; McCreery, R. L., Electroanalytical performance of carbon films with near-atomic flatness. *Analytical Chemistry* **2001,** 73, 893-900.

44. Ranganathan, S.; McCreery, R.; Majji, S. M.; Madou, M., Photoresist-derived carbon for microelectromechanical systems and electrochemical applications. *Journal of the Electrochemical Society* **2000,** 147, 277-282.

45. McDermott, M. T.; Kneten, K.; McCreery, R. L., Anthraquinonedisulfonate adsorption, electron-transfer kinetics, and capacitance on ordered graphite-electrodes - the important role of surface-defects. *Journal of Physical Chemistry* **1992,** 96, 3124-3130.

46. McDermott, M. T.; McCreery, R. L., Scanning-tunneling-microscopy of ordered graphite and glassy-carbon surfaces - electronic control of quinone adsorption. *Langmuir* **1994,** 10, 4307-4314.

47. McCreery, R. L.; Cline, K. K.; McDermott, C. A.; McDermott, M. T., Control of reactivity at carbon electrode surfaces. *Colloids and Surfaces A-Physicochemical and Engineering Aspects* **1994,** 93, 211-219.

48. Chen, P. H.; McCreery, R. L., Control of electron transfer kinetics at glassy carbon electrodes by specific surface modification. *Analytical Chemistry* **1996,** 68, 3958-3965.

49. Ranganathan, S.; Kuo, T. C.; McCreery, R. L., Facile preparation of active glassy carbon electrodes with activated carbon and organic solvents. *Analytical Chemistry* **1999,** 71, 3574-3580.

50. Kepley, L. J.; Bard, A. J., Ellipsometric, electrochemical, and elemental characterization of the surface phase produced on glassy-carbon electrodes by electrochemical activation. *Analytical Chemistry* **1988,** 60, 1459-1467.

51. Gonon, F. G.; Fombarlet, C. M.; Buda, M. J.; Pujol, J. F., Electrochemical treatment of pyrolytic carbon-fiber electrodes. *Analytical Chemistry* **1981,** 53, 1386-1389.

52. Mazur, S.; Matusinovic, T.; Cammann, K., Organic-reactions of oxide-free carbon surfaces, an electroactive derivative. *Journal of the American Chemical Society* **1977,** 99, 3888-3890.

53. Rice, R. J.; McCreery, R. L., Effects of wavelength, pulse duration and power-density on laser activation of glassy-carbon electrodes. *Journal of Electroanalytical Chemistry* **1991,** 310, 127-138.

54. Delamar, M.; Hitmi, R.; Pinson, J.; Saveant, J. M., Covalent modification of carbon surfaces by grafting of functionalized aryl radicals produced from electrochemical reduction of diazonium salts. *Journal of the American Chemical Society* **1992,** 114, 5883-5884.

55. Barbier, B.; Pinson, J.; Desarmot, G.; Sanchez, M., Electrochemical bonding of amines to carbon-fiber surfaces toward improved carbon-epoxy composites. *Journal of the Electrochemical Society* **1990,** 137, 1757-1764.

56. Deinhammer, R. S.; Ho, M.; Anderegg, J. W.; Porter, M. D., Electrochemical oxidation of amine-containing compounds - a route to the surface modification of glassy-carbon electrodes. *Langmuir* **1994,** 10, 1306-1313.

57. Downard, A. J.; bin Mohamed, A., Suppression of protein adsorption at glassy carbon electrodes covalently modified with tetraethylene glycol diamine. *Electroanalysis* **1999,** 11, 418-423.

58. Ssenyange, S.; Anariba, F.; Bocian, D. F.; McCreery, R. L., Covalent bonding of alkene and alkyne reagents to graphitic carbon surfaces. *Langmuir* **2005,** 21, 11105-11112.

59. Allongue, P.; Delamar, M.; Desbat, B.; Fagebaume, O.; Hitmi, R.; Pinson, J.; Saveant, J. M., Covalent modification of carbon surfaces by aryl radicals generated from the electrochemical reduction of diazonium salts. *Journal of the American Chemical Society* **1997,** 119, 201-207.

60. Kariuki, J. K.; McDermott, M. T., Nucleation and growth of functionalized aryl films on graphite electrodes. *Langmuir* **1999,** 15, 6534-6540.

61. Kariuki, J. K.; McDermott, M. T., Formation of multilayers on glassy carbon electrodes via the reduction of diazonium salts. *Langmuir* **2001,** 17, 5947-5951.

62. Combellas, C.; Kanoufi, F.; Pinson, J.; Podvorica, F. I., Time-of-flight secondary ion mass spectroscopy characterization of the covalent bonding between a carbon surface and aryl groups. *Langmuir* **2005,** 21, 280-286.

63. Nowak, A. M.; McCreery, R. L., Characterization of carbon/nitroazobenzene/titanium molecular electronic junctions with photoelectron and Raman spectroscopy. *Analytical Chemistry* **2004,** 76, 1089-1097.

64. Kalakodimi, R. P.; Nowak, A. M.; McCreery, R. L., Carbon/molecule/metal and carbon/molecule/metal oxide molecular electronic junctions. *Chemistry of Materials* **2005,** 17, 4939-4948.

65. Wightman, R. M., Microvoltammetric electrodes. *Analytical Chemistry* **1981,** 53, 1125-1134.

66. Pons, S.; Fleischmann, M., The behavior of microelectrodes. *Analytical Chemistry* **1987,** 59, A1391-A1399.

67. Kawagoe, K. T.; Jankowski, J. A.; Wightman, R. M., Etched carbon-fiber electrodes as amperometric detectors of catecholamine secretion from isolated biological cells. *Analytical Chemistry* **1991,** 63, 1589-1594.

68. Slevin, C. J.; Gray, N. J.; Macpherson, J. V.; Webb, M. A.; Unwin, P. R., Fabrication and characterisation of nanometre-sized platinum electrodes

for voltammetric analysis and imaging. *Electrochemistry Communications* **1999,** 1, 282-288.

69. Katemann, B. B.; Schulte, A.; Schuhmann, W., Constant-distance mode scanning electrochemical microscopy. Part II: High-resolution SECM imaging employing Pt nanoelectrodes as miniaturized scanning probes. *Electroanalysis* **2004,** 16, 60-65.

70. Bard, A. J.; Faulkner, L. R., Electrochemical methods: Fundamentals and applications, Second Edition. **2000**.

71. Ewing, A. G.; Dayton, M. A.; Wightman, R. M., Pulse voltammetry with microvoltammetric electrodes. *Analytical Chemistry* **1981,** 53, 1842-1847.

72. Strein, T. G.; Ewing, A. G., Characterization of submicron-sized carbon electrodes insulated with a phenol allylphenol copolymer. *Analytical Chemistry* **1992,** 64, 1368-1373.

73. Huang, W. H.; Pang, D. W.; Tong, H.; Wang, Z. L.; Cheng, J. K., A method for the fabrication of low-noise carbon fiber nanoelectrodes. *Analytical Chemistry* **2001,** 73, 1048-1052.

74. Meulemans, A.; Poulain, B.; Baux, G.; Tauc, L.; Henzel, D., Micro carbon electrode for intracellular voltammetry. *Analytical Chemistry* **1986,** 58, 2088-2091.

75. Wang, C. Y.; Chen, Y. J.; Wang, F. X.; Hu, X. Y., Fabrication of nanometer-sized carbon electrodes by the controllable electrochemical deposition. *Electrochimica Acta* **2005,** 50, 5588-5593.

76. Nagale, M. P.; Fritsch, I., Individually addressable, submicrometer band electrode arrays. 1. Fabrication from multilayered materials. *Analytical Chemistry* **1998,** 70, 2902-2907.

77. Wehmeyer, K. R.; Deakin, M. R.; Wightman, R. M., Electroanalytical properties of band electrodes of submicrometer width. *Analytical Chemistry* **1985,** 57, 1913-1916.

78. Szabo, A.; Cope, D. K.; Tallman, D. E.; Kovach, P. M.; Wightman, R. M., Chronoamperometric current at hemicylinder and band microelectrodes-theory and experiment. *Journal of Electroanalytical Chemistry* **1987,** 217, 417-423.

79. Seibold, J. D.; Scott, E. R.; White, H. S., Diffusional transport to nanoscopic band electrodes. *Journal of Electroanalytical Chemistry* **1989,** 264, 281-289.

80. Morris, R. B.; Franta, D. J.; White, H. S., Electrochemistry at Pt band electrodes of width approaching molecular dimensions-breakdown of transport-equations at very small electrodes. *Journal of Physical Chemistry* **1987,** 91, 3559-3564.

81. Caston, S. L.; McCarley, R. L., Characteristics of nanoscopic Au band electrodes. *Journal of Electroanalytical Chemistry* **2002,** 529, 124-134.

82. Wang, J.; Brennsteiner, A.; Sylwester, A. P.; Renschler, C. L., Preparation and characterization of band nanoelectrodes made of carbonized polyacrylonitrile films. *Electroanalysis* **1991,** 3, 505-509.

83. Wang, J. Y.; Rongrong, X.; Baomin, T.; Wang, J. Y.; Renschler, C. L.; White, C. A., Nanoband electrodes for electrochemical stripping measurements down to the attomole range. *Analytica Chimica Acta* **1994,** 293, 43-48.

84. Wightman, R. M.; Wipf, D. O., *Electroanalytical chemistry*. Marcel Dekker: New York, 1989; p 267-353.

85. Davies, T. J.; Compton, R. G., The cyclic and linear sweep voltammetry of regular and random arrays of microdisc electrodes: Theory. *Journal of Electroanalytical Chemistry* **2005,** 585, 63-82.

86. Streeter, I.; Fietkau, N.; Del Campo, J.; Mas, R.; Munoz, F. X.; Compton, R. G., Voltammetry at regular microband electrode arrays: Theory and experiment. *Journal of Physical Chemistry C* **2007,** 111, 12058-12066.

87. Simm, A. O.; Banks, C. E.; Ward-Jones, S.; Davies, T. J.; Lawrence, N. S.; Jones, T. G. J.; Jiang, L.; Compton, R. G., Boron-doped diamond microdisc arrays: Electrochemical characterisation and their use as a substrate for the production of microelectrode arrays of diverse metals (Ag, Au, Cu) via electrodeposition. *Analyst* **2005,** 130, 1303-1311.

88. Ugo, P.; Moretto, L. M.; Bellomi, S.; Menon, V. P.; Martin, C. R., Ion-exchange voltammetry at polymer film-coated nanoelectrode ensembles. *Analytical Chemistry* **1996,** 68, 4160-4165.

89. Yang, M. H.; Qu, F. L.; Lu, Y. S.; He, Y.; Shen, G. L.; Yu, R. Q., Platinum nanowire nanoelectrode array for the fabrication of biosensors. *Biomaterials* **2006,** 27, 5944-5950.

90. Liu, L.; Jia, N. Q.; Zhou, Q.; Yan, M. M.; Jiang, Z. Y., Electrochemically fabricated nanoelectrode ensembles for glucose biosensors. *Materials Science & Engineering C-Biomimetic and Supramolecular Systems* **2007,** 27, 57-60.

91. Hulteen, J. C.; Menon, V. P.; Martin, C. R., Template preparation of nanoelectrode ensembles - Achieving the 'pure-radial' electrochemical-response limiting case. *Journal of the Chemical Society-Faraday Transactions* **1996,** 92, 4029-4032.

92. Menon, V. P.; Martin, C. R., Fabrication and evaluation of nanoelectrode ensembles. *Analytical Chemistry* **1995,** 67, 1920-1928.

93. Baker, W. S.; Crooks, R. M., Independent geometrical and electrochemical characterization of arrays of nanometer-scale electrodes. *Journal of Physical Chemistry B* **1998,** 102, 10041-10046.

94. Jeoung, E.; Galow, T. H.; Schotter, J.; Bal, M.; Ursache, A.; Tuominen, M. T.; Stafford, C. M.; Russell, T. P.; Rotello, V. M., Fabrication and characterization of nanoelectrode arrays formed via block copolymer self-assembly. *Langmuir* **2001,** 17, 6396-6398.

95. Madou, M., *Fundamentals of Microfabrication*. 2002.

96. Finot, E.; Bourillot, E.; Meunier-Prest, R.; Lacroute, Y.; Legay, G.; Cherkaoui-Malki, M.; Latruffe, N.; Siri, O.; Braunstein, P.; Dereux, A., Performance of interdigitated nanoelectrodes for electrochemical DNA biosensor. *Ultramicroscopy* **2003**, 97, 441-449.

97. Jiao, L. Y.; Gao, H. J.; Zhang, G. M.; Xie, G. Y.; Zhou, X.; Zhang, Y. Y.; Zhang, Y. Y.; Gao, B.; Luo, G.; Wu, Z. Y.; Zhu, T.; Zhang, J.; Liu, Z. F.; Mu, S. C.; Yang, H. F.; Gu, C. Z., Fabrication of metallic nanostructures by negative nanoimprint lithography. *Nanotechnology* **2005,** 16, 2779-2784.

98. Ssenyange, S.; Du, R.; McDermott, M. T., Fabrication of arrays of carbon micro- and nanostructures via electrochemical etching. *Micro & Nano Letters* **2009,** 4, 22-26.

99. Ssenyange, S.; Taylor, J.; Harrison, D. J.; McDermott, M. T., A glassy carbon microfluidic device for electrospray mass spectrometry. *Analytical Chemistry* **2004,** 76, 2393-2397.

100. Kiema, G. K.; Ssenyange, S.; McDermott, M. T., Microfabrication of glassy carbon by electrochemical etching. *Journal of the Electrochemical Society* **2004,** 151, C142-C148.

101. Nagale, M. P.; Fritsch, I., Individually addressable, submicrometer band electrode arrays. 2. Electrochemical characterization. *Analytical Chemistry* **1998,** 70, 2908-2913.

102. Ueno, K.; Hayashida, M.; Ye, J. Y.; Misawa, H., Fabrication and electrochemical characterization of interdigitated nanoelectrode arrays. *Electrochemistry Communications* **2005,** 7, 161-165.

103. Blackstock, J. J. Fabrication and characterization of ultra-flat thin-film material surfaces for nanoscale research and device applications. Ph.D thesis, University of Alberta, Edmonton, 2005.

104. Schueller, O. J. A.; Brittain, S. T.; Marzolin, C.; Whitesides, G. M., Fabrication and characterization of glassy carbon MEMS. *Chemistry of Materials* **1997,** 9, 1399-1406.

105. Schueller, O. J. A.; Brittain, S. T.; Whitesides, G. M., Fabrication of glassy carbon microstructures by pyrolysis of microfabricated polymeric precursors. *Advanced Materials* **1997,** 9, 477-482.

106. Schueller, O. J. A.; Brittain, S. T.; Whitesides, G. M., Fabrication of glassy carbon microstructures by soft lithography. *Sensors and Actuators a-Physical* **1999,** 72, 125-139.

107. Kostecki, R.; Song, X.; Kinoshita, K., Electrochemical analysis of carbon interdigitated microelectrodes. *Electrochemical and Solid State Letters* **1999,** 2, 465-467.

108. Xu, H.; Malladi, K.; Wang, C.; Kulinsky, L.; Song, M.; Madou, M., Carbon post-microarrays for glucose sensors. *Biosensors & Bioelectronics* **2008,** 23, 1637-1644.

109. Heller, I.; Kong, J.; Williams, K. A.; Dekker, C.; Lemay, S. G., Electrochemistry at single-walled carbon nanotubes: The role of band structure and quantum capacitance. *Journal of the American Chemical Society* **2006,** 128, 7353-7359.

110. Campbell, J. K.; Sun, L.; Crooks, R. M., Electrochemistry using single carbon nanotubes. *Journal of the American Chemical Society* **1999,** 121, 3779-3780.

111. Koehne, J.; Li, J.; Cassell, A. M.; Chen, H.; Ye, Q.; Ng, H. T.; Han, J.; Meyyappan, M., The fabrication and electrochemical characterization of carbon nanotube nanoelectrode arrays. *Journal of Materials Chemistry* **2004,** 14, 676-684.

112. Tu, Y.; Lin, Y. H.; Ren, Z. F., Nanoelectrode arrays based on low site density aligned carbon nanotubes. *Nano Letters* **2003,** 3, 107-109.

Chapter 2. Characterization of Pyrolyzed SU-8 Carbon Films (P8)

This chapter is focused mainly on the fabrication and characterization of thin carbon films prepared by the pyrolysis of a commercial negative photoresist, SU-8. Spin coated SU-8 resist films were first exposed to ultraviolet light. Then they were pyrolyzed in a quartz tube furnace with flowing inert gas. Their composition and properties were subsequently characterized using atomic force microscopy (AFM), X-ray photoelectron spectroscopy (XPS), Raman and electrochemistry.

2.1 Introduction

Carbon has been widely used as an electrode substrate in electrochemistry due to its wide potential window, low cost, good electrical conductivity, and good biocompatibility.[1] For example, carbon fibers have been extensively applied as electrochemical probes for in vivo monitoring in living tissues.[2] Graphite and hard carbon are widely used in the Li ion battery applications due to the Li intercalation/de-intercalation capacity.[3] Glassy carbons (GC) are commonly used in analytical chemistry due to the low background current.[1] Mesoporous carbon is widely used as catalyst supporters for the fuel cell research due to the strong adsorption and high conductivity.[4] In recent years, increasing attentions have been drawn to the fabrication of low-cost, disposable carbon film electrodes.

Carbon film electrodes have advantages over bulk carbons. For example, the main source of irreproducibility in using a glassy carbon electrode has been irreproducible surface preparation. Polishing is the most popular surface pre-treatment method employed in labs. It is difficult, however, to reproduce polishing procedures especially from lab to lab.[5] Single use, disposable carbon films don't need the polishing pre-treatment and can be used as electrodes directly. Other advantages of carbon films include controllable shape, thickness and dimensions. All these lead to a wide variety of applications.[6-16] Although bulk graphite materials show black colors, thin films (thickness < 80 nm) of graphite-based-carbon have been shown to be partially transparent in the visible wavelength range and thus have been used in spectroscopic applications.[6-8] Carbon based molecular electronics have been proposed by grafting organic molecules onto a thin carbon film surface.[9-11] Recently, much emphasis has been put on carbon film electrodes with micrometer dimensions. Microfabricated carbon film electrodes patterned by photolithography have been used as microelectrode detectors in the applications of microfluidic chips,[12] interdigitated microelectrode arrays,[13,14] and even more complex microstructures for batteries[15] and micromechanical systems.[16] All these applications have stimulated the development of carbon film electrodes.

Carbon films can be fabricated using a wide variety of techniques. Thick carbon film electrodes can be fabricated by screen printed methods.[17-20] By pushing commercial carbon inks through a pattered screen, graphite film electrodes with different dimensions can be obtained.[20] McDermott and coworkers[21] have described the fabrication of carbon thin films by electron-beam deposition. The carbon films deposited onto H-terminated silicon surface show an extremely flat surface and strong adhesion to the substrate. Carbon film electrodes consisting of sp^2 and sp^3 carbon atoms prepared by electron-cyclotron-resonance (ECR) plasma sputtering have been reported.[22] This type of carbon films is also quite flat and shows high conductivity. Other fabrication methods of carbon film electrodes also include deposition from plasma,[23] ion-sputtering,[24] cathode arc deposition,[25] and pyrolysis of polymers.[26-28] Among all these methods, pyrolysis of polymer precursors has been widely studied both theoretically[29-31] and experimentally.[32-34]

The treatment of organic materials at high temperature in inert atmosphere to produce solid carbon is well-known.[35,36] This process is known as pyrolysis or carbonization and involves cross-linking and side chain elimination from the original polymer. Recently, a number of groups have revisited carbonization as a means to produce carbon materials with various shapes and sizes. Extremely flat carbon-film electrodes can be produced by the pyrolysis of spin-coated photoresist films on a silicon substrate.[26-28] These types of carbon surfaces have found unique applications as substrates for molecular junction studies.[11,37] Patterning techniques have been combined with carbonization to prepare micro-sized carbonaceous structures. Whitesides and co-workers used soft-lithographic techniques to pattern polymeric precursors, the pyrolysis of which resulted in various carbon structures including free-standing microelectromechanical systems (MEMS).[38-40] Madou has investigated the photolithographic patterning and carbonization of various photoresist polymers.[15,16,41,42] The fabrication of high aspect ratio, 3D structures for MEMS applications is possible through careful control of exposure, soft-baking and development time.[16,42] Ordered arrays of carbon nanostructures can be prepared by the pyrolysis of various block co-polymer films.[43,44] The size and spatial arrangement of these structures are governed by the original polymer film.

Carbon films pyrolyzed from photoresists (PPF) have been demonstrated.[26-28] Photoresists can be classified into positive photoresists and negative photoresists based on their different response to light. A positive photoresist is a type of photoresist in which portion of the photoresist exposed to light become soluble in the photoresist developer. A negative photoresist behaves in an opposite manner. One of the main ingredients of positive phtotresists is novolac resin. Novalac resin is a type of phenol formaldehyde resin. As mentioned in Chapter 1, phenol formaldehyde resin is also one of the major polymer precursors for the fabrication of glassy carbons (GC). Most of photoresists used for the fabrication of PPF are positive photoresists, therefore, PPF and GC share the same polymer precursor.

The current work, a commercial negative photoresist SU-8 has been chosen as the polymer precursor. Since its introduction by researchers at IBM, SU-8 resists have been used in both optical lithography[45] and e-beam lithography.[46] SU-8 resists are negative resists. Compared with positive photoresist, whose

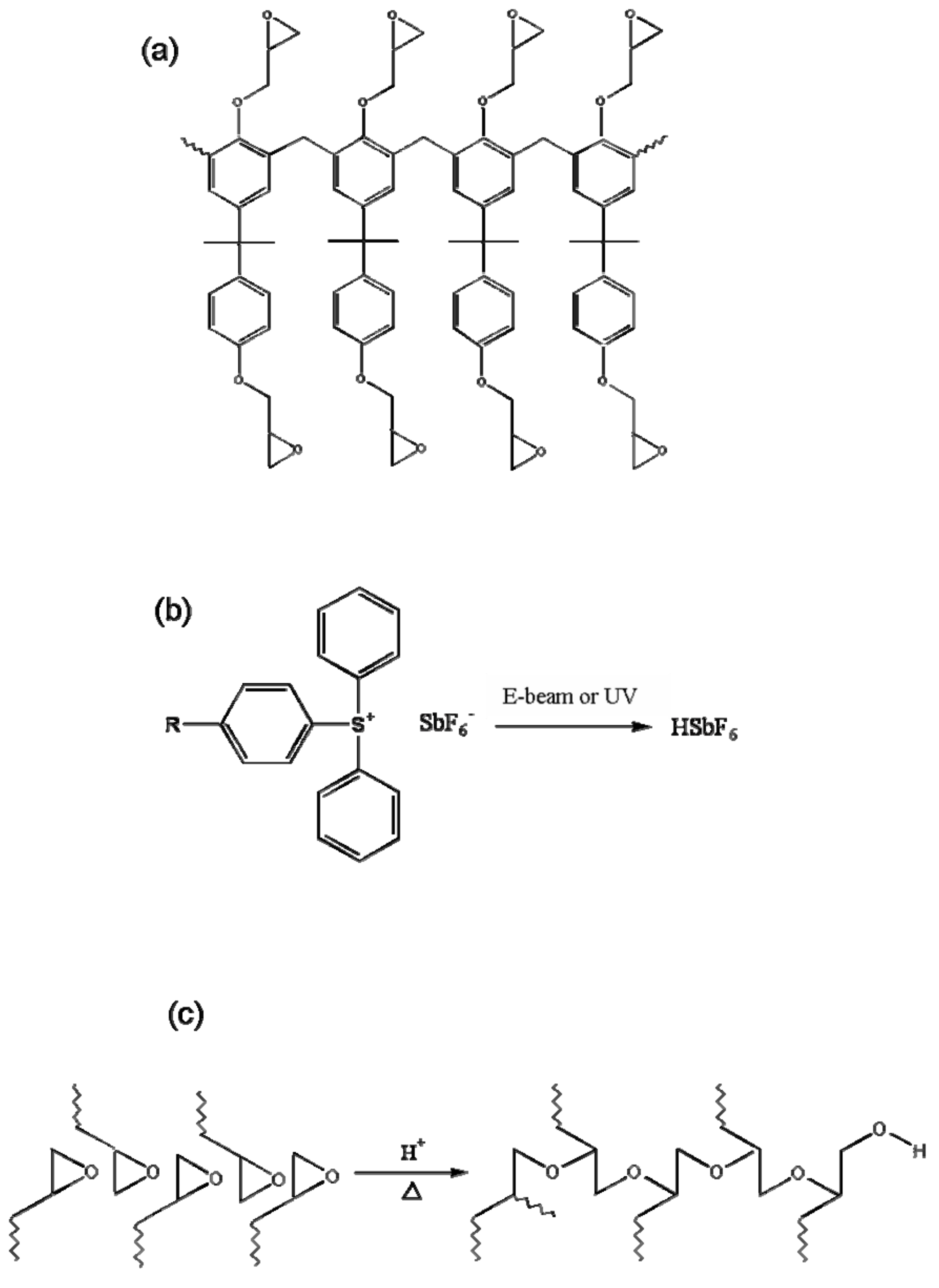

Figure 2.1. Chemical structures of (a) the Bisphenol A novolak resin oligomer, (b) photo acid generator (triarylsulfonium hexafluroantimonate), and (c) their chain reaction catalyzed by protons.

ingredients are predominantly and extensively cross-linked aromatic polymers (molecular weight > 5000 g/mol),[47] negative resists are composed of polymer monomers, which are less cross-linked and have a much lower molecular weight. For example, the major component of SU-8 is a Bisphenol A Novolak epoxy oligomer whose molecular weight is about 1398 g/mol.[48] A photo acid generator (PAG) in the form of triarylsulfonium hexafluroantimonate salt is added for the cross-linking of the polymer when exposed to UV light or an electron beam.[46] The chemical structures of the oligomer and the PAG are shown in Figure 2.1. When exposed to UV light or an electron beam, the PAG decomposes to form hexafluoroantimonic acid. The acid protonates the epoxides on the oligomer. The protonated ions then react with neutral epoxides to initiate a series of cross-linking reactions, thus yielding a highly cross-linked and insoluble polymer network. High cross-linking of polymer precursors is very important for the formation of carbon structures by pyrolysis.[49] Non- or low crosslinked polymer evaporates at high temperature before pyrolysis can start.[41,42]

In this chapter, carbon film electrodes were fabricated by pyrolysis from thin film of negative photoresist SU-8. After coating onto silicon wafers, the SU-8 samples were exposed to UV light to initiate the cross-linking and subsequently carbonized at high temperature with reducing atmosphere in a quartz tube furnace. The resulting carbon films were characterized by AFM, XPS, Raman spectroscopy and electrochemistry. The results are compared with other type of carbon films.[21,28] As SU-8 is also widely used as an e-beam resist, nanometer sized SU-8 structures can be patterned by e-beam lithography conveniently. The fabrication and characterization of nanometer sized SU-8 will be described in the Chapter 3.

2.2 Experimental Section

2.2.1 Reagents and materials

Sulfuric acid (H_2SO_4, Fisher), Hydrogen peroxide (H_2O_2, Fisher), Potassium chloride (KCl, Fisher), $K_3Fe(CN)_6$ (Caledon), and $Ru(NH_3)_6Cl_3$ (Sterm Chemicals) were used as received. Aqueous solutions were prepared using distilled/deionized water (18 M Ω·cm).

2.2.2 Preparation of pyrolyzed SU-8 carbon films (P8)

Prime grade Si(100), p-type, 500 μm thick, with a resistivity of 0.001-0.005 Ω·cm, prime grade Si(100), un-doped, 525 μm thick, with a resistivity of 3000-28000 Ω·cm, and quartz wafers, 500 μm thick with a roughness of 6 Å were purchased from University Wafer (South Boston, MA). Wafers were diced into 1 cm × 1 cm and cleaned with hot piranha solution (75% H_2SO_4: 25% H_2O_2) for 15 min to remove the organic surface contaminants. [*Warning: Piranha solution should be handled with extreme care; it is a strong oxidant and reacts violently with many organic materials. It also presents an explosion danger. All work should be performed under a fume hood.*] The substrates were dehydrated on a 200°C hot plate for 5 min before using. A Speciality Coating model P6708 spin coater was used to coat the substrate. The resist was NANO^{TM} SU-8 2000.1 manufactured by MicroChem Corp. (Newton, MA). The resist was spin-coated onto the substrates at a cycle speed of 4000 rpm for 30 s as suggested by the manufacturer. The resulting samples were softly baked at 65^{o}C for 1 min and 90^{o}C for 2 min. The samples were then exposed to UV light (405 nm) for 30 min, which is longer than the recommended exposure time by the manufacturer. The excess exposure ensures extensive crossing that leads to a sufficiently high molecular weight so that resist does not disappear on heating before the onset of pyrolysis. Post exposure baking (PEB) was carried out for 1 min at 65^{o}C followed by 10 min at 90^{o}C. Finally the samples were developed using MicroChem SU-8 developer for 60 s, followed by a 10 s immersion in isopropyl alcohol and N_2 blow drying.

The samples were pyrolyzed in a tube furnace (Lindberg) fitted with a quartz tube. Pyrolysis was conducted in an environment of forming gas (95% nitrogen + 5% hydrogen, Praxair, Edmonton) as reported previously.[26] Before heating, the tube was flushed with the forming gas for 1 h to ensure the reducing environment. The samples were heated at a rate of 10^{o}C/min and held at 1000^{o}C for 30 min. The samples were then gradually cooled down to room temperature. During the whole process, the tube was flushed by a continuous flow of forming gas to provide a reducing atmosphere.

2.2.3 Film thickness and resistivity measurements

The thickness of carbon film was measured by AFM. Five transmission electron microscopy (TEM) grids were put at different spots on sample surface when samples were exposed to UV. These grids behave like small masks and micron sized patterns can be generated on the surface. After pyrolysis, the edge of patterned structures was used to measure the thickness. Multiple measurements were carried out on each sample.

P8s fabricated on a 4 inch quartz wafer surface were used for the resistivity measurement. Sheet resistance of P8s was measured with a Keithley 2400 Source Meter connected with a 4-point probe. Figure 2.2 shows the photo of the four-probe system used in our experiment.

The schematic of four-point probe is shown on Figure 2.3. This probe consists of four equally spaced tungsten metal tips with finite radius. The diameter or width of thin film samples need to be approximately 40 times larger than the probe spacing in order to get an accurate measurement.[24]

Figure 2.2. Four-point probe system.

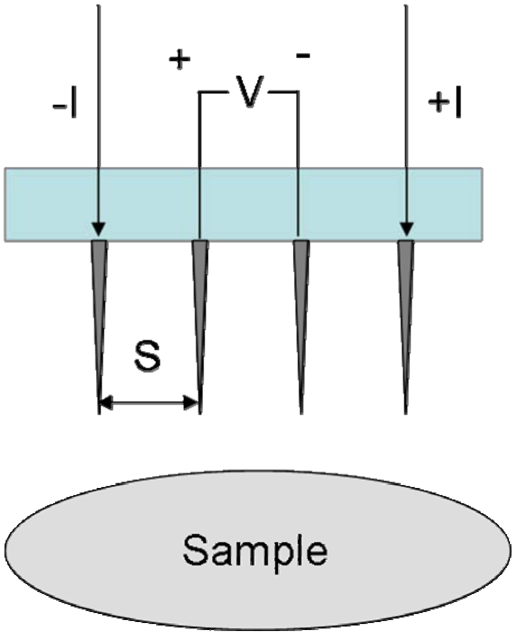

Figure 2.3. Schematic of four-point probe configuration.

The equation used for the calculation of sheet resistance is as follows.

$$R_s = \frac{\pi}{\ln 2}\left(\frac{V}{I}\right) \qquad (2.1)$$

where R_s = sheet resistance, V = voltage applied to the inner probes, I = current measured at the outer probes.

The resistivity can be calculated by multiplying the sheet resistance times the thickness of the carbon layer

$$\rho = R_s t \qquad (2.2)$$

where ρ = resistivity. t = thickness of the film.

2.2.4 Physical/chemical characterization

A “tape test” has been used to test the adhesion between the carbon films and underneath substrates by several groups.[26,28] Generally, an adhesive tape was pressed to stick to the surface of a carbon film electrode and then pulled away, well adhered carbon films are undisrupted while poorly adhered ones are peeled off.

Atomic force microscopy (AFM) was carried out using Multimode instrument from Digital Instruments (Santa Barbra, CA). Images were collected with Si_3N_4 cantilevers (Nanoprobes, Digital Instruments) with a spring constant of 0.12 N/m in the air. The images presented in this chapter are representatives of at least 5 images taken at different locations on each sample. Root mean square (RMS) roughness values for whole images were determined with the manufacturer’s software provided.

Raman spectroscopy measurements were carried out at room temperature in ambient atmosphere with Renishaw inVia Raman Microscope. An Ar ion excitation laser (514.5 nm) focused to a 5 μm spot was used. The spectral resolution of this system is about 1 cm^{-1}. The Raman spectra were recorded over the spectral region between 1000 and 1800 cm^{-1}, which provides the key information on the microstructure of carbon.

X-ray photoelectron spectra (XPS) were acquired with the Kratos Axis Ultra Spectrometer equipped with a monochromatic Al Kα source (1486.6 eV) operating at 15 mA and 14 kV. The pressure in the chamber was $\sim 8\times10^{-10}$ Torr at the time of measurement. For XPS depth profiling the sample was sputtered with

4 keV Ar^+ ions with a beam current of 0.3 μA on the sample. CASAXPS (V2.3.5) software (CASAXPS Software Ltd., UK) was used for the curve fitting. The spectra were corrected by a Shirley background subtraction and were then analyzed using nonlinear least-square fitting procedures.

Electrochemical experiments employed a bipotentiostat model AFCBP1 (Pine), a homemade silver/silver chloride (Ag/AgCl, saturated KCl) reference electrode, and a platinum wire as the counter electrode.

2.3 Results and Discussion

2.3.1 Film adhesion

An important issue in the fabrication of carbon film electrodes is the adhesion between the carbon and the substrate. It is known that carbon adheres poorly to a variety of substrates.[52,53] A simple "tape test" is commonly used to test the adhesion of thin films to substrates. The P8 samples prepared by our method passed the tape test (all the five P8 samples attempted passed the tape test). We attribute the strong adhesion in these films to the formation of a SiC layer at the carbon-Si interface. Spectroscopic evidence for the formation of this SiC layer will be presented later in this chapter.

2.3.2 Surface topography

Figure 2.4 shows tapping mode AFM images of 1 × 1 μm area of P8 sample. A line profile along a 1 μm line below shows the variation in z-axis height. A root mean square (RMS) roughness of 0.37 nm is measured.

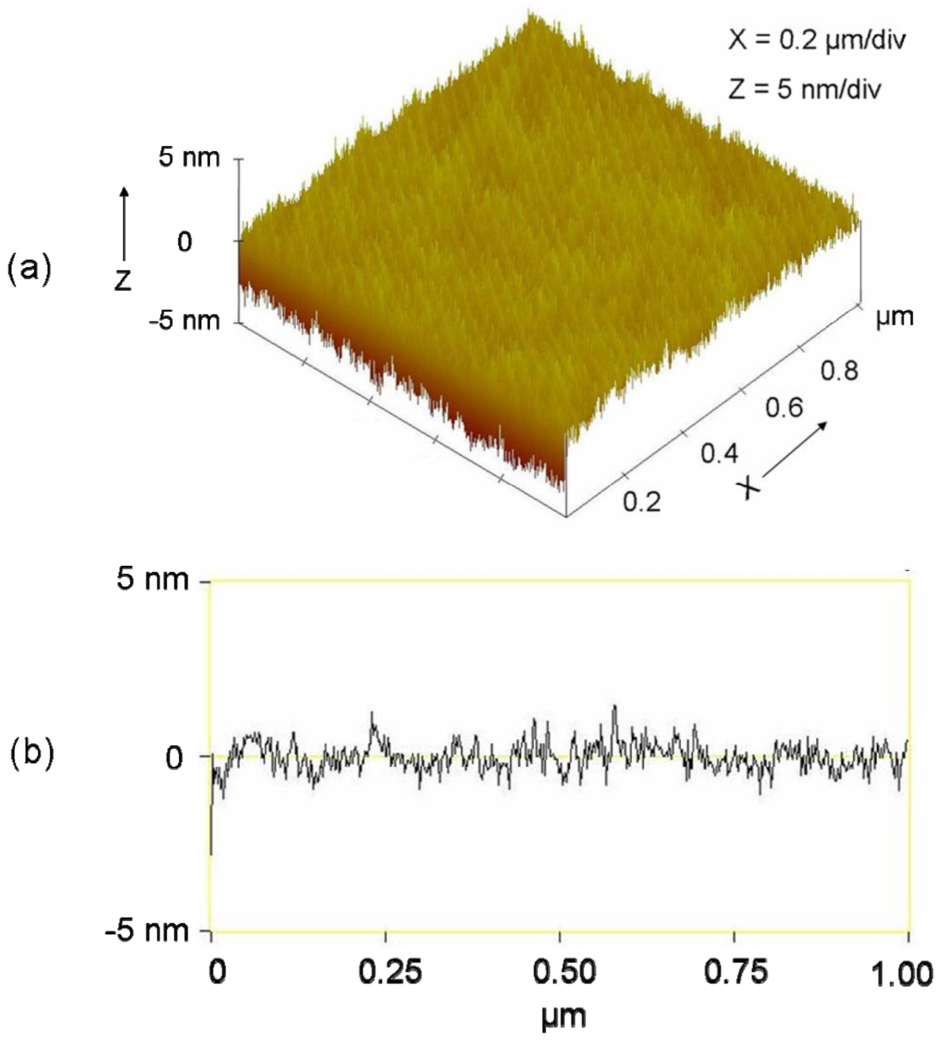

Figure 2.4. (a) AFM image of a 1 × 1 µm area of a pyrolyzed SU-8 carbon film. (b) Cross-sectional profile illustrates an RMS roughness of 0.4 nm.

AFM images similar to Figure 2.4 were obtained at random locations on different samples and provided similar results. No pinholes were observed on the carbon film surface by either AFM or SEM.

Table 2.1. RMS roughness results for different type of carbon films.

Type of carbon films	Ref.	RMS
P8	This work	0.39 ± 0.3 nm[a,b]
PPF	28	< 0.5 nm
E-beam carbon film	21	< 0.1 nm
Pyrolyzed e-beam carbon film	21	< 0.5nm

[a] Value reported is mean ± standard deviation from measurements of 5 samples

[b] RMS values are based on AFM images of 1 × 1 μm area

AFM measured roughness values have been reported for a number of different types of carbon film. For comparison, our values and some literature values are listed in Table 2.1. Although lab-to-lab comparison of AFM measured roughness is complicated by variations in tip shape and other imaging parameters, the data in Table 2.1 show that the P8s prepared in this work have comparable roughness to previously studied films. Such extreme flatness is very important for their potential applications in, for example, molecular electronics.

2.3.3 Film thickness and resistivity measurements

The thickness of P8 films was measured by AFM. Figure 2.5 shows an AFM image of the edge of a carbon film which was patterned using a TEM grid.

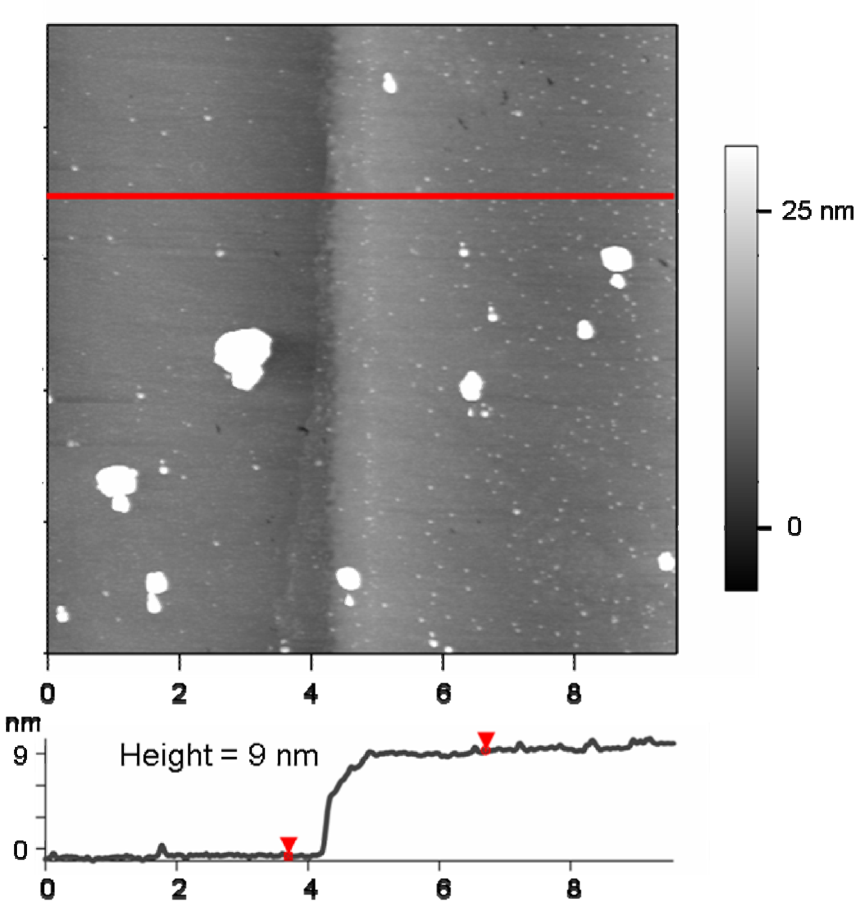

Figure 2.5. Thickness measurement of carbon film.

The sectional profile shows a carbon film thickness of 9 nm. Four independently prepared samples were used and multiple measurements (N = 5) were carried out on each sample. The thickness measured was in the 9 – 14 nm range. The average thickness was 11 nm.

These four carbonized SU-8 films yield a sheet resistance (R_s) value of $(5 \pm 4) \times 10^3\ \Omega/\square$ based on 4-probe resistance measurements. Considering the film thickness of 11 ± 3 nm, an average resistivity ($\rho = R_s \times$ thickness) of $6 \times 10^{-5}\ \Omega\cdot\mathrm{m}$ is obtained. The reported resistivity for other carbonized resists and for a common glassy carbon (Tokai) prepared at 1000°C is $\sim 5 \times 10^{-5}\ \Omega\cdot\mathrm{m}$.[27,54] While the resistivity of this material is significantly higher than that of metals (e.g., for Cu, $\rho = 1.7 \times 10^{-8}\ \Omega\cdot\mathrm{m}$), it is comparable to other graphitic materials.

2.3.4 Composition

The composition of carbonized materials is commonly characterized by the amount of oxygen on the surface or in the bulk. Typically the atomic ratio between oxygen and carbon (O/C) determined by XPS is the parameter used for characterization.[55] Figure 2.6 (a) contains survey spectra while Figures 2.6(b) and 2.6(c) are high resolution XPS spectra in the C 1s and O 1s region of a SU-8 film before and after carbonization. The C 1s spectrum of the SU-8 film, corrected for charging,[56] exhibits two peaks as shown in Figure 2.6(b). The peak at 284.6 eV corresponds to aliphatic and aromatic carbons in the polymer. The peak at 286.1 eV is diagnostic of carbon bound to oxygen in various forms.[57] The pyrolyzed material exhibits a single peak at 284.6 eV similar to that observed for ordered

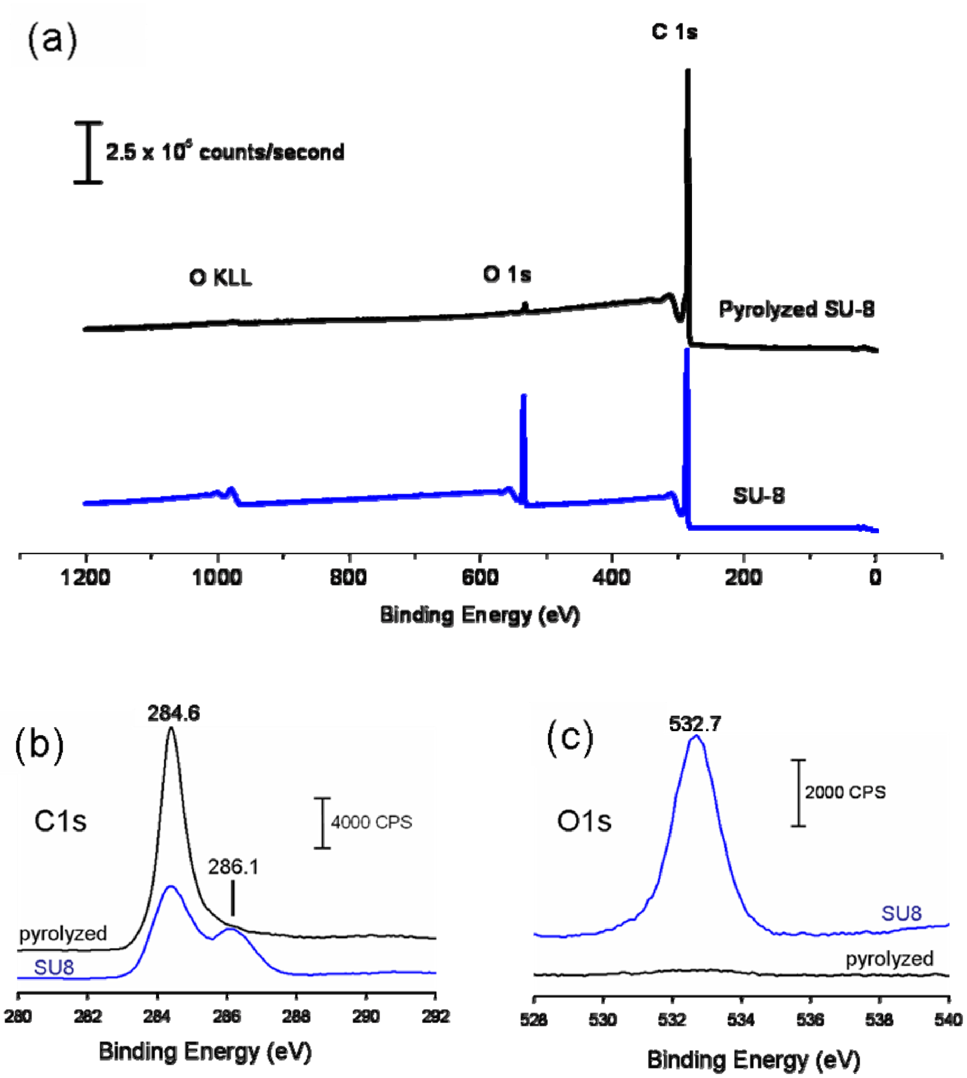

Figure 2.6. (a) XPS spectra of a SU-8 film before and after pyrolysis; (b) XPS spectrum of a pyrolyzed SU-8 film for the C 1s region; (c) XPS spectrum of the O 1s region.

graphite.[58] In the O 1s region [Figure 2.6 (c)], the SU-8 polymer exhibits a large oxygen peak at 532.7 eV that decreases significantly after pyrolysis. It is clear from the XPS spectra that a significant loss of oxygen accompanies carbonization. The O/C ratio of the SU-8 film is quite high (21.8 ± 0.2%) as expected based on the molecular structure of the polymer. The material resulting from the pyrolysis of SU-8 exhibits an O/C ratio 0.53 ± 0.4%. For comparison, polished glassy carbon, a commonly disordered graphitic material, yields an O/C ratio of 8-15%, while vacuum heat treated GC exhibits O/C of 1.5%.[55] Other photoresist formulations that have been carbonized exhibit an O/C ratio of 2.3%.[27] These results show that the films produced in this procedure are primarily carbon with a low level of surface oxygen. It is likely that pyrolysis in the reducing atmosphere of forming gas results in a material with a partially hydrogen-terminated surface.[59]

The composition of the entire carbon film can be probed with a combination of XPS and sputtering. Figure 2.7 (a) and (b) show a series of XPS spectra in the C 1s and Si 2p regions collected at a P8 carbon film following Ar^+ sputtering for various times. The peak at 284.6 eV is similar to that observed for ordered graphite and corresponds to carbon in a graphite structure.[58] And the peak at 99.7 eV is attributed to Si(0) based on previously publications.[60,61] The P8 sample used in the experiment has a thickness of ~14 nm. The sampling depth for an XPS measurement on carbon was reported to be about 10 nm, which is close to the carbon film thickness.[62] As the sputtering time increases, the carbon film gets thinner. The intensity of the C 1s peak at 284.6 eV decreases while the intensity of the Si 2p peak at 99.7 eV increases due to the etching of the carbon material. The

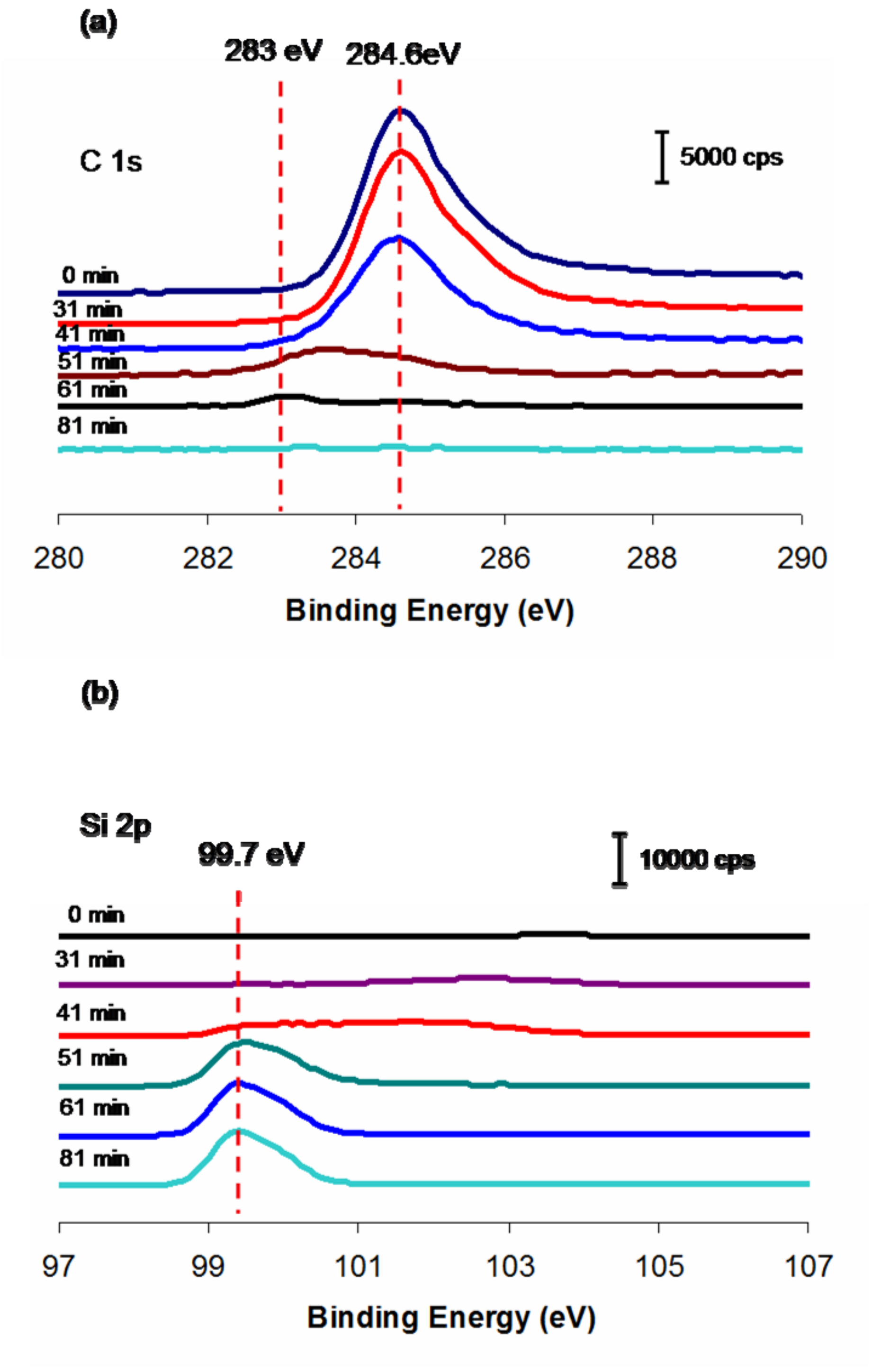

Figure 2.7. C 1s (a) and Si 2p (b) XPS spectra at different Ar^+ sputtering time intervals for pyrolyzed SU-8 on silicon surfaces.

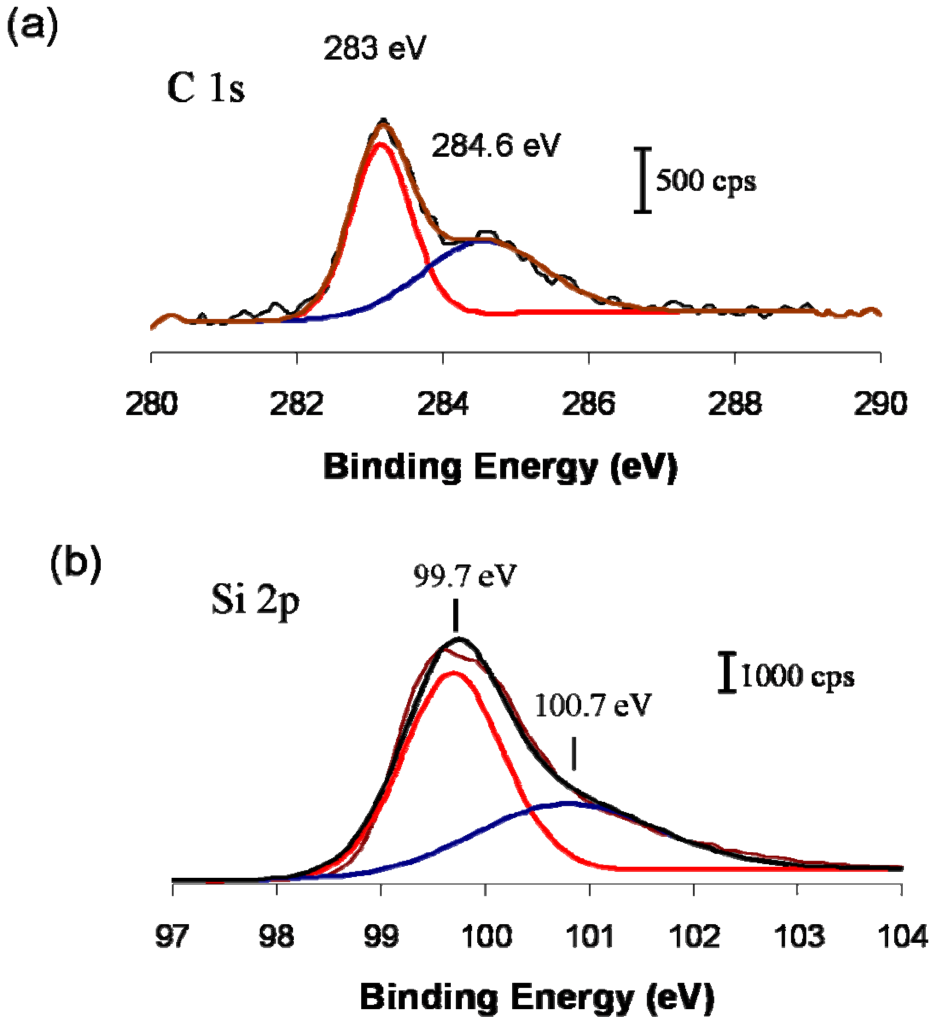

Figure 2.8. Curve fitting analysis of C 1s (a) and Si 2p (b) at etching time of 56 min. Shown are the raw data (brown line), fitted spectrum (black line), and the fitted component peaks (red and blue lines).

C 1s peak, attributed to graphitic carbon disappears completely after 50 to 60 min of sputtering and a small peak at 283 eV emerges (61 min spectrum) that is attributed to carbon in SiC.[60,61] A snapshot of the transition of the carbon XPS signal from graphite to SiC is more clearly illustrated in the spectrum following 56 min of sputtering shown in Figure 2.8(a). The spectral curve fitting analysis in Figure 2.8(a) shows the emergence of the SiC peak at 283 eV as the graphitic carbon peak at 284.6 eV diminishes. For the same sputtering time of 56 min [Figure 2.8 (b)], we also observe a Si 2p signal at 100.7 eV that corresponds to Si in SiC. These XPS results provide a strong evidence for the existence of a thin SiC layer at the interface of the pyrolyzed carbon structures and the underlying Si substrate. We estimate that the SiC region is a few atomic layers thick and acts as an adhesion layer between the film and the substrate.

2.3.5 Microstructure

The microstructure of carbon materials is generally described in terms of the size of the graphitic microcrystallites in the material. The Raman spectrum of carbon is sensitive to the material's microstructure. Raman spectroscopy was thus employed to probe the microstructure of carbonized SU-8. A representative spectrum in the 1000 to 1800 cm^{-1} region is shown in Figure 2.9, along with a spectrum of GC for comparison.

The overall lower intensities observed for the pyrolyzed SU-8 is the result of the low thickness of the carbon film, which is ~15 nm based on the measurement by AFM. The band at 1590 cm^{-1} is assigned as the G band commonly observed in sp^2 hybridized graphitic material. The position of this band is consistent with the microstructure exhibiting extremely small microcrystallite size.[62] The observed D band at 1350 cm^{-1} is diagnostic of disorder in carbon materials. The area ratio of the D to G band correlates with graphite microcrystallite size.[64] In Figure 2.9, the D and G bands are poorly resolved and the D/G ratio is close to unity. Both of these observations are consistent with a

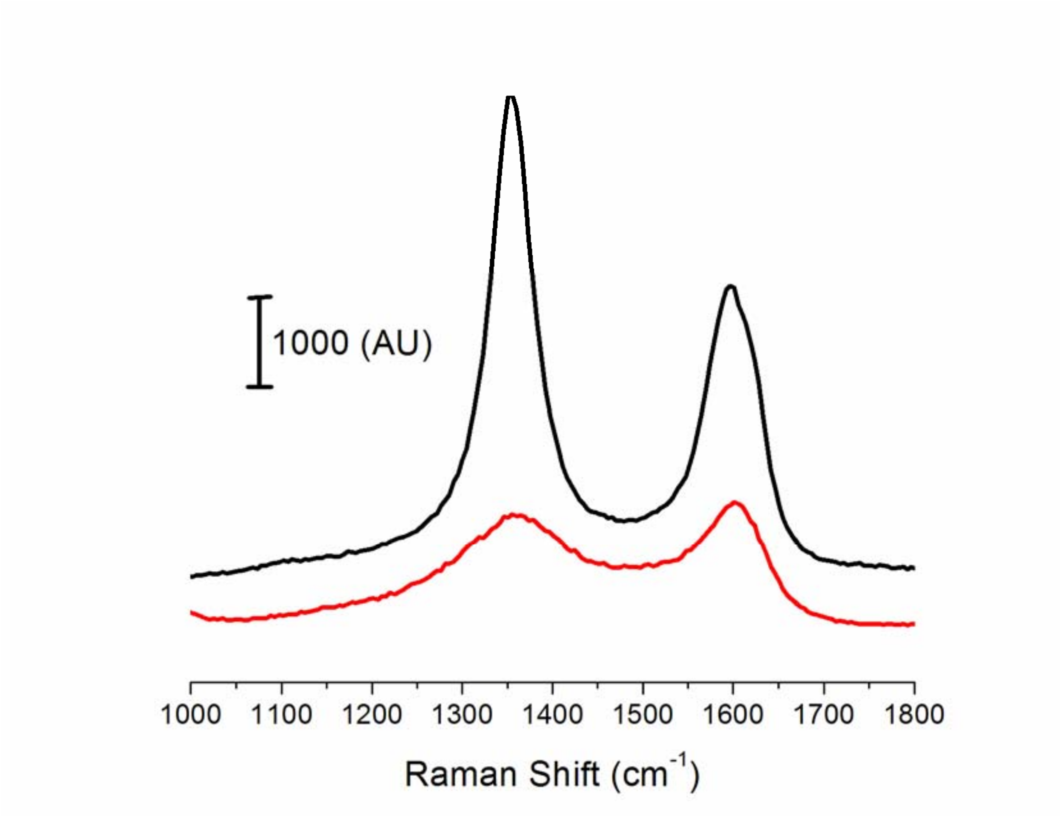

Figure 2.9. Raman spectra of a pyrolyzed SU-8 film (red) and a polished glassy carbon (black).

material comprised of a mixture of disordered graphite and amorphous carbon. Ordinarily, the graphitization process happens at 2700 °C.[41,42] It is believed that the nucleation of small graphitic nanocrystallites would start at lower temperature.[27] The formation of such graphitic crystallites at positive resist derived carbon has been observed.[27] Our Raman results in Figure 2.9 also show some graphite crystal formation which agrees with previously report. [27]

2.3.6 Electrochemical characterization

The electrochemical reactivity of P8 samples was probed by examining electron transfer to certain redox systems. Cyclic voltammetry (CV) was used as a measurement of the electron transfer kinetics. Two redox systems, $Fe(CN)_6^{3-/4-}$ and $Ru(NH_3)_6^{3+/2+}$ were chosen due to their various sensitivities to carbon surface structures. $Ru(NH_3)_6^{3+/2+}$ is an outer-sphere redox system and is widely known as "surface insensitive".[55,65] $Fe(CN)_6^{3-/4-}$ is sensitive to the state of an electrode surface although the mechanism of catalytic interactions is not clear.[55,65] It is known that carbon films pyrolyzed from polymer precursor is structurally and electronically similar to GC.[28] Electron transfer (ET) reactivity of P8s was compared to that of a polished GC. Uncorrected cyclic voltammograms for both polished GC and P8 samples for $Fe(CN)_6^{3-/4-}$ and $Ru(NH_3)_6^{3+}$ are shown in Figure 2.10. In a cyclic voltammogram, the potential difference between the cathodic and anodic peak (ΔE_p) is a measure of electron transfer rate. A low ΔE_p is diagnostic of a higher rate. Visual comparison of the voltammograms in Figure 2.10 shows a slightly lower ΔE_p for P8 films for both redox species.

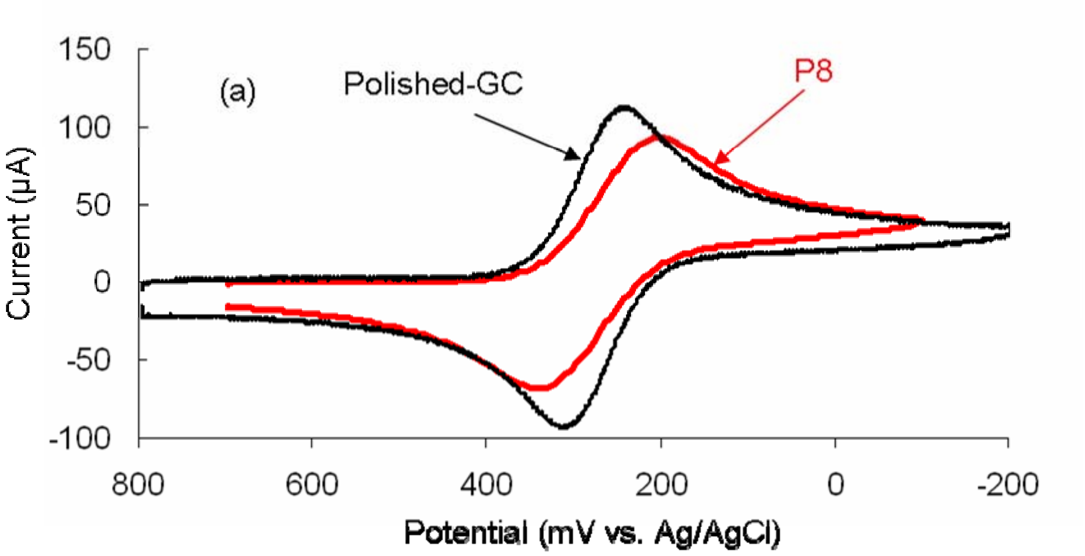

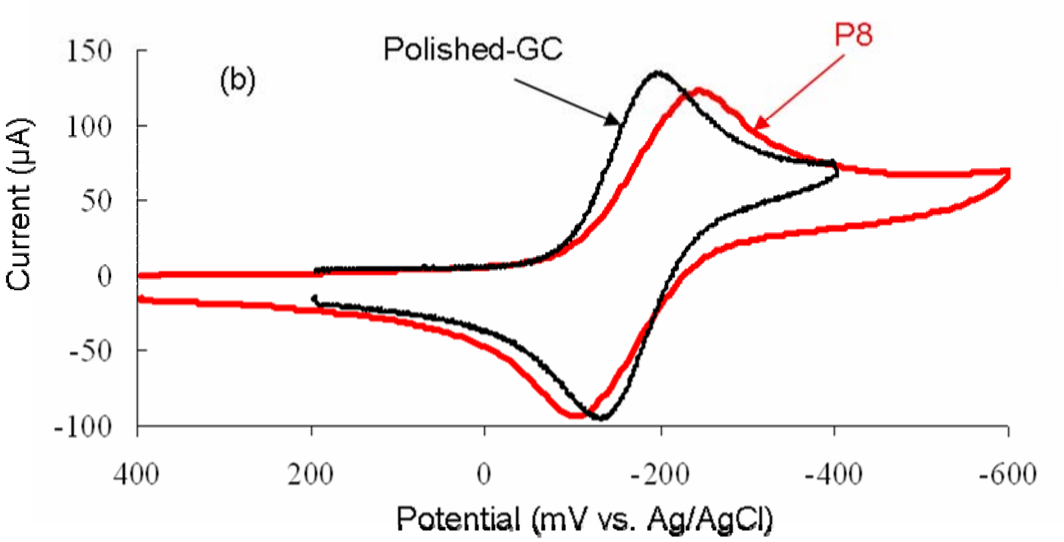

Figure 2.10. Cyclic voltammetric results for several redox systems on polished GC (black line) and P8 electrodes (red line). (a) 1 mM $Fe(CN)_6^{3-}$ (1 M KCl), $\nu = 100$ mV/s. (b) 1 mM $Ru(NH_3)_6^{3+}$ (1 M KCl), $\nu = 100$ mV/s.

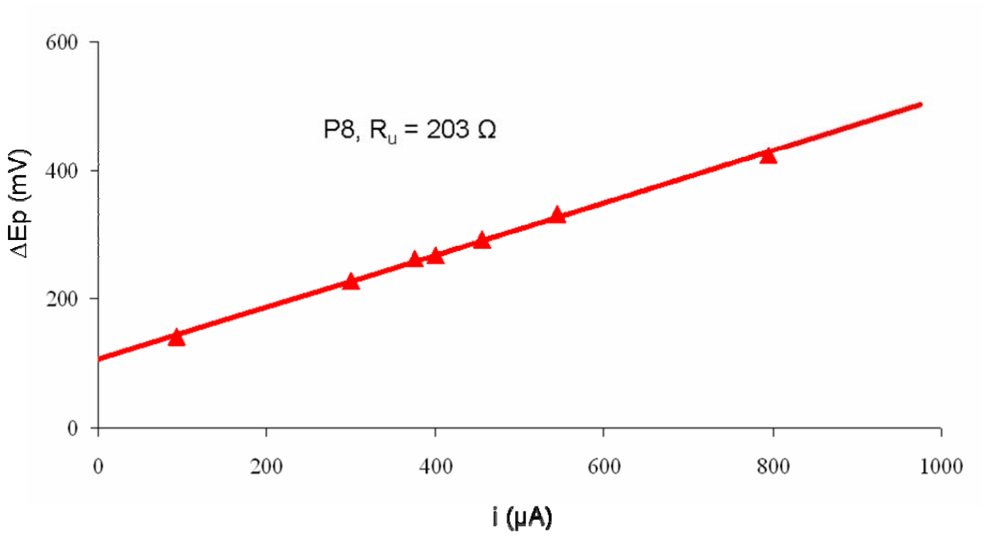

Figure 2.11. Plots of ΔE_p vs. peak current from cyclic voltammetry (ν = 100 mV/s) of $Fe(CN)_6^{3-}$ (1 M KCl) at P8. The concentration of $Fe(CN)_6^{3-}$ was varied from 1 to 10 mM to affect the different peak currents. The slope of each least-square linear fit yields $2R_u$.

In order to quantitatively compare ΔE_p values, the contribution from the film resistance should be accounted for. The film resistivity can have a large effect on the observed ΔE_p and can be corrected by the following equation:[28]

$$\Delta E_{p.corr} = \Delta E_{p,obs} - 2|i|R_u \tag{2.3}$$

where $\Delta E_{p,\,corr}$ is the corrected ΔE_p, i is the voltammetric peak current, and R_u is the uncompensated cell resistance. It is assumed here that the resistance of carbon films is a large component of R_u in these measurements. R_u can be determined from the slope of a plot of $\Delta E_{p,\,obs}$ versus i from voltammograms at a common

Table 2.2. Heterogeneous electron transfer rate constants for P8 and PPF samples.

Type of carbon electrode	Ref.	$Fe(CN)_6^{3-/4-}$		$Ru(NH_3)_6^{3+/2+}$	
		ΔE_p (mV)	k^o (cm/s)	ΔE_p (mV)	k^o (cm/s)
P8	This work	106 ± 11[a]	0.004	72 ± 8[a]	0.018
Polished GC	This work	68	0.024	72	0.018
	28		0.034		0.037
PPF	28		0.012		0.020
7 nm E-beam evaporated carbon film (ECF)	21		0.0027		0.019
Pyrolyzed 7 nm ECF	21		0.014		0.046

[a] The reported uncertainties are the standard deviation from the measurements of 5 different samples.

scan rate for solution by varying concentrations (Figure 2.11). The R_u values calculated from five different P8 samples are 198 ± 12 Ω. Table 2.2 shows the values of ΔE_p of P8s after correcting for ohmic error for different redox systems. Heterogeneous electron transfer rate constants, k^0, were determined from $\Delta E_{p,\, corr}$ values via the method of Nicholson.[65] ET rates of other type of carbon electrode based on previous reports are also listed and compared with our results.

The results in Table 2.2 show that P8 film yield similar ET rate for $Ru(NH_3)_6^{3+/2+}$ but lower ET rate for $Fe(CN)_6^{3-/4-}$ than GC. It is known that the ET rate for $Fe(CN)_6^{3-/4-}$ at a carbon electrode is very sensitive to surface preparation procedures.[55,64] Carbon film electrodes treated with activated carbon/isopropyl alcohol (AC/IPA) was reported previously.[21,28] This treatment has been shown to significantly lower the amount of organic impurities on carbon electrodes and increase the ET rate for $Fe(CN)_6^{3-/4-}$. In our experiment, the P8s were used without similar pretreatment. The ET rate, however, is likely sufficient for most applications.

2.4 Conclusions

Carbon film electrodes were fabricated by pyrolysis of SU-8 photoresist film in inert atmosphere and their composition and properties were subsequently characterized. The carbon films have similar smoothness as PPF and pyrolyzed ECF. The surface O/C ratio is much lower than that of GC and PPF. For both outer-sphere and surface sensitive redox systems, the resistance-corrected electron transfer rates observed on PPF and P8 carbon films are compared and the electron transfer rate on the P8 surface is little lower than that on PPF.

2.5 References:

1. McCreery, R. L., Carbon electrodes: Structural effects on electron transfer kinetics. In *Electroanalytical chemistry*, Bard, A. J., Ed. 1991; pp 221-374.
2. Wu, W. Z.; Huang, W. H.; Wang, W.; Wang, Z. L.; Cheng, J. K.; Xu, T.; Zhang, R. Y.; Chen, Y.; Liut, J., Monitoring dopamine release from single living vesicles with nanoelectrodes. *Journal of the American Chemical Society* **2005,** 127, 8914-8915.
3. Teixidor, G. T.; Zaouk, R. B.; Park, B. Y.; Madou, M. J., Fabrication and characterization of three-dimensional carbon electrodes for lithium-ion batteries. *Journal of Power Sources* **2008,** 183, 730-740.
4. Li, X. G.; Hsing, I. M., Electrooxidation of formic acid on carbon supported Pt_xPd_{1-x} (x=0-1). *Electrochimica Acta* **2006,** 51, 3477-3483.
5. McDermott, M. T.; McDermott, C. A.; McCreery, R. L., Scanning tunneling microscopy of carbon surfaces-relationships between electrode-kinetics, capacitance, and morphology for glassy-carbon electrodes. *Analytical Chemistry* **1993,** 65, 937-944.
6. Donner, S.; Li, H. W.; Yeung, E. S.; Porter, M. D., Fabrication of optically transparent carbon electrodes by the pyrolysis of photoresist films: Approach to single-molecule spectroelectrochemistry. *Analytical Chemistry* **2006,** 78, 2816-2822.

7. Bonifas, A. P.; McCreery, R. L., In-situ optical absorbance spectroscopy of molecular layers in carbon based molecular electronic devices. *Chemistry of Materials* **2008,** 20, 3849-3856.

8. Tian, H.; Bergren, A. J.; McCreery, R. L., Ultraviolet-visible spectroelectrochemistry of chemisorbed molecular layers on optically transparent carbon electrodes. *Applied Spectroscopy* **2007,** 61, 1246-1253.

9. Anariba, F.; McCreery, R. L., Electronic conductance behavior of carbon-based molecular junctions with conjugated structures. *Journal of Physical Chemistry B* **2002,** 106, 10355-10362.

10. Anariba, F.; Steach, J. K.; McCreery, R. L., Strong effects of molecular structure on electron transport in carbon/molecule/copper electronic junctions. *Journal of Physical Chemistry B* **2005,** 109, 11163-11172.

11. Kalakodimi, R. P.; Nowak, A. M.; McCreery, R. L., Carbon/molecule/metal and carbon/molecule/metal oxide molecular electronic junctions. *Chemistry of Materials* **2005,** 17, 4939-4948.

12. Hebert, N. E.; Snyder, B.; McCreery, R. L.; Kuhr, W. G.; Brazill, S. A., Performance of pyrolyzed photoresist carbon films in a microchip capillary electrophoresis device with sinusoidal voltammetric detection. *Analytical Chemistry* **2003,** 75, 4265-4271.

13. Kostecki, R.; Song, X.; Kinoshita, K., Electrochemical analysis of carbon interdigitated microelectrodes. *Electrochemical and Solid State Letters* **1999,** 2, 465-467.

14. Kostecki, R.; Song, X. Y.; Kinoshita, K., Influence of geometry on the electrochemical response of carbon interdigitated microelectrodes. *Journal of the Electrochemical Society* **2000,** 147, 1878-1881.

15. Park, B. Y.; Taherabadi, L.; Wang, C. L.; Zoval, J.; Madou, M. J., Electrical properties and shrinkage of carbonized photoresist films and the implications for carbon microelectromechanical systems devices in conductive media. *Journal of the Electrochemical Society* **2005,** 152, J136-J143.

16. Wang, C. L.; Madou, M., From MEMS to NEMS with carbon. *Biosensors & Bioelectronics* **2005,** 20, 2181-2187.

17. Reeder, G. S.; Heineman, W. R., Electrochemical characterization of a microfabricated thick-film carbon sensor for trace determination of lead. *Sensors and Actuators B-Chemical* **1998,** 52, 58-64.

18. Wang, J.; Pedrero, M.; Sakslund, H.; Hammerich, O.; Pingarron, J., Electrochemical activation of screen-printed carbon strips. *Analyst* **1996,** 121, 345-350.

19. Wring, S. A.; Hart, J. P., Chemically modified, screen-printed carbon electrodes. *Analyst* **1996,** 117, 1281-1286.

20. Corgier, B. P.; Marquette, C. A.; Blum, L. J., Diazonium-protein adducts for graphite electrode microarrays modification: Direct and addressed electrochemical immobilization. *Journal of the American Chemical Society* **2005,** 127, 18328-18332.

21. Blackstock, J. J.; Rostami, A. A.; Nowak, A. M.; McCreery, R. L.; Freeman, M. R.; McDermott, M. T., Ultraflat carbon film electrodes prepared by electron beam evaporation. *Analytical Chemistry* **2004,** 76, 2544-2552.

22. You, T. Y.; Niwa, O.; Tomita, M.; Ichino, T.; Hirono, S., Electrochemical oxidation of alkylphenols on ECR-sputtered carbon film electrodes with flat sub-nanometer surfaces. *Journal of the Electrochemical Society* **2002,** 149, E479-E484.

23. Creatore, M.; Rieter, S. M.; Barrell, Y.; Van De Sanden, M. C. M.; Vernhes, R.; Martinu, L., Optical and chemical characterization of expanding thermal plasma-deposited carbon-containing silicon dioxide-like films. *Thin Solid Films* **2008,** 516, 8547-8553.

24. Zhu, X. D.; Ding, F.; Naramoto, H.; Narumi, K., AFM investigation on surface evolution of amorphous carbon during ion-beam-assisted deposition. *Applied Surface Science* **2006,** 253, 1480-1483.

25. Tochitsky, E. I.; Stanishevskii, A. V.; Kapustin, I. A.; Akulich, V. V.; Selifanov, O. V., Structure and properties of carbon-films prepared by pulsed vacuum-arc deposition. *Surface & Coating Technology* **1991,** 47, 292-298.

26. Kim, J.; Song, X.; Kinoshita, K.; Madou, M.; White, B., Electrochemical studies of carbon films from pyrolyzed photoresist. *Journal of the Electrochemical Society* **1998,** 145, 2314-2319.

27. Ranganathan, S.; McCreery, R.; Majji, S. M.; Madou, M., Photoresist-derived carbon for microelectromechanical systems and electrochemical applications. *Journal of the Electrochemical Society* **2000,** 147, 277-282.

28. Ranganathan, S.; McCreery, R. L., Electroanalytical performance of carbon films with near-atomic flatness. *Analytical Chemistry* **2001,** 73, 893-900.

29. Chen, Y. F.; Chen, Z. Q.; Xiao, S. Y.; Liu, H. B., A novel thermal degradation mechanism of phenol-formaldehyde type resins. *Thermochimica Acta* **2008,** 476, 39-43.

30. Ma, W.; Wang, S.; Cui, J. P.; Zhang, S. T.; Fan, B. C.; He, Y. Z., Thermal decomposition kinetic model of phenolic resin. *Acta Physico-Chimica Sinica* **2008,** 24, 1090-1094.

31. Trick, K. A.; Saliba, T. E.; Sandhu, S. S., A kinetic model of the pyrolysis of phenolic resin in a carbon/phenolic composite. *Carbon* **1997,** 35, 393-401.

32. Yudin, V. E.; Goykhman, M. Y.; Balik, K.; Glogar, P.; Gubanova, G. N.; Kudriavtsev, V. V., Carbonization behaviour of some polyimide resins reinforced with carbon fibers. *Carbon* **2000,** 38, 5-12.

33. Ko, T. H.; Kuo, W. S.; Chang, Y. H., Raman study of the microstructure changes of phenolic resin during pyrolysis. *Polymer Composites* **2000,** 21, 745-750.

34. Kim, S. H.; Park, N. J.; Oh, M., Determination of epoxy resin type in emc by pyrolysis-GC and GC/MS. *Polymer-Korea* **1999,** 23, 401-412.

35. Mantell, C. L., *Carbon and Graphite Handbook*. Interscience Publishers: New York, 1968; p 72-105.

36. Kinoshita, K., *Carbon: Electrochemical and physiochemical properties*. John Wiley & Sons Inc.: New York, 1988; p 226 - 292.

37. McCreery, R.; Dieringer, J.; Solak, A. O.; Snyder, B.; Nowak, A. M.; McGovern, W. R.; DuVall, S., Molecular rectification and conductance switching in carbon-based molecular junctions by structural rearrangement accompanying electron injection. *Journal of the American Chemical Society* **2003,** 125, 10748-10758.

38. Schueller, O. J. A.; Brittain, S. T.; Marzolin, C.; Whitesides, G. M., Fabrication and characterization of glassy carbon MEMS. *Chemistry of Matererials* **1997,** 9, 1399-1406.

39. Schueller, O. J. A.; Brittain, S. T.; Whitesides, G. M., Fabrication of glassy carbon microstructures by pyrolysis of microfabricated polymeric precursors. *Advanced Materials* **1997,** 9, 477-480.

40. Shah, H. V.; Brittain, S. T.; Huang, Q.; Hwi, S.-J.; Whitesides, G. M.; Smith Jr., D. W., Bis-o-diynylarene (BODA) derived polynapthalenes as precursors to GC microstructures. *Chemistry of Matererials* **1999,** 11, 2623-2625.

41. Singh, A.; Jayaram, J.; Madou, M.; Akbar, S., Pyrolysis of negative photoresists to fabricate carbon structures for microelectromechanical systems and electrochemical applications. *Journal of the Electrochemical Society* **2002,** 149, E78-E83.

42. Wang, C. L.; Jia, G. Y.; Taherabadi, L. H.; Madou, M. J., A novel method for the fabrication of high-aspect ratio C-MEMS structures. *Journal of Microelectromechanical System* **2005,** 14, 348-358.

43. Kowalewski, T.; Tsarevsky, N. V.; Matyjaszewski, K., Nanostructured carbon arrays from block copolymers of polyacrylonitrile. *Journal of the American Chemical Society* **2002,** 124, 10632-10633.

44. Tang, C. B.; Tracz, A.; Kruk, M.; Zhang, R.; Smilgies, D. M.; Matyjaszewski, K.; Kowalewski, T., Long-range ordered thin films of block copolymers prepared by zone-casting and their thermal conversion into ordered nanostructured carbon. *Journal of the American Chemical Society* **2005,** 127, 6918-6919.

45. Lorenz, H.; Despont, M.; Fahrni, N.; Brugger, J.; Vettiger, P.; Renaud, P., High-aspect-ratio, ultrathick, negative-tone near-UV photoresist and its applications for mems. *Sensors and Actuators a-Physical* **1998,** 64, 33-39.

46. Aktary, M.; Jensen, M. O.; Westra, K. L.; Brett, M. J.; Freeman, M. R., High-resolution pattern generation using the epoxy novolak SU-8 2000 resist by electron beam lithography. *Journal of Vacuum Science & Technology B* **2003,** 21, L5-L7.

47. Hanabata, M.; Oi, F.; Furuta, A., Novolak design concept for high-performance positive photoresists. *Polymer Engineering and Science* **1992,** 32, 1494-1499.

48. Sundaramurthy, A.; Schuck, P. J.; Conley, N. R.; Fromm, D. P.; Kino, G. S.; Moerner, W. E., Toward nanometer-scale optical photolithography:

Utilizing the near-field of bowtie optical nanoantennas. *Nano Letters* **2006,** 6, 355-360.

49. Liang, C. D.; Hong, K. L.; Guiochon, G. A.; Mays, J. W.; Dai, S., Synthesis of a large-scale highly ordered porous carbon film by self-assembly of block copolymers. *Angewandte Chemie-International Edition* **2004,** 43, 5785-5789.

50. Yang, H. H.; McCreery, R. L., Effects of surface monolayers on the electron-transfer kinetics and adsorption of methyl viologen and phenothiazine derivatives on glassy carbon electrodes. *Analytical Chemistry* **1999,** 71, 4081-4087.

51. Solak, A. O.; Eichorst, L. R.; Clark, W. J.; McCreery, R. L., Modified carbon surfaces as "Organic electrodes" that exhibit conductance switching. *Analytical Chemistry* **2003,** 75, 296-305.

52. Mattson, J. S.; Smith, C. A., Optically transparent carbon-film electrodes for infrared spectroelectrochemistry. *Analytical Chemistry* **1975,** 47, 1122-1125.

53. Thin film evaporation source reference. The R. D. Mathis Company: Long Beach, 1987.

54. Park, B. Y.; Yaherabadi, L.; Wang, C. L.; Zoval, J.; Madou, M. J., Electrical properties and shrinkage of carbonized photoresist films and the implications for carbon microelectromechanical systems devices in conductive media. *Journal of the Electrochemical Society* **2005,** 152, J136-J143.

55. Chen, P. H.; McCreery, R. L., Control of electron transfer kinetics at glassy carbon electrodes by specific surface modification. *Analytical Chemistry* **1996,** 68, 3958-3965.

56. Burrell, M. C.; Chera, J. J., Charge correction of the binding energy scale in XPS analysis of polymers using surface deposition of PDMS. *Surface and Interface Analysis* **1999,** 27, 811-815.

57. Sundberg, P.; Larsson, R.; Folkesson, B., On the core electron binding energy of carbon and the effective charge of the carbon atom. *Journal of Electron Spectroscopy and Relatated Phenomena* **1988,** 46, 19-29.

58. Hinnen, C.; Imbert, D.; Siffre, J. M.; Marcus, P., An in situ XPS study of sputter-deposited aluminium thin films on graphite. *Applied Surface Science* **1994,** 78, 219-231.

59. Kuo, T.; McCreery, R., Surface chemistry and electron transfer kinetics of hydrogen-modified glassy carbon. *Analytical Chemistry* **1999,** 71, 1553-1560.

60. Eicke, A.; Bilger, G., XPS and SIMS characterization of metal oxide/amorphous silicon-carbon interfaces. *Surface and Interface Analysis* **1988,** 12, 344-350.

61. Ji, M.; Zhu, J.; Ma, M.; Wu, J.; Liu, X.; Jin, B.; Yang, B.; He, P.; Ruan, Y., SiC formation at the interface of polyimide Langmuir-Blodgett film and silicon. *Journal of Applied Physics* **1996,** 80, 2471-2474.

62. Shen, W.; Li, Z.; Liu, Y., Surface chemical functional groups modification of porous carbon. *Recent Patents on Chemical Engineering* **2008,** 1, 27-40.

63. Besold, J.; Thielsch, R.; Matz, N.; Frenzel, C.; Born, R.; Mobius, A., Surface and bulk properties of electron beam evaporated carbon films. *Thin Solid Films* **1997,** 293, 96-102.

64. Wang, Y.; Alsmeyer, D. C.; McCreery, R. L., Raman spectroscopy of carbon materials: Structural basis of observed spectra. *Chemistry of Materials.* **1990,** 2, 557-563.

65. Chen, P. H.; Fryling, M. A.; McCreery, R. L., Electron-transfer kinetics at modified carbon electrode surfaces - the role of specific surface sites. *Analytical Chemistry* **1995,** 67, 3115-3122.

66. Nicholson, R. S., Theory and application of cyclic voltammetry for measurement of electrode reaction kinetics. *Analytical Chemistry* **1965,** 37, 1351-1355.

Chapter 3. Fabrication and Characterization of Graphitic Carbon Nanostructures with Controllable Size, Shape and Position

This chapter is focused on the fabrication of graphitic carbon nanostructures by the combination of electron-beam lithography (EBL) and high-temperature carbonization. Various graphite carbon nanostructures have been fabricated by this method by carefully choosing suitable EBL parameters and ensuring a long post baking time before carbonization. The shrinkage of SU-8 nanostructures before and after the carbonization was characterized by both SEM and AFM techniques. Attempts to fabricate extremely close line arrays and nanogaps were tried. Some technical limitations of this method are also discussed.

3.1 Introduction

The incorporation of carbon materials in micro- and nanoscale devices is being widely investigated due to the promise of enhanced functionality. Challenges in the positioning and addressability of carbon nanotubes provide the motivation for the development of new processes to produce nanoscale carbon materials. This chapter reports the fabrication of conducting, nanometer sized carbon structures using a combination of electron beam lithography (EBL) and carbonization. EBL is used to directly write predefined nanometer sized patterns in a thin layer of negative SU-8 resist in controllable locations. Careful heat treatment results in carbon nanostructures with the size, shape and location originally defined by EBL.

Carbon materials continue to deliver a huge impact to nanotechnology. Over the past ten years, the synthesis and applications of carbon nanotubes have been at the forefront of nanoscience research.[1-4] The synthesis[5] and modification[6] of carbon nanotubes are well-developed. The manipulation of individual nanotubes to fabricate devices, however, remains a challenge. For example, carbon nanotube electronic devices are commonly fabricated by controlled chemical vapor deposition growth of segregated nanotubes on a patterned catalyst layout on the device. Although this method has been successful for nanoscale chemical sensors[7] and diodes,[8,9] the successful rate for functioning devices is approximately 5%. Despite this low rate of success, the size and electronic properties of carbon nanotubes remain attractive for nanoscale devices. This work was motivated by my belief that other types of carbon nanostructures will also prove useful in these applications.

Pyrolysis, sometimes also called carbonization, is a chemical decomposition process at high temperature. At high temperature and inert environment, organic materials decompose, leaving carbon as the residue. Most of hydrogen, nitrogen and oxygen atoms are released as gas products.[10] Recently, pyrolysis has been used to fabricate carbon film and carbon microstructures by several groups. McCreery and coworkers have described the fabrication of pyrolyzed photoresist carbon films (PPF).[11,12] Photoresist films were spin coated on silicon wafers and then pyrolyzed at 1000°C in a forming gas (95% N_2 and 5% H_2) atmosphere. Carbon films with extremely flat surfaces were obtained. Whitesides and coworkers[13-15] have reported a set of carbon microstructures fabricated from the carbonization of soft-lithographic patterned polymeric precursors. Madou and coworkers[16-19] have investigated photolithographic patterning and carbonization of various photoresist polymers. The fabrication of high aspect ratio, 3D structures for MEMS applications is possible through careful control of exposure, soft-baking and development time.[17,19]

The fabrication of nanometer sized carbon structure by carbonization has also been reported. Chengdu et al.[20] have reported the systhesis of ordered nanoporous carbon films by carbonization of self-assembled block copolymers. The difficulty in carbonization of nanostructures is due to the possible melting or evaporation at high temperature. It was believed that a high degree of cross-linking is very important in the survival of nanometer sized polymer precursors during the pyrolysis process. Ordered arrays of carbon nanostructures have also been prepared by the pyrolysis of highly cross-linked block co-polymer films.[21,22]

The work presented here combines direct-write, nanometer scale patterning with carbonization to fabricate graphitic carbon nanostructures. We employ EBL and a negative EBL resist as the basis for my fabrication. EBL combined with lift-off techniques has been applied to fabricate metal nanolines of 10 nm diameter.[23] Direct writing of nanometer structures is enabled in this work by using an epoxy based negative photoresist (SU-8) that will cross-link in response to electron beam exposure. This resist has also been used as a precursor for carbon film electrodes in Chapter 2 and for carbon based MEMS fabrication.[24,25] We have prepared EBL written nanostructures on Si, and quartz substrates and have characterized the pyrolysis induced size changes of the resulting material.

3.2 Experimental

3.2.1 Sample preparation

Silicon (100) wafers (p-type, doped, 1 Ω·cm^2, 500 μm thick) and quartz substrates were purchased from University Wafer (South Boston, MA). Both types of substrates were diced and cleaned with the hot piranha solution (75% H_2SO_4: 25% H_2O_2) and dehydrated on a 200^{o}C hot plate for 5 min before using. [*Warning: Piranha solution should be handled with extreme care; it is a strong oxidant and reacts violently with many organic materials. It also presents an explosion danger. All work should be performed under a fume hood*.]

NANO^{TM} SU-8 2000.1 resist manufactured by MicroChem Corp. (Newton, MA) was used. The resist was spin-coated onto the substrates at a cycle speed of 4000 rpm for 30 s. The samples were then soft baked at 65^{o}C for 1 min and at 90^{o}C for 2 min. EBL was performed with a Raith 150 e-beam lithography system from Raith GmbH Company. Figure 3.1 shows a photo of the Raith 150 system used in this research. EBL parameters were optimized for the 150 nm SU-8 films used here as described previously.[26] The gun voltage was typically 20 keV. Due to the extremely high resist sensitivity of SU-8, exposures were carried out at 7.5 μm aperture size to ensure a relatively low current. Exposure doses were 10 μC/cm^2

and pixel-to-pixel step is 20 nm. For the non-conducting substrates, a thin (3 nm) layer of Au was evaporated on top of the SU-8 before e-beam exposure. Post exposure baking (PEB) was carried out for 1 min at 65°C followed by 10 min at 90°C. Finally the samples were developed using MicroChem SU-8 developer for 60 s, followed by a 10 s immersion in isopropyl alcohol and N_2 blow drying.

Figure 3.1. Raith 150 E-beam lithography system.

The samples were pyrolyzed in a tube furnace (Lindberg) fitted with a quartz tube by a two step heating procedure. Pyrolysis of nanostuctures can be conducted both in a vacuum sealed environment and in an environment of forming gas (95% nitrogen + 5% hydrogen, Praxair, Edmonton). The samples were first heated to 200°C at a rate of 10°C/min and held for 30-60 min. This pre-carbonization bake was necessary to increase the cross-linking density of the SU-8.[27,28] To carbonize the nanostructures, the temperature was ramped to high temperature (1000°C) at 10°C/min and held for 1 hour. After that, the samples were gradually cooled down to room temperature. During the whole process, the tube was flushed by a continuous flow of forming gas to provide a reducing atmosphere. A simple scheme illustrating the fabrication procedure is shown in Figure 3.2.

3.2.2 Characterization

A Hitachi S4800 Scanning Electron Microscopy (SEM) was used to characterize the nanostructures before and after the pyrolysis. Atomic force microscopy (AFM) was performed with a MFP-3D (Asylum Research, Santa Barbara, CA). Images were collected with Si cantilevers in tapping mode.

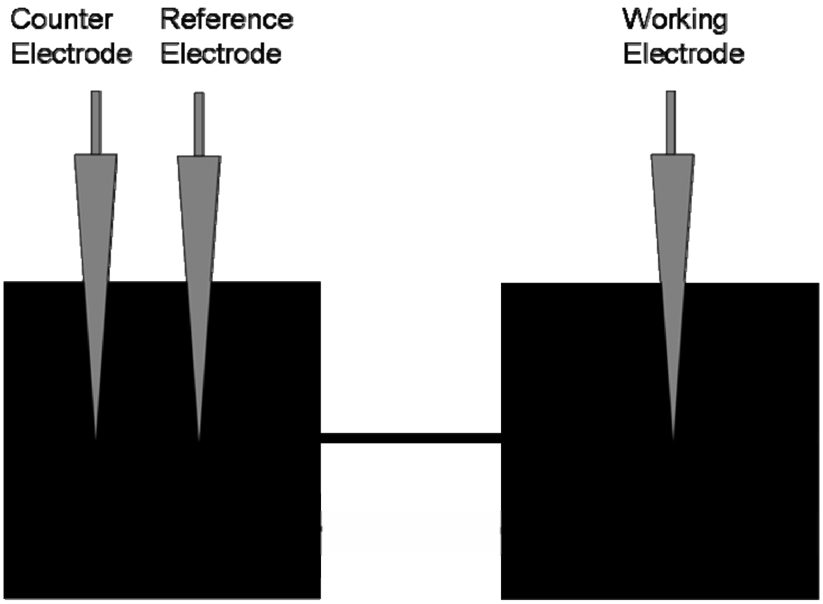

Scheme 3.1. Three-probe setting for resistance measurement.

Resistivity of carbon nanowires were measured by a bipotentiostat model AFCBP1 (Pine). Scheme 3.1 shows the three-probe setting for the resistance measurement. A linear scan voltage signal from -2 V to 2 V was applied between the reference electrode and working electrode with a scan rate of 100 mV/s. The current response was recorded.

3.3 Results and Discussion

3.3.1 Pre-carbonization baking

A simple scheme illustrating the fabrication procedure is shown in Figure 3.2. Briefly, a 150 nm thick layer of SU-8 is spin-coated onto a substrate (Si, Si_3N_4 or quartz). A pattern is written into the SU-8 with EBL and the unexposed SU-8 is developed and rinsed from the substrate. The sample is baked and then pyrolyzed.

Compared with the pyrolysis process for the fabrication of pyrolyzed SU-8 carbon film (P8) described in Chapter 2, the pyrolysis process of micro and nanometer sized SU-8 structures includes a pre-carbonization bake process. The survival of micron or nanometer sized SU-8 structures to the pyrolysis procedure relies greatly on the pre-carbonization bake, which ensures maximum cross-linking. Figure 3.3 shows the optical images of samples before and after the pyrolysis. Without the pre-baking step, the resin structures melted on the sample surface as shown in Figure 3.3 (b). The predefined shapes were preserved after the pyrolysis with the pre-carbonization baking step as shown in Figure 3.3 (c). The cross-linking induced by the pre-bake ensures a 100% survival rate otherwise the

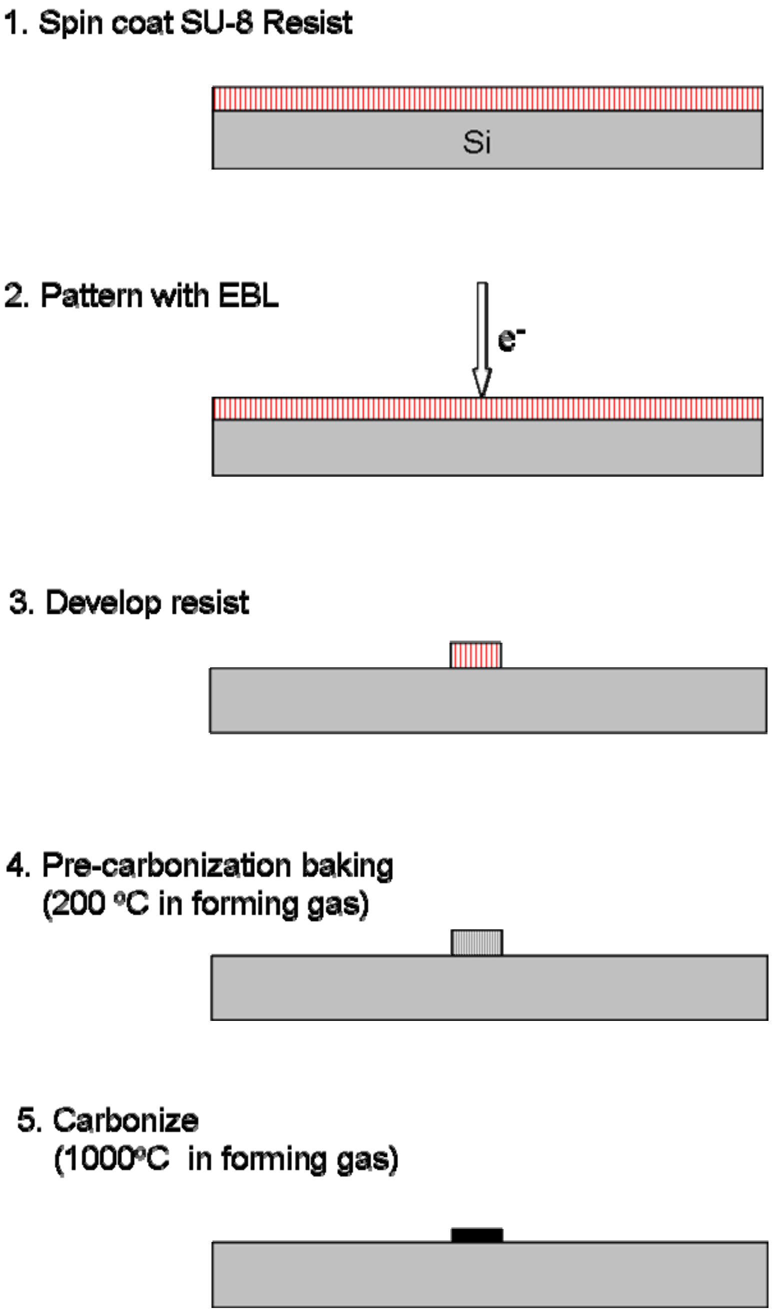

Figure 3.2. Scheme illustrating the process of combining EBL and pyrolysis for the fabrication of carbon nanostructures.

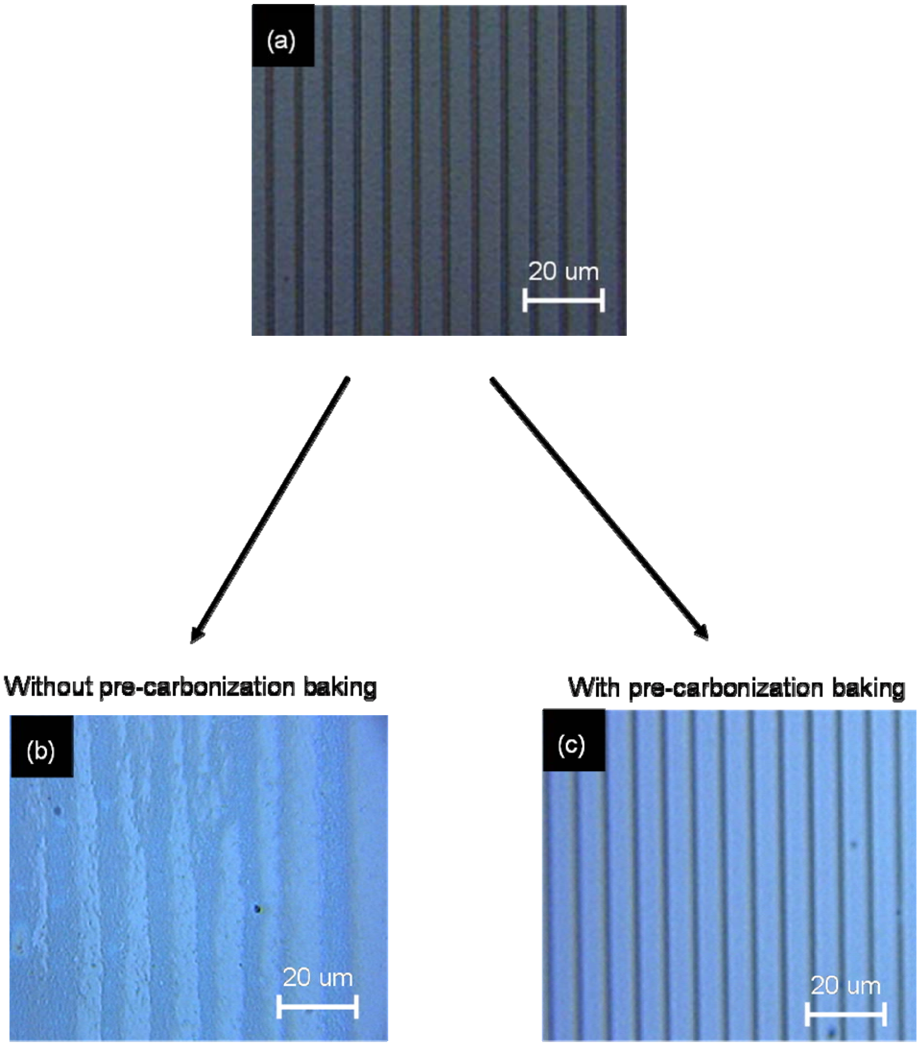

Figure 3.3. Optical images of (a) SU-8 microband array before pyrolysis; (b) pyrolyzed carbon microband array without pre-carbonization baking and (c) pyrolyed carbon microband array with pre-carbonization baking.

structures occasionally either melt or evaporate. Highly cross-linked SU-8 structures maintain their shape during carbonization because the glass transition temperature (T_g) of the material continually increases as the material is carbonized.[24,27,28] This situation can be ensured by controlling the heating rate at 10°C/min.

3.3.2 Size change before and after pyrolysis

Although SU-8 structures with dimensions of tens of nanometers survive the carbonization process (see, for example, Figure 3.7), a significant amount of material is lost during pyrolysis. It is known that polymeric materials, including photoresist, shrink under carbonization conditions.[13,18,24,29] We have examined both the vertical and horizontal shrinkage of nanometer sized SU-8 structures upon carbonization using a combination of AFM and SEM. A set of linear structures on a Si substrate of various widths were imaged with AFM before and after pyrolysis. Figure 3.4 contains examples of topographic images that reveal vertical shrinkage from 60 nm initial thickness to 15 nm. This represents a 75% decrease in thickness due to a loss of material during the pyrolysis treatment. This thickness change is independent of structure width as shown in Figure 3.4.

The ability of our fabrication process to produce structures with pre-defined lateral size relies heavily on a low degree of horizontal shrinkage. An experiment involving SEM imaging before and after pyrolysis reveals that structures with initial widths ranging from 600 to 20 nm exhibit a lateral shrinkage of 3% or less.

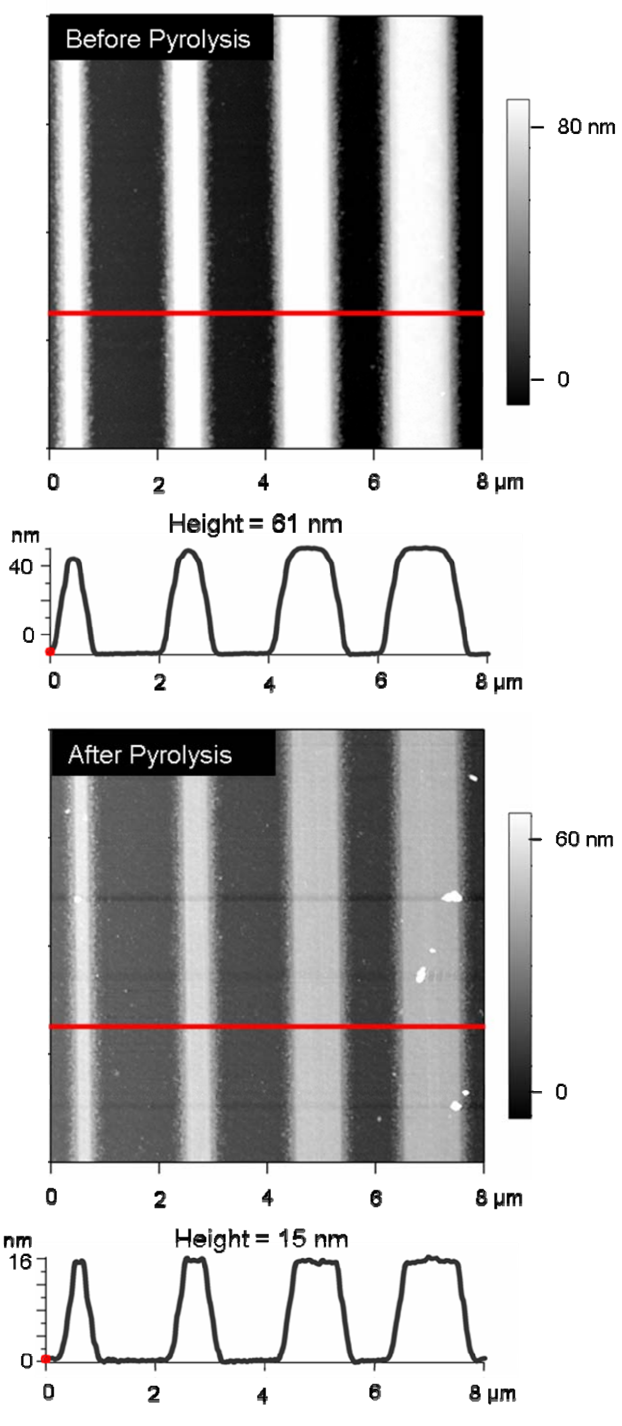

Figure 3.4. Contact mode AFM images of EBL fabricated SU-8 structures before and after pyrolysis.

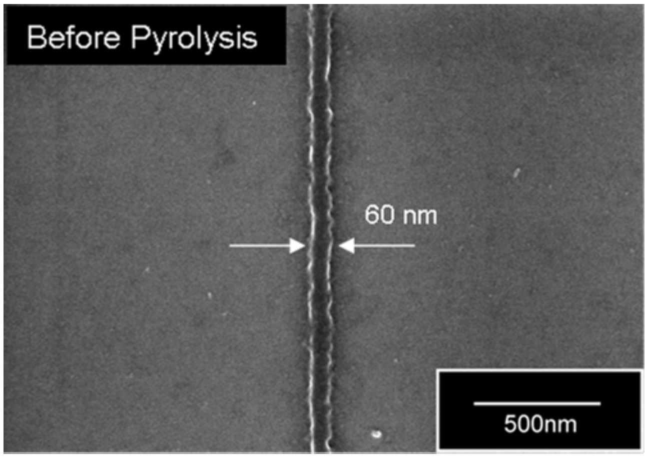

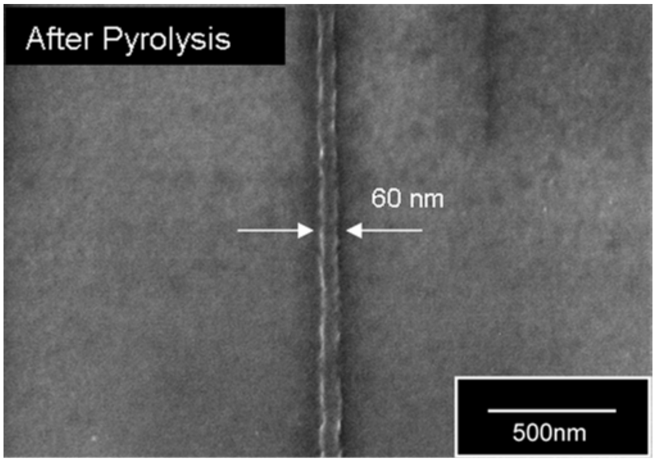

Figure 3.5. SEM images of a 60 nm SU-8 nanowire before and after pyrolysis.

Figure 3.5 shows the SEM images of one sample before and after pyrolysis. From the SEM images, the band width remains ~60 nm before and after pyrolysis. This is consistent with observations for the horizontal shrinkage of micron-sized patterns of photoresist.[19,29] The negligible lateral shrinkage can be attributed to the strong adhesion between SU-8 and the Si substrate. In addition, adhesion is also enhanced by the formation of a SiC interfacial layer induced by the pyrolysis process. The XPS depth profile results were consistent with a very thin SiC layer, which has been detailed discussed in Chapter 2.

3.3.3 Roughness of carbon nanoband surface

Pyrolyzed photoresist carbon films are well known for smooth surface topography. This advantage can also be extended to nanostructures. Figure 3.6 shows the AFM images of a 200 nm wide nanoband and the section plot along a red line, which is drawn lengthwise across the nanoband surface. The RMS roughness (RMS = 0.4 nm) of the band surface was obtained, which is similar to that of the bulk film samples described in Chapter 2. Such an extremely flat surface can be important for potential applications in molecular electronics.

3.3.4 Carbon nanostructures that can be fabricated

We have found that virtually any patterns that can be written with EBL can be carbonized with high fidelity on silicon and quartz substrates. Figure 3.7 contains SEM and AFM images of examples of carbon nanostructures that were created with this methodology. Figure 3.7 (a) and (b) shows the SEM and AFM

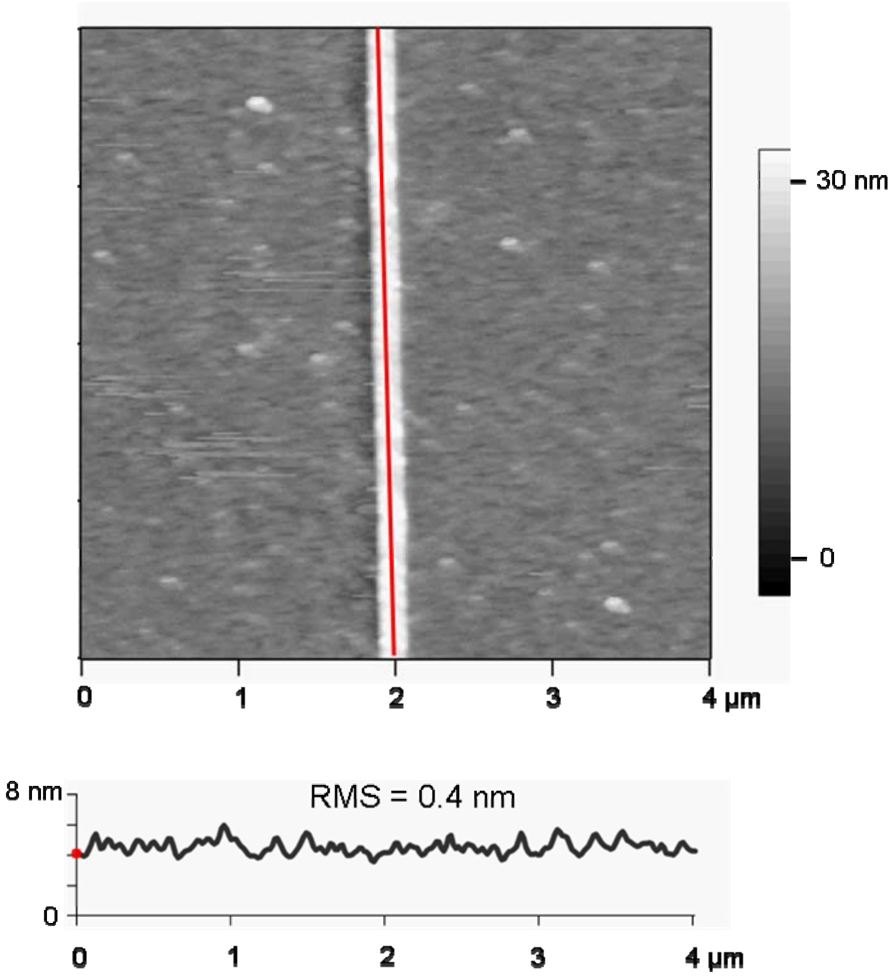

Figure 3.6. AFM image of carbon nanoband and section plot along the red line.

images of 50 nm lines separated by 1 μm. Figure 3.7 (c) is an SEM image of arrays of 50 nm wide lines separated by various widths. The consequence of the strong adhesion between the carbon nanostructures and the Si substrate is that the sizes of the structures pre-defined by EBL are maintained throughout the pyrolysis process. This enables the fabrication of closely spaced structures. The 50 nm wide carbon lines in Figure 3.7 (d) are separated by 50 nm. The 50 nm spacing of carbon nanowire arrays represents the lower limit I have obtained to date. The use of thin (~150 nm) SU-8 films as a starting point and EBL to define the lateral size enables the creation of closely spaced carbon structures with nanoscale dimensions.

Shapes other than lines can also be fabricated. Figure 3.7 (e) is a SEM image of an array of 40 nm diameter carbon disks. The disks appear to be rings due to the scattering of the SEM beam at the edges. Figure 3.7 (f) is an image of the University of Alberta seal and the logo of the McDermott's group, consisting of 50 nm line widths, illustrating that curved and complex structures maintain excellent fidelity through the carbonization process.

The fabrication of carbon nanostructures with dimensions less than 40 nm was attempted. Figure 3.8 shows the SEM and AFM images of a 20 nm wide carbon line. The height of the line is less than 2 nm. The exposure dose (2 $\mu C/cm^2$) used here is much lower than the previous one (10 $\mu C/cm^2$). The postexposure baking (PEB) step is also omitted in order to minimize the diffusion of protons. It is well known that the diffusion of the photoacid generator (PGA) during PEB step generates unwanted cross-linking reactions around predefined

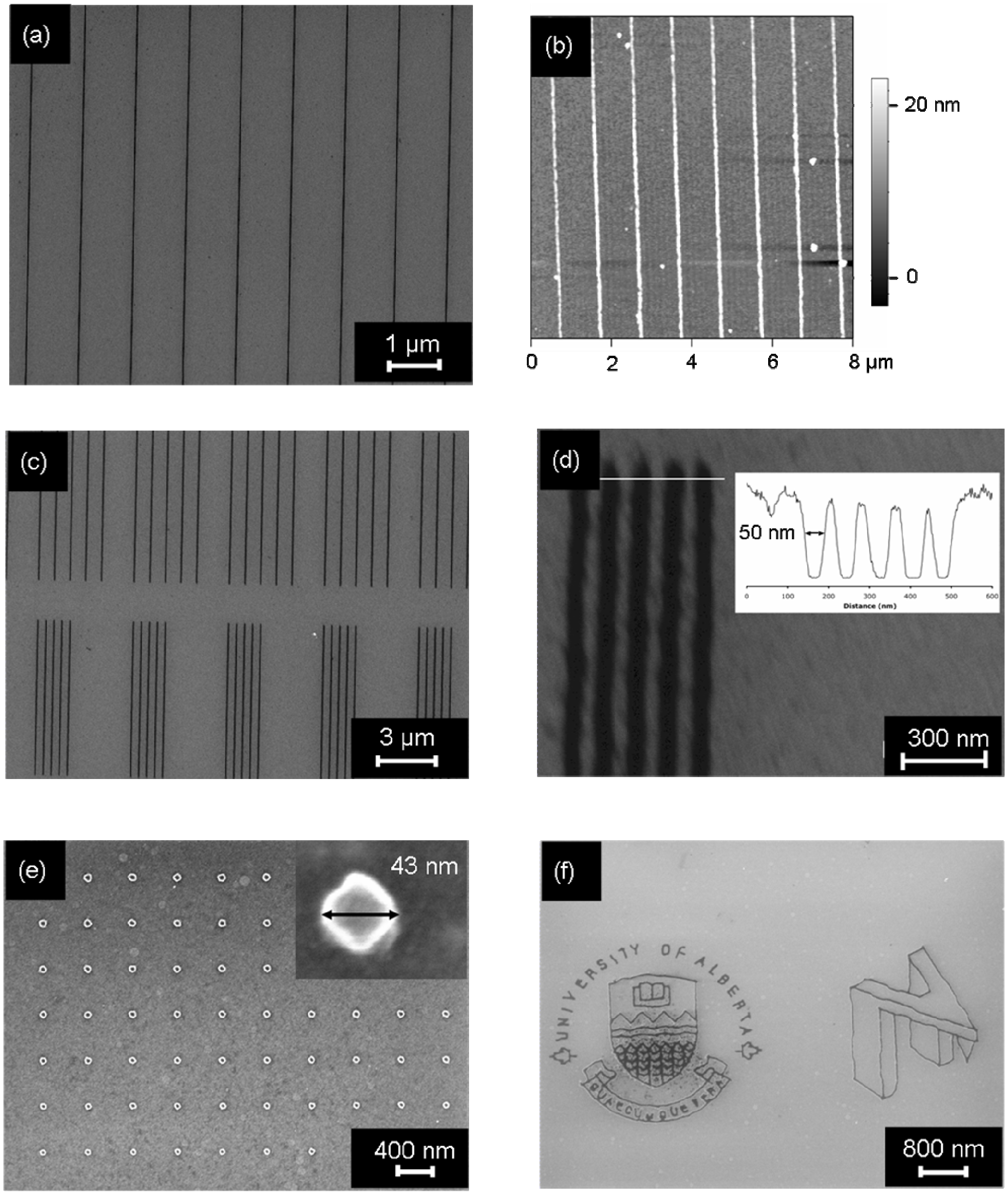

Figure 3.7. SEM and AFM images of various carbon nanostructures. (a) SEM image of 50 nm line array. (b) AFM image of 50 nm line array. (c) SEM image of line arrays with different width. (d) SEM image of an array of 50 nm wide carbon lines separated by 50 nm. (e) SEM image of 40 nm diameter disk array. (f) SEM image of University of Alberta seal and logo of the McDermott's group with 50 nm linewidths.

area and leads to a low resolution.[26,30] With the same patterning conditions with a PEB step, line width increased to ~50 nm. Figure 3.8 shows that 20 nm wide carbon lines can be successfully fabricated, however, the size is very difficult to control. It is noteworthy that the fabrication of carbon nanostructures less than 40 nm is technically challenging with this methodology.

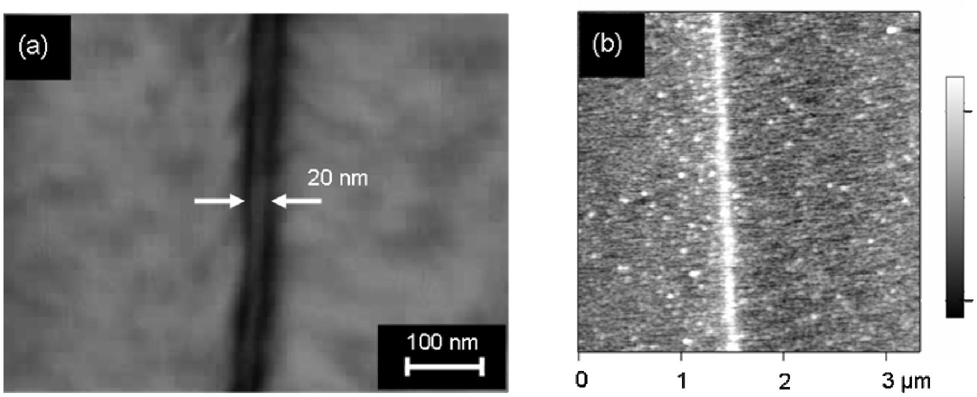

Figure 3.8. (a) SEM image and (b) AFM image of a 20 nm carbon line.

Nanometer sized gaps between nanosized conductors have potential applications in molecular junctions.[31,32] The ability of this technique to fabricate nano-gaps was assessed. Nanoband structures with 200 nm, 100 nm and 20 nm gaps have been designed and written on silicon surface by EBL. The SEM images of the samples are shown in Figure 3.9. Figure 3.9 (a) shows a 200 nm gap as predefined by the design. Figure 3.9 (b) shows a 60 nm gap instead of the intended 100 nm gap. And no gap was obtained when attempting to write a 20 nm gap as shown in Figure 3.9 (C). All attempts to fabricate nanogaps less than

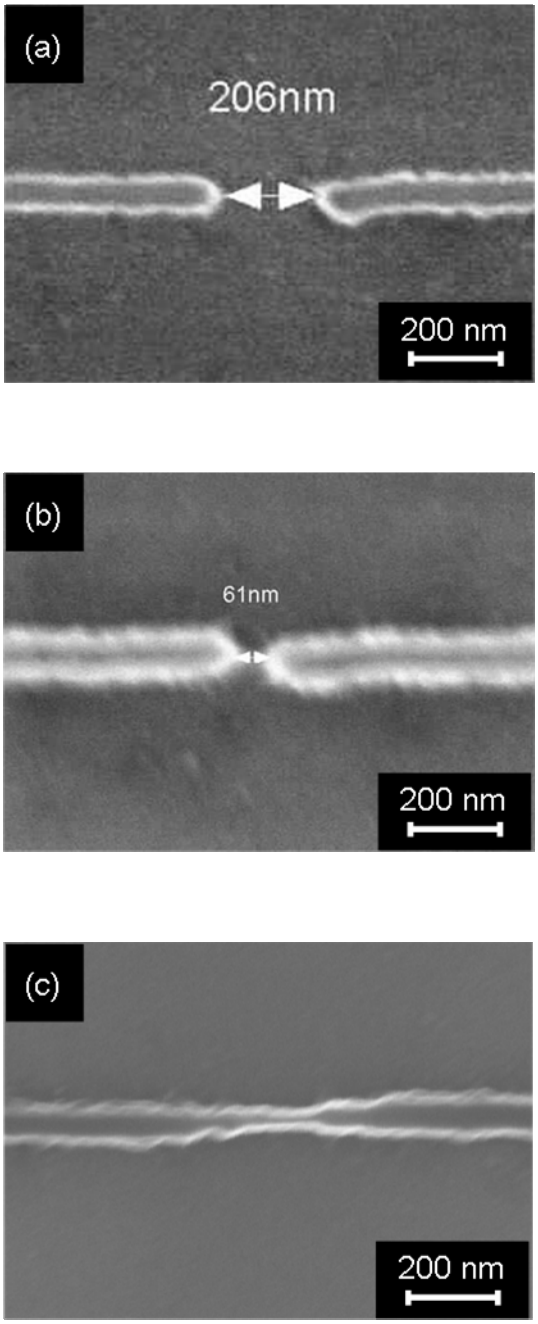

Figure 3.9. SEM images of nanogap samples with different gap designs (a) 200 nm, (b) 100 nm and (c) 20 nm.

50 nm failed. This could be attributed to the limitations of the diffusion of protons[33] and overlaps of scattering electrons. When the two lines are close enough, the scattering electrons around both lines can overlap, leading to a high dose in the region between the two lines. This results in the unwanted exposure.

3.3.5 Resistivity

Typically, carbon nanotube materials must be coupled with microfabricated contact pads in order to apply and measure voltage and current.[1, 2] Connectivity to metal nanowires is typically made through a second lithographic step to deposit metal pads. An important benefit of the combination of EBL and pyrolysis is the ease of establishing connectivity to the macroscopic world. The procedure described here can fabricate connected structures with dimensions from nanometers to millimeters.

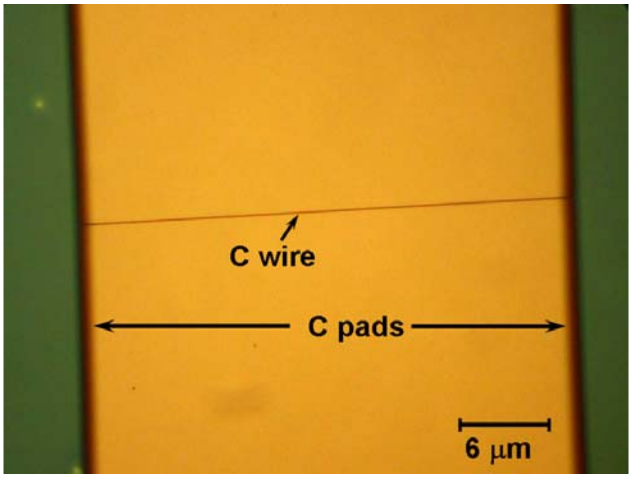

Figure 3.10. Optical micrograph of a 200 nm wide carbon line connected at each end by a carbon pad. The wire spans about 30 μm.

Figure 3.10 shows an optical image of a simple structure consisting of a 200 nm wide carbon wire connected to two pads. The pads in this case are squares, 500 μm on a side. Importantly, both the wire and the pads were fabricated and pyrolyzed during the same process. We should point out that the writing of larger structures requires significant EBL time and cost; however, the combination of EBL to fabricate a master for a higher throughput technique like nanoimprint lithography could potentially lead to a cost effective process for a large number of devices. Despite the cost restrictions, it is clear that complex carbon devices with dimensions from nanometers to millimeters are possible.

A carbon wire was fabricated on a quartz substrate with the following dimensions that were verified with SEM and AFM: length = ~60 μm, width = ~100 nm, thickness = ~6 nm (Figure 3.11). Figure 3.11 (c) shows the current-voltage (I-V) response of the 100-nm-wide carbon wire that is linear and demonstrates Ohmic behavior. The slope of the I-V curve yields a resistance of 0.96 MΩ. The resistivity of the nanoband can be calculated from the equation:

$$R = \rho \frac{l}{A} \tag{3.1}$$

where R = resistance, ρ = resistivity, l = length of carbon nanowire. A = the cross-section area of carbon nanoband or nanowire, which presumably equals to band width (w) times thickness (h). A resistivity of ~1×10^{-5} Ω·m was thus calculated based on equation 3.1.

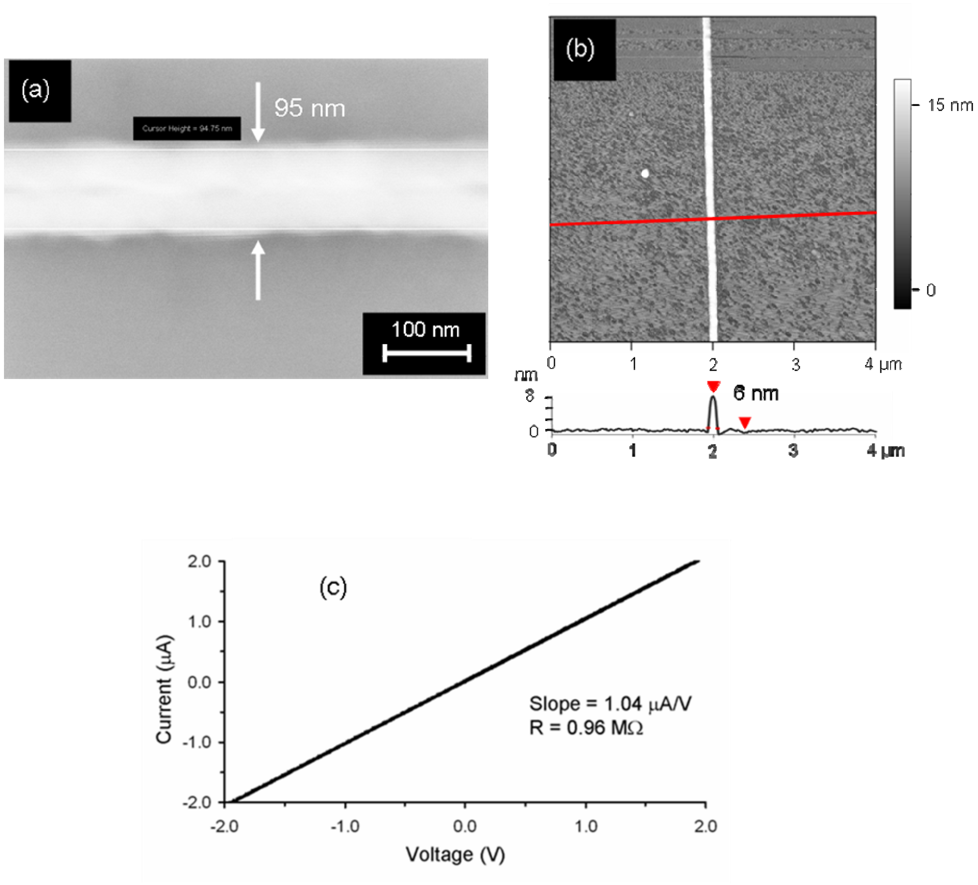

Figure 3.11. (a) SEM image, (b) AFM image and (c) current-voltage curve of a 100 nm wide carbon nanowire.

A set of 100 μm long carbon band structures have been fabricated with widths ranging from 100 nm to 20 μm. Their resistances were measured and the resistivities were calculated and listed in Table 3.1.

Table 3.1. Resistivities of carbon micro and nanoband structures.[a]

Widths[a,b]	Thickness (nm)[a,c]	Resistance (kΩ)[a]	Resistivity (Ω·m)[a]
115 ± 18 nm	9 ± 3	$(2.9 \pm 2.0) \times 10^{3}$	$(3.4 \pm 2.7) \times 10^{-5}$
310 ± 10 nm	11 ± 3	$(1.5 \pm 0.8) \times 10^{3}$	$(5.0 \pm 2.3) \times 10^{-5}$
615 ± 13 nm	11 ± 2	$(6.2 \pm 1.5) \times 10^{2}$	$(4.3 \pm 1.1) \times 10^{-5}$
5.0 ± 0.1 μm	12 ± 3	$(7.8 \pm 0.8) \times 10$	$(4.5 \pm 0.8) \times 10^{-5}$
20.0 ± 0.1 μm	11 ± 3	$(2.0 \pm 0.3) \times 10$	$(4.6 \pm 0.7) \times 10^{-5}$

[a] Values reported are mean ± standard deviation. Five samples were used for the measurement.

[b] Band widths were measured by SEM

[c] Band widths were measured by AFM

Carbonized SU-8 films on quartz substrates at 1000 °C yield an average resistivity of 5.7×10^{-5} Ω·m as described in Chapter 2. The reported resistivity for other carbonized resists and for a common glassy carbon (Tokai) prepared at 1000°C is ~5×10^{-5} Ω·m.[10] Our experimental results demonstrate that the resistivities of carbon micro or nanostructures are close to the macroscopic carbon films prepared by pyrolysis of SU-8 films and by extension, to bulk graphitic carbon materials.

3.4 Conclusions

In this chapter, we have shown that nanometer sized graphitic carbon structures can be fabricated with a combination of EBL and heat treatment. EBL enables a variety of shapes and sizes to be fabricated at predefined locations. The carbonized nanostructures exhibit structure and properties similar to other forms of disordered carbon materials and adhere strongly to the underlying substrate through an interfacial layer of SiC. The resistivity of the nanosctructures is similar to that of bulk disordered carbon materials. This will enable their use in electrochemistry, sensing and in other nanoscale applications. We note that the fabrication of these graphitic carbon nanostructures must occur in the initial stages of production of an integrated device. The high temperature required for carbonization limits the number of pre-pyrolysis fabrication steps that can be applied.

3.5 References

1. Martel, R.; Schmidt, T.; Shea, H. R.; Hertel, T.; Avouris, P., Single- and multi-wall carbon nanotube field-effect transistors. *Applied Physics Letters* **1998,** 73, 2447-2449.
2. Rueckes, T.; Kim, K.; Joselevich, E.; Tseng, G. Y.; Cheung, C. L.; Lieber, C. M., Carbon nanotube-based nonvolatile random access memory for molecular computing. *Science* **2000,** 289, 94-97.
3. Katz, E.; Willner, I., Biomolecule-functionalized carbon nanotubes: Applications in nanobioelectronics. *Chemphyschem* **2004,** 5, 1085-1104.
4. Ciambelli, P.; Sannino, D.; Sarno, M., Carbon nanotubes, building blocks of nanotechnology. *Chimica Oggi-Chemistry Today* **2005,** 23, 22-28.
5. Awasthi, K.; Srivastava, A.; Srivastava, O. N., Synthesis of carbon nanotubes. *Journal of Nanoscience and Nanotechnology* **2005,** 5, 1616-1636.
6. Bahr, J. L.; Tour, J. M., Covalent chemistry of single-wall carbon nanotubes. *Journal of Materials Chemistry* **2002,** 12, 1952-1958.
7. Kong, J.; Franklin, N. R.; Zhou, C. W.; Chapline, M. G.; Peng, S.; Cho, K. J.; Dai, H. J., Nanotube molecular wires as chemical sensors. *Science* **2000,** 287, 622-625.
8. Lee, J. U.; Gipp, P. P.; Heller, C. M., Carbon nanotube p-n junction diodes. *Applied Physics Letters* **2004,** 85, 145-147.
9. Bosnick, K.; Gabor, N.; McEuen, P., Transport in carbon nanotube p-i-n diodes. *Applied Physics Letters* **2006,** 89, 163121-163121.

10. McCreery, R. L., Carbon electrodes: Structural effects on electron transfer kinetics. In *Electroanalytical chemistry*, Bard, A. J., Ed. New York, 1991; pp 221-374.

11. Ranganathan, S.; McCreery, R. L., Electroanalytical performance of carbon films with near-atomic flatness. *Analytical Chemistry* **2001,** 73, 893-900.

12. McCreery, R. L.; Wu, J.; Kalakodimi, R. P., Electron transport and redox reactions in carbon-based molecular electronic junctions. *Physical Chemistry Chemical Physics* **2006,** 8, 2572-2590.

13. Schueller, O. J. A.; Brittain, S. T.; Marzolin, C.; Whitesides, G. M., Fabrication and characterization of glassy carbon MEMS. *Chemistry Materials* **1997,** 9, 1399-1406.

14. Schueller, O. J. A.; Brittain, S. T.; Whitesides, G. M., Fabrication of glassy carbon microstructures by pyrolysis of microfabricated polymeric precursors. *Advanced Materials* **1997,** 9, 477-480.

15. Shah, H. V.; Brittain, S. T.; Huang, Q.; Hwi, S.-J.; Whitesides, G. M.; Smith Jr., D. W., Bis-o-diynylarene (BODA) derived polynapthalenes as precursors to glassy carbon microstructures. *Chemistry of Materials* **1999,** 11, 2623-2625.

16. Park, B. Y.; Taherabadi, L.; Wang, C. L.; Zoval, J.; Madou, M. J., Electrical properties and shrinkage of carbonized photoresist films and the implications for carbon microelectromechanical systems devices in

conductive media. *Journal of the Electrochemical Society* **2005,** 152, J136-J143.

17. Wang, C. L.; Madou, M., From MEMS to NEMS with carbon. *Biosensors & Bioelectronics* **2005,** 20, 2181-2187.

18. Singh, A.; Jayaram, J.; Madou, M.; Akbar, S., Pyrolysis of negative photoresists to fabricate carbon structures for microelectromechanical systems and electrochemical applications. *Journal of the Electrochemical Society* **2002,** 149, E78-E83.

19. Wang, C. L.; Jia, G. Y.; Taherabadi, L. H.; Madou, M. J., A novel method for the fabrication of high-aspect ratio C-MEMS structures. *Journal of Microelectromechanical Systems* **2005,** 14, 348-358.

20. Liang, C. D.; Hong, K. L.; Guiochon, G. A.; Mays, J. W.; Dai, S., Synthesis of a large-scale highly ordered porous carbon film by self-assembly of block copolymers. *Angewandte Chemie-International Edition* **2004,** 43, 5785-5789.

21. Kowalewski, T.; Tsarevsky, N. V.; Matyjaszewski, K., Nanostructured carbon arrays from block copolymers of polyacrylonitrile. *Journal of the American Chemical Society* **2002,** 124, 10632-10633.

22. Tang, C. B.; Tracz, A.; Kruk, M.; Zhang, R.; Smilgies, D. M.; Matyjaszewski, K.; Kowalewski, T., Long-range ordered thin films of block copolymers prepared by zone-casting and their thermal conversion into ordered nanostructured carbon. *Journal of the American Chemical Society* **2005,** 127, 6918-6919.

23. Vieu, C.; Carcenac, F.; Pepin, A.; Chen, Y.; Mejias, M.; Lebib, A.; Manin-Ferlazzo, L.; Couraud, L.; Launois, H., Electron beam lithography: Resolution limits and applications. *Applied Surface Science* **2000,** 164, 111-117.

24. Park, B. Y.; Yaherabadi, L.; Wang, C. L.; Zoval, J.; Madou, M. J., Electrical properties and shrinkage of carbonized photoresist films and the implications for carbon microelectromechanical systems devices in conductive media. *Journal of the Electrochemical Society* **2005,** 152, J136-J143.

25. Wang, C. L.; Madou, M., From MEMS to NEMS with carbon. *Biosensors & Bioelectronics* **2005,** 20, 2181-2187.

26. Aktary, M.; Jensen, M. O.; Westra, K. L.; Brett, M. J.; Freeman, M. R., High-resolution pattern generation using the epoxy novolak SU-8 resist by EBL. *Journal of Vacuum Science & Technology B* **2003,** 21, L5-L7.

27. Feng, R.; Farris, R. J., Influence of processing conditions on the thermal and mechanical properties of SU8 negative photoresist coatings. *Journal of Micromechanics and Microengineering* **2003,** 13, 80-88.

28. Feng, R.; Farris, R. J., The characterization of thermal and elastic constants for an epoxy photoresist SU8 coating. *Journal of Materials Science* **2002,** 37, 4793-4799.

29. Ranganathan, S.; McCreery, R.; Majji, S. M.; Madou, M., Photoresist-derived carbon for microelectromechanical systems and electrochemical applications. *Journal of the Electrochemical Society* **2000,** 147, 277-282.

30. Glezos, N.; Argitis, P.; Velessiotis, D.; Raptis, I.; Hatzakis, M.; Hudek, P.; Kostic, I., Aqueous base development and acid diffusion length optimization in negative epoxy resist for electron beam lithography. *Journal of Vacuum Science & Technology B* **2000,** 18, 3431-3434.

31. Kergueris, C.; Bourgoin, J. P.; Palacin, S.; Esteve, D.; Urbina, C.; Magoga, M.; Joachim, C., Electron transport through a metal-molecule-metal junction. *Physical Review B* **1999,** 59, 12505-12513.

32. Mahapatro, A. K.; Ying, J. W.; Ren, T.; Janes, D. B., Electronic transport through ruthenium-based redox-active molecules in metal-molecule-metal nanogap junctions. *Nano Letters* **2008,** 8, 2131-2136.

33. Bilenberg, B.; Jacobsen, S.; Schmidt, M. S.; Skjolding, L. H. D.; Shi, P.; Boggild, P.; Tegenfeldt, J. O.; Kristensen, A., High resolution 100 kV electron beam lithography in SU-8. *Microelectronic Engineering* **2006,** 83, 1609-1612.

Chapter 4. Electrochemistry of Single and Array Graphitic Carbon Nanoband Electrodes

This chapter focuses on the electrochemical characterization of graphitic carbon nanoband electrodes. As is mentioned in Chapter 3, EBL can be used to directly write predefined nanometer-sized wires in the thin layer of a negative resist on an appropriate substrate. Careful heat treatment results in carbon nanostructures. These nanometer sized carbon wires can then be used as nanoband electrodes by connecting both ends to gold pads as current collectors. In this chapter, both single and array nanoband electrodes were constructed and their electrochemical properties were investigated and compared with the existing theory.

4.1 Introduction

Since being introduced by Wightman[1] and Fleishmann[2] independently, electrodes with micro and nanometer dimensions have received much interest.[3-10] Compared with conventional electrodes, micro- and nanoelectrodes have advantageous characteristics, such as higher mass transfer efficiency, smaller RC cell time constants, lower iR drop, higher signal-noise ratio, and higher current density, etc.[3,4] These advantages have led to exciting applications in electrochemical studies,[5] biological analysis[6-7] and sensor research.[8-10] Chapter 1 and several reviews provide more detailed information.[11,12]

Carbon electrodes have been widely used in electroanalytical chemistry. Compared to metal electrodes, carbon electrodes have lower background current within a wider potential range. This makes them suitable for highly sensitive detection.[13] Additionally, carbon is a versatile electrode material that can undergo various chemical and electrochemical modifications to produce functionalized surfaces and thus influence reactivity.[13-15] Such surface modifications make a carbon electrode a good support for the immobilization of biomolecules[8,16] and make them very attractive for biosensor applications.[7] Although carbon electrodes exhibit excellent electrochemical characteristics, they can only detect a limited number of analytes due to a high overpotential.[4]

The fabrication of carbon disk or cone nanoelectrodes has been demonstrated by several groups.[17-24] These electrodes are typically fabricated from carbon fibers by an etching-coating method. This method consists of two basic processes. First, carbon fibers are etched to sharp tips by electrochemical or flame etching methods. Second, an insulating layer is coated on the tip. With increasing temperature, the insulating layer contracts and solidifies, and a sharp tip of the carbon fiber is exposed with nanometer diameter. The disk nanoelectrodes can be fabricated as small as 1 nm.[21] Carbon fiber nanocone or nanodisk electrodes have been used for nanosensors,[8] scanning electrochemical microscopy (SECM),[25] real time monitoring of living vesicles,[7] and metal electrodeposition.[26] Carbon nanotubes can also be used as nanoelectrodes.

Recently, the fabrication of nanoelectrode arrays from carbon nanotubes has been introduced.[27-29] Their application to DNA detection was also investigated.[30,31]

In addition to disk shaped nanoelectrodes, band nanoelectrodes are another set of widely used nanoelectrodes. The current observed at the nanoband electrodes shows quasi-steady state behavior with a much higher current density than disk or cone geometries of similar size. This makes them more advantageous because the current can be easily measured.[3] Nanoband electrodes can be prepared by sealing thin metal[32-37] or carbon films[38] into a suitable insulator. The pretreatment of the electrodes, however, is challenging. Grinding or cutting the film edge electrodes leads to uncertainties about the exposed electrode area.[32] Excessive polishing needs to be avoided to prevent the metal film from recessing into the insulating material, which leads to the decrease of the limiting current and non-steady state behavior.[34] Au band electrodes with widths from 3 to 150 nm have been prepared by evaporating Au film onto a silane-modified glass substrate.[35] The real electrode surface area was 20-500 times larger than that expected from the thickness of the Au film.

The development of micro and nanofabrication techniques in the microelectronic industries has led to the creation of submicron-sized structures. In particular, e-beam lithography (EBL) has been widely used to fabricate nanostructures down to tens of nanometers. We are motivated to use this well-developed nanofabrication technique to fabricate nano carbon electrodes with accurately controlled size. In this chapter, we report a reproducible nanofabrication method for single and array carbon nanoband electrodes using a combination of electron beam lithography (EBL) and carbonization. The dimensions of individual electrodes and interband distance can be precisely controlled by EBL and preserved during the carbonization process. Their electrochemical properties were also investigated at different scan rates and their voltammetric behaviors were compared with the classic theory.

4.2 Experimental

4.2.1 Reagents

Hexaammineruthenium chloride ($Ru(NH_3)_6Cl_3$, Strem Chemicals), potassium ferricyanide ($K_3Fe(CN)_6$, Caledon), and potassium chloride (KCl, Aldrich) were all used as received. All solutions were prepared using distilled/deionized water (18 MΩ·cm). 4-Nitroazobenzene (NAB) diazonium tetrafluoroborate was synthesized according to the previous reports.[39]

4.2.2 Characterization

All electrochemical experiments were performed in an inverted three-electrode cell. The cell was connected to an EG&G Parc-263A electrochemical system (Princeton Applied Research, USA) with platinum auxiliary and home made Ag/AgCl (sat. KCl) as reference electrode. Scanning electron microscopy (SEM) images were recorded on a Hitachi S4800 operating at 5-20 kV, and atomic force microscopy (AFM) was performed with a MFP-3D instrument (Asylum Research, Santa Barbara, CA) using conductive Ti-Pt coated silicon tips

(NSC21/Ti-Pt, MikroMasch USA). Images were acquired in contact and conductive modes with the bias voltage setting at 2 V (tip vs. sample).

4.2.3 Mask preparation

Masks for the patterns of current collectors and electrochemical windows were designed in L-Edit software (Pasadena, CA). The designs were written on a Nanofilm chrome blank photomask by a Heidelberg DWL laser mask generator (HeidelBerg, Germany). The patterns were then developed in a Shipley developer solution and transferred to the bottom chrome layer by chemical etching in a Chrome Etch Semi Grade solution (Arch Chemicals Inc., Norwalk CT). The remaining photoresist was removed by rinsing with acetone (Fisher). Before use, the mask was immersed in cold "piranha" solution for two hours, followed by rinsing with distilled water and drying by N_2.

4.2.4 Construction of nano band electrodes

Both photolithography and e-beam lithography were performed in the NanoFab (micro and nanofabrication facility in University of Alberta) clean room with class 100 work areas. The humidity within the lithography room was controlled between 45 to 55%.

Silicon wafers (100, N-type, doped, 500 μm thick, University Wafers, Boston) were cleaned with fresh piranha solution before use. Figure 4.1 illustrates the process of the fabrication procedure of the nanoband electrode. Briefly, a thin layer of SU-8 2000.1 (MicroChem Corp.) was spin coated onto the substrate and

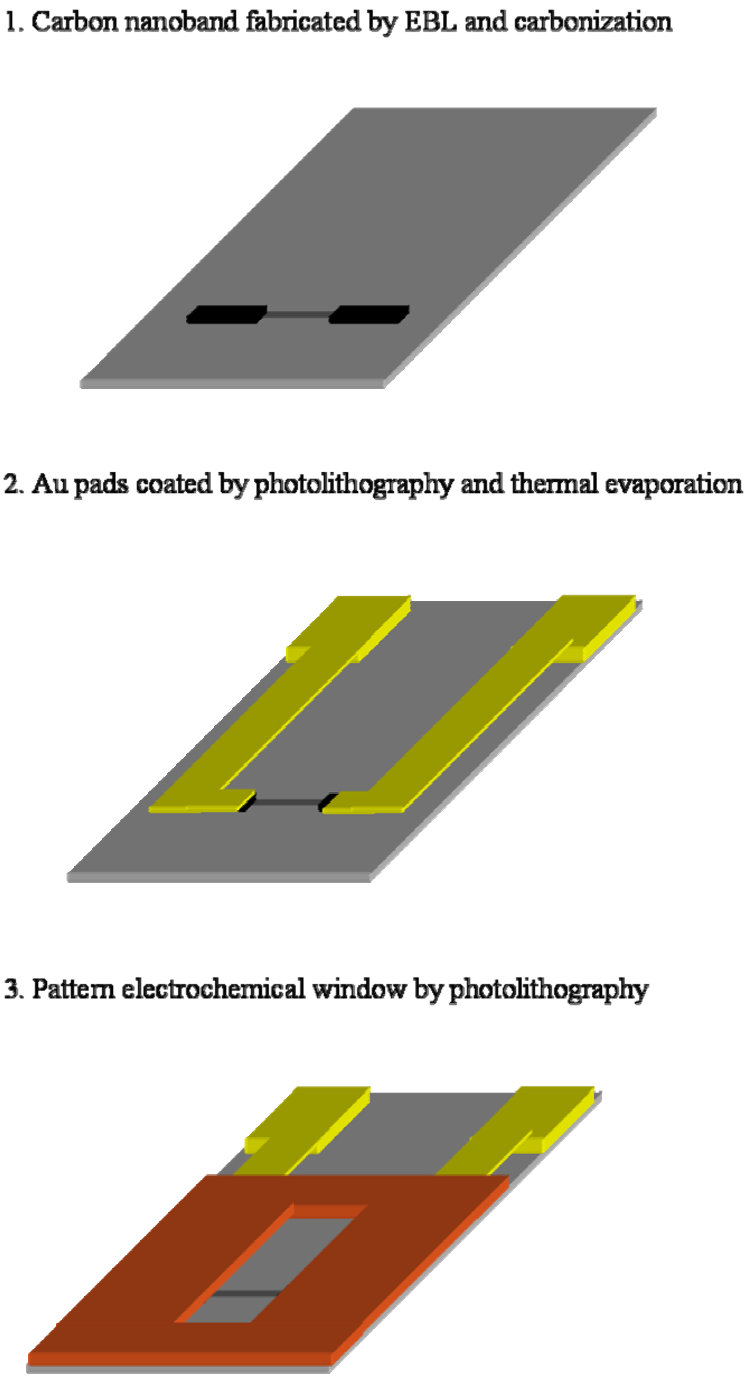

1. Carbon nanoband fabricated by EBL and carbonization

2. Au pads coated by photolithography and thermal evaporation

3. Pattern electrochemical window by photolithography

Figure 4.1. The procedure of fabricating carbon nanoband electrodes.

soft baked (60 s at 65ºC and then 120 s at 90ºC). Nanowires were written into the SU-8 with standard electron beam lithography (EBL), baked at 200ºC for 1 h and then carbonized at 1000ºC for 0.5 h in a tube furnace (Lindberg) with a continuous flow of forming gas (95% N_2 + 5% H_2) as described in Chapter 3. Nanoband electrodes were constructed from carbon nanowires. In order to use the nanowires as electrodes, both ends of the carbon nanowire should be contacted with metal pads as the current collector, which was patterned by a lift-off method with photolithography and thermal evaporation. Thin films of chromium (1 nm Cr film) and gold (80 nm Au film) were deposited using a thermal evaporation system (Torr International, Inc.). Figure 4.2 (a) shows the photo of the fabricated electrode.

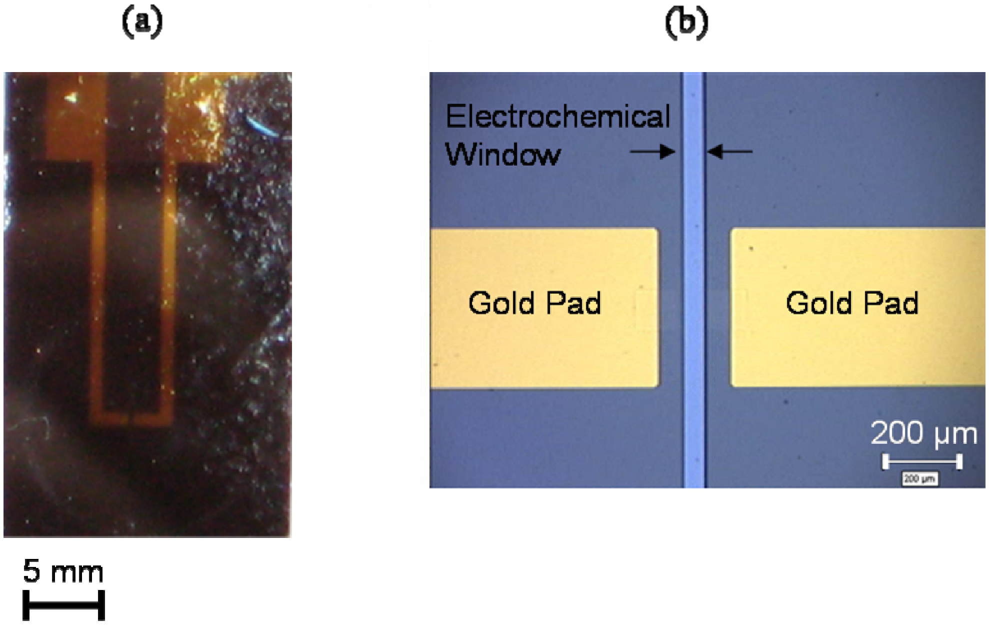

Figure 4.2. (a) Photo of the entire electrode with current collector and (b) optical image of the electrochemical window.

For electrochemical characterization, a thick layer of positive photoresist AZ 4330-RS (AZ Electronic Materials, Somerville, N.J.) was spin coated on the sample surface to serve as an insulating layer to prevent electrochemical reactions taking place at the gold pads. A 50 μm wide rectangular opening was patterned in the photoresist layer by standard photolithography to partially expose the carbon nanowire as an electrochemical window. Optical image of the electrochemical window is shown on Figure 4.2 (b).

4.2.5 Electrochemical characterization and modification of carbon band nanoelectrodes.

Electrochemical experiments were carried out in a home-made electrochemical cell equipped with a platinum wire as the counter and a home-made Ag/AgCl reference electrode.

4.3 Results and discussion

4.3.1 Electrode size

An accurate measure of the electrode area is required in order to correlate measured results with known theories of nanoband electrodes. The length of the electrode is determined by the electrochemical window defined by photolithography (~50 μm). The electrode width was measured by SEM. Figure 4.3 shows the SEM images of both single and array carbon nanoband electrodes used in this work. The insets are images with higher magnification. The widths of both single and array element electrodes are about 200 nm, which is predefined by

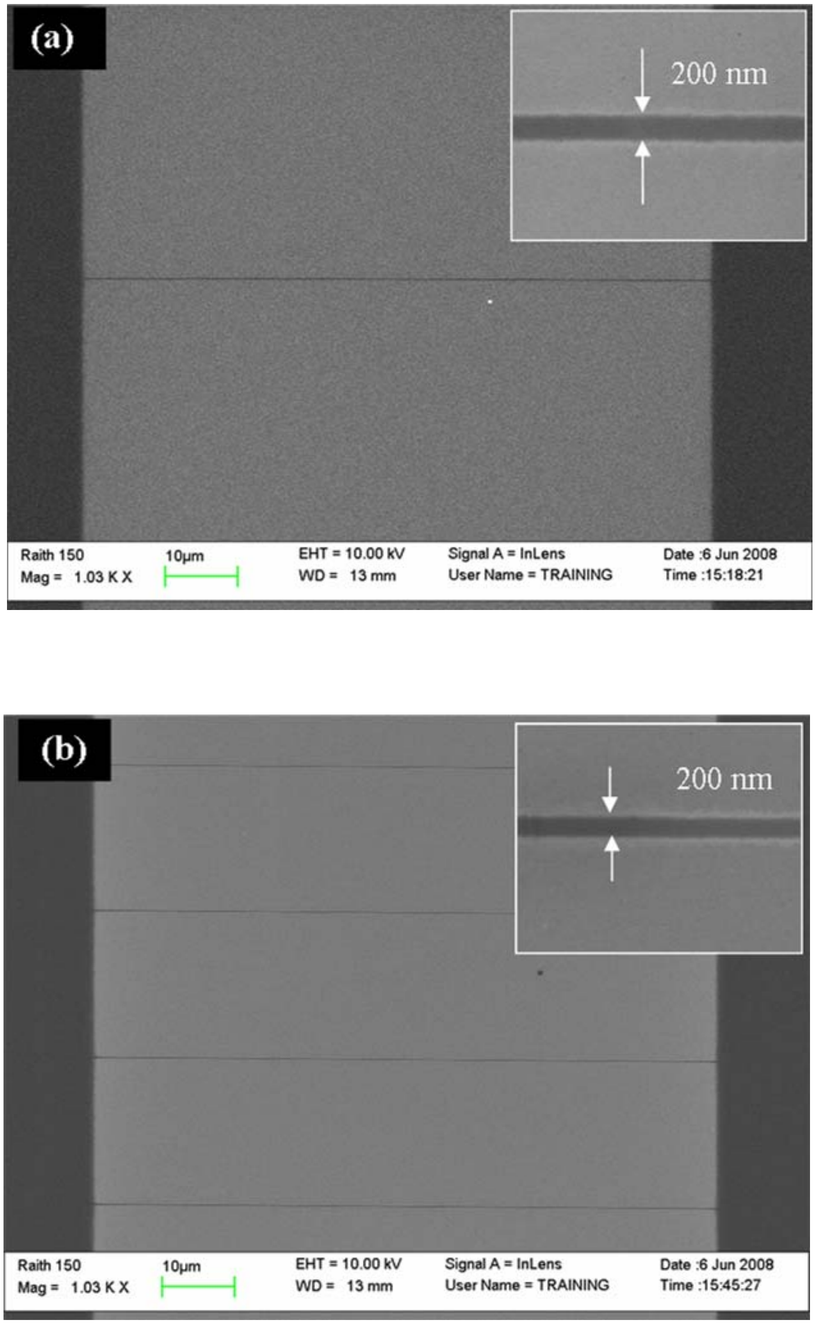

Figure 4.3. SEM images of carbon single band and band array nanoelectrodes. (a) Single band nanoelectrode, (b) band array nanoelectrode (interband distance: 20 µm).

EBL. In EBL, backscattered electrons lead to unwanted exposure around the desired exposure region.[40] The influence of this proximity effect on the actual width of the electrode is difficult to assess by SEM alone. Conductive AFM (CAFM) was also used in this work to measure the width of the electrode and the results were compared with the SEM images. Figure 4.4 shows the scheme of a CAFM. Compared with ordinary AFM, CAFM employs metal coated AFM tips and a controllable DC bias voltage between the tip and sample. Thus, both the topographic and current signals can be obtained simultaneously. In our experiment, a 2 V tip vs. sample bias voltage was applied while imaging and the corresponding current was recorded. Conductive regions on the sample generate a higher tip current than less conductive areas.

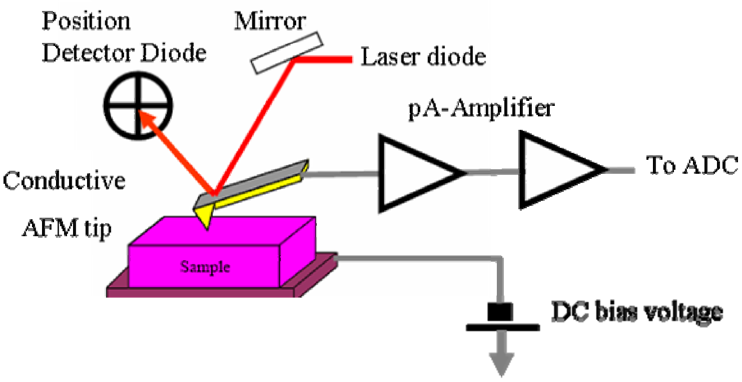

Figure 4.4. Scheme of conductive AFM.

Figure 4.5 shows the height mode [Figure 4.5(a)] and the current [Figure 4.5(b)] images of the nanoband electrode. The bottom plots in Figure 4.5 are corresponding cross sectional profiles along the red lines highlighted. As shown

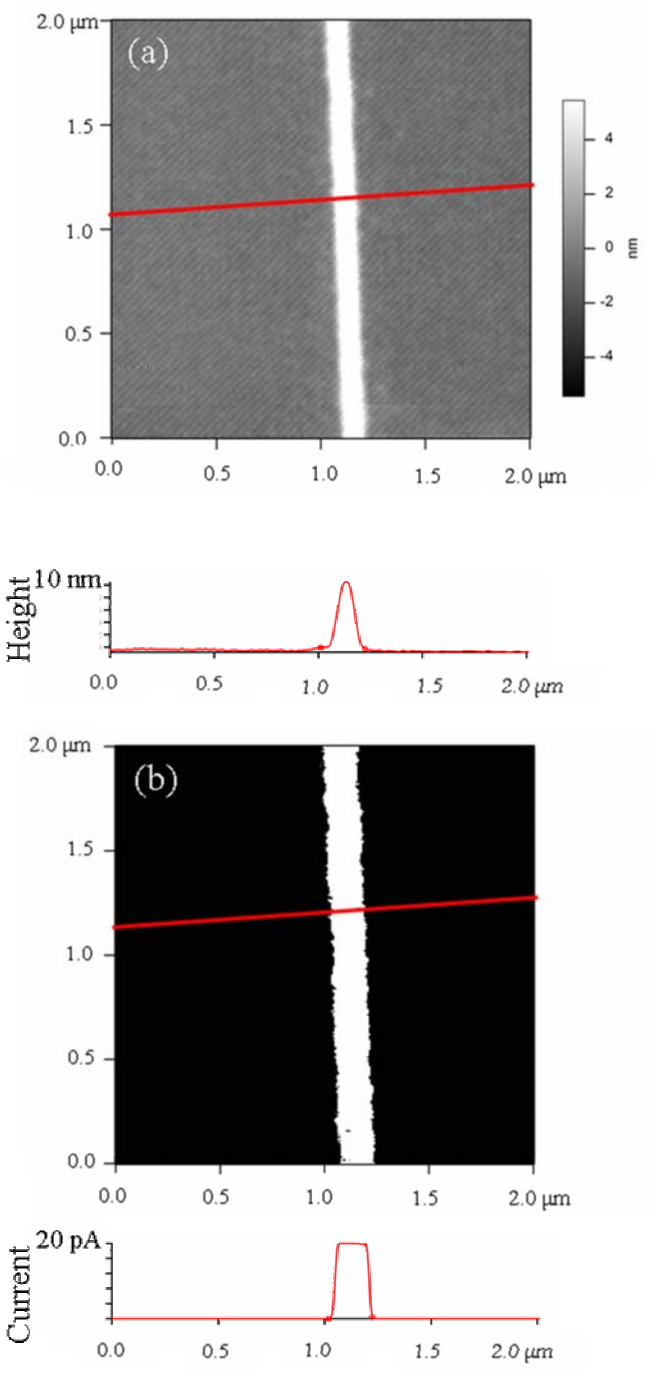

Figure 4.5. Conductive-AFM images of a carbon nanoband electrode in the height mode (a) and conductive mode (b). The bottom plots are the corresponding signals when tips run across the sample surface which is labeled by red lines.

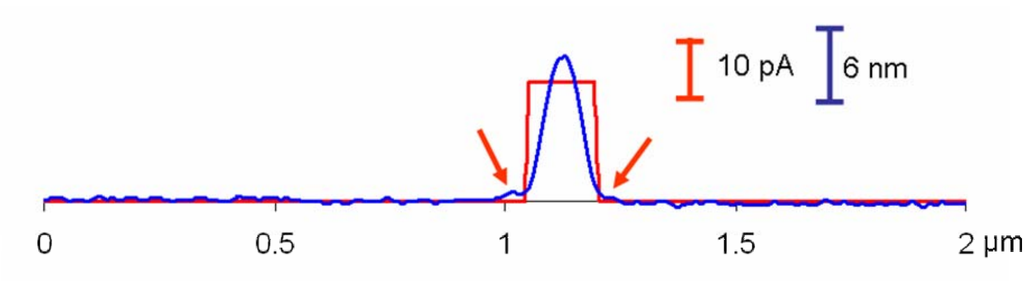

Figure 4.6. Overlay of height (blue) and current (red) cross-sectional profiles from Figure 4.5.

in the current image in Figure 4.4(b), the current at the carbon nanoband is about 20 pA, which is the maximum current output of the CAFM preamplifier. The current at the non-carbon surface is almost zero, although the silicon wafer is doped. This apparent lower conductivity can be explained by the native oxide layer on the silicon surface. The electrode size was measured to be about 203 nm from both height and conductive images, which is very close to the measurement obtained by SEM.

The height and conductive profiles are overlayed for comparison in Figure 4.6. The height plot shows a very narrow "shoulder" zone near the foot of the band as labelled by arrows in Figure 4.6. This is a very thin and narrow zone adjacent to the exposed area likely created by backscattering. By overlaying the conductive and height plots, we can see that the corresponding conductive signal shows zero current at the shoulder. This means that the "shoulder" area is less conductive. Therefore, the contributions of this shoulder to the final width of the electrode were omitted. In subsequent experiments, the widths of band nanoelectrodes were measured mainly by SEM.

4.3.2 Single electrode

A set of single electrodes with different widths, from 200 nm to 40 μm, were fabricated. Figure 4.7 shows the cyclic voltammograms in 5 mM $Ru(NH_3)_6Cl_3$ (1 M KCl) at a scan rate of 400 mV/s collected at these electrodes. The band electrodes used are 200 nm [Figure 4.7(a)], 1 μm [Figure 4.7(b)], 10 μm [Figure 4.7(c)], and 40 μm wide [Figure 4.7(d)], respectively. With increasing width, the voltammograms start with a sigmoidal shape (200 nm electrode) and gradually change to peak shaped (40 μm electrode). The shape of voltammograms is mainly governed by the ratio of diffusion layer thickness to electrode width (X_d/W).[3] The mass transport to the electrode surface can be described by one of two modes, linear diffusion and nonlinear diffusion. When the diffusion layer thickness is much larger than the electrode width ($X_d/W >> 1$), the diffusion is mainly nonlinear diffusion. Under these conditions current in a CV reaches a steady state for a circular geometry or a quasi-steady state for a band geometry, resulting in a sigmoid shape voltammogram. The current response for a nano-band electrode can be calculated based on equation 4.1.[41]

$$i = 2\pi nFDCl \ / \ln\left(4Dt \ / \ r_0^2\right) \tag{4.1}$$

In this equation, D is the bulk solution diffusion coefficient, t is time, n is the number of electrons involved in the electron-transfer reaction, C is the concentration of the species undergoing electron-transfer, F is the Faraday constant, l is the electrode length, and r is the radius of equivalent hemicylinder,

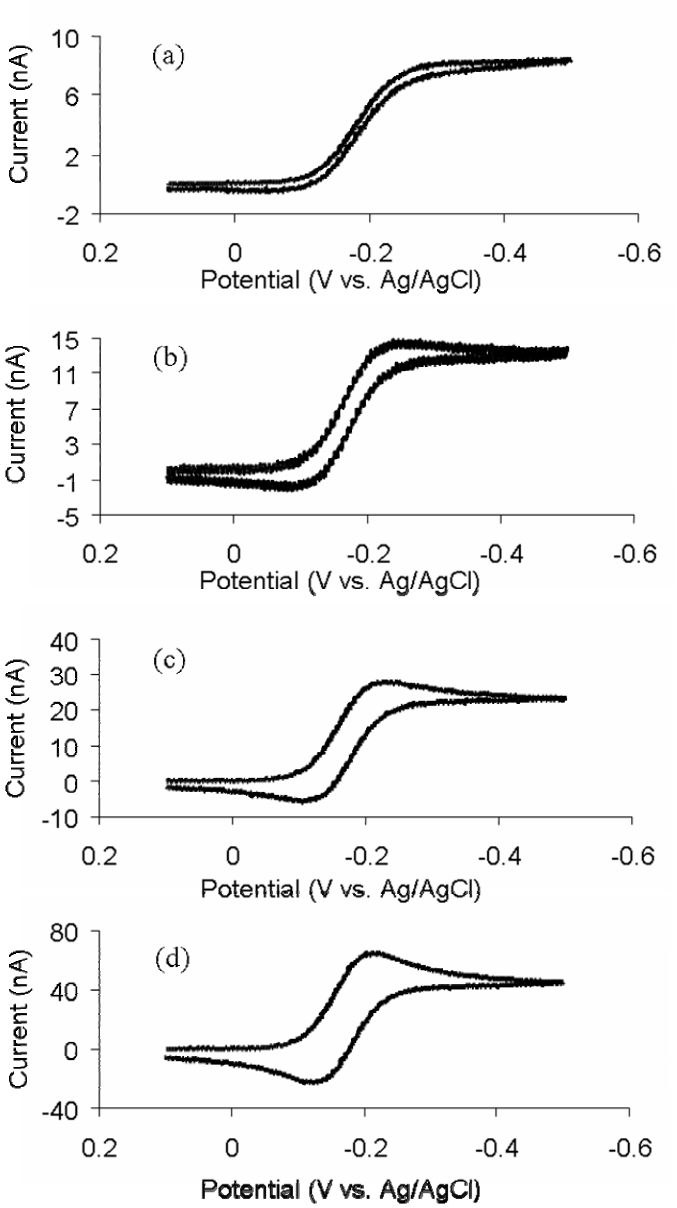

Figure 4.7. Cyclic Voltammograms of single electrodes with different width at a scan rate of 400 mV/s in 5 mM $Ru(NH_3)_6Cl_3$ and 1 M KCl. (a) 200 nm, (b) 1 μm, (c) 10 μm, (d) 40 μm.

which is equal to the width of the band electrode divided by π ($r = w/\pi$).

When the diffusion layer thickness is much smaller than the electrode width ($X_d/W << 1$), the mass transport is mainly controlled by linear diffusion, and voltammograms observed under these conditions are peak shaped. The peak current can be calculated by equation 4.2.

$$i_p = 2.69 \times 10^5 n^{3/2} A D^{1/2} C \nu^{1/2} \tag{4.2}$$

Where A is the electrode area and ν is the scan rate.

In cyclic voltammetry experiments, time scale (t) and diffusion layer thickness (X_d) can be calculated by the following equations.[42]

$$t = RT/Fv \tag{4.3}$$

$$X_D = (\pi Dt)^{1/2} \tag{4.4}$$

In this equation, t is time scale, X_D is the diffusion layer thickness, D is the bulk solution diffusion coefficient, v is the concentration potential scan rate, F is the Faraday constant. The diffusion coefficient (D) equals 6.5×10^{-6} cm^2/s for $Ru(NH_3)_6^{3+}$ based on a previous publication.[43] Based on equation 4.3 and 4.4, diffusion layer thicknesses at different scan rates are calculated and listed in Table 4.1.

The diffusion layer thickness, X_D, equals 13 μm at a scan rate of 400 mV/s. Thus only the 200 nm electrode has a much smaller width than the diffusion layer thickness. Therefore, the current response is mainly controlled by nonlinear diffusion and the voltammogram shows a sigmoidal shape [Figure 4.7 (a)]. The 40 μm electrode has a much larger width than diffusion layer thickness and the current response is mainly controlled by the linear diffusion. The voltammogram exhibits a peak shape [Figure 4.7 (d)]. The other two electrodes have current response at the transition from nonlinear diffusion to linear diffusion due to the X_d/W ratio. Their voltammograms are expected to be more or less peak shaped depending on their electrode width, as shown by Figure 4.7 (b) and Fig. 4.7 (c).

Table 4.1. Diffusion layer thicknesses at different scan rates.

Scan rate	Diffusion layer thickness [a] (X_D)	Scan rate	Diffusion layer thickness [a] (X_D)
10 mV/s	72 μm	100 mV/s	22 μm
20 mV/s	51 μm	200 mV/s	16 μm
30 mV/s	41 μm	400 mV/s	13 μm
40 mV/s	36 μm	600 mV/s	9 μm
50 mV/s	32 μm	800 mV/s	8 μm
60 mV/s	30 μm	1 V/s	7 μm
70 mV/s	27 μm	2 V/s	5 μm
80 mV/s	26 μm	8 V/s	2.5 μm
90 mV/s	24 μm	10 V/s	2 μm

[a] Values are calculated from equation 4.3 and 4.4.

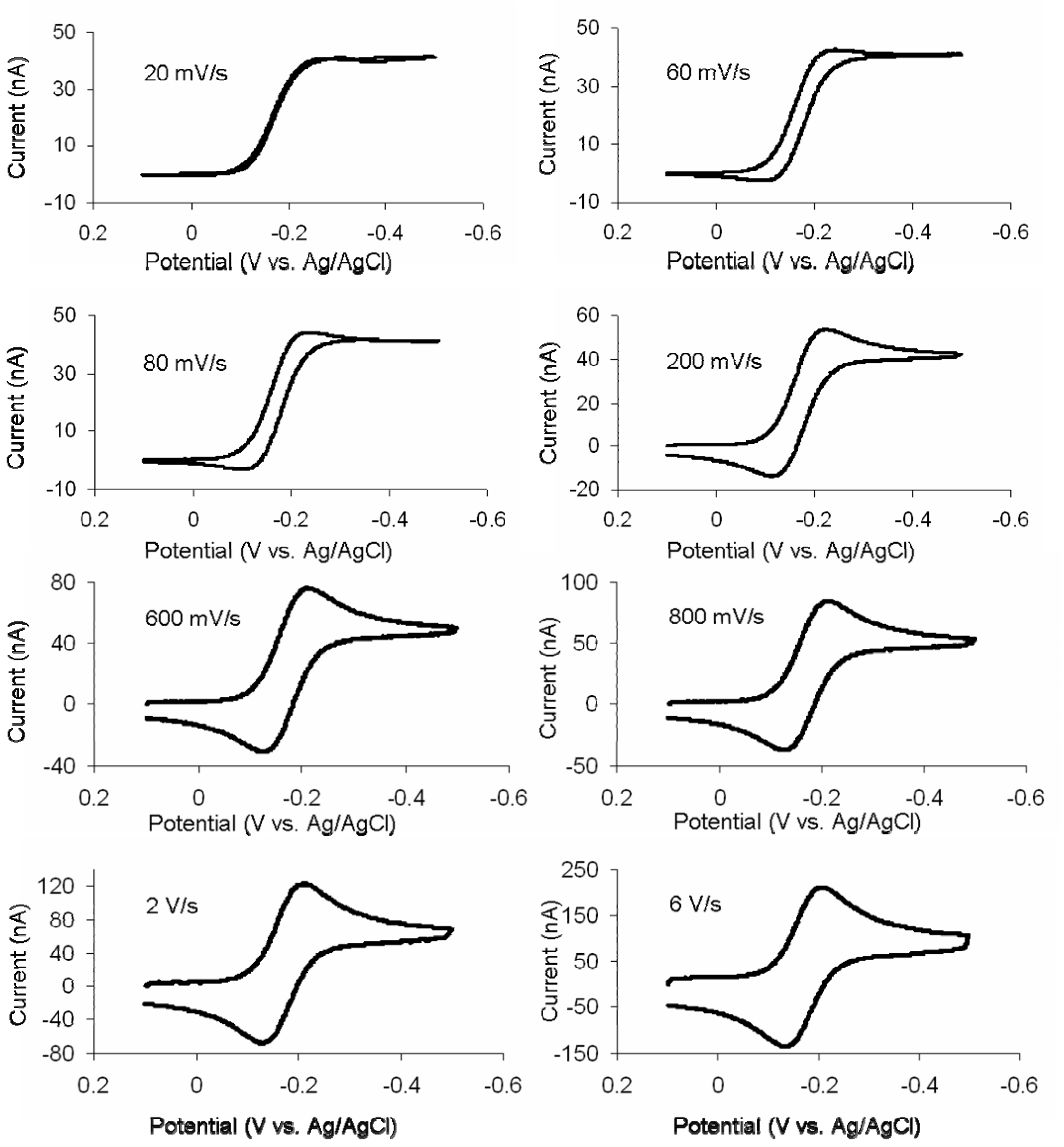

Figure 4.8. Cyclic voltammograms of 40 μm width carbon band electrode in 5 mM $Ru(NH_3)_6Cl_3$ and 1 M KCl at different scan rates.

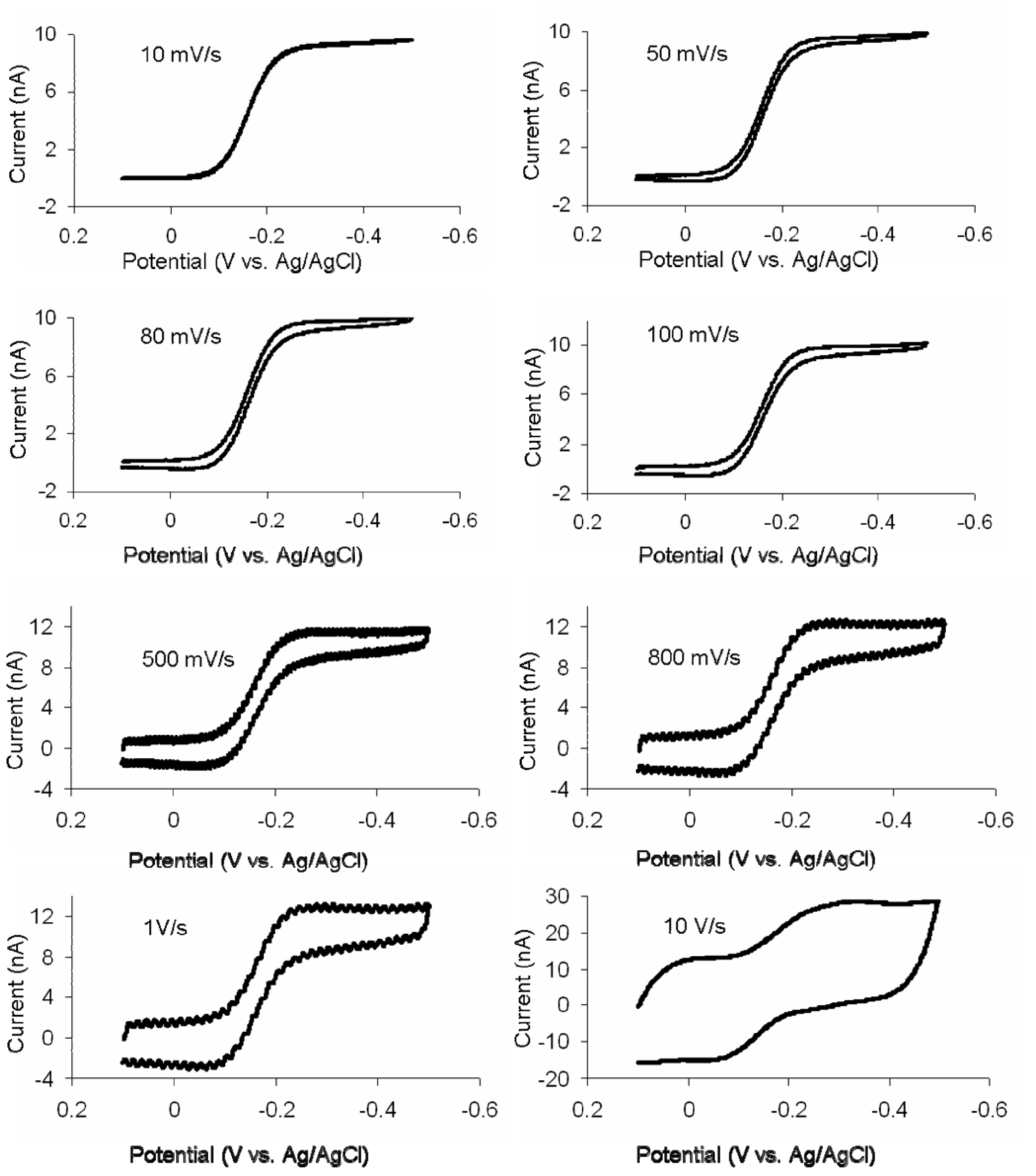

Figure 4.9. Cyclic voltammograms of 200 nm width carbon band electrode in 5 mM $Ru(NH_3)_6Cl_3$ and 1 M KCl at different scan rates.

The voltammogram shape is not only affected by the electrode width, but also by the scan rate. The voltammetric scan rate defines the time scale of the experiment and governs X_d. Figure 4.8 and Figure 4.9 show cyclic voltammograms for the carbon band electrode of 40 μm and 200 nm width, respectively. Both electrodes show sigmoid shaped voltammograms at low scan rate. When the scan rate increased, the voltammograms of the 200 nm electrode maintained the sigmoidal shape while those of the 40 μm electrode changed from sigmoidal shape to peak shape gradually. This can also be explained by MT theory. At low scan rate, the diffusion layer thickness is relatively high, while at high scan rate, the diffusion layer is thin. Thus, with the increasing of scan rate, the ratio of X_d/W is decreasing and leads to the mass transport mode changing from hemispherical to planar.

The variation of the MT controlled current for the 200 nm and 40 μm electrodes was analyzed by plotting log ($i_{p/l}$) versus log (ν), where $i_{p/l}$ is the limiting current or peak current. As noted previously, the scan rate (ν) determines the time scale of the voltammogram (t). Equations 4.1 and 4.2 describe the dependence of i on t. Figure 4.10 plots the data for the two different width electrodes and also the expected trend from equations 4.1 and 4.2. For the 200 nm electrode, the experimental currents coincide with the predictions based on nonlinear diffusion quite well. The plot shows quasi-steady-state current with a slight slope of 0.15. For the 40 μm band electrode, at low scan rate (ν < 100 mV/s), the current responses are much larger than the predictions calculated from

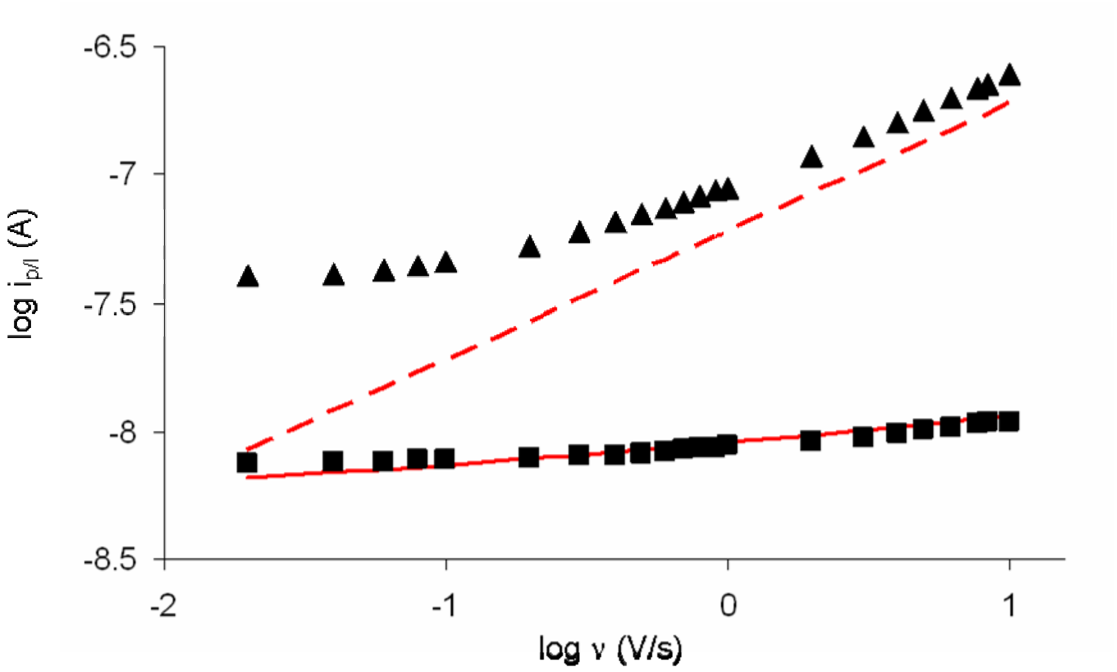

Figure 4.10. Logarithm of the $i_{p/l}$ vs. logarithm of the scan rate ν. (■) represents the experiment limiting current from 200 nm electrode; (▲) represents the experiment limiting or peak current from 40 µm electrode. The solid red line is based on calculation from equation 4.1; the dashed red line is based on the calculation from equation 4.2.

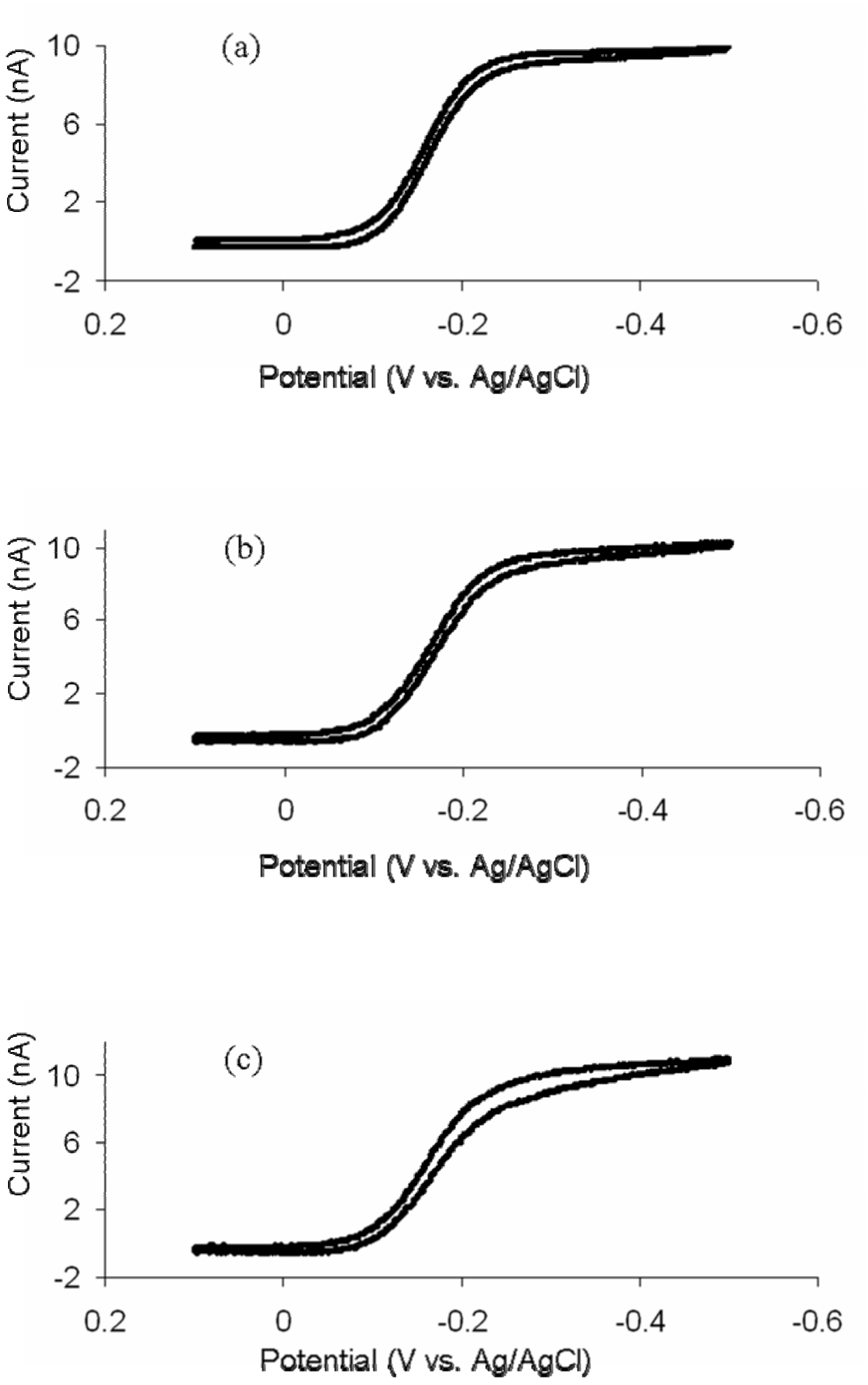

Figure 4.11. Cyclic voltammograms of carbon nanoband electrode with different width (a) 260 nm, (b) 340 nm and (c) 480 nm. Electrolyte: 5 mM $Ru(NH_3)_6Cl_3$ + 1 M KCl, scan rate: 100 mV/s.

equation 4.2. This is because mass transport is mainly controlled by nonlinear diffusions at low scan rates. At higher scan rates, the current is closer to the predictions based on the linear diffusion model. The voltammograms change from sigmoidal shape to peak shape as shown in Figure 4.8. At the scan rate range applied in the experiment, the current response for 40 μm is always larger than the predictions from equation 4.2. This is because the diffusion layer thickness is still comparable to the electrode width even at 10 V/s and hemicylindrical diffusion thus contributes partially to the current.

Table 4.2. Calculated currents based on equation 4.1 and measured limiting currents of carbon band nanoelectrodes with different width.

Electrode width (nm)	260 nm	340 nm	480 nm
Calculated current (nA)	8.6	9.0	9.6
Measured current (nA)	9.3 ± 2.3[a]	9.8 ± 2.1[a]	10.2 ± 1.8[a]

[a] Values reported are mean ± standard deviation, based on a minimum of 6 independent measurements.

For the band nanoelectrode, the limiting current is mainly governed by the length of the electrode, which is much larger than the width. Figure 4.11 shows the cyclic voltammograms of three carbon band electrodes with different widths. Their corresponding theoretical limiting currents were calculated from equation 4.1 and are listed in Table 4.2. Both theoretical and experimental results indicate that the limiting currents of nanoband electrodes are fairly insensitive to the electrode width.

One advantage of nanoband electrodes fabricated by EBL and pyrolysis is their precisely controllable dimensions, which can be reproducibly constructed. As no polishing or etching steps are required, the electrode surface areas can be predefined and obtained directly.

4.3.3 Electrode array

Micro- or nanoelectrode arrays have attracted much interest in the field of electrochemistry due to their unique electrochemical properties, such as reduced iR drop and steady-state diffusion currents.[3] Compared with a single nanoelectrode, they possess an advantage of large absolute currents that can be more easily measured.[44] All these advantageous properties make micro- or nanoelectrode arrays widely applied in electrochemical analysis[45] and sensor technology.[46]

Nanoband electrode arrays were fabricated with different spacings between individual bands. Previous investigations have shown that electrode arrays exhibit scan-rate dependence with four distinct voltammetric diffusion regimes.[3] The regimes depend on characteristic dimensions of the array relative to the thickness of the diffusion layer that develops at each element of the array. The relationships can be easily understood upon considering the four limiting situations identified in Figure 4.12. In Figure 4.12(a), the time scale of the experiment is sufficiently small that the diffusion layer at each band element of the array is small with respect to the width of the band electrode ($X_D << W$). Linear diffusion is then observed at each band electrode and the current from the array is proportional to the overall electroactive surface area. The voltammogram is expected to be peak-shaped. For a large experimental time scale, as shown by Figure 4.12 (b), the diffusion layer is larger than the width of the band but still smaller than the interband distance ($W < X_D < D$). Nonlinear diffusion occurs at each band electrode of the array and the current response should be quasi-steady-state with a sigmoid shape. When the time scale of the experiment further increases, the diffusion layer is larger than D but less than L ($D < X_D < L$). The diffusion layers developing at each element band will overlap and result in the creation of an apparent linear diffusion layer that extends over the entire array [Figure 4.12 (c)]. The voltammograms become peak shape again. Eventually, the diffusion layer further increase and exceeds L [Figure 4.12 (d)] and quasi-steady-state diffusion is again observed. The voltammograms become sigmoid in shape.

Using EBL and pyrolysis, we have fabricated two nanoband electrode arrays composed of eight individual nanobands with the following parameters: $R_1 = 200$ nm, $D_1 = 10$ μm, $L_1 = 40$ μm [Figure 4.13(a)] and $R_2 = 200$ nm, $D_2 = 100$ μm, $L_2 = 40$ μm [Figure 4.13(b)]. Except for the situation described by Figure 4.12 (a), which requires a scan rate higher than 500 V/s, the other three mass transport situations have been tested experimentally at our electrode arrays. Figure 4.14 shows the voltammograms taken in 5 mM $Ru(NH_3)_6^{3+}$ (1 M KCl) at different scan rates. At high scan rate of 8000 mV/s, the diffusion layer thickness (X_D) is 2.5 μm, which is calculated from equation 4.3 and 4.4. This value is much larger than the band width but smaller than the interband spacing for both electrode arrays. The mass transport at both electrode arrays is controlled by nonlinear

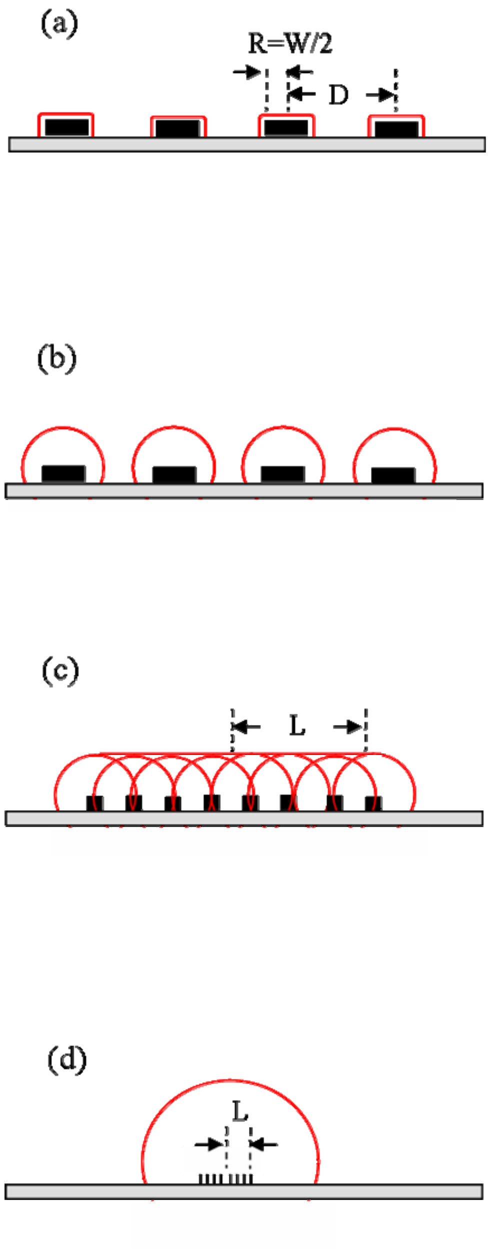

Figure 4.12. Scheme of diffusion layers at band array electrodes. *W*: width of each band electrode; *R*: equal to the half of *W*; *D*: interband spacing distance; *L*, half of the width of the array; (a) linear; (b) nonlinear diffusion at each electrode element; (c) linear; (d) nonlinear diffusion layer for the entire array by overlap of individual diffusion layers due to each element.

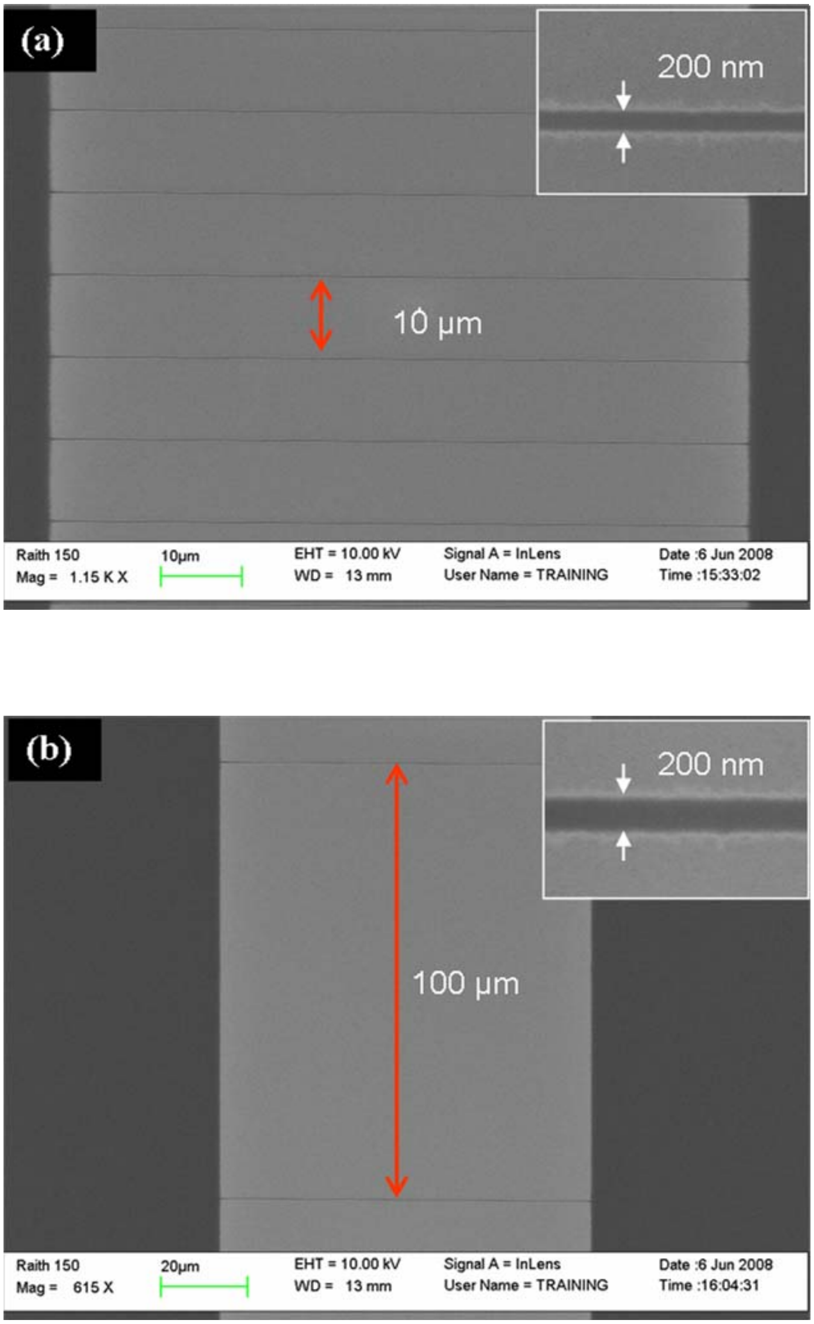

Figure 4.13. SEM images of carbon band array nanoelectrodes. (a) Eight 200 nm wide bands with interband distance of 10 µm, (b) eight 200 nm wide bands with interband distance of 100 µm.

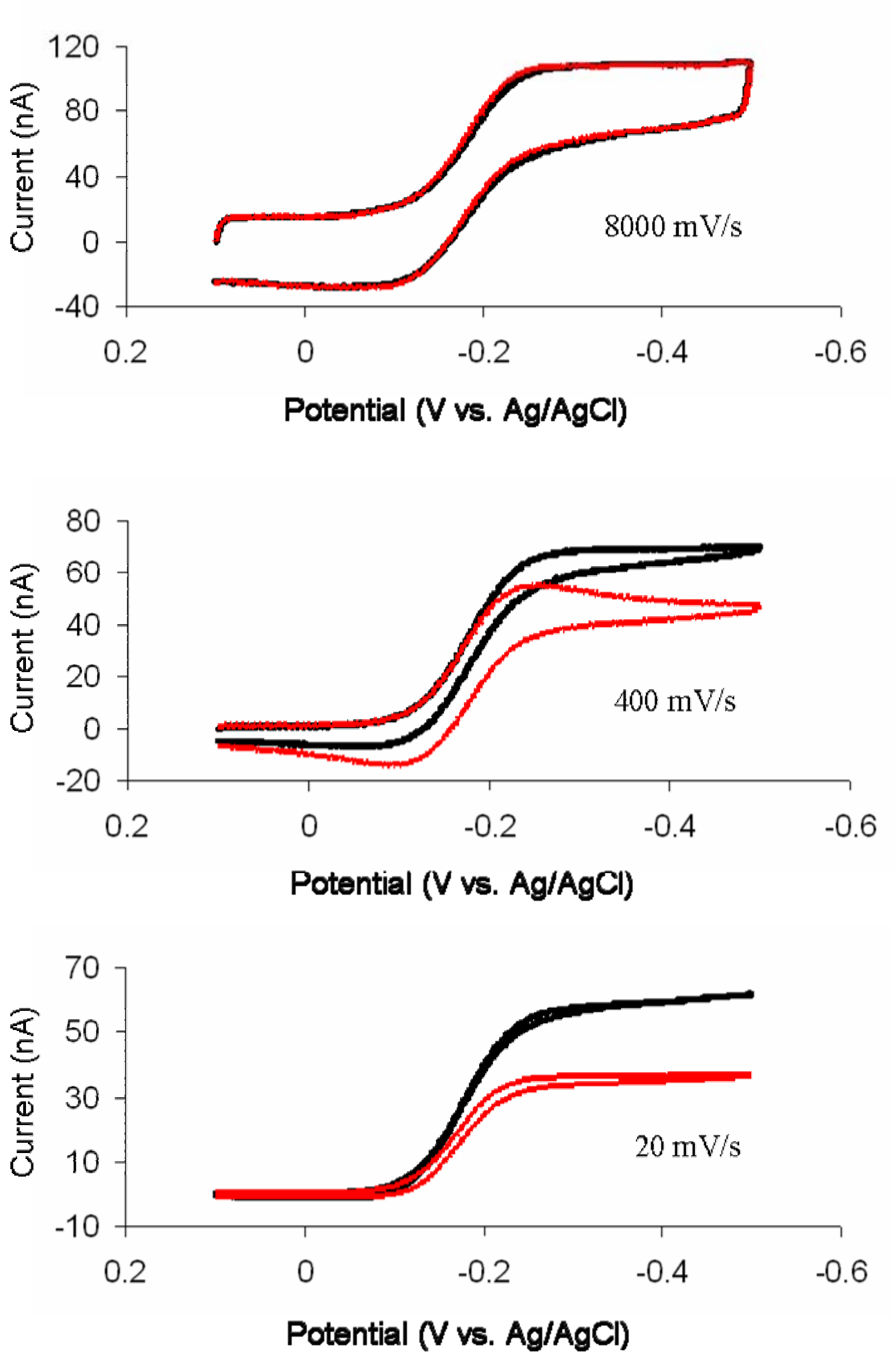

Figure 4.14. CV voltammograms at different scan rates on different electrode arrays. The red line is the voltammograms from array with 10 µm gap; the black line is the voltammograms from array with 100 µm gap.

diffusion. As shown by Figure 4.14(a), voltammograms for both electrode arrays exhibit a sigmoidal shape and the limiting currents are quasi-steady state. At intermediate scan rate of 400 mV/s, the diffusion layer thickness is increased (X_D = 12 μm). For the electrode with 10 μm spacing, the diffusion layers around individual bands overlap because the diffusion layer thickness is larger than the interband spacing. The voltammogram appears peak-shaped [Figure 4.14 (b)]. This voltammetric behavior, which is similar to that on planar macroelectrodes, is primarily a result of linear diffusion that arises from overlapping nonlinear diffusion layers. For an electrode array with a 100 μm gap, the diffusion layers do not overlap for the condition of ν = 400 mV/s. Therefore, the diffusion is still quasi-steady-state with a sigmoid shaped voltammogram. The much larger limiting current observed is because nonlinear diffusion is more efficient than linear diffusion. When the scan rate is further reduced to 20 mV/s, the diffusion layer thickness (X_D = 51 μm) is roughly the same as the length the electrode. Voltammograms for both electrode arrays thus become sigmoid shaped with different current [Figure 4.14 (c)]. All our results demonstrate that the voltammetric behavior of nanoband electrode arrays is dependent on band width, interband spacing and scan rate. When nanoband electrode arrays are employed as electrochemical detectors, optimum performance can be obtained if individual nanobands behave as isolated bands. Nanoband electrode arrays with optimized band width and interband spacing can be constructed by EBL and pyrolysis.

4.3.2 Electrochemical modification of carbon nanoband electrode

The electrochemical reduction of phenyl diazonium salts on carbon band nanoelectrodes was investigated. Electrochemically assisted covalent modification of a carbon surface with diazonium salts has been widely researched. Pinson et al. were the first to report the electrochemical process.[47] It was believed that in situ radicals were generated which coupled to the carbon surface.[48] Monolayer or multilayer films can be obtained by electrochemical reduction of diazonium salts.[48,49] McCreery and coworkers also reported a series of papers about the covalent modification of carbon film electrodes and their application in molecular electronics. Recently, a significant amount of effort has been put forth to the modification of nanoelectrodes via the electrochemical reduction of diazonium salts, such as carbon nanotubes[50] and nanofibers[51], and their application for the immobilization of bio-molecules onto the surface of the nanometer sized carbon structures.[52]

Figure 4.15 shows the cyclic voltammogram of 10 mM nitroazobenzene (NAB) diazonium salt (0.5 M H_2SO_4) at a nanoelectrode with dimensions 200 nm wide and 40 μm long. During the first sweep (black line), an obvious reduction current was observed. This is attributed to the reduction of NAB diazonium cations to form NAB radicals. The reduction currents were greatly reduced on the second and third scans, which is attributed to the blocking by the NAB film on the electrode surface formed during the first sweep.

Figure 4.16 shows the AFM images of the carbon nanoband electrode before and after electrochemical reduction of NAB diazonium salt. The carbon

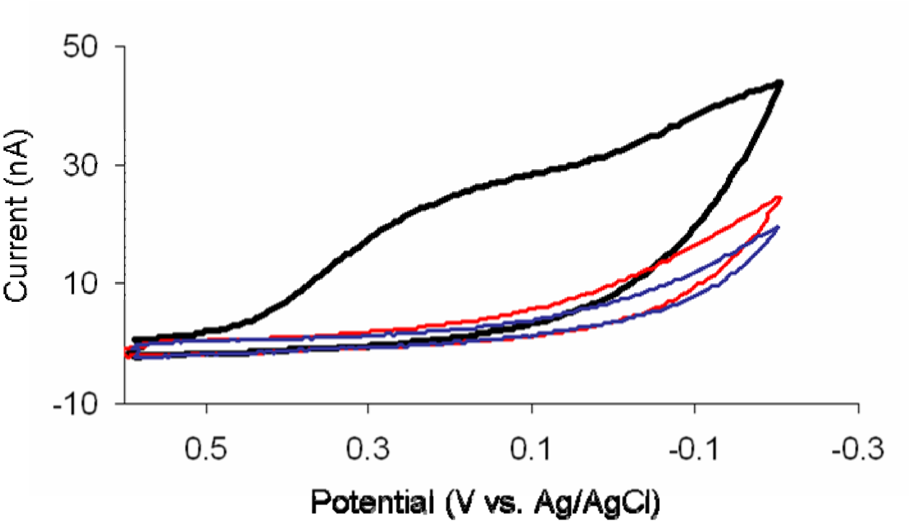

Figure 4.15. Cyclic voltammogram of the electrochemical reduction of 10 mM nitroazobenzene (NAB) diazonium tetrafluoroborate (in 0.5 M H_2SO_4). Scan rate = 200 mV/s. Black line, red line and blue line are first scan, second scan and third scan respectively.

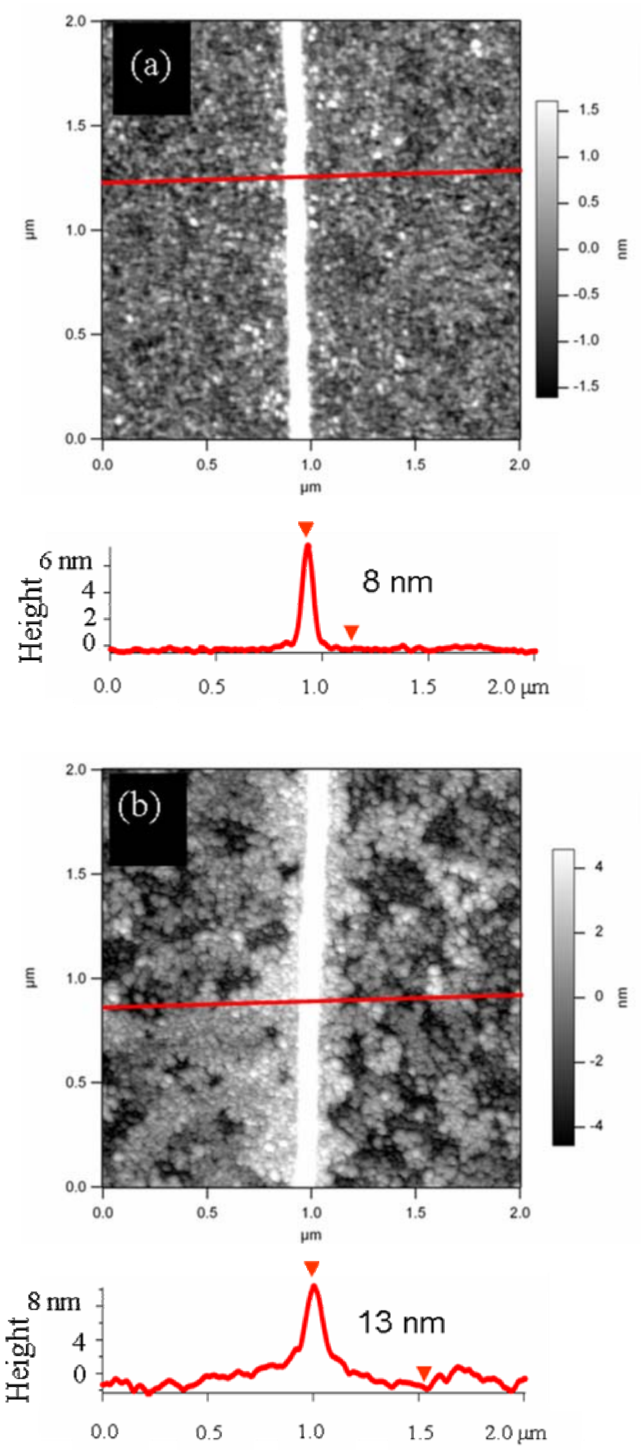

Figure 4.16. AFM images of carbon nanoband electrode (a) before and (b) after electrochemical reduction of 4-nitroazobenzene (NAB) diazonium salt. Bottom: AFM height profile of the carbon nanoband electrode (along the red line highlighted on the images).

nanoband electrode shows an increase in height as a result of the deposited layer. The average AFM height before and after modification was found to be 8 nm and 13 nm, respectively. The AFM image of the sample shows a much rougher surface on the Si background than before the modification. This implies NAB molecules adsorbed on both the carbon surface and the native silicon oxide surface. The increased roughness on the silicon surface can be attributed to three possible reasons: (1) Radicals are forming at the carbon electrode and then diffusing to the silicon oxide surface; (2) radicals are coupling in solution and then physically adsorbed on the silicon oxide surface; (3) pinholes in the native oxide layer is acting as reactive sites, which generate radicals bonded to the surface.

4.4 Conclusion

A reliable and reproducible procedure for fabricating single and array carbon nanoband electrodes has been demonstrated. Both the band width and interband spacing can be precisely controlled. Nanoband electrodes with various band widths have been constructed. Their voltammetric behaviors show good agreement with the classical theoretical predictions. Nanoband electrode arrays with different interband spacing have also been fabricated. The voltammetric behaviors observed are dependent on both the interband spacing and scan rate. The isolation or overlap of diffusion layers of individual nanoband at variable scan rates was illustrated.

Nanoband electrode surface can be modified with aryl films via electrochemical reduction of diazonium salts, which can be beneficial for immobilization of biomolecules. We are expecting the carbon nanoelectrodes and arrays will be valuable for applications as electrochemical detectors and biosensors

4.5 References:

1. Wightman, R. M., Microvoltammetric electrodes. *Analytical Chemistry* **1981,** 53, 1125A-1134A.
2. Pons, S.; Fleischmann, M., The behavior of microelectrodes. *Analytical Chemistry* **1987,** 59, A1391-A1399.
3. Amatore, C., Electrochemistry at ultramicroelectrodes. In *Physical Electrochemistry: Principles, Methods and Applications* Rubinstein, I., Ed. CRC Press: **1995**, pp 131-204.
4. Niwa, O., Electroanalytical chemistry with carbon film electrodes and micro and nano-structured carbon film-based electrodes. *Bulletin of The Chemical Society of Japan* **2005,** 78, 555-571.
5. Galus, Z.; Schenk, J. O.; Adams, R. N., Electrochemical-behavior of very small electrodes in solution - double potential step, cyclic voltammetry and chronopotentiometry with current reversal. *Journal of Electroanalytical Chemistry* **1982,** 135, 1-11.
6. Van Gerwen, P.; Laureyn, W.; Laureys, W.; Huyberechts, G.; De Beeck, M. O.; Baert, K.; Suls, J.; Sansen, W.; Jacobs, P.; Hermans, L.; Mertens, R., Nanoscaled interdigitated electrode arrays for biochemical sensors. *Sensors and Actuators B-Chemical* **1998,** 49, 73-80.
7. Wu, W. Z.; Huang, W. H.; Wang, W.; Wang, Z. L.; Cheng, J. K.; Xu, T.; Zhang, R. Y.; Chen, Y.; Liut, J., Monitoring dopamine release from single living vesicles with nanoelectrodes. *Journal of the American Chemical Society* **2005,** 127, 8914-8915.

8. Fei, J. J.; Wu, K. B.; Wang, F.; Hu, S. S., Glucose nanosensors based on redox polymer/glucose oxidase modified carbon fiber nanoelectrodes. *Talanta* **2005,** 65, 918-924.

9. Liu, L.; Jia, N. Q.; Zhou, Q.; Yan, M. M.; Jiang, Z. Y., Electrochemically fabricated nanoelectrode ensembles for glucose biosensors. *Materials Science & Engineering C-Biomimetic and Supramolecular Systems* **2007,** 27, 57-60.

10. Zhu, M. Z.; Jiang, Z. D.; Jing, W. X., Fabrication of polypyrrole-glucose oxidase biosensor based on multilayered interdigitated ultramicroelectrode array with containing trenches. *Sensors and Actuators B-Chemical* **2005,** 110, 382-389.

11. Arrigan, D. W. M., Nanoelectrodes, nanoelectrode arrays and their applications. *Analyst* **2004,** 129, 1157-1165.

12. Zoski, C. G., Ultramicroelectrodes: Design, fabrication, and characterization. *Electroanalysis* **2002,** 14, 1041-1051.

13. McCreery, R. L., Advanced carbon electrode materials for molecular electrochemistry. *Chemical Review* **2008,** 108, 2646-2687.

14. McCreery, R.; Dieringer, J.; Solak, A. O.; Snyder, B.; Nowak, A. M.; McGovern, W. R.; DuVall, S., Molecular rectification and conductance switching in carbon-based molecular junctions by structural rearrangement accompanying electron injection. *Journal of the American Chemical Society* **2003,** 125, 10748-10758.

15. McCreery, R. L.; Viswanathan, U.; Kalakodimi, R. P.; Nowak, A. M., Carbon/molecule/metal molecular electronic junctions: the importance of "contacts". *Faraday Discussions* **2006,** 131, 33-43.

16. Corgier, B. P.; Marquette, C. A.; Blum, L. J., Diazonium-protein adducts for graphite electrode microarrays modification: Direct and addressed electrochemical immobilization. *Journal of the American Chemical Society* **2005,** 127, 18328-18332.

17. Wang, C. Y.; Chen, Y. J.; Wang, F. X.; Hu, X. Y., Fabrication of nanometer-sized carbon electrodes by the controllable electrochemical deposition. *Electrochimica Acta* **2005,** 50, 5588-5593.

18. Chen, S. L.; Kucernak, A., The voltammetric response of nanometer-sized carbon electrodes. *Journal of Physical Chemistry B* **2002,** 106, 9396-9404.

19. Strein, T. G.; Ewing, A. G., Characterization of submicron-sized carbon electrodes insulated with a phenol allylphenol copolymer. *Analytical Chemistry* **1992,** 64, 1368-1373.

20. Zhang, X. J.; Zhang, W. M.; Zhou, X. Y.; Ogorevc, B., Fabrication, characterization, and potential application of carbon fiber cone nanometer-size electrodes. *Analytical Chemistry* **1996,** 68, 3338-3343.

21. Chen, S. L.; Kucernak, A., Fabrication of carbon microelectrodes with an effective radius of 1 nm. *Electrochemistry Communications* **2002,** 4, 80-85.

22. Kawagoe, K. T.; Jankowski, J. A.; Wightman, R. M., Etched carbon-fiber electrodes as amperometric detectors of catecholamine secretion from isolated biological cells. *Analytical Chemistry* **1991,** 63, 1589-1594.

23. Conyers, J. L.; White, H. S., Electrochemical characterization of electrodes with submicrometer dimensions. *Analytical Chemistry* **2000,** 72, 4441-4446.

24. Huang, W. H.; Pang, D. W.; Tong, H.; Wang, Z. L.; Cheng, J. K., A method for the fabrication of low-noise carbon fiber nanoelectrodes. *Analytical Chemistry* **2001,** 73, 1048-1052.

25. Li, X. M.; Geng, Q. H.; Wang, Y. Y.; Si, Z. K.; Jiang, W.; Zhang, X. L.; Jin, W. R., Micropatterning of active enzyme with a high-resolution by scanning electrochemical microscopy coupled with a nanometer-sized carbon fiber disk tip. *Electrochimica Acta* **2007,** 53, 2016-2024.

26. Chen, S. L.; Kucernak, A., Electrodeposition of platinum on nanometer-sized carbon electrodes. *Journal of Physical Chemistry B* **2003,** 107, 8392-8402.

27. Koehne, J.; Li, J.; Cassell, A. M.; Chen, H.; Ye, Q.; Ng, H. T.; Han, J.; Meyyappan, M., The fabrication and electrochemical characterization of carbon nanotube nanoelectrode arrays. *Journal of Materials Chemistry* **2004,** 14, 676-684.

28. Tu, Y.; Lin, Y. H.; Ren, Z. F., Nanoelectrode arrays based on low site density aligned carbon nanotubes. *Nano Letters* **2003,** 3, 107-109.

29. Tu, Y.; Lin, Y. H.; Yantasee, W.; Ren, Z. F., Carbon nanotubes based nanoelectrode arrays: Fabrication, evaluation, and application in voltammetric analysis. *Electroanalysis* **2005,** 17, 79-84.

30. Li, J.; Ng, H. T.; Cassell, A.; Fan, W.; Chen, H.; Ye, Q.; Koehne, J.; Han, J.; Meyyappan, M., Carbon nanotube nanoelectrode array for ultrasensitive DNA detection. *Nano Letters* **2003,** 3, 597-602.

31. Koehne, J.; Chen, H.; Li, J.; Cassell, A. M.; Ye, Q.; Ng, H. T.; Han, J.; Meyyappan, M., Ultrasensitive label-free DNA analysis using an electronic chip based on carbon nanotube nanoelectrode arrays. *Nanotechnology* **2003,** 14, 1239-1245.

32. Seibold, J. D.; Scott, E. R.; White, H. S., Diffusional transport to nanoscopic band electrodes. *Journal of Electroanalytical Chemistry* **1989,** 264, 281-289.

33. Morris, R. B.; Franta, D. J.; White, H. S., Electrochemistry at Pt band electrodes of width approaching molecular dimensions - breakdown of transport-equations at very small electrodes. *Journal of Physical Chemistry* **1987,** 91, 3559-3564.

34. Wehmeyer, K. R.; Deakin, M. R.; Wightman, R. M., Electroanalytical properties of band electrodes of submicrometer width. *Analytical Chemistry* **1985,** 57, 1913-1916.

35. Caston, S. L.; McCarley, R. L., Characteristics of nanoscopic Au band electrodes. *Journal of Electroanalytical Chemistry* **2002,** 529, 124-134.

36. Nagale, M. P.; Fritsch, I., Individually addressable, submicrometer band electrode arrays. 1. Fabrication from multilayered materials. *Analytical Chemistry* **1998,** 70, 2902-2907.

37. Nagale, M. P.; Fritsch, I., Individually addressable, submicrometer band electrode arrays. 2. Electrochemical characterization. *Analytical Chemistry* **1998,** 70, 2908-2913.

38. Wang, J.; Brennsteiner, A.; Sylwester, A. P.; Renschler, C. L., Preparation and characterization of band nanoelectrodes made of carbonized polyacrylonitrile films. *Electroanalysis* **1991,** 3, 505-509.

39. Ranganathan, S.; Steidel, I.; Anariba, F.; McCreery, R. L., Covalently bonded organic monolayers on a carbon substrate: A new paradigm for molecular electronics. *Nano Letters* **2001,** 1, 491-494.

40. Anderson, E. H.; Olynick, D. L.; Chao, W. L.; Harteneck, B.; Veklerov, E., Influence of sub-100 nm scattering on high-energy electron beam lithography. *Journal of Vacuum Science & Technology B* **2001,** 19, 2504-2507.

41. Kovach, P. M.; Caudill, W. L.; Peters, D. G.; Wightman, R. M., Faradaic electrochemistry at microcylinder, band, and tubular band electrodes. *Journal of Electroanalytical Chemistry* **1985,** 185, 285-295.

42. Bard, A. J.; Faulkner, L. R., *Electrochemical Methods: Fundamentals and Applications*. Wiley: New York, **1980**, pp435-436.

43. Blackstock, J. J.; Rostami, A. A.; Nowak, A. M.; McCreery, R. L.; Freeman, M. R.; McDermott, M. T., Ultraflat carbon film electrodes

prepared by electron beam evaporation. *Analytical Chemistry* **2004,** 76, 2544-2552.

44. Szunerits, S.; Walt, D. R., Fabrication of an optoelectrochemical microring array. *Analytical Chemistry* **2002,** 74, 1718-1723.

45. Feeney, R.; Kounaves, S. P., On-site analysis of arsenic in groundwater using a microfabricated gold ultramicroelectrode array. *Analytical Chemistry* **2000,** 72, 2222-2228.

46. Cui, H. F.; Ye, J. S.; Chen, Y.; Chong, S. C.; Sheu, F. S., Microelectrode array biochip: Tool for in vitro drug screening based on the detection of a drug effect on dopamine release from PC12 cells. *Analytical Chemistry* **2006,** 78, 6347-6355.

47. Delamar, M.; Hitmi, R.; Pinson, J.; Saveant, J. M., Covalent modification of carbon surfaces by grafting of functionalized aryl radicals produced from electrochemical reduction of diazonium salts. *Journal of the American Chemical Society* **1992,** 114, 5883-5884.

48. Kariuki, J. K.; McDermott, M. T., Formation of multilayers on glassy carbon electrodes via the reduction of diazonium salts. *Langmuir* **2001,** 17, 5947-5951.

49. Allongue, P.; Delamar, M.; Desbat, B.; Fagebaume, O.; Hitmi, R.; Pinson, J.; Saveant, J. M., Covalent modification of carbon surfaces by aryl radicals generated from the electrochemical reduction of diazonium salts. *Journal of the American Chemical Society* **1997,** 119, 201-207.

50. Bahr, J. L.; Tour, J. M., Highly functionalized carbon nanotubes using in situ generated diazonium compounds. *Chemistry of Materials* **2001,** 13, 3823-3824.

51. Baker, S. E.; Tse, K. Y.; Hindin, E.; Nichols, B. M.; Clare, T. L.; Hamers, R. J., Covalent functionalization for biomolecular recognition on vertically aligned carbon nanofibers. *Chemistry of Materials* **2005,** 17, 4971-4978.

52. Lee, C. S.; Baker, S. E.; Marcus, M. S.; Yang, W. S.; Eriksson, M. A.; Hamers, R. J., Electrically addressable biomolecular functionalization of carbon nanotube and carbon nanofiber electrodes. *Nano Letters* **2004,** 4, 1713-1716.

Chapter 5. Electrodeposition of Gold Nanoparticles on the Pyrolyzed SU-8 Carbon Film Electrodes

In this chapter, the electrochemical deposition of gold nanoparticles onto pyrolyzed SU-8 carbon film (P8) electrodes was investigated. Cyclic voltammetry (CV), chronoamperometry (CA), and SEM were used to study the nucleation and crystal growth on the P8 surfaces in aqueous solution. Classical electrochemical techniques, such as cyclic voltammetry and chronoamperometry, were used to study the mechanism and kinetics of the deposition process in a quantitative way. SEM was used to directly visualize the gold nanoparticles deposited on the carbon surface.

5.1 Introduction

Study of metallic nanoparticles has attracted a lot of interest due to their unusual optical, thermal, chemical, and physical properties.[1-3] Gold nanoparticles have certainly been among the most popular due to their applications for electrocatalysis,[4-7] microelectronics,[8] sensing,[9] and bio-molecular immobilization.[10-14] Au nanoparticles can be synthesized using a wide variety of techniques and methods, such as vapour deposition,[15,16] arc discharge,[17] sol-gel,[18] chemical reduction of $[AuCl_4]^-$,[19,20] and electrodeposition.[21-23] Electrodeposition is a convenient and fast method for the preparation of metallic nanocrystallites on large areas of conductive substrates. An advantage of electrodeposition over other fabrication methods, i.e. precipitation, is the ability to control the degree of supersaturation by controlling the potential applied to the working electrode.

The electrodeposition of metal nanoparticles on carbon electrode surfaces has been widely studied theoretically and experimentally. Penner and co-workers published a series of papers on the electrodeposition of metal nanoparticles on highly oriented pyrolytic graphite (HOPG) surfaces.[16,24-27] By controlling the deposition potential, the nucleation and growth of metal particles occur via an instantaneous nucleation and a diffusion-limited growth mechanism, which results in narrow particle size distributions.[25] The electrodeposition of gold nanoparticles has also been carried out on glassy carbon (GC) electrode surfaces.[4,28-30] Schmidt et al. suggested that gold electrocrystallization on glassy carbon follow three dimensional nucleation and diffusion-controlled growth.[30] Examination of gold nucleation on glassy carbon from chloride solutions indicated that progressive nucleation occurs in the early stages, whereas at longer time instantaneous nucleation takes place.[30] Trejo et al. have studied the temperature effect on Au electrodeposition on the GC electrode.[31,32] They found that progressive nucleation occurred at 30°C and 40°C, while instantaneous nucleation happened at 50°C. Finot et al. reported that crystal size and density of gold nanoparticles electrodeposited on glassy carbon could be controlled by variation of deposition potentials and deposition time.[10] Liu et al. demonstrated that Au electrodeposition on amorphous carbon film follows the progressive nucleation.[33] The size and coverage of three-dimensional gold nanoparticles can be adjusted by controlling the deposition time.

Carbon film electrodes fabricated from photoresists have recently been introduced.[34-39] Pyrolyzed photoresist carbon films exhibit extremely flat surfaces and relatively active electrochemical properties.[34,35] Their applications for molecular electronics[36-38] and microelectromechanical systems[39] were also reported. In this chapter, Au electrodeposition on pyrolyzed SU8 carbon films was investigated. Both cyclic voltammetry and chronoamperometry have been applied. The cyclic voltammogram of Au reduction is significantly different on PPF and GC electrodes. Current transients obtained indicate a progressive nucleation at the early stage of the deposition process, which was also observed by SEM images. The particle size and density at the electrode surface was measured by SEM. The relationship between particle morphology and both deposition potential and concentration was studied and is discussed.

5.2 Experimental Section

5.2.1 Chemicals

Potassium tetrachloroaurate (III) (Aldrich) and sulphuric acid (Fisher) were used as received. All aqueous solutions were prepared using distilled/deionized water (18 MΩ/cm).

5.2.2 Electrode preparation

GC electrodes (Tokai GC-20, Electrosynthesis Company, NY) were polished on Micropolish polishing cloth (Buehler) with three different grade alumina slurries: 1.0 micron, 0.3 micron, and 0.05 micron, respectively. The electrodes were rinsed, sonicated for ten minutes after every polishing. Pyrolyzed photoresist film (PPF) electrodes and pyrolyzed SU-8 carbon film (P8) electrodes were prepared as previously described in Chapter 2. The electrodes were used without pre-treatment steps.

5.2.3 Electrodeposition of Au nanoparticles

The electrochemical experiments were performed with an inverted three-electrode cell. The electrodes were connected to the EG&E Parc-263A electrochemical system (Princeton Applied Research, USA). A platinum wire was used as auxiliary electrode which was separated from the bulk solution using a glass frit. In this chapter, all potentials were referred to the Ag/AgCl (sat. KCl).

Gold particles were electrochemically deposited on the electrodes by means of potential step and cyclic voltammetry technique. The cyclic voltammetries were initially carried out between 1.0 V and 0.0 V at 100 mV/s, starting from 1.0 V and negative followed positive scan. The potential steps were from 1.1 V to the final deposition potential for a period of 1-2000 seconds. A series of concentrations of the $KAuCl_4$ deposition solution and different deposition overpotentials were investigated. The electrolyte solutions were saturated with argon gas before using.

5.2.4 Surface characterization

Scanning Electron Microscopy images were recorded on a Hitachi S4800 operation at 5-20 kV with different magnifications. XPS analysis was carried out with the Kratos Axis Ultra Spectrometer equipped with a monochromatic Al Kα source (1486.6 eV). The pressure in the chamber was $\sim 8\times10^{-10}$ Torr at the time of measurement. For XPS depth profiling the sample was sputtered with 4 keV Ar^+ ions with a beam current of 0.3 μA on the sample. The instrument was calibrated on the basis of the C 1s peak.

5.3 Results and Discussion

5.3.1 Cyclic voltammetric study

Various concentrations of $KAuCl_4$ (0.5 M H_2SO_4) were used for electrodeposition. Three different carbon electrodes, GC, PPF, and P8, were studied. Figure 5.1 (a) shows the cyclic voltammogram of 100 μM $AuCl_4^-$ at a scan rate of 100 mV/s at a GC electrode. A cathodic shoulder appears at ~0.75 V and a sharp peak at 0.45 V was observed. These results are essentially the same as those obtained by Finot et al.[10] The initial wave at 0.75 V is attributed to the reduction of adsorbed $AuCl_4^-$ and the peak at 0.45 V is due to the reduction of the solution bound $AuCl_4^-$ to Au.[10,31,32] Figure 5.1 (b) shows the voltammograms at a PPF electrode. Two cathodic peaks at about 0.45 V and 0.28 V are observed. The current of the first wave at 0.45 V is about twice that at 0.28 V. Similar voltammetric results have also been obtained at the P8 electrode. As shown in Figure 5.1 (c), two reduction waves are apparent. One peak at 0.45 V is about the

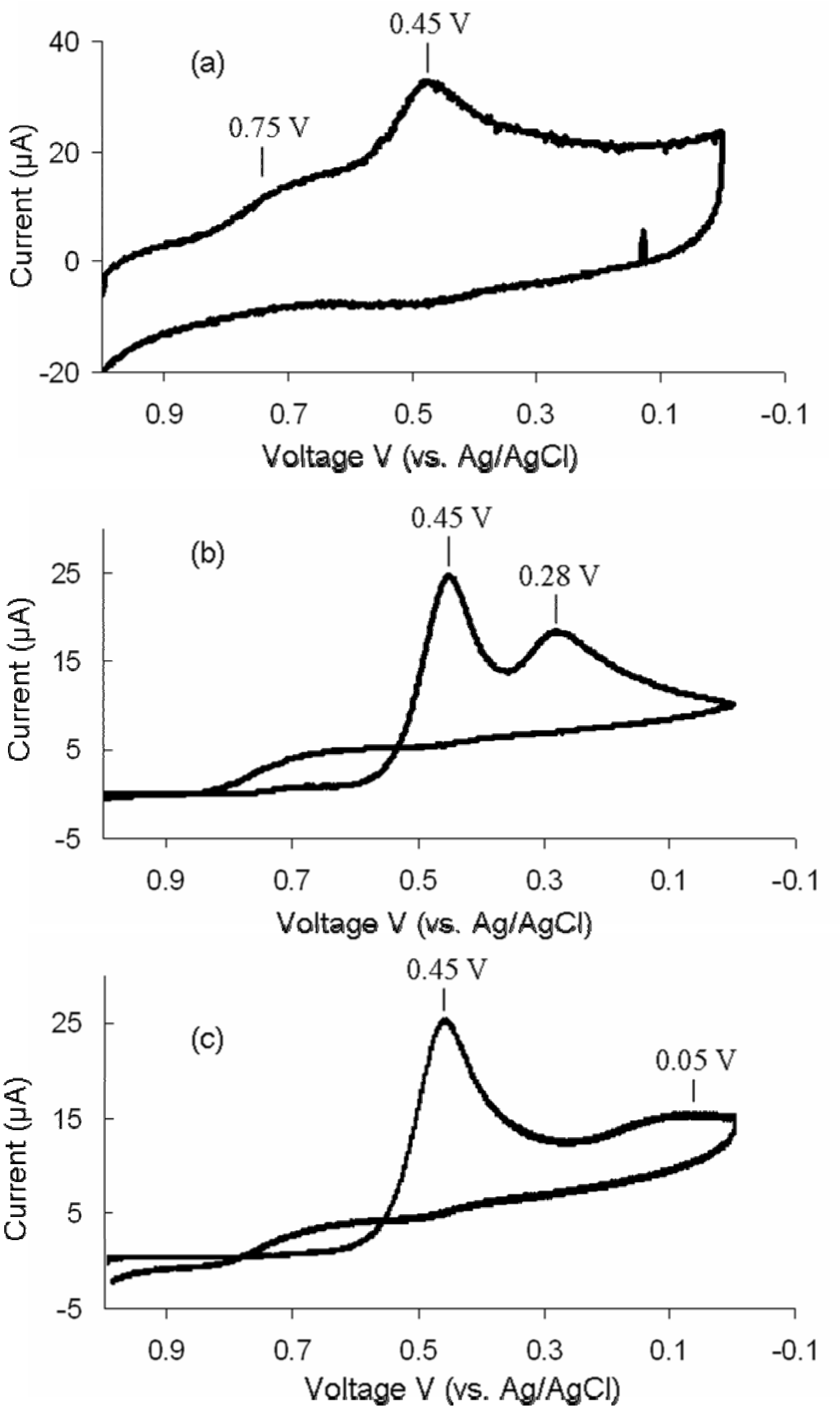

Figure 5.1. Cyclic voltammograms at 100 μM $KAuCl_4$ (0.5 H_2SO_4) at a scan rate of 100 mV/s at (a) polished GC, (b) PPF, and (c) P8.

same position as that on the PPF electrode while the second more negative wave is much broader. The initial cathodic wave observed on the GC electrodes at ~0.75 V, however, is not observed on either PPF or P8 samples, which implies relatively weak adsorption of $AuCl_4^-$ on these surfaces.

The cathodic peaks observed at ~0.5 V and ~0.2 V on the PPF electrode are attributed to the $AuCl_4^-/AuCl_2^-$ and $AuCl_2^-/Au(0)$ redox couples, which are described by the following half-cell reactions:[30]

$$AuCl_4^- + 2e^- \rightleftarrows AuCl_2^- + 2\,Cl^- \qquad E^0_{Au(III)/Au(I)} = 0.925\text{ V}$$

$$AuCl_2^- + e^- \rightleftarrows Au(0) + 2Cl^- \qquad E^0_{Au(I)/Au(0)} = 1.150\text{ V}$$

It is noteworthy that the potential of the Au(I)/Au(0) couple is more positive than the Au(III)/Au(I) couple, therefore, the electrodeposition of $AuCl_4^-$ on GC electrode commonly reported is a three electron process leading to Au metal without an intermediate of $AuCl_2^-$.[10,30] The two step reduction process obtained on both PPF and P8 electrodes can be attributed to a large overpotential for the reduction of Au(I) to Au(0) on these surfaces. We interpret this to indicate a lower nucleation rate for Au deposition on the film electrodes than on GC. The more negative potential required for the reduction of $AuCl_2^-$ to Au metal on the P8 electrode surface implies a lower nucleation rate than on PPF.

Cyclic voltammograms for metal deposition generally display a crossover of current due to more facile metal depositions on the bulk metals than on the carbon substrates.[31,40-42] Once the initial nucleation is established, greater current is observed due to the further growth of these nuclei and their increasing surface area. In our experiment, such a crossover phenomenon was not observed on the polished GC surface [Figure 5.1 (a)]. Similar phenomena were also obtained by Finot et al.[10] As shown in Figure 5.1 (b) and (c), the crossover phenomenon is observed on both PPF and P8 electrodes. The difference can be explained by the different overpotential required for nucleation on each electrode surface. After the initial Au nuclei are deposited, the overpotential of subsequent reduction of $AuCl_4^-$ is greatly reduced, and hence the corresponding currents increase. The same effect is not obvious on GC because a much lower overpotential for Au nucleation is required due to $AuCl_4^-$ adsorption.

5.3.2 Analysis of the nucleation mode

Chronoamperometric studies were performed to investigate the nucleation of Au electrodeposition. Figure 5.2 (a) shows the current response to a potential step from 1.1 to 0.0 V in 1 mM $KAuCl_4$ (0.5 M H_2SO_4). The initial sharp current spike corresponds to the charging of the double layer. Following the decay of the double layer charging current, the current increases again before a slower decrease. The increase in current is attributed to the formation and growth of the Au nuclei. The current reaches a maximum at ~36 ms in Figure 5.2 (a) due to a mass transport limit reached because of the overlap of neighbouring diffusion fields around each Au nuclei. The current maximum is typical behaviour for nucleation and crystal growth in electrodeposition. After the current maximum, a diffusion limited current delay is observed, which is linear with $t^{-1/2}$.

Two limiting cases for the mechanism of metal nanoparticle nucleation can be distinguished: instantaneous nucleation and progressive nucleation.[43] In the instantaneous nucleation mechanism, all the nuclei are rapidly created in the first stage of the process and the number of nuclei remains constant throughout the growth. In the progressive nucleation mechanism, new nuclei are continuously formed during the entire deposition process.

Scharifker and Hills[44] have developed theoretical models to describe the two nucleation mechanisms. The models for instantaneous and progressive nucleation are given by equation 5.3 and 5.4, respectively.[44,45]

For instantaneous nucleation:

$$\left(\frac{I}{I_{\max}}\right)^2 = \frac{1.9542}{\left(\frac{t}{t_{\max}}\right)}\left\{1-\exp\left[-1.2564\left(\frac{t}{t_{\max}}\right)\right]\right\}^2 \qquad (5.3)$$

For progressive nucleation:

$$\left(\frac{I}{I_{\max}}\right)^2 = \frac{1.2254}{\left(\frac{t}{t_{\max}}\right)}\left\{1-\exp\left[-2.3367\left(\frac{t}{t_{\max}}\right)^2\right]\right\}^2 \qquad (5.4)$$

where I_{max} is the current maximum, and t_{max} is the time at which the current maximum is observed. A convenient criterion to distinguish between these two

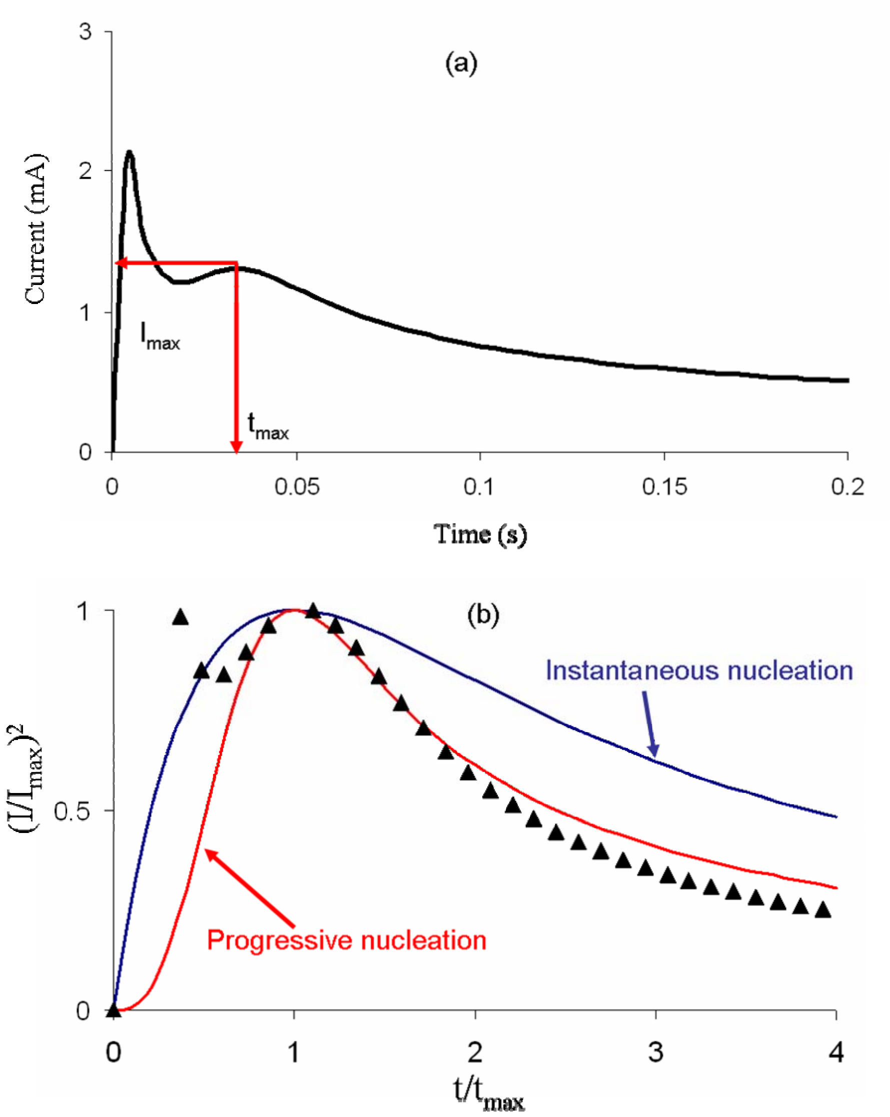

Figure 5.2. (a) I-t transients of the electrodeposition of Au nanoparticles on P8 at the potential of 0.0 V in 1 mM $KAuCl_4$ (0.5 M H_2SO_4). (b) Comparison of the experimental gold nucleation on P8s to the theoretical nucleation models.

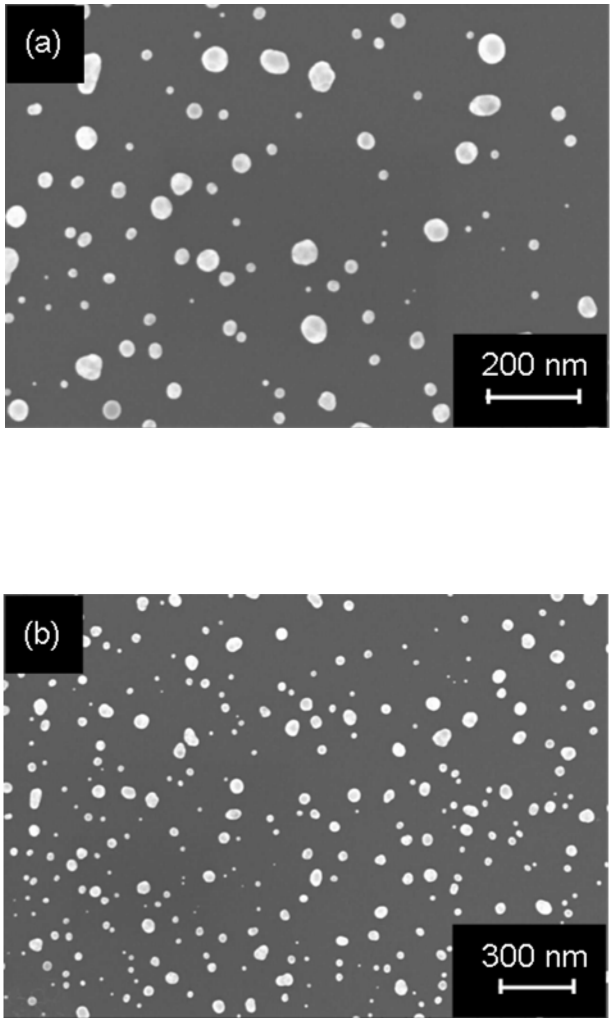

Figure 5.3. SEM images with different magnification scales of Au nanopartices prepared by electrodeposition on P8 at 0.0 V vs. Ag/AgCl for 10 s in 1 mM $KAuCl_4$ and 0.5 M H_2SO_4.

cases is to plot $(I/I_{max})^2$ vs. t/t_{max} and then to compare the experimental data with the theoretical plots.[45,46]

A non-dimensional plot of $(I/I_{max})^2$ vs. t/t_{max} based on the experimental data is shown on Figure 5.2 (b). The experimental data are compared to the theoretical plots for instantaneous and progressive nucleation. The first three points in the experimental data are attributed to the charging current. As shown in Figure 5.2 (b), our experimental data agree more closely with the progressive nucleation mechanism.

SEM was used to verify the progressive nucleation mechanism for our electrodes. Figure 5.3 shows SEM images of Au nanoparticles electrodeposited on P8 at various magnification scales. The size of Au nanoparticles is widely distributed from 10 nm to 100 nm range. This is the characteristic of the progressive nucleation mechanism, which implies the continuous formation of new nuclei during the deposition process.

5.3.3 Concentration and overpotential effects

The influence of parameters, such as solution concentration and electrode overpotential on particle density and size, has been investigated for GC and other electrodes.[10,30] The influence of $AuCl_4^-$ concentration and overpotential was thus explored at our P8 carbon film electrodes. The effect of $AuCl_4^-$ concentration on the particle size and density on P8 was examined by SEM. Figure 5.4 represents the results for 0.1, 0.2, and 1.0 mM $KAuCl_4$ concentrations. For all three concentrations, deposition was carried out at 0.0 V for 1 s.

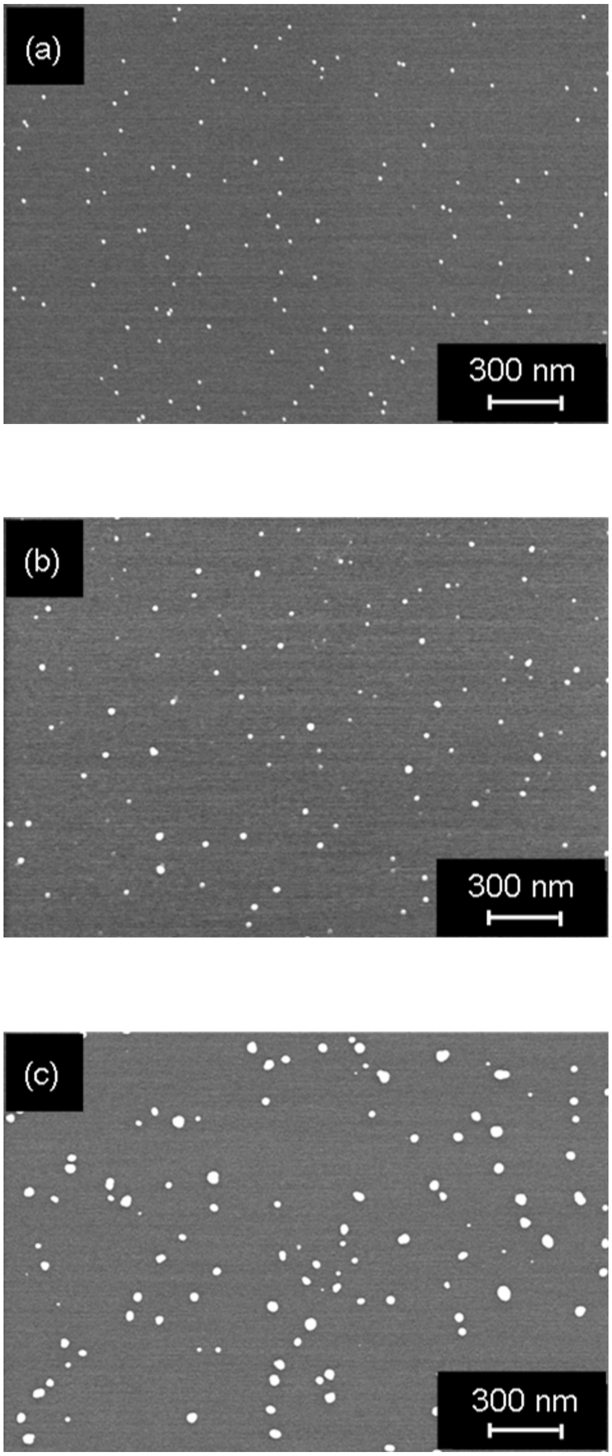

Figure 5.4. SEM images of Au nanoparticles electrodeposited on P8 electrodes from a series of $KAuCl_4$ concentrations: (a) 100 µM, (b) 200 µM, and (c) 1 mM.

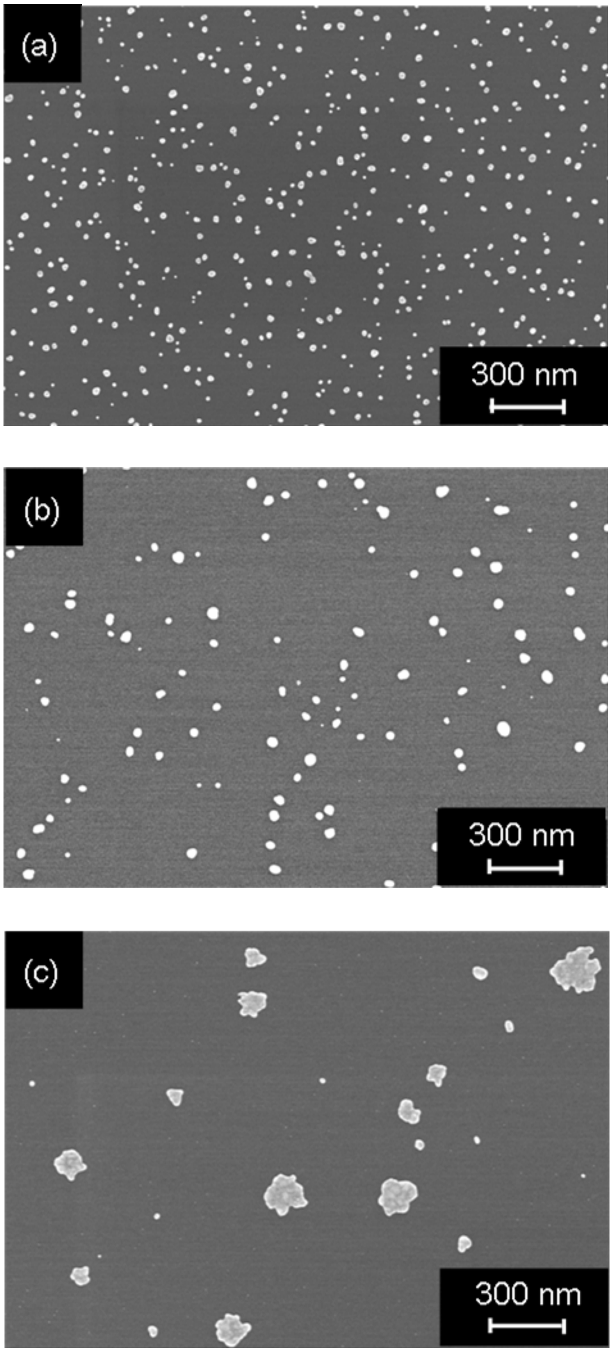

Figure 5.5. SEM images of the Au nanoparticles electrodeposited on P8 at different potentials: (a) -200 mV, (b) 0 mV, and (c) 400 mV; electrolyte: 1 mM $KAuCl_4$ + 0.5 M H_2SO_4, t = 1 s for all images.

The particle densities and sizes obtained from SEM image analysis are listed in Table 5.1. The data was obtained based on the measurements for 20 different spots on each sample surface. The nanoparticle number density reflects the number of nucleation sites on the electrode surfaces. Schmidt et al.[30] have reported that Au particle density is approximately constant at a given overpotential, and independent of gold solution concentration on GC surfaces. Our experimental results are consistent with this conclusion.

Table 5.1. Results from SEM image analysis for electrochemically deposited gold nanoparticles at various $KAuCl_4$ concentrations.

Concentration (mM)	Particle density[a] ($/\mu m^2$)	Particle size[a] (nm)
0.1	32 ± 8	15 ± 2
0.2	35 ± 6	25 ± 5
1	29 ± 10	60 ± 15

[a] Values reported are mean ± standard deviation. More than 20 different spots on the electrode surface were chosen for the measurement.

Overpotential plays an important role in the nucleation and growth.[10,30] Higher overpotential generally leads to a larger number of nucleation sites. The relationship between the overpotential and the active site density on P8 electrodes was examined by SEM. Figure 5.5 shows the results for potentials of -0.2 V, 0.0 V and 0.4 V, respectively. All density values were obtained based on the measurements of more than 20 different spots on each electrode surface. It was found that deposition potential greatly affects the density and size of Au nuclei as summarized in Table 5.2. The experimental results indicate a close relationship between the density of the active sites and the deposition potential. Higher nuclei densities can be obtained by increasing the deposition overpotential as is expected.[10,30]

Table 5.2. Results from SEM image analysis for electrochemically deposited gold nanoparticles at various deposition potentials.

Deposition potential (V vs. Ag/AgCl)	Particle density[a] (/µm^2)	Particle size[a] (nm)
-0.2	114 ± 15	30 ± 9
0	29 ± 10	60 ± 15
0.4	5 ± 2	132 ± 82

[a] Values reported are mean ± standard deviation. More than 20 different spots on the electrode surface were chosen for the measurement.

The difference of the nuclei size at different potentials corresponds to the different diffusion modes. Less negative deposition potential leads to low density nuclei on the electrode surface. The diffusion zone around each nucleus is radial while those at more negative potentials are overlapped and the rate of mass transport is greatly reduced.

5.3.4 Growth process

Once nuclei are formed on the electrode surface, they will grow. Three growth modes, layer-by-layer growth (Frank-van der Merwe mode), island growth on predeposited monolayers mode (Stanski-Krastanov mode), and island growth (Volmer-Weber mode), have been proposed for metal electrodeposition based on the different binding energy between the electro-reduced metal adatom and the substrate and the crystallographic misfit between the adatom and substrate lattices.[43] When strong affinity exists between the substrate and deposits, the electrodeposition likely follows a two-dimensional process (Frank-van Der Merwe mode) until a complete monolayer is obtained. Frank-van Der Merwe mechanism, Figure 5.6 (a), described the mode by which the atoms cover the whole surface before a second layer is grown. In the case of weak adhesion between the substrate and the deposits, the electrodeposition generally follows the Volmer-Weber mode. Particles will grow three-dimensionally to minimize the particle-substrate interaction. A thin film will finally be formed once the particles have grown large enough to touch each other, then it is referred to as the Volmer Weber mode [Figure 5.6 (c)]. If the growth process is a combination of the above two modes by first covering the surface and then growing by island structures, it is referred to as the Stranski-Krastanov mode [Figure 5.6 (b)]. Metal deposition on the carbon surfaces follows the Volmer-Weber mode due to the weak binding energy between the metal particles and carbon surfaces.[43]

The growth process of electrodeposited gold on P8 electrode surfaces was studied. The morphologies of the gold particles obtained at different deposition

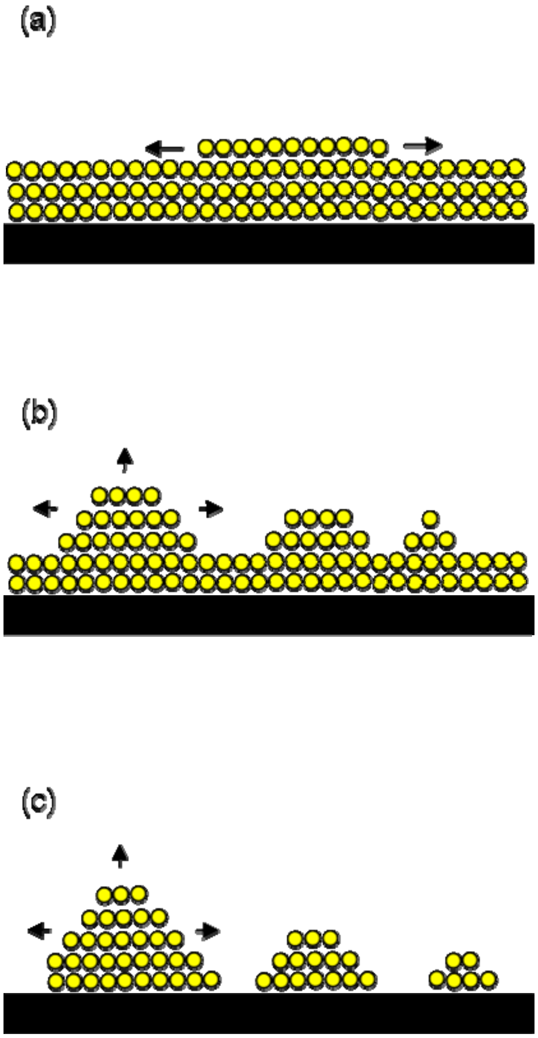

Figure 5.6. Different growth modes of metal deposition on foreign substrate. (a) Layer by layer growth (Frank-van Der Merwe mode), (b) island growth on predeposited monolayers mode (Stranski-Krastanov mode) and (c) island growth (Volmer-Weber mode).

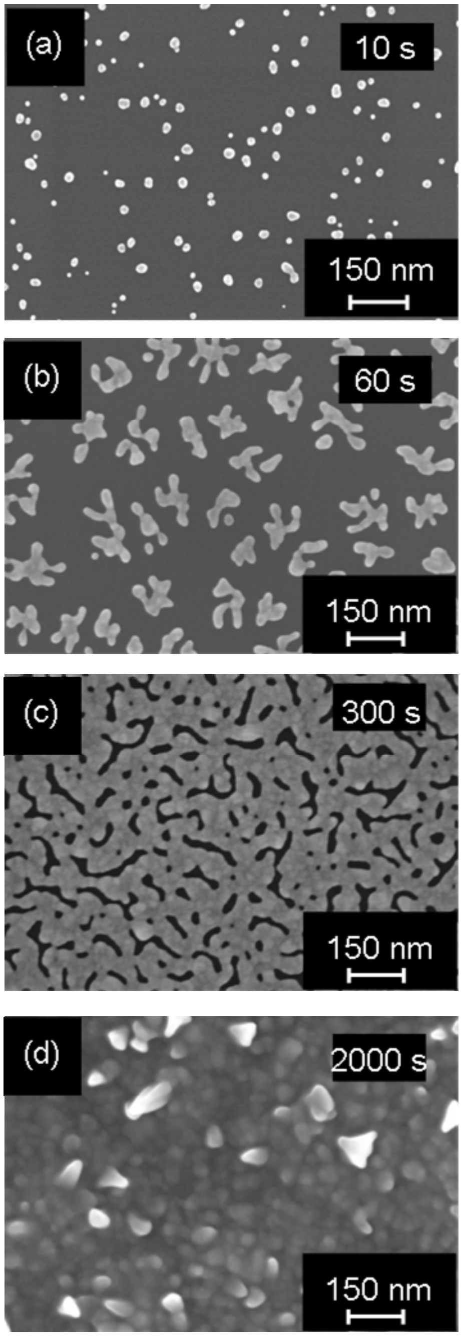

Figure 5.7. SEM images of the Au particles electrodeposited on the P8 surfaces at the potential of 0.0 V vs. Ag/AgCl for 10 s (a), 60 s (b), 300 s (c), and 2000 s (d), respectively. Electrolyte: 1.0 mM $KAuCl_4$ and 0.5 M H_2SO_4.

time were characterized by SEM. Figure 5.7 shows the SEM images of the electrode surfaces at different deposition times. At a short deposition time of 10 s [Figure 5.7 (a)], the electrode surface consists of a large quantity of gold nanoparticles. The isolated particles are randomly distributed on the electrode surface. Their size is not uniform because of the progressive nucleation discussed in section 5.3.2. Of all the three growth modes, only the Volmer-Weber mode leads to the formation of nanoparticles. Therefore, Au electrodeposition on P8 surfaces follows the Volmer-Weber mode. Figure 5.7 (b), (c) and (d) are the SEM images of the electrode surfaces after gold deposition for 60 s, 300 s, and 2000 s, respectively. The transformation of Au nuclei to a complete Au film is illustrated in the SEM images in Figure 5.7.

Isolated Au nanoparticles result from deposition at 10 s. After 60 s of deposition, Au islands of various shapes are forming, which is similar to those observed by Bardotti et al.[47] The observed Au island structure during the deposition process show that the coalescence happens, which generally describes the film growth process. The coalescence is attributed to diffusion by some researchers.[47-49] Bardotti et al. reported that Au clusters can diffuse, aggregate, and form island structures on the HOPG surfaces.[47] The driving force for the coalescence is likely attributed to the tendency to minimize the surface energy.[48] The cluster diffusion on the substrate surface has been observed.[48] The mobility of gold nanoparticles on a flat surface was also reported by Gates et al.[49] Further deposition (300 s) results in the formation of a near complete 2-dimensional film.

Eventually, long time deposition (2000 s) leads to the formation of a continuous gold film on the P8 surface.

5.3.5 Analysis of the Au/C interface

The presence of an intermetallic layer at the interface between gold and semi-conductor surfaces is well known.[50-54] Depth-profiling analysis by XPS has revealed the interface between Au nanoparticles and Si substrate.[50,51] Gheber et al. investigated the interface formation between an evaporated gold film and hydrogen-terminated Si(111).[52] They reported that the first monolayer of gold covered uniformly on the silicon surface and formed strong Au-Si bonds (gold silicide). Sundaravel et al. studied the deposition of gold film onto a bromine passivated Si(111) substrate under high vacuum conditions.[53] Chemical shifts in the XPS peaks of Si 2P and Au 4f demonstrated the formation of a silicide compound. The interfacial characterization of gold nanostructures on silicon surface has been carried out by Buriak and co-workers.[54] In addition to the direct observation of the heteroepitaxial interface of Au crystallites on silicon by high resolution TEM, extra diffraction spots were also observed by diffraction with a 20 nm probe. These extra spots were likely attributed to the presence of crystalline gold silicides. The presence of a similar sandwiched intermetallic layer at the interface between gold and Ge,[55] GaAs and InP[56] was also reported.

The formation of a gold carbide (Au-C) layer, however, has not been observed at the Au/C interface. Gold carbides are believed to be thermodynamically unfavorable.[57,58] Gold carbides are very unstable although their formation has been observed as ionized clusters in the gas phase.[59,60] Zhen and co-workers investigated the interface formation between diamond carbon films and Au films before and after annealing at 500°C under a vacuum condition.[61] No shifts of Au 4f peaks were observed by the depth profile XPS analysis in both cases, which indicated no interface reactions between Au and diamond. Similar conclusions were also obtained by other researchers.[58,62] Liu et al. studied the electrodeposition of Au nanoclusters on an amorphous carbon electrode.[63] The interface between Au nanoclusters and carbon surfaces was characterized by XPS. No shift of the Au 4f peak was observed, excluding the possibility of gold carbide formation. Dai and co-workers studied the coating of various metals on suspended carbon nanotubes (CNTs).[64,65] They concluded that the interaction between Au particles and CNTs is very weak, which is presumably van der Waals in nature. Graphitic electrodes are well known for the high chemical inertness of the ordered sp^2 carbon network at a basal plane.[64] The interaction between gold and graphite basal plane was suggested to be through van der Waals forces and does not involve a chemical bond.[55] Penner and co-workers studied the electrodeposition of noble metals on graphite surfaces.[66,67] They also believed that the interaction between the deposited metal particles and "the coordinately saturated graphite basal plane surface" is based on weak van der Waals.[66] The electrodeposition of Au nanoparticles on GC electrodes has been investigated by different researchers,[4,5,7,10,11,28,29] but the focus was upon the nucleation process and applications, and not the nature of the interface. GC and

PPF surfaces likely have some oxides and edge plane sites[68] that may lead to a stronger interaction than van Der Waals forces normally ascribed to basal planes.

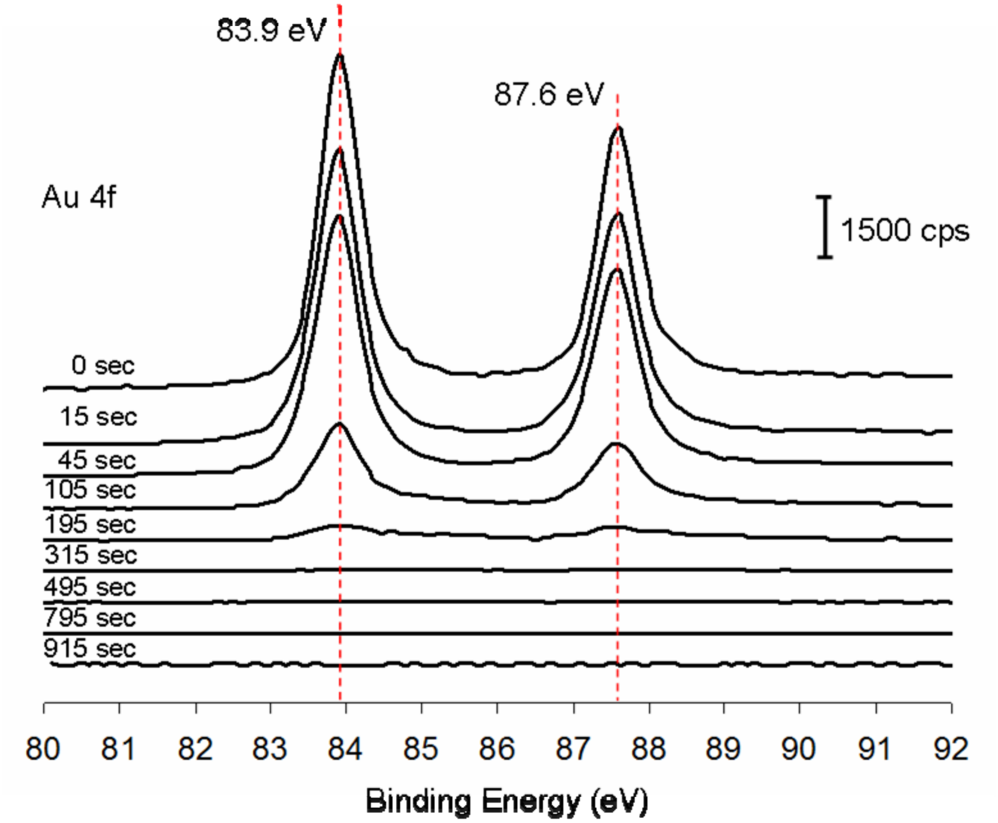

Figure 5.8. Au 4f XPS spectra at different Ar$^+$ sputtering time intervals of Au on P8, formed by electrodeposition for 300 s at 0.0 V vs. Ag/AgCl. Electrolyte: 1.0 mM $KAuCl_4$ (0.5 M H_2SO_4).

Depth-profiling analysis by XPS was carried out to characterize the interface between gold and P8 surfaces. Figure 5.8 shows the Au 4f XPS spectra of an Au/C sample at different Ar$^+$ sputtering time intervals. The sample was prepared by the electrodeposition at 0.0 V vs. Ag/AgCl for 300 s in 1.0 mM $KAuCl_4$ (0.5 M H_2SO_4). Au $4f_{7/2}$ and Au $4f_{5/2}$ peaks located at 83.9 and 87.6 eV are consistent with those of Au foils.[50] No shift of Au 4f peak was observed, which was different to those observed on semi-conductor surfaces.[50,51,55,56] This observation excluded the formation of gold carbides on the P8 sample surface. To the best of our knowledge, the interaction between Au and GC or PPF surfaces had not been investiagated. The van der Waals force is presumably playing an important role on the interaction at the Au/C interface.[66,67] However, the possibility of hydrogen bonds formed between the C-OH, C=O, and COOH at edge plane sites[68] and the metal oxide at the nanoparticle surface can not be excluded.

5.3.6 Nucleation and growth steps of the Au electrodeposition process

An electrodeposition process, takeing place at the interface between the electrode surface and the electrolyte solution, consists of the following individual steps as shown in Figure 5.9:[69]

(1) Mass transfer of reactants from the bulk solution to the electrode/electrolyte interface via diffusion

(2) Electron transfer from the electrode to the ions and formation of metal adatoms on the electrode surface

(3) Metal phase formation via nucleation and growth.

For the Au electrodeposition process on the P8 carbon electrode, the possible nucleation and growth steps, such as the electroreduction, nucleation, coalescence, etc., are described in Figure 5.10. Figure 5.10 (a) represents the initial conditions prior to the onset of the electrochemical reaction. At the

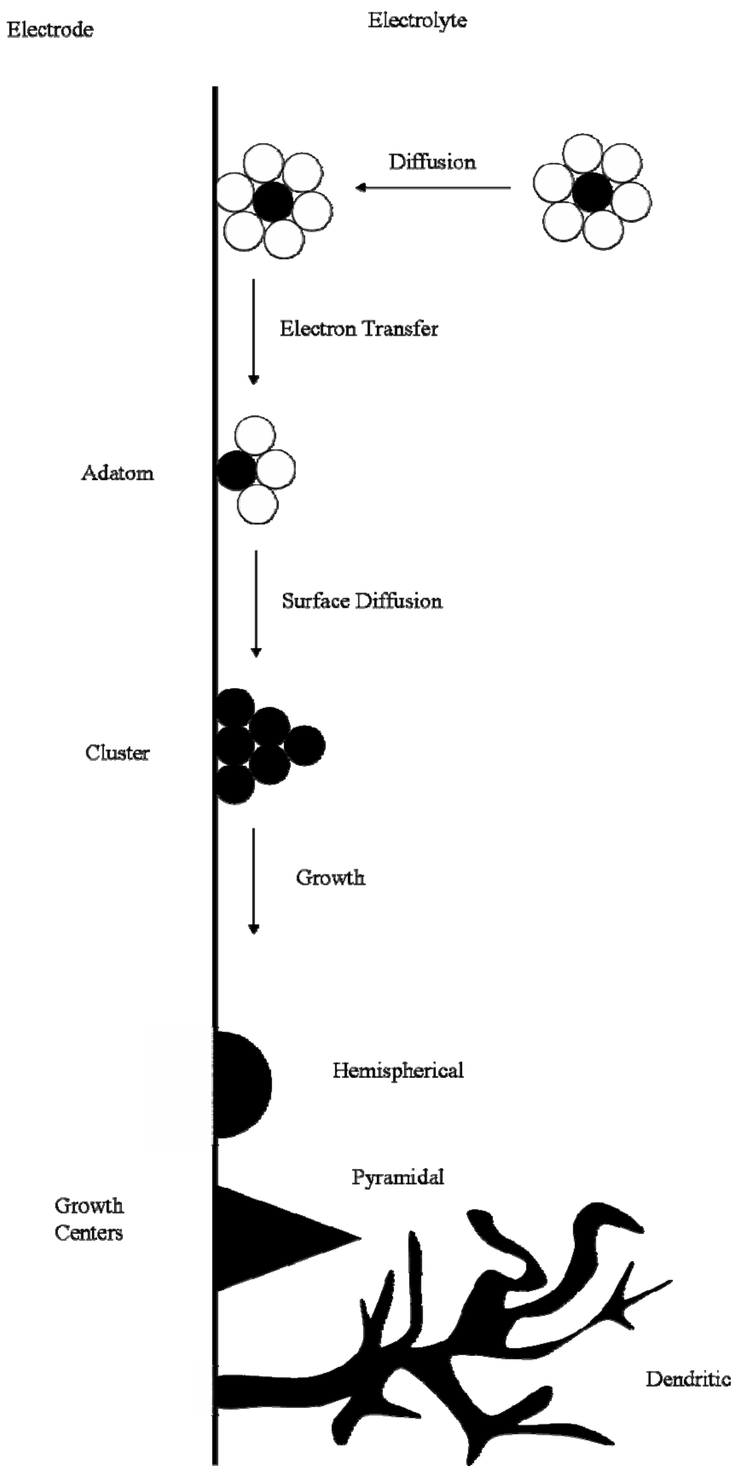

Figure 5.9. Possible nucleation and growth steps of an electrodeposition process (adapted from reference 69).

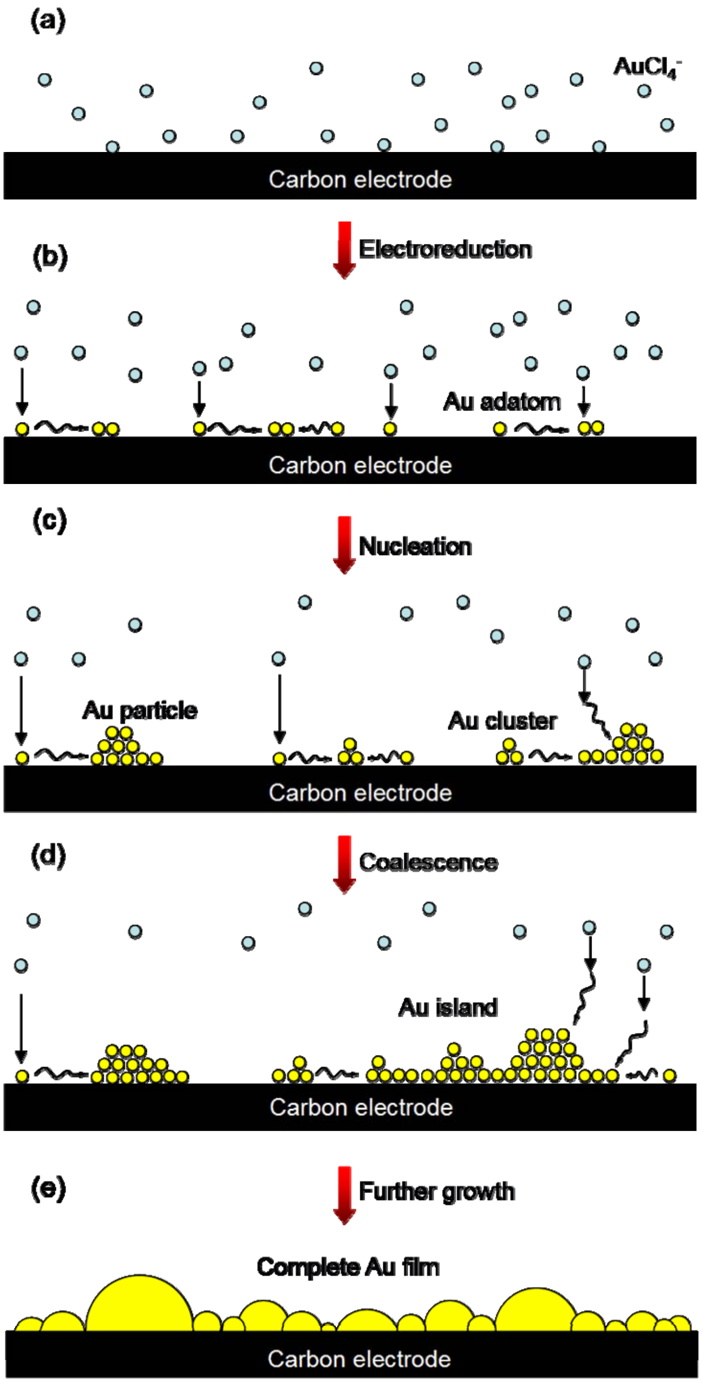

Figure 5.10. Schematic presentation of different stages at the Au electrodeposition process. Blue circles represent $AuCl_4^-$ ions, while yellow ones represent Au(0) atoms.

beginning of electrodeposition, $AuCl_4^-$ ions are diffusing to the electrode surface and then reduced as adatoms [Figure 5.10 (b)]. The electrochemical reaction is as follows:

$$AuCl_4^- + C^* + 3\,e^- \rightarrow Au(C^*) + 4\,Cl^-$$

where C* refers to as the carbon electrode surface. Due to the weak Au/C interaction at the carbon electrode surface, Au adatoms are contacted with the carbon surface by van der Waals.[66] Adatoms can diffuse along the surface to seek low energy positions, such as defects or edge plane sites on the carbon surface. These adatoms may then group together and form a nucleus to minimize the surface energy.

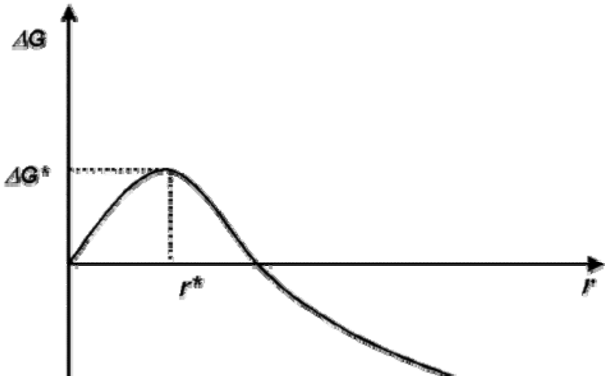

Figure 5.11. Illustration of the free energy as a function of the growth particle size (adapted from reference 70)

A nucleus is primarily formed from the grouping of a critical number of adatoms. The stability of adatoms can be increased by grouping together and forming a large sized cluster.[70] The free energy of a cluster, ΔG, is the sum of the free energy due to the formation of a new volume and the free energy due to the new surface created. ΔG has a positive maximum at a critical size, r^* (as shown in Figure 5.11).[70] A cluster with a critical size is called the critical nucleus. Clusters larger than the critical size will become stable and further decrease their free energy by growing and forming a nucleus. Au nuclei are produced by the electroreduction of $AuCl_4^-$ ions and the further grouping of adatoms on the electrode surface as shown in Figure 5.10 (c).

As the electrodeposition process procedes, further electroreduction of $AuCl_4^-$ ions can occur at either other sites on the carbon electrode or at gold nuclei. Reduction at the carbon electrode surface will result in new nuclei, which is characteristic of progressive nucleation as discussed in Section 5.3.2. Electroreduction at already formed gold nuclei will result in particle growth and island formation. Due to the weak Au/C interaction, both Au adatoms and clusters can diffuse along the graphite surface until they aggregate with the nearest neighbors and form a more stable structure.[21] These diffusion and coalescence processes lead to the formation of Au islands, as shown in Figure 5.10 (d). When the deposition process is continued, the coverage of Au island structures increases, leading to the formation of a complete Au film as shown in Figure 5.10 (e).

5.4 Conclusions

Electrochemistry and SEM analysis have been applied to investigate the electrodeposition process of gold nanoparticles to P8 carbon film electrodes. Current-time transients show that the electrodeposition follows the classical progressive nucleation mechanism. SEM characterization demonstrates that the early stage of the deposition process is affected by both deposition potential and gold concentration. A less negative deposition potential leads to lower particle density and larger particle size, while a more negative potential leads to higher particle density and smaller particle size. The gold concentration also plays an important role in controlling the particle size during the deposition process. Our results show that the particles density is approximately constant at a given overpotential, and is independent of the deposition solution concentrations. The Au deposition on the P8 electrode surfaces follows the Volmer-Weber growth mechanism. Three-dimensional gold particles are initially formed on the P8 surface. With the continued growth, the coalescence of Au particles was observed. The coalescence leads to the interconnection of Au islands and forms a partial 2-dimentional film covering the P8 surface. The electrode surface was completely covered by long time metal film deposition.

5.5 References

1. Valden, M.; Lai, X.; Goodman, D. W., Onset of catalytic activity of gold clusters on titania with the appearance of nonmetallic properties. *Science* **1998,** 281, 1647-1650.
2. El-Sayed, M. A., Some interesting properties of metals confined in time and nanometer space of different shapes. *Accounts of Chemical Research* **2001,** 34, 257-264.
3. Murphy, C. J., Nanocubes and nanoboxes. *Science* **2002,** 298, 2139-2140.
4. El-Deab, M. S.; Sotomura, T.; Ohsaka, T., Oxygen reduction at electrochemically deposited crystallographically oriented Au(100)-like gold nanoparticles. *Electrochemistry Communications* **2005,** 7, 29-34.
5. El-Deab, M. S.; Sotomura, T.; Ohsaka, T., Oxygen reduction at Au nanoparticles electrodeposited on different carbon substrates. *Electrochimica Acta* **2006,** 52, 1792-1798.
6. Alexeyeva, N.; Laaksonen, T.; Kontturi, K.; Mirkhalaf, F.; Schiffrin, D. J.; Tammeveski, K., Oxygen reduction on gold nanoparticle/multi-walled carbon nanotubes modified glassy carbon electrodes in acid solution. *Electrochemistry Communications* **2006,** 8, 1475-1480.
7. Raj, C. R.; Abdelrahman, A. I.; Ohsaka, T., Gold nanoparticle-assisted electroreduction of oxygen. *Electrochemistry Communications* **2005,** 7, 888-893.
8. Schon, G.; Simon, U., A fascinating new field in colloid science - small ligand-stabilized metal-clusters and possible application in

microelectronics .1. state-of-the-art. *Colloid and Polymer Science* **1995,** 273, 101-117.

9. Raj, C. R.; Okajima, T.; Ohsaka, T., Gold nanoparticle arrays for the voltammetric sensing of dopamine. *Journal of Electroanalytical Chemistry* **2003,** 543, 127-133.

10. Finot, M. O.; Braybrook, G. D.; McDermott, M. T., Characterization of electrochemically deposited gold nanocrystals on glassy carbon electrodes. *Journal of Electroanalytical Chemistry* **1999,** 466, 234-241.

11. Finot, M. O.; McDermott, M. T., Characterization of n-alkanethiolate monolayers adsorbed to electrochemically deposited gold nanocrystals on glassy carbon electrodes. *Journal of Electroanalytical Chemistry* **2000,** 488, 125-132.

12. Aoun, S. B.; Taniguchi, I., Highly catalytic electrode for glucose electro-oxidation based on au nanoparticles electrodeposited onto HOPG substrate. *Chemistry Letters* **2007,** 36, 898-899.

13. Authier, L.; Grossiord, C.; Brossier, P.; Limoges, B., Gold nanoparticle-based quantitative electrochemical detection of amplified human cytomegalovirus DNA using disposable microband electrodes. *Analytical Chemistry* **2001,** 73, 4450-4456.

14. Yanez-Sedeno, P.; Pingarron, J. M., Gold nanoparticle-based electrochemical biosensors. *Analytical and Bioanalytical Chemistry* **2005,** 382, 884-886.

15. Magnusson, M. H.; Deppert, K.; Malm, J. O.; Bovin, J. O.; Samuelson, L., Size-selected gold nanoparticles by aerosol technology. *Nanostructured Materials* **1999**, 12, 45-48.

16. Cross, C. E.; Hemminger, J. C.; Penner, R. M., Physical vapor deposition of one-dimensional nanoparticle arrays on graphite: Seeding the electrodeposition of gold nanowires. *Langmuir* **2007,** 23, 10372-10379.

17. Lung, J. K.; Huang, J. C.; Tien, D. C.; Liao, C. Y.; Tseng, K. H.; Tsung, T. T.; Kao, W. S.; Tsai, T. H.; Jwo, C. S.; Lin, H. M.; Stobinski, L., Preparation of gold nanoparticles by arc discharge in water. *Journal of alloys and compounds* **2007,** 434, 655-658.

18. Schimpf, S.; Lucas, M.; Mohr, C.; Rodemerck, U.; Bruckner, A.; Radnik, J.; Hofmeister, H.; Claus, P., Supported gold nanoparticles: In-depth catalyst characterization and application in hydrogenation and oxidation reactions. *Catalysis Today* **2002,** 72, 63-78.

19. Chen, W.; Cai, W. P.; Liang, C. H.; Zhang, L. D., Synthesis of gold nanoparticles dispersed within pores of mesoporous silica induced by ultrasonic irradiation and its characterization. *Materials Research Bulletin* **2001,** 36, 335-342.

20. Brust, M.; Walker, M.; Bethell, D.; Schiffrin, D. J.; Whyman, R., Synthesis of thiol-derivatized gold nanoparticles in a 2-phase liquid-liquid system. *Journal of the Chemical Society-Chemical Communications* **1994**, 7, 801-802.

21. Xiao, F.; Mo, Z. R.; Zhao, F. Q.; Zeng, B. Z., Ultrasonic-electrodeposition of gold-platinum alloy nanoparticles on multi-walled carbon nanotubes - ionic liquid composite film and their electrocatalysis towards the oxidation of nitrite. *Electrochemistry Communications* **2008,** 10, 1740-1743.

22. Tsai, M. C.; Yeh, T. K.; Tsai, C. H., Electrodeposition of platinum-ruthenium nanoparticles on carbon nanotubes directly grown on carbon cloths for methanol oxidation. *Materials Chemistry and Physics* **2008,** 109, 422-428.

23. Wang, L. P.; Mao, W.; Ni, D. D.; Di, J. W.; Wu, Y.; Tu, Y. F., Direct electrodeposition of gold nanoparticles onto indium/tin oxide film coated glass and its application for electrochemical biosensor. *Electrochemistry Communications* **2008,** 10, 673-676.

24. Zoval, J. V.; Stiger, R. M.; Biernacki, P. R.; Penner, R. M., Electrochemical deposition of silver nanocrystallites on the atomically smooth graphite basal plane. *Journal of Physical Chemistry* **1996,** 100, 837-844.

25. Zoval, J. V.; Lee, J.; Gorer, S.; Penner, R. M., Electrochemical preparation of platinum nanocrystallites with size selectivity on basal plane oriented graphite surfaces. *Journal of Physical Chemistry B* **1998,** 102, 1166-1175.

26. Penner, R. M., Mesoscopic metal particles and wires by electrodeposition. *Journal of Physical Chemistry B* **2002,** 106, 3339-3353.

27. Walter, E. C.; Zach, M. P.; Favier, F.; Murray, B. J.; Inazu, K.; Hemminger, J. C.; Penner, R. M., Metal nanowire arrays by electrodeposition. *Chemphyschem* **2003,** 4, 131-138.

28. El-Deab, M. S.; Sotomura, T.; Ohsaka, T., Size and crystallographic orientation controls of gold nanoparticles electrodeposited on GC electrodes. *Journal of the Electrochemical Society* **2005,** 152, C1-C6.

29. El-Deab, M. S.; Sotomura, T.; Ohsaka, T., Morphological selection of gold nanoparticles electrodeposited on various substrates. *Journal of the Electrochemical Society* **2005,** 152, C730-C737.

30. Schmidt, U.; Donten, M.; Osteryoung, J. G., Gold electrocrystallization on carbon and highly oriented pyrolytic graphite from concentrated solutions of LiCl. *Journal of the Electrochemical Society* **1997,** 144, 2013-2021.

31. Trejo, G.; Gil, A. F.; Gonzalez, I., Electrodeposition of gold in ammoniacal medium: Influence of substrate and temperature. *Journal of Applied Electrochemistry* **1996,** 26, 1287-1294.

32. Trejo, G.; Gil, A. F.; Gonzalez, I., Temperature effect on the electrocrystallization processes of gold in ammoniacal medium. *Journal of the Electrochemical Society* **1995,** 142, 3404-3408.

33. Liu, A. P.; Zhu, J. Q.; Han, J. C.; Wu, H. P.; Jiang, C. Z., Fabrication and characterization of gold nanoclusters on phosphorus incorporated tetrahedral amorphous carbon electrode. *Electrochemistry Communications* **2008,** 10, 827-830.

34. Ranganathan, S.; McCreery, R. L., Electroanalytical performance of carbon films with near-atomic flatness. *Analytical Chemistry* **2001,** 73, 893-900.

35. Kim, J.; Song, X.; Kinoshita, K.; Madou, M.; White, B., Electrochemical studies of carbon films from pyrolyzed photoresist. *Journal of the Electrochemical Society* **1998,** 145, 2314-2319.

36. Anariba, F.; DuVall, S. H.; McCreery, R. L., Mono- and multilayer formation by diazonium reduction on carbon surfaces monitored with atomic force microscopy "scratching". *Analytical Chemistry* **2003,** 75, 3837-3844.

37. Nowak, A. M.; McCreery, R. L., Characterization of carbon/nitroazobenzene/titanium molecular electronic junctions with photoelectron and Raman spectroscopy. *Analytical Chemistry* **2004,** 76, 1089-1097.

38. Kalakodimi, R. P.; Nowak, A. M.; McCreery, R. L., Carbon/molecule/metal and carbon/molecule/metal oxide molecular electronic junctions. *Chemistry of Materials* **2005,** 17, 4939-4948.

39. Ranganathan, S.; McCreery, R.; Majji, S. M.; Madou, M., Photoresist-derived carbon for microelectromechanical systems and electrochemical applications. *Journal of the Electrochemical Society* **2000,** 147, 277-282.

40. Gunawardena, G.; Hills, G.; Montenegro, I.; Scharifker, B., Electrochemical nucleation .1. General-considerations. *Journal of Electroanalytical Chemistry* **1982,** 138, 225-239.

41. Gunawardena, G.; Hills, G.; Montenegro, I., Electrochemical nucleation .2. The electrodeposition of silver on vitreous carbon. *Journal of Electroanalytical Chemistry* **1982,** 138, 241-254.

42. Gunawardena, G.; Hills, G.; Montenegro, I.; Scharifker, B., Electrochemical nucleation .3. The electrodeposition of mercury on vitreous carbon. *Journal of Electroanalytical Chemistry* **1982,** 138, 255-271.

43. Paunovic, M.; Schlesinger, M., Chapter 7: Nucleatin and growth models. In *Fundamentals of Electrochemical Deposition, Second Edition*, John Wiley & Sons, Inc.: 2006; Vol. 7, pp 113-138.

44. Scharifker, B.; Hills, G., Theoretical and experimental studies of multiple nucleation. *Electrochimica Acta* **1983,** 28, 879-889.

45. Mostany, J.; Mozota, J.; Scharifker, B. R., 3-dimensional nucleation with diffusion controlled growth .2. The nucleation of lead on vitreous carbon. *Journal of Electroanalytical Chemistry* **1984,** 177, 25-37.

46. Scharifker, B. R.; Mostany, J., 3-dimensional nucleation with diffusion controlled growth .1. Number density of active-sites and nucleation rates per site. *Journal of Electroanalytical Chemistry* **1984,** 177, 13-23.

47. Bardotti, L.; Prevel, B.; Treilleux, M.; Melinon, P.; Perez, A., Deposition of preformed gold clusters on HOPG and gold substrates: influence of the substrate on the thin film morphology. *Applied Surface Science* **2000,** 164, 52-59.

48. Lee, Y. L.; Maa, J. R., Nucleation and growth of condensate clusters on solid-surfaces. *Journal of Materials Science* **1991,** 26, 6068-6072.

49. Gates, A. D.; Robins, J. L., Cluster mobility calculations for gold particles on (100) NaCl surfaces. *Surface Science* **1988,** 194, 13-43.

50. Zhao, L. Y.; Siu, A. C. L.; Petrus, J. A.; He, Z. H.; Leung, K. T., Interfacial bonding of gold nanoparticles on a H-terminated Si(100) substrate obtained by electro- and electroless deposition. *Journal of the American Chemical Society* **2007,** 129, 5730-5734.

51. Sohn, Y.; Pradhan, D.; Radi, A.; Leung, K. T., Interfacial electronic structure of gold nanoparticles on Si(100): Alloying versus quantum size effects. *Langmuir* **2009,** 25, 9557-9563.

52. Gheber, L. A.; Hershfinkel, M.; Gorodetsky, G.; Volterra, V., Investigation of the composition and electrical properties of gold H-terminated silicon(111) interface. *Thin Solid Films* **1998,** 320, 228-235.

53. Sundaravel, B.; Sekar, K.; Kuri, G.; Satyam, P. V.; Dev, B. N.; Bera, S.; Narasimhan, S. V.; Chakraborty, P.; Caccavale, F., XPS and SIMS analysis of gold silicide grown on a bromine passivated Si(111) substrate. *Applied Surface Science* **1999,** 137, 103-112.

54. Sayed, S. Y.; Wang, F.; Mallac, M.; Meldrum, A.; Egerton, R. F.; Buriak, J. M., Heteroepitaxial growth of gold nanostructures on silicon by galvanic displacement. *ACS Nano* **2009,** 3, 2809-2817.

55. Magagnin, L.; Maboudian, R.; Carraro, C., Gold deposition by galvanic displacement on semiconductor surfaces: Effect of substrate on adhesion. *Journal of Physical Chemistry B* **2002,** 106, 401-407.

56. Sayed, S. Y.; Daly, B.; Buriak, J. M., Characterization of the interface of gold and silver nanostructures on InP and GaAs synthesized via galvanic displacement. *Journal of Physical Chemistry C* **2008,** 112, 12291-12298.

57. Pan, L. S., *Diamond: Electronic Properties and Application*. Springer: 1995.

58. Tachibana, T.; Williams, B. E.; Glass, J. T., Correlation of the electrical-properties of metal contacts on diamond films with the chemical nature of the metal-diamond interface .1. Gold contacts - a non-carbide-forming metal. *Physical Review B* **1992,** 45, 11968-11974.

59. Buttner, M.; Oelhafen, P., XPS study on the evaporation of gold submonolayers on carbon surfaces. *Surface Science* **2006,** 600, 1170-1177.

60. Gibson, J. K., Laser ablation and gas-phase reactions of small gold cluster ions, $Au_n^{(+)}$ (1 <= n <= 7). *Journal of Vacuum Science & Technology a-Vacuum Surfaces and Films* **1998,** 16, 653-659.

61. Zhen, C. M.; Wang, X. Q.; Wu, X. C.; Liu, C. X.; Hou, D. L., Au/p-diamond ohmic contacts deposited by RF sputtering. *Applied Surface Science* **2008,** 255, 2916-2919.

62. Wang, Y. Y.; Liu, X. Q.; Zhen, C. M.; Gong, H. X.; Yan, Z. J.; Yang, Y. H.; Ma, S. Y., Ohmic contacts and interface properties of Au/Ti/p-

diamnond prepared by RF sputtering. *Surface and Interface Analysis* **2000,** 29, 478-481.

63. Liu, A. P.; Zhu, J. Q.; Han, J. C.; Wu, H. P.; Jiang, C. Z., Fabrication and characterization of gold nanoclusters on phosphorus incorporated tetrahedral amorphous carbon electrode. *Electrochemistry Communications* **2008,** 10, 827-830.

64. Zhang, Y.; Franklin, N. W.; Chen, R. J.; Dai, H. J., Metal coating on suspended carbon nanotubes and its implication to metal-tube interaction. *Chemical Physics Letters* **2000,** 331, 35-41.

65. Zhang, Y.; Dai, H. J., Formation of metal nanowires on suspended single-walled carbon nanotubes. *Applied Physics Letters* **2000,** 77, 3015-3017.

66. Penner, R. M., Mesoscopic metal particles and wires by electrodeposition. *Journal of Physical Chemistry B* **2002,** 106, 3339-3353.

67. Walter, E. C.; Murray, B. J.; Favier, F.; Kaltenpoth, G.; Grunze, M.; Penner, R. M., Noble and coinage metal nanowires by electrochemical step edge decoration. *Journal of Physical Chemistry B* **2002,** 106, 11407-11411.

68. McCreery, R. L., Advanced carbon electrode materials for molecular electrochemistry. *Chemical Reviews* **2008,** 108, 2646-2687.

69. Walsh, F. C.; Herron, M. E., Electrocrystallization and electrochemical control of crystal-growth - fundamental considerations and electrodeposition of metals. *Journal of Physics D: Applied Physics* **1991,** 24, 217-225.

70. Burda, C.; Chen, X. B.; Narayanan, R.; El-Sayed, M. A., Chemistry and properties of nanocrystals of different shapes. *Chemical Reviews* **2005,** 105, 1025-1102.

Chapter 6. Gold Electrodeposition on Carbon Micro- and Nanoband Electrodes: Potential New Surface Enhanced Raman Scattering Substrates

This chapter is mainly focused on the electrodeposition of gold nanoparticles on micro- and nanoband electrodes. Multi-branched or dendritic shaped Au particles were deposited on the electrode surface. Particle morphology was found to be closely related to mass transport (MT) to the electrode surface. Multi-branched gold nanoparticles were subsequently used as surface enhanced Raman scattering (SERS) substrates. Strong SERS signals for a molecular layer adsorbed on the nanoband supported gold nanoparticles were observed and the enhancement factor (EF) was calculated.

6.1 Introduction

Metal nanoparticles have attracted increasing attention due to their unique optical, thermal and chemical properties.[1-3] Both the size and shape play important roles in tuning the properties.[4] For example, the absorption spectra of gold nanoparticles depend on their shape.[5,6] Cubes and spheres have only one plasmon band at ~540 nm. Rods, dogbones, tetrapods, and blocks have multiple plasmon bands from 525 nm to 775 nm.

SERS is a phenomenon in which there is strong enhancement of the Raman scattering efficiency for molecules adsorbed on nano-scale metal features. SERS is a highly sensitive technique, which can generate signal intensities ranging from 10^3 to 10^{14} times that of normal Raman scattering. Therefore, SERS has become an attractive technique for detecting submonolayer adsorbates,[7] trace amounts of analyte,[8] and under certain conditions, single molecules.[9-14]

Two types of mechanisms have been proposed to interpret the enhancement phenomena observed in SERS experiments.[14] One is an electromagnetic (EM) enhancement mechanism, generated by surface plasmon resonance on roughened metal surfaces or metal nanoparticles exposed to radiation. The other is a chemical mechanism (CM), also known as the charge-transfer (CT) mechanism. In this mechanism, the enhancement is attributed to the charge transfer between the adsorbate and metal surface that increases the polarizibility of the adsorbate.

Au nanoparticles have been widely used as SERS substrates. Both the shape and size can affect their SERS enhancement.[4,6] Metal particles with multi-branched shapes, such as nanostars[15-17] and nanoflowers,[18-21] have been synthesized and characterized recently. The presence of sharp edges and tips has been shown to increase the electric field enhancement.[16] Modeling of dendritic structures by Koch curve fractals predicts that maximum SERS activity arises from molecules adsorbed at high apexes of dendritic aggregates.[22] Bakr et al. also suggested that nanoparticles with multi-branched structure can exhibit large local electromagnetic field enhancements near the sharp-featured branched tips.[23] Enhancement of the light intensity relative to the incident field by approximately

3000-fold was obtained according to the finite different time domain (FDTD) simulation.[23] Stellacci and co-workers predicted that multi-branched metal particles would find applications as materials for SERS.[23] A similar conclusion was also reached by Kumar and co-workers, based on calculations of the SERS response with nanostar shaped Au nanoparticles.[24] The use of multi-branched Au nanoparticles as an efficient Raman-active tag has been reported and strong SERS effects were observed.[25] More examples of the synthesis and applications of multi-branched gold nanoparticles as SERS substrates are continually being reported.[17,18,25-27] It is reported that SERS enhancement factors (EF) as high as 2.2 $\times 10^5$ can be obtained.[18]

In this chapter, we describe the electrochemical deposition of multi-branched Au nanoparticles. The Au nanoparticles were deposited on a nanoband electrode surface. Due to the small size of the electrode, rapid mass transport of $AuCl_4^-$ anions via nonlinear diffusion results in Au nanoparticles with multi-branched or dendritic shapes. The size and shape evolution was investigated by SEM. The optical enhancement properties were tested by SERS. Thiol molecules were used to modify the Au particle surfaces and these were characterized by SERS.

6.2 Experimental Section

6.2.1 Chemicals

Potassium tetrachloroaurate (III) (Aldrich), sulphuric acid (Fisher), 4-Aminothiophenol (4-ATP, Fisher), ethanol (Fisher), dimethyl sulfoxide (DMSO, Fisher) were all used as received. All aqueous solutions were prepared using distilled/deionized water (18 MΩ/cm).

6.2.2 Electrode preparation

Carbon nanoband electrodes were fabricated by the combination of E-beam lithography and pyrolysis as presented in Chapter 4. Film edge electrodes were made from pyrolyzed SU8 carbon film electrodes. Film electrodes were first spin-coated with a thin layer of SU8 then baked at 100°C for 5 minutes. For the single band electrode, the sample was cut to expose the fresh edge surface for the electrodeposition. Array nanoband electrodes were patterned by photolithography to define the space (100 μm) between the edge surfaces based on previous publications.[28,29] The exposed carbon film was etched away by applying a voltage of 2.0 V vs. Ag/AgCl in 0.1 M NaOH based on previous reports.[28-30] The newly etched surface was then rinsed with water and used for electrodeposition.

6.2.3 Electrodeposition of Au nanoparticles

Electrochemical depositions were carried out with an EG&G Parc-263A electrochemical system (Princeton Applied Research, USA). A platinum wire was used as the auxiliary electrode which was separated from the bulk solution using a glass frit. In this chapter, all potentials are referred to the Ag/AgCl(sat. KCl).

Gold particles were electrochemically deposited on the electrodes by potential step as described in Chapter 5. The potential steps were from 1.1 V to a stated deposition potential for various time period. An electrolyte solution of 0.1 or 1 mM $KAuCl_4$ (in 0.5 M H_2SO_4) was used for the deposition.

6.2.4 SEM imaging

Scanning Electron Microscopy (SEM) images were recorded on a Hitachi S4800 operating at 5-20 kV. Various magnifications (from 1k to 60k) were employed and the working distance (WD) was ~8 mm.

6.2.5 SERS and Raman measurements

SERS and Raman spectra were collected with a Renishaw inVia Raman Microscope equipped with Peltier charge-coupled device (CCD) detectors and a Leica microscope. A line focused diode laser (785 nm) was employed. A 50× objective microscope (nominal aperture 0.75) was used to focus the laser to a 5 μm wide, 35 μm long spot, and collect the back-scattered light from the samples. Power at sample was varied between 0.85 mW and 85 μW. The spectra were analyzed using Wire 2.0 software from Renishaw.

Samples for SERS were prepared by immersing in 10 mM 4-Aminothiophenol (4-ATP) ethanol solution for 1 hour and then rinsed with ethanol three times before measurements. About 0.1 ml of 4-ATP solution (5 M in DMSO) or solid state 4-ATP powders (< 1 g) were put on a clean single crystal silicon wafer surface for the normal Raman spectrum. The silicon wafer was also used as Raman sample for the depth profile measurement. Intensity of band at 520

cm^{-1} was collected when sample stage was moving up and down with a step of 1 μm.

6.3 Results and Discussion

6.3.1 Electrochemical characterization of Au deposition on nanoband electrodes

Cyclic voltammetry was used to characterize gold electrodeposition on the carbon nanoband electrode. Figure 6.1 shows a cyclic voltammogram for Au electrodeposition on a carbon nanoband electrode at a scan rate of 100 mV/s. The electrode was 100 nm wide and 100 μm long. A cathodic current is observed at a potential near 0.8 V on the forward cathodic sweep. This cathodic current is attributed to the reduction of $AuCl_4^-$ to Au(0).[31] A cross-over of the cathodic current is observed at a potential of 0.4 V. The current cross-over is characteristic of a nucleation process, caused by an increase in active surface area due to the formation and growth of nuclei as discussed in Chapter 5.[32]

Au electrodeposition on the carbon nanoband electrodes was also investigated by potential step. Figure 6.1 (b) shows the current response in 1 mM $KAuCl_4$ at a potential of 0 V for first 0.4 s. A pseudo-steady state current is obtained, which is attributed to the nonlinear diffusion to the nanoband electrode surface. Figure 6.1 (c) is a magnification of the current over the first 20 ms. Current fluctuations with two maxima at 3 ms and 5 ms are observed. The current maxima transients are related to nucleation during the electrodeposition process.[33-35] Different mathematical models, such as the progressive nucleation

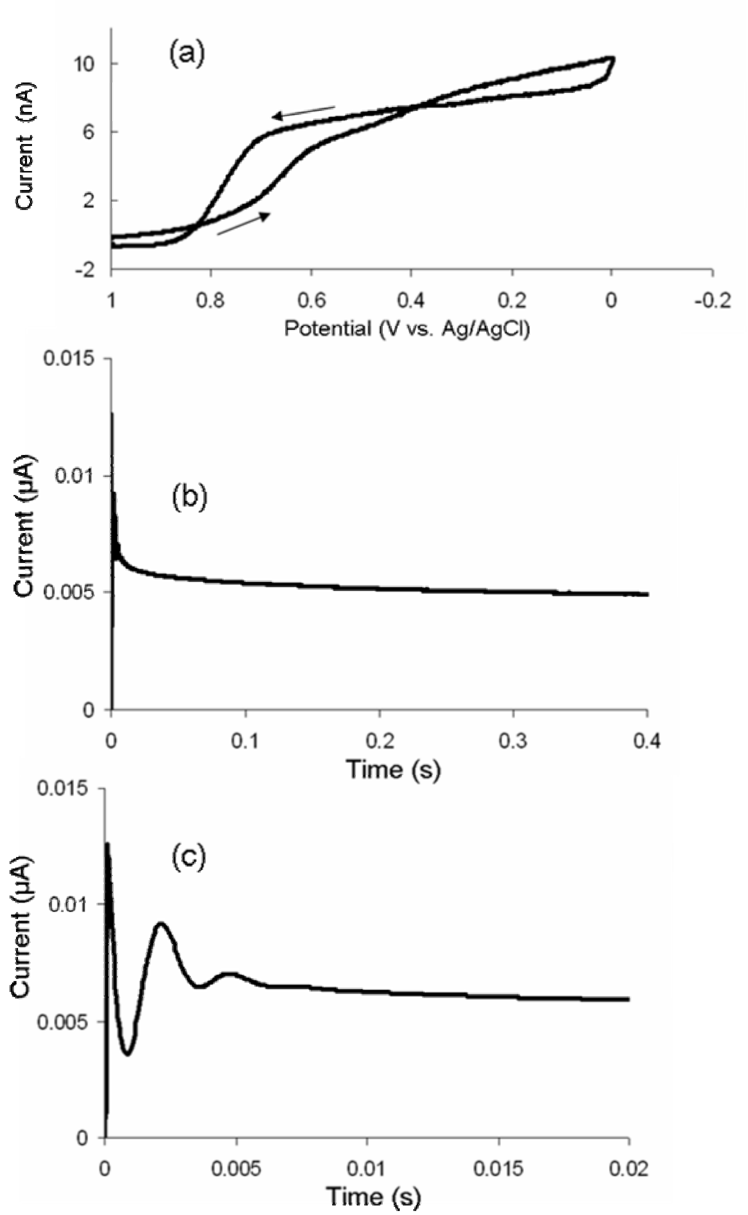

Figure 6.1. (a) Cyclic voltammogram on a 100 nm wide carbon nanoband electrode (ν=100 mV/s), (b) I-t transients on a 100 nm wide carbon nanoband electrode at the potential of 0.0 V for the first 0.4 s, and (c) I-t transients for the first 0.02 s. Deposition solution is 1 mM $KAuCl_4$ with 0.5 M H_2SO_4.

model and instantaneous nucleation model, have been proposed by Scharifker and Hills.[33] Attempts to quantitatively analyze the two maxima with the mathematic models, however, were unsuccessful. The reason may be attributed to the high mass transport flux to the nanoelectrode, which differs greatly from the linear diffusion considered in these models. The reason for the current oscillation is currently unknown.

6.3.2 SEM characterization of Au particles electrodeposited on carbon nanoband electrodes

Deposition time plays an important role in the shape and size evolution of electrodeposited Au on carbon as shown in Chapter 5. Figure 6.2 shows the SEM images of Au nanoparticles deposited on carbon nanoelectrodes at different deposition times. When the deposition time is short (2 s), small nuclei were observed as shown in Figure 6.2 (a). These particles were roughly 80 nm in size and were randomly distributed along the carbon nanoband like a diamond necklace. They were multi-branched, nanostar shaped, instead of the commonly observed spherical shape. For increased deposition time (5 s), the size of these particles increases to ~120 nm as shown in Figure 6.2 (b). A SEM image at higher magnification of the particles deposited at 5 s is shown in Figure 6.2 (e). These particles show multi-branched structures with 4-6 protruding tips. Deposition at longer time leads to the formation of dendritic structures as shown in Figure 6.2 (c) and (d). Dendritic particles show more sharp featured tips. Our hypothesis is that these highly structured nanoparticles result from the enhanced mass transport

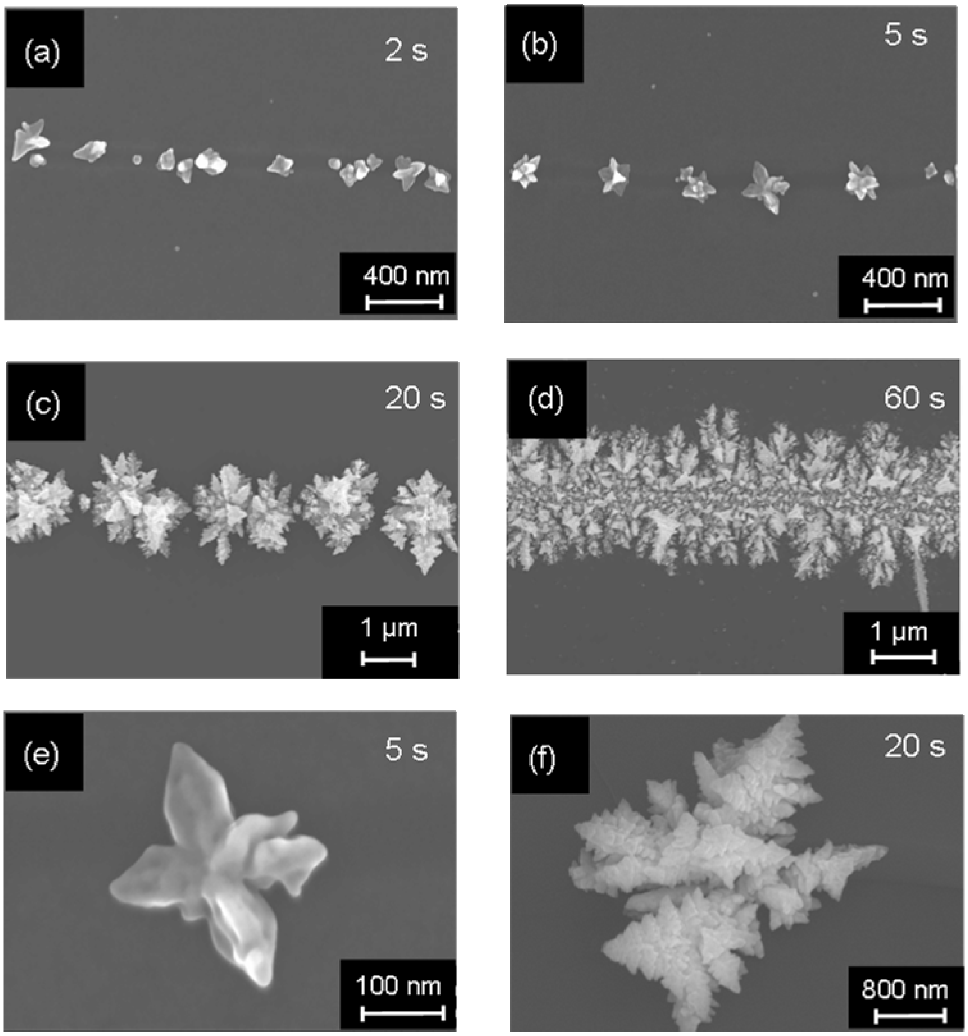

Figure 6.2. SEM images of Au nanoparticles deposited on a carbon nanoband electrode with the potential of 0 V (vs. Ag/AgCl) for (a) 2 s, (b) 5 s, (c) 20 s, and (d) 60 s, respectively. (e) and (f) are higher magnification SEM images of Au particles at deposition times of 5 s and 20 s, respectively. Electrolyte: 0.1 mM $K[AuCl_4]$ and 0.5 M H_2SO_4.

at nanoband electrodes. We thus explored the effect of electrode size on particle shape.

6.3.3 Relationship between particle shapes with electrode sizes.

We believe that the mass transfer (MT) plays an important role in determining the particle shape during the electrodeposition at nanoband electrodes. It is well known that diffusion can be classified to nonlinear diffusion and linear diffusion, which is governed by the ratio of diffusion layer thickness to electrode size (X_D/W).[36] Nonlinear diffusion is more efficient than linear diffusion. At band shape electrodes, when the diffusion layer thickness is larger than electrode width ($X_D > W$), nonlinear diffusion is prevailing. On the contrary, when the electrode width is larger than the diffusion layer thickness ($W > X_D$), the diffusion mode is governed by linear diffusion.

Table 6.1. Ratio of diffusion layer thickness to electrode width and diffusion mode at different electrode surfaces.

Electrode Width	150 nm	60 μm	200 μm
X_D/W	1120	2.8	0.84
Diffusion mode	Nonlinear	Nonlinear	Linear

Carbon band electrodes of different widths (150 nm, 60 μm and 200 μm) were fabricated by a combination of EBL and pyrolysis. The diffusion layer thickness (X_D) in our experiment is 168 μm as calculated according to $X_D = (\pi D t)^{1/2}$,[37] where D is the diffusion coefficient which equals to 9×10^{-6} cm^2/s

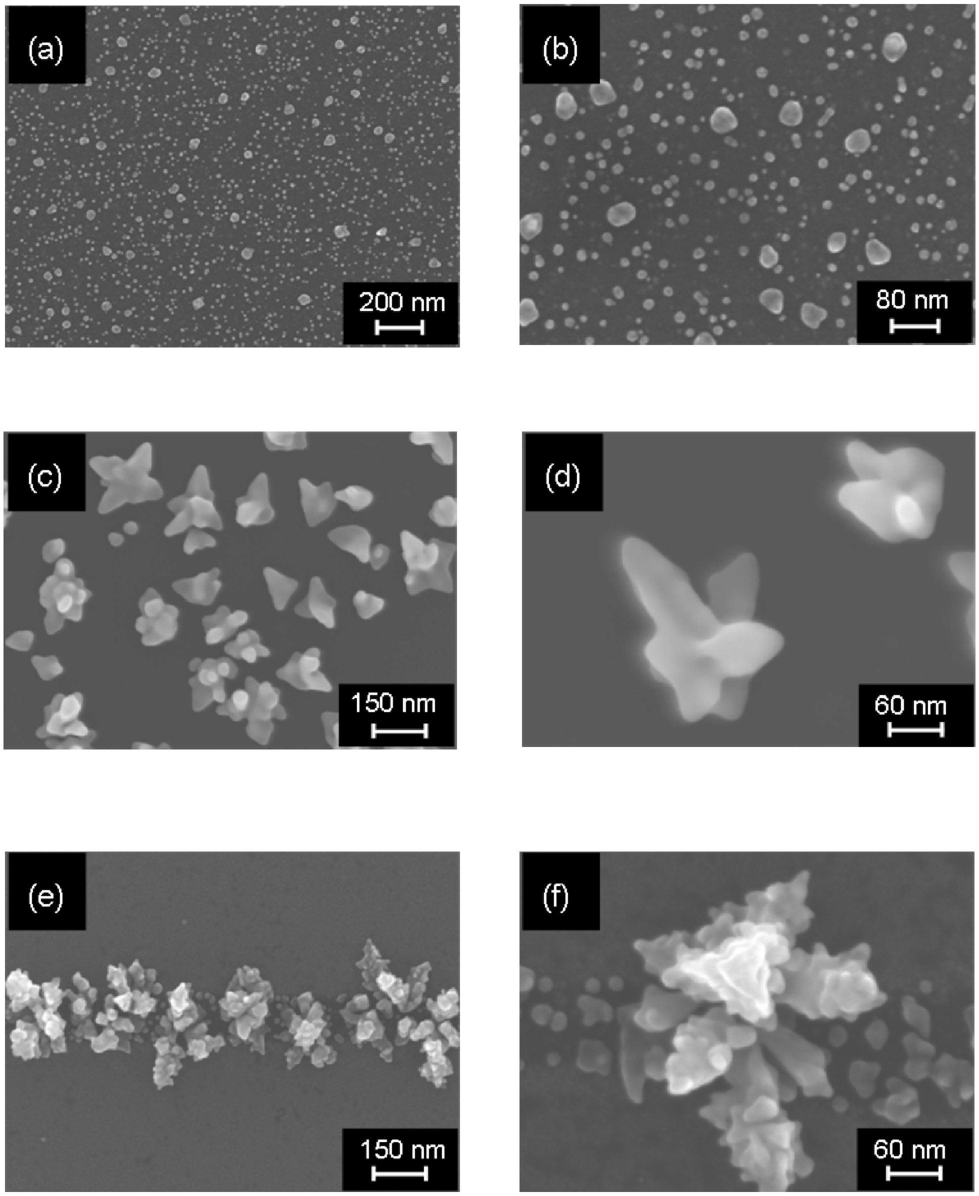

Figure 6.3. SEM images of the Au particles deposited at 200 μm wide carbon microband electrode [(a) and (b)], at 60 μm wide carbon microband electrode [(c) and (d)], and at 150 nm wide carbon nanoband electrode [(e) and (f)] at the potential of 0 V (vs. Ag/AgCl) for 10 s. Electrolyte: 1.0 mM $KAuCl_4$ and 0.5 M H_2SO_4.

based on previous publication,[38] and t = 10 s. The diffusion mode on the electrode surface can be obtained from the ratio of diffusion layer thickness to electrode width (X_D/W) which is summarized in Table 6.1.

Figure 6.3 shows SEM images of Au particles deposited on electrode surfaces with different electrode sizes. Figure 6.3 (a) and (b) show the SEM images of Au particles deposited on the 200 µm wide carbon microelectrode surface. The particles show spherical morphology with a broad size distribution, similar to that observed on the carbon film electrodes described in Chapter 5. Figures 6.3 (c) and (d) show the Au particles on a 60 µm wide carbon microelectrode surface. Unlike those observed on a 200 µm electrode, particles deposited on a 60 µm electrode are multi-branched structures. Similar shapes were also observed on 150 nm electrode as shown in Figure 6.3 (e) and (f). The highly efficient nonlinear diffusion around the 150 nm electrode and the 60 µm electrode leads to branched structures while the 200 µm electrode likely under linear diffusion and produces spherical particles similar to the complete film in Chapter 5.

6.3.4 Multi-branched or dendritic Au particles deposited on film edge electrodes

Film edge electrodes, as reviewed in Chapter 1, are widely employed as nanoband electrodes.[39-41] Film edge electrodes have a sandwich structure. A conductive film on a glass or silicon wafer surface was sealed on the top with a resin film. The edge surface was exposed to the solution as a nanoband electrode. Gold film edge electrodes with the widths ranging from 3 to 150 nm have been

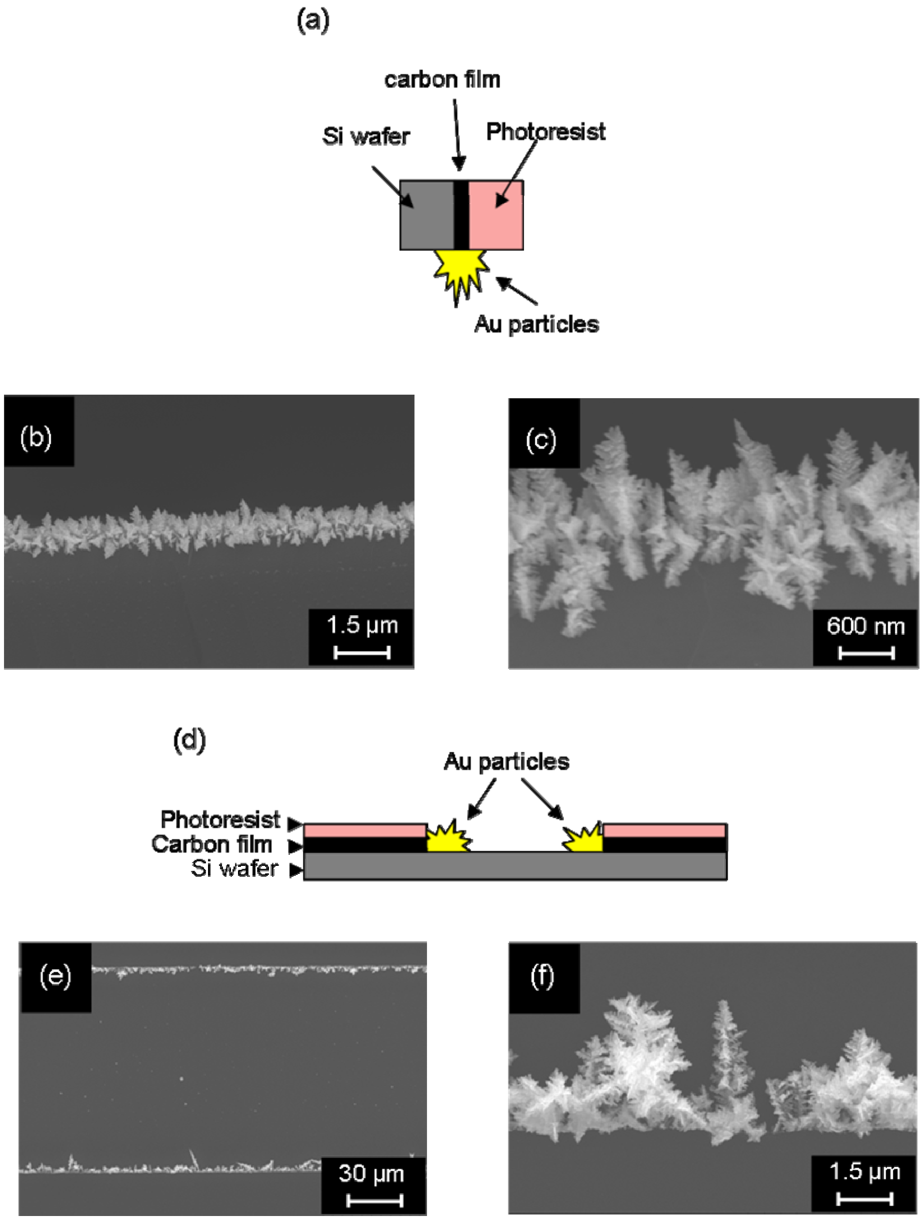

Figure 6.4. (a) Schematic image of Au electrodeposition on a carbon film edge electrode, (b) and (c) are the SEM images of Au dendritic particles on the carbon film edge electrode at different magnifications, (d) schematic image of Au deposition on a film edge electrode array, (e) and (f) are the SEM images of Au particles on film edge electrode array. Au electrodeposition was carried out at 0 V (vs. Ag/AgCl) for 10 s in 1 mM $KAuCl_4$ (0.5 M H_2SO_4).

prepared by McCarley and coworkers.[40] These electrodes exhibit sigmoidal shaped voltammograms due to nonlinear diffusion.

Film edge electrodes have been used as an alternative to our nanoband electrodes made by EBL. The fabrication of these film edge electrodes requires standard photolithographic processes and is thus, more economical than EBL. Both single and array nanoband electrodes have been fabricated. The carbon film thickness is roughly 11 nm based on previous measurements described in Chapter 2. Au electrodeposition on the electrode surfaces was carried out. Multi-branched or dendritic particles which were aligned along the film edge were successfully deposited on these types of electrodes. Figure 6.4 (a) and (d) show schematic illustrations of the electrodeposition on single and array film edge nanoband electrode surfaces, respectively. Figure 6.4 (b) and (c) show the SEM images of Au particles deposited on the single film edge electrode surfaces. Figure 6.4 (e) and (f) show those on the film edge array electrode surface. Dendritic Au particles were observed on the surface of the film edge electrodes, similar to the nanobands prepared via EBL.

6.3.5 SERS application on dendritic gold nanoparticles

Both nanostar and dendritic shaped gold particles have been reported to show strong SERS effects.[17,18] Similar phenomena were also observed in our samples. The optical enhancement in our multi-branched particles was demonstrated by the SERS spectra of adsorbed 4-Aminothiophenol (4-ATP). Figure 6.6 shows a normal Raman spectrum of solid state 4-ATP [Figure 6.6 (a)] as well as SERS spectra of a 4-ATP monolayer adsorbed at Au nanoparticles on 150 nm and 200 μm carbon band electrodes. Assignments and wave number positions for the Raman spectrum of the solid 4-ATP and the SERS spectrum of 4-ATP are summarized in Table 6.2.[42-44] Strong SERS peaks were observed on 4-ATP layer chemisorbed on the multi-branched Au nanoparticles on 150 nm nanoband electrode surface as shown in Figure 6.5 (red line). For comparison, the Raman spectrum from 4-ATP layer adsorbed on the Au nanoparticles deposited at 200 μm carbon band is also provided (blue line). The intensities of the Raman bands for this substrate are much lower, implying a decreased SERS effect. The strong SERS signals observed on Au nanoparticles deposited on the 150 nm electrode can be attributed to their multi-branched structures. These multi-branched structures have high local electromagnetic field at their tips and are expected to show strong optical enhancement.[23]

Table 6.2. SERS peak frequencies and assignments for 4-aminothiophenol (4-ATP).[42-44]

Raman	SERS	Assignment
1087 cm^{-1}	1080 cm^{-1}	CS stretch
	1142 cm^{-1}	CH bend
1171 cm^{-1}	1180 cm^{-1}	CH bend
	1430 cm^{-1}	CC stretch
1596 cm^{-1}	1569 cm^{-1}	CC ring stretch
1620 cm^{-1}	1618 cm^{-1}	NH bend

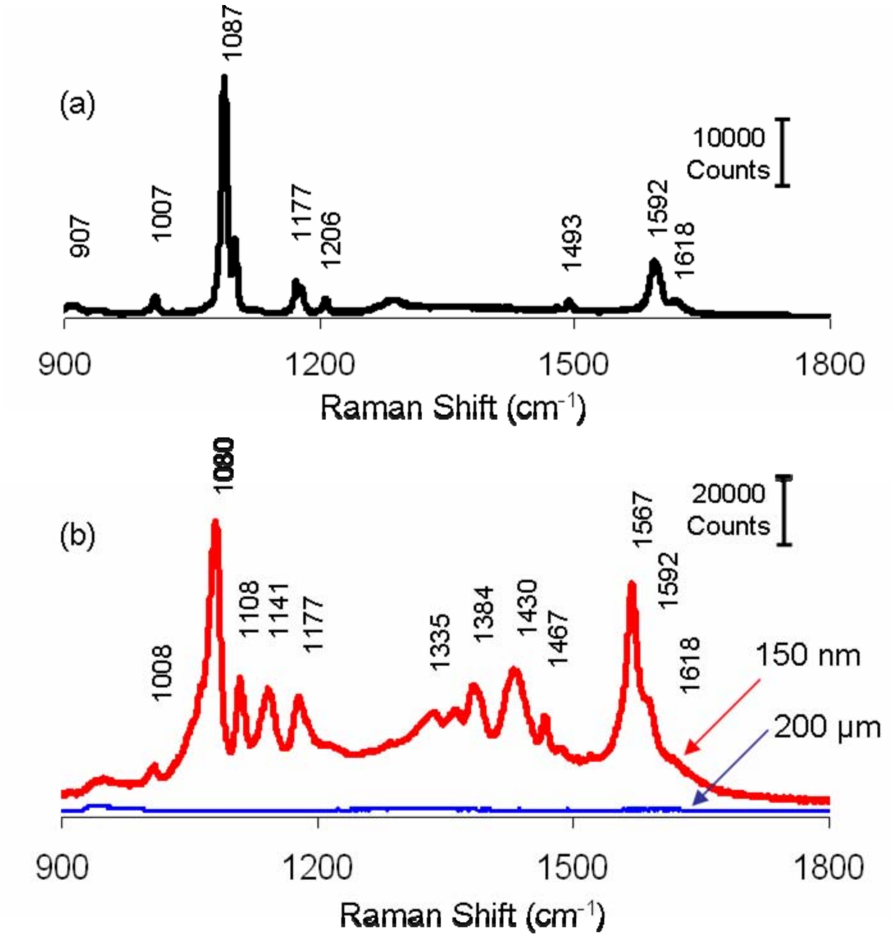

Figure 6.5. (a) the normal Raman spectrum of 4-ATP in solid state, and (b) SERS spectrum of 4-ATP adsorbed at the Au nanoparticles electrodeposited on the 150 nm carbon band electrode (red line) and Raman signals of 4-ATP adsorbed at the Au nanoparticles electrodeposited on the 200 μm carbon band electrode (blue line).

6.3.6. SERS enhancement factor

The enhancement factor (EF) is a very important parameter to evaluate SERS substrate. In order to calculate the EF, we measured the non-SERS Raman spectrum of 4-ATP solution (5 M in DMSO). The SERS spectrum obtained from Au nanoparticles and solution Raman spectrum of 4-ATP are shown in Figure 6.6. The intensity of strong C-S stretch peaks (1080 cm^{-1} in the SERS spectrum and 1087 cm^{-1} at Raman spectrum respectively) was chosen for the comparison and calculation. The EF value can be calculated according to the following equation.[45]

$$EF = (I_{SERS} / N_{ads})/(I_{bulk} / N_{bulk}) \tag{6.1}$$

where I_{SERS} and I_{bulk} are the measured intensities of $\nu_{(C\text{-}S)}$ in SERS and Raman spectra, respectively. N_{ads} is the illuminated molar number of 4-ATP adsorbed on Au nanoparticles surfaces by a laser, while N_{bulk} is the molar number of 4-ATP in the solution within the laser illumination volume.

In order to calculate N_{ads}, we first estimated the total surface area of Au nanoparticles. It has been reported that the reduction of Au surface oxides can be used to determine the surface area of Au nanoparticles.[31] The surface area of Au nanoparticles deposited on our nanoparticle was estimated by the electrochemical reduction of surface oxides. First, the electrode was oxidized at 1.4 V for 5s. Then a potential sweep (ν = 200 mV/s) from 1.4 V to 0.6 V (vs. Ag/AgCl) was applied to the electrode. Figure 6.7 shows the voltammogram. A reduction charge of 2.4×10^{-9} C was obtained by integrating the shaded area. It has been previously

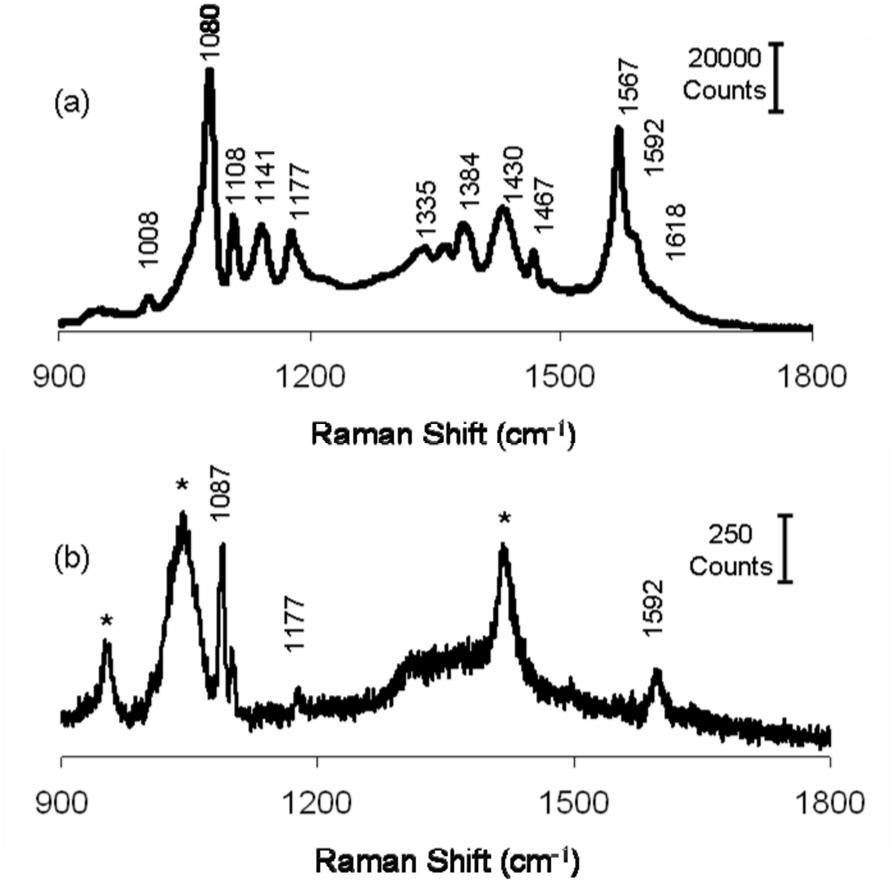

Figure 6.6. (a) SERS spectra of 4-ATP adsorbed on Au particles at 150 nm wide carbon nanoband electrode, (b) normal Raman spectra of 5 M 4-ATP solution dissolved in DMSO (peaks labelled with stars are attribute to DMSO).

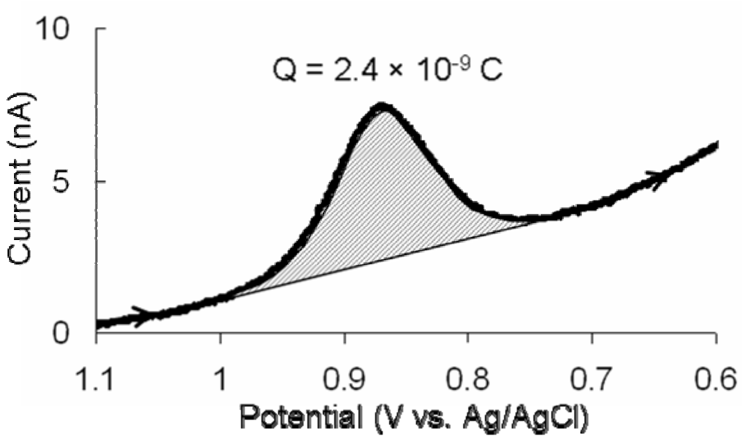

Figure 6.7. Linear sweep voltammogram for the reduction of Au surface oxides from electrochemical deposited Au nanoparticles on carbon nanoband electrode, Electrolyte: 0.5 M H_2SO_4.

determined that a flat Au surface yields a value of 489 μC/cm^2 for the charge required to reduce surface oxides.[31,46] Using this value, the surface area of Au nanoparticles on the 150 nm band electrode is: $\frac{2.4\times10^{-9}C}{4.89\times10^{-4}C/cm^2}=4.9\times10^{-6}cm^2$.

In our SERS experiment, the laser was line-focused to a spot 5 μm wide and 35 μm long. The laser spot was positioned across the nanoband (100 nm wide, 50 μm long) as illustrated by Figure 6.8. N_{ads}, thus, can be calculated from the product of total adsorbed molar number and the fraction of illuminated area, which equals to the ratio of the width of laser spot to the length of nanoelectrode ($W_{laser}/L_{electrode}$). The calculation of N_{ads} is defined as follows:

$$N_{ads}=N_{total}\times\frac{W_{laser}}{L_{electrode}}=\left(\Gamma_{4-ATP}\times A_{Au}\right)\times\frac{W_{laser}}{L_{electrode}} \tag{6.2}$$

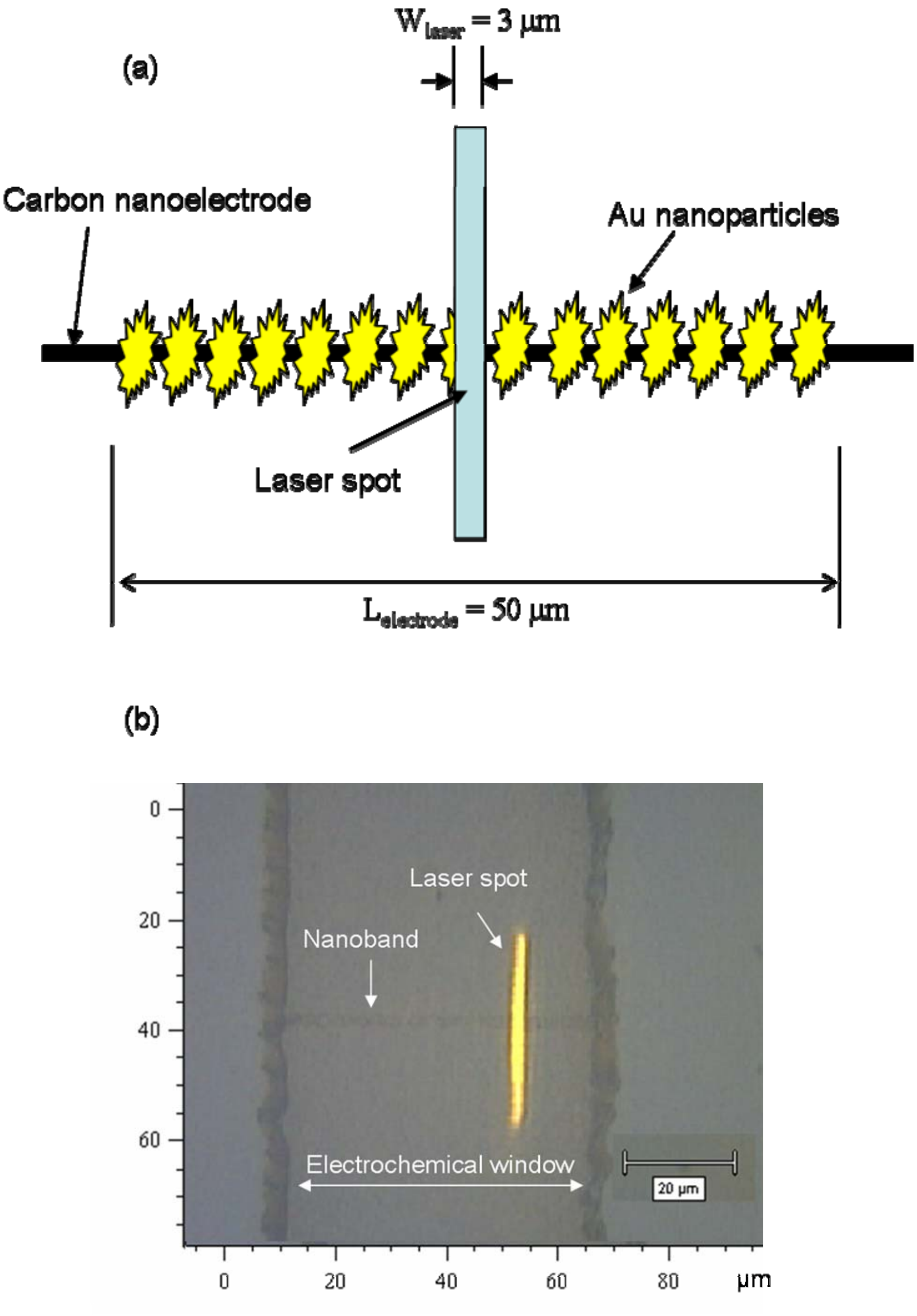

Figure 6.8. (a) Scheme and (b) optical photo of laser spot on nanoband electrode (50 ×).

where N_{total} is the total adsorbed 4-ATP on the Au particles, W_{laser} is the width of the laser spot, $L_{electrode}$ is the length of nanoband electode, $\Gamma_{4\text{-ATP}}$ is the surface density of adsorbed 4-ATP on the Au surface ($\Gamma_{4\text{-ATP}} = 7.6 \pm 0.7 \times 10^{-10}$ mol·cm^{-2}),[47,48] and A_{Au} is the total surface area of Au particles electrodeposited on the nanoband electrode.

N_{bulk} is calculated based on a reported method.[45] For a confocal Raman microscope, N_{bulk} can not be calculated directly as conventional Raman spectroscopy. As shown in Figure 6.9 (a), the focused laser leads to a waist profile in an aqueous solution.[45] All the molecules within the illuminated volume of solution contribute to N_{bulk} with different collection efficiency due to the sensitive depth resolution.[45] For example, the molecule at the ideally focused plane contributes more intensity than those at the less focused. In order to determine N_{bulk}, effective layer, h, as defined by equation 6.3 was introduced by Cai et al.[45] The definition of an effective layer was based on the following assumptions:

1) All the molecules within the effective layer have the same collection efficiency and contribute the same to intensity as those on the ideally focused plane
2) The effective illumination volume equals the product of the area of ideally focused laser spot (A_{laser}) and the effective layer thickness (h)
3) The theoretical intensity contributed from the molecule within the effective illuminated volume equals the measured intensity.

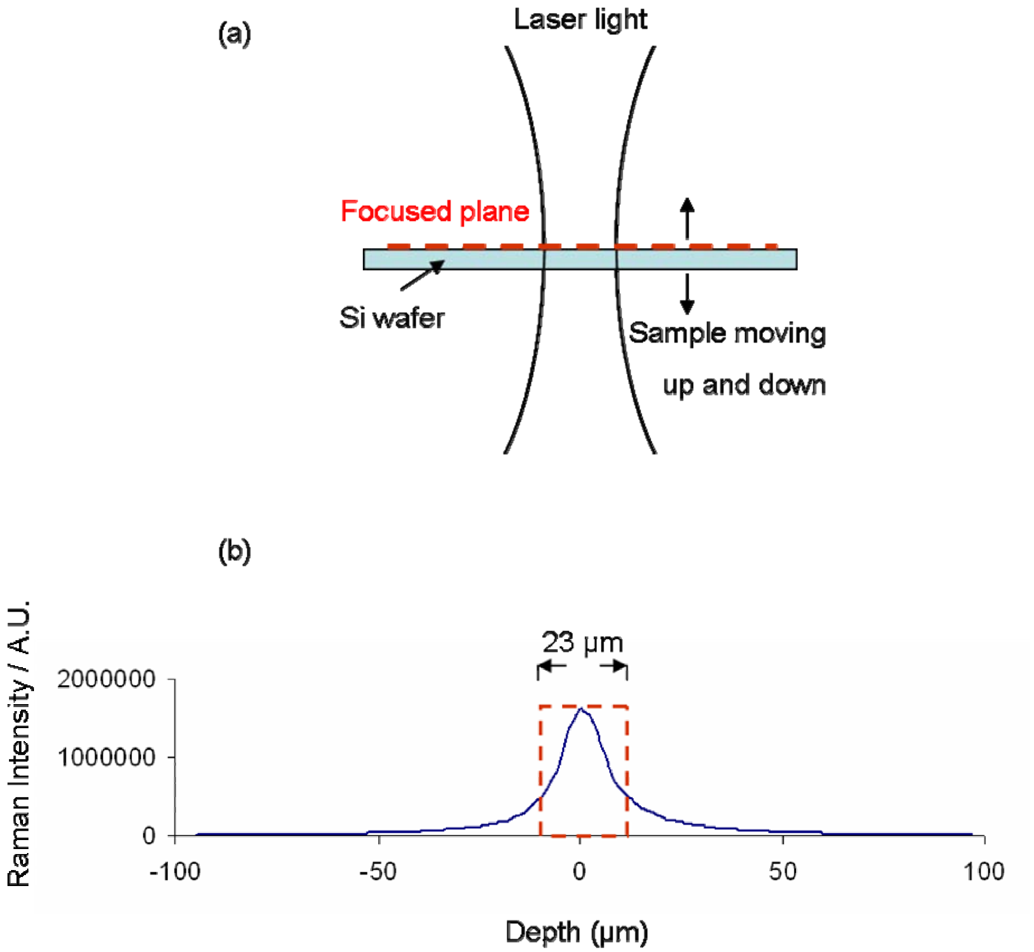

Figure 6.9. (a) Illustration of waist profile of a focused laser beam in aqueous solution, (b) Raman depth profile spectra of the integrated intensity of 520.6 cm^{-1} for a Si wafer.

A depth profile spectrum is used to calculate the effective layer thickness. In our experiment, a single crystal silicon wafer was used for the depth profile measurement. The integrated intensity of the strongest band for Si at 520 cm^{-1} was collected when the silicon wafer was moved through the laser focus with a step of 1 µm. Figure 6.9 (b) shows the resulting depth profile spectrum. The effective layer thickness, *h* (23 µm), was calculated according to equation 6.3.

$$h = \frac{\int_{-\infty}^{\infty} I(z)dz}{I_{\max}} \tag{6.3}$$

where $I_{(z)}$ is the measured intensity, I_{max} is the maximum of the measured intensity.

The effectively molecule number, N_{bulk}, can be calculated based on the following equation.

$$N_{bulk} = A_{laser} hC \tag{6.4}$$

where A_{laser} (A_{laser} = 5µm × 35 µm) is the area of focused laser spot, *C* (5 M) is the concentration of 4-ATP solution.

The measured integral intensity ratio of $\nu_{(C\text{-}S)}$ (~1080 cm^{-1}), $I_{SERS}/I_{Bulk} = 90 \pm 15$, was obtained based on measurements at five different positions on a carbon nanoband electrode. Then we calculated the EF from equation 6.1 as follows:

$$EF = (I_{SERS}/N_{ads})/(I_{bulk}/N_{bulk}) = (\frac{I_{SERS}}{I_{bulk}}) \times \frac{L_{electrode} \times L_{laser} \times h \times c}{\Gamma_{4-ATP} \times A_{Au}}$$

$$= (90 \pm 15) \times \frac{(35 \pm 1) \times 10^{-6} \times (51 \pm 1) \times 10^{-6} \times (23 \pm 1) \times 10^{-6} \times (5 \pm 1) \times 10^{3}}{(7.6 \pm 0.7) \times 10^{10} \times (4.9 \pm 0.1) \times 10^{-6}}$$

$$= (5 \pm 2) \times 10^{6}$$

EF values for 4-ATP SAMS on Au nanoparticles with different shapes, such as spheres, cubes, dogbone, has been determined in the range of 10^3 to 10^4 with a similar method by Dong and coworkers.[49] The higher EF value (~ 5 × 10^6) obtained in our samples is likely attributed to the multi-branched structures.

6.4 Conclusions

In this chapter, Au nanoparticles electrodeposited on the nanoband, microband and film edge electrodes were investigated. Multi-branched or dendritic shaped Au particles can be obtained on both micro and nanoband electrode surfaces. The particles shape is closely related to the mass transport around the electrodes. Multi-branched Au nanoparticles grown on carbon nanoband electrode surfaces were used as SERS substrates. Strong SERS effects of adsorbed thiol molecule on the Au particles were observed. The intensity of vibrational band, $\nu_{(C\text{-}S)}$, were compared between the SERS and non-SERS spectrum and EF of about 5 × 10^6 was also obtained.

6.5 References

1. Valden, M.; Lai, X.; Goodman, D. W., Onset of catalytic activity of gold clusters on titania with the appearance of nonmetallic properties. *Science* **1998,** 281, 1647-1650.
2. El-Sayed, M. A., Some interesting properties of metals confined in time and nanometer space of different shapes. *Accounts of Chemical Research* **2001,** 34, 257-264.
3. Murphy, C. J., Nanocubes and nanoboxes. *Science* **2002,** 298, 2139-2140.
4. Kelly, K. L.; Coronado, E.; Zhao, L. L.; Schatz, G. C., The optical properties of metal nanoparticles: The influence of size, shape, and dielectric environment. *Journal of Physical Chemistry B* **2003,** 107, 668-677.
5. Gupta, G.; Tanaka, D.; Ito, Y.; Shibata, D.; Shimojo, M.; Furuya, K.; Mitsui, K.; Kajikawa, K., Absorption spectroscopy of gold nanoisland films: optical and structural characterization. *Nanotechnology* **2009,** 20, 1-9.
6. Chen, H. J.; Kou, X. S.; Yang, Z.; Ni, W. H.; Wang, J. F., Shape- and size-dependent refractive index sensitivity of gold nanoparticles. *Langmuir* **2008,** 24, 5233-5237.
7. Jeanmaire, D. L.; Vanduyne, R. P., Surface Raman spectroelectrochemistry .1. heterocyclic, aromatic, and aliphatic-amines adsorbed on anodized silver electrode. *Journal of Electroanalytical Chemistry* **1977,** 84, 1-20.

8. Sant'Ana, A. C.; Corio, P.; Temperini, M. L. A., The SERS effect in trace analysis: The role of nanostructured surfaces. *Quimica Nova* **2006,** 29, 805-810.

9. Delfino, I.; Bizzarri, A. R.; Cannistraro, S., Single-molecule detection of yeast cytochrome c by surface-enhanced Raman spectroscopy. *Biophysical Chemistry* **2005,** 113, 41-51.

10. Constantino, C. J. L.; Lemma, T.; Antunes, P. A.; Aroca, R., Single-molecule detection using surface-enhanced resonance Raman scattering and Langmuir-Blodgett monolayers. *Analytical Chemistry* **2001,** 73, 3674-3678.

11. Kneipp, K.; Kneipp, H.; Bohr, H. G., Single-molecule SERS spectroscopy. In *Surface-Enhanced Raman Scattering: Physics and Applications*, Springer-Verlag Berlin: Berlin, **2006**, 103, pp 261-277.

12. Kneipp, K.; Wang, Y.; Kneipp, H.; Perelman, L. T.; Itzkan, I.; Dasari, R.; Feld, M. S., Single molecule detection using surface-enhanced Raman scattering (SERS). *Physical Review Letters* **1997,** 78, 1667-1670.

13. Kneipp, K.; Kneipp, H.; Kartha, V. B.; Manoharan, R.; Deinum, G.; Itzkan, I.; Dasari, R. R.; Feld, M. S., Detection and identification of a single DNA base molecule using surface-enhanced Raman scattering (SERS). *Physical Review E* **1998,** 57, R6281-R6284.

14. Kneipp, K.; Kneipp, H.; Manoharan, R.; Itzkan, I.; Dasari, R. R.; Feld, M. S., Surface-enhanced Raman scattering (SERS) - a new tool for single molecule detection and identification. *Bioimaging* **1998**, 6, 104-110.

15. Nehl, C. L.; Liao, H. W.; Hafner, J. H., Optical properties of star-shaped gold nanoparticles. *Nano Letters* **2006,** 6, 683-688.

16. Hao, F.; Nehl, C. L.; Hafner, J. H.; Nordlander, P., Plasmon resonances of a gold nanostar. *Nano Letters* **2007,** 7, 729-732.

17. Khoury, C. G.; Vo-Dinh, T., Gold nanostars for surface-enhanced Raman scattering: synthesis, characterization and optimization. *Journal of Physical Chemistry C* **2008,** 112, 18849-18859.

18. Guo, S.; Wang, L.; Wang, E., Templateless, surfactantless, simple electrochemical route to rapid synthesis of diameter-controlled 3D flowerlike gold microstructure with "clean" surface. *Chemical Communications* **2007**, 30, 3163-3165.

19. Jena, B. K.; Raj, C. R., Seedless, surfactantless room temperature synthesis of single crystalline fluorescent gold nanoflowers with pronounced SERS and electrocatalytic activity. *Chemistry of Materials* **2008,** 20, 3546-3548.

20. Li, M. F.; Zhao, G. H.; Geng, R.; Hu, H. K., Facile electrocatalytic redox of hemoglobin by flower-like gold nanoparticles on boron-doped diamond surface. *Bioelectrochemistry* **2008,** 74, 217-221.

21. Wang, L.; Guo, S. J.; Zhai, J. F.; Hu, X. G.; Dong, S. J., Ultrathin platinum-group metal coated hierarchical flowerlike gold microstructure: Electrochemical design and characterization. *Electrochimica Acta* **2008,** 53, 2776-2781.

22. Micic, M.; Klymyshyn, N.; Lu, H. P., Finite element method simulations of the near-field enhancement at the vicinity of fractal rough metallic surfaces. *Journal of Physical Chemistry B* **2004,** 108, 2939-2947.

23. Bakr, O. M.; Wunsch, B. H.; Stellacci, F., High-yield synthesis of multi-branched urchin-like gold nanoparticles. *Chemistry of Materials* **2006,** 18, 3297-3301.

24. Kumar, P. S.; Pastoriza-Santos, I.; Rodriguez-Gonzalez, B.; Abajo, F. J. G. d.; Liz-Marzan, L. M., High-yield synthesis and optical response of gold nanostars. *Nanotechnology* **2008,** 19, 1-6.

25. Xie, J. P.; Zhang, Q. B.; Lee, J. Y.; Wang, D. I. C., The synthesis of SERS-active gold nanoflower tags for in vivo applications. *Acs Nano* **2008,** 2, 2473-2480.

26. Song, W.; Cheng, Y. C.; Jia, H. Y.; Xu, W. Q.; Zhao, B., Surface enhanced Raman scattering based on silver dendrites substrate. *Journal of Colloid and Interface Science* **2006,** 298, 765-768.

27. Watling, K.; Hope, G. A.; Woods, R., SERS investigation of gold dissolution in chloride and cyanide media. *Journal of the Electrochemical Society* **2005,** 152, D103-D108.

28. Ssenyange, S.; Du, R.; McDermott, M. T., Fabrication of arrays of carbon micro- and nanostructures via electrochemical etching. *Micro & Nano Letters* **2009,** 4, 22-26.

29. Ssenyange, S.; Taylor, J.; Harrison, D. J.; McDermott, M. T., A glassy carbon microfluidic device for electrospray mass spectrometry. *Analytical Chemistry* **2004,** 76, 2393-2397.

30. Kiema, G. K.; Ssenyange, S.; McDermott, M. T., Microfabrication of glassy carbon by electrochemical etching. *Journal of the Electrochemical Society* **2004,** 151, C142-C148.

31. Finot, M. O.; Braybrook, G. D.; McDermott, M. T., Characterization of electrochemically deposited gold nanocrystals on glassy carbon electrodes. *Journal of Electroanalytical Chemistry* **1999,** 466, 234-241.

32. Schmidt, U.; Donten, M.; Osteryoung, J. G., Gold electrocrystallization on carbon and highly oriented pyrolytic graphite from concentrated solutions of LiCl. *Journal of the Electrochemical Society* **1997,** 144, 2013-2021.

33. Scharifker, B.; Hills, G., Theoretical and experimental studies of multiple nucleation. *Electrochimica Acta* **1983,** 28, 879-889.

34. Scharifker, B. R.; Mostany, J., 3-dimensional nucleation with diffusion controlled growth .1. Number density of active-sites and nucleation rates per site. *Journal of Electroanalytical Chemistry* **1984,** 177, 13-23.

35. Mostany, J.; Mozota, J.; Scharifker, B. R., 3-dimensional nucleation with diffusion controlled growth .2. The nucleation of lead on vitreous carbon. *Journal of Electroanalytical Chemistry* **1984,** 177, 25-37.

36. Amatore, C., Electrochemistry at ultramicroelectrodes. In *Physical Electrochemistry: Principles, Methods and Applications*, Rubinstein, I., Ed. CRC press: Rubinstein, 1995; pp 131-204.

37. Bard, A. J.; Faulkner, L. R., *Electrochemical Methods: Fundamentals and Applications*. Wiley: New York, 1980; pp 165-166.

38. A.L.Horvath, *Handbook of Aqueous Electrolyte Solutions*. Ellis Horwood: New York, 1985; p 290.

39. Arrigan, D. W. M., Nanoelectrodes, nanoelectrode arrays and their applications. *Analyst* **2004**, 129, 1157-1165.

40. Caston, S. L.; McCarley, R. L., Characteristics of nanoscopic Au band electrodes. *Journal of Electroanalytical Chemistry* **2002,** 529, 124-134.

41. Morris, R. B.; Franta, D. J.; White, H. S., Electrochemistry at Pt band electrodes of width approaching molecular dimensions - breakdown of transport-equations at very small electrodes. *Journal of Physical Chemistry* **1987,** 91, 3559-3564.

42. Dong-Feng Zhang, L.-Y. N., Li Jiang, Peng-Gang Yin, Ling-Dong Sun, Hua Zhang, Rui Zhang, Lin Guo, and Chun-Hua Yan, Branched gold nanochains facilitated by polyvinylpyrrolidone and their SERS effects on p-aminothiophenol. *Journal of physical Chemistry C* **2008,** 112, 16011-16016.

43. Osawa, M.; Matsuda, N.; Yoshii, K.; Uchida, I., Charge-transfer resonance Raman process in surface-enhanced Raman-scattering from p-aminothiophenol adsorbed on silver - Herzberg-Teller contribution. *Journal of Physical Chemistry* **1994,** 98, 12702-12707.

44. Matsuda, N.; Yoshii, K.; Ataka, K.; Osawa, M.; Matsue, T.; Uchida, I., Surface-enhanced infrared and Raman studies of electrochemical

reduction of self-assembled monolayers formed from para-nitrothiophenol at silver. *Chemistry Letters* **1992**, 1385-1388.

45. Cai, W. B.; Ren, B.; Li, X. Q.; She, C. X.; Liu, F. M.; Cai, X. W.; Tian, Z. Q., Investigation of surface-enhanced Raman scattering from platinum electrodes using a confocal Raman microscope: dependence of surface roughening pretreatment. *Surface Science* **1998,** 406, 9-22.

46. Finot, M. Deposition and modification of gold nanocrystals on glassy carbon electrodes. PhD thesis, University of Alberta, Edmonton, 2000.

47. Mohri, N.; Inoue, M.; Arai, Y.; Yoshikawa, K., Kinetic-study on monolayer formation with 4-aminobenzenethiol on a gold surface. *Langmuir* **1995,** 11, 1612-1616.

48. Yoon, J. K.; Kim, K.; Shin, K. S., Raman scattering of 4-aminobenzenethiol sandwiched between Au nanoparticles and a macroscopically smooth Au substrate: effect of size of Au nanoparticles. *Journal of Physical Chemistry C* **2009,** 113, 1769-1774.

49. Hu, X.; Wang, T.; Wang, L.; Dong, S., Surface-enhanced Raman scattering of 4-aminothiolphenol self-assembled monolayers in sandwich structure with nanoparticle shape dependence: off-surface plasmon resonce condition. *Journal of Physical Chemistry C* **2007,** 111, 6962-6969.

Chapter 7. Conclusions and Future work

7.1 Conclusions of this thesis.

The research in this thesis is focused on carbon structures fabricated via pyrolysis of a commercial negative resist (SU-8). Both carbon film and nanometer sized carbon structures were successfully fabricated and their applications as nanoband electrodes and substrate for metal electrodeposition were also investigated.

Spin-coated SU-8 films were first exposed to UV light. They were subsequently graphitized via pyrolysis in inert atmosphere at 1000^{o}C. The graphitic microstructure of the pyrolyzed material was probed with Raman spectroscopy, which indicates the resulting material is highly graphitized. These carbon films have extremely flat surfaces (RMS = 0.4 nm) and show good electrochemical activity to common redox systems.

We further extended pyrolysis of SU-8 to create nanometer sized graphitic carbon structures by using electron-beam lithography (EBL). One of the major challenges of our procedure is to ensure the survival of the SU-8 nanostructures throughout the pyrolysis procedure. We have found that successful pyrolysis depends greatly on the degree of cross-linking in the SU-8 nanostructures. We ensure a highly cross-linked structure in the epoxy-based resist by pre-baking the nanostructures at ~200^{o}C before pyrolysis. EBL allows for the precise control of shape, size and location of these carbon nanostructures. The size and shape of the nano-structures has been characterized by scanning electron microscopy (SEM) and scanning force microscopy (SFM). The lateral sizes of the nano SU8 structure before and after pyrolysis are probed by SEM. The results show that the lateral size is maintained during the pyrolysis even for structures with widths of 18 nm. SFM results indicate a vertical shrinkage of about 80% after pyrolysis.

The application of the carbon nanostructures as single and array carbon nanoband electrodes was investigated. The dimensions of individual electrodes and interband distance can be precisely controlled by EBL and preserved during the carbonization process. Cyclic voltammograms obtained at nanoband electrodes shows a limiting current which is characteristic of nonlinear diffusion to cylindrical ultramicroelectrodes. Their voltammetric behaviors are consistent with theoretical predictions.

Both carbon film and carbon nanoband electrodes have been used as substrates for metal electrodeposition. The electrodeposition process of gold nanoparticle on the carbon film electrodes follows Volmer-Weber growth mechanism. Three-dimensional gold particles are initially formed. The subsequent coalescence leads to a continual Au film formation on the carbon surface. In the early stage of the deposition process, the electrodeposition follows the classical progressive nucleation mechanism. Both deposition potentials and gold concentration play an important role. Less negative deposition potential leads to lower particle density and large particle size, while more negative potential leads to higher particle density and smaller particle size.

Au electrodeposition on the nanoband electrodes was also investigated. Multi-branched Au nanoprtoicles deposited on a nanoband electrode were observed. Rapid mass transport (MT) of Au cations via nonlinear diffusion results in Au nanoparticles with multi-branched or dendritic shapes. These Au nanoparticles were used as SERS substrates. Strong SERS effects of adsorbed thiol molecule layer on nanoband supported Au particles were observed and EF of ~ 5×10^6 can be obtained.

7.2 Suggestions for Future Work.

7.2.1 Optically Transparent Electrodes (OTEs)

One potential application of carbon film electrodes is OTEs. Conductive films based OTES have been widely used in the investigations of spectroelectrochemistry (SEC),[1,2] single molecule spectroscopy,[3] biosensor,[4,5] and solar cells.[6,7] Currently, most of these electrodes rely on indium tin oxide (ITO), fluorine tin oxide (FTO) and metal thin films. The ITO and FTO, however, are known for some limitations, such as limited indium available on earth, unstable in the acid or base solution, and poor transparency in the near-infrared region.[3,6,8] Graphite carbon electrodes are well known for low cost, chemical stability under strong acidic and alkaline conditions, and easy surface modification.[9]

Although the color of bulk graphite materials is black, very thin carbon films (< 80 nm) are partially transparent in the visible wavelength range.[3] As mentioned in Chapter 2, the thickness of P8 electrodes is less than 20 nm.

Therefore, P8 carbon film electrodes on quartz would be a good candidate for OTEs.

7.2.2 Interdigitated Array Nanoelectrodes (IDANs)

Interdigitated array electrodes (IDAEs) refer to a series of parallel band electrodes where alternating bands are connected together like interdigitated fingers as shown in Figure 7.1. The two electrodes, placed in close proximity of each other, are named as generator and collector electrode respectively. For reversible redox systems, the redox species are electrogenerated at the generator electrode then they diffuse to the adjacent collector electrode, where it recovered to the original state. Further diffusion between collector electrode and generator electrode makes this redox process cycling and greatly enhances the current signals.[10]

Currently, most IDAEs are prepared from metal films. Carbon electrodes are well known for wider potential window and larger over-potential for water as compared to noble metal electrodes. This feature is expected to improve the sensitivity of electrochemical reactions for redox-active biological molecules because their reactions are slow on metal electrodes.[11] Isasaki et al. have reported a detection limit of 0.5 fmol for 5 μL of dopamine (100 pM) with an IDE carbon microelectrode consisting of 300 pairs, 5 μm finger widths and gaps, and 2 mm finger length.[11] The author expected a lower detection limit can be obtained if a smaller IDA carbon electrode can be employed.[11]

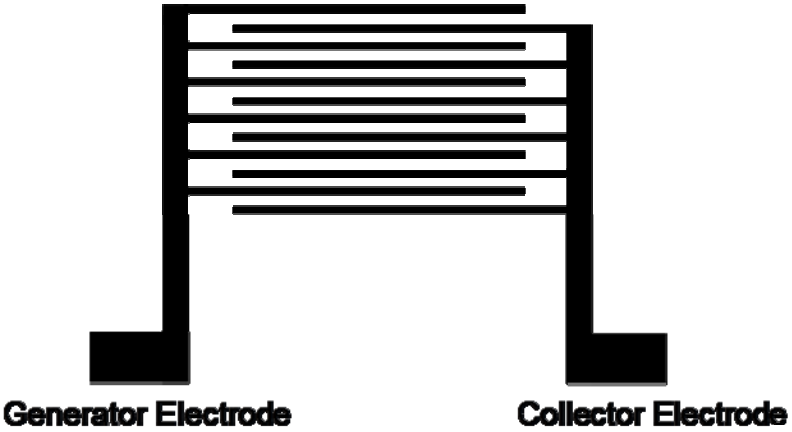

Figure 7.1. Schemic view of an interdigitated array electrode.

In this thesis, carbon nanowire arrays with an interband spacing ranging from 40 nm to 100 μm were fabricated. Their application as IDAEs would be of significant interest to electrochemical detection.

7.2.3 SERS application of dendritic Au particles on film edge electrode.

Chapter 6 demonstrated the high efficient nonlinear diffusion around nanoelectrodes leading to the formation of Au particles with branched or dendritic structures. Similarly, 1-dimensionally aligned dendritic shaped Au particles were also observed on the film edge electrode.

Compared with the fabrication of nanoband electrodes with EBL, the fabrication of film edge electrodes requires only standard photolithography process and is thus more economically efficient. The strong optical enhancement observed on multi-branched or dendritic Au particles was theoretically and experimentally studied. In addition, the strong SERS effect was observed on our multi-branched or dendritic particles. Dendritic Au particles deposited on film edge electrodes are expected to be good candidates for SERS substrates.

7.3 References

1. Dai, Y.; Swain, G. M.; Porter, M. D.; Zak, J., New horizons in spectroelectrochemical measurements: Optically transparent carbon electrodes. *Analytical Chemistry* **2008,** 80, 14-22.
2. Tian, H.; Bergren, A. J.; McCreery, R. L., Ultraviolet-visible spectroelectrochemistry of chemisorbed molecular layers on optically transparent carbon electrodes. *Applied Spectroscopy* **2007,** 61, 1246-1253.
3. Donner, S.; Li, H. W.; Yeung, E. S.; Porter, M. D., Fabrication of optically transparent carbon electrodes by the pyrolysis of photoresist films: Approach to single-molecule spectroelectrochemistry. *Analytical Chemistry* **2006,** 78, 2816-2822.
4. Choi, C. K.; Margraves, C. H.; Jun, S. I.; English, A. E.; Rack, P. D.; Kihm, K. D., Opto-electric cellular biosensor using optically transparent indium tin oxide (ITO) electrodes. *Sensors* **2008,** 8, 3257-3270.
5. Shah, S. S.; Lee, J. Y.; Verkhoturov, S.; Tuleuova, N.; Schweikert, E. A.; Ramanculov, E.; Revzin, A., Exercising spatiotemporal control of cell attachment with optically transparent microelectrodes. *Langmuir* **2008,** 24, 6837-6844.
6. Wang, X.; Zhi, L. J.; Mullen, K., Transparent, conductive graphene electrodes for dye-sensitized solar cells. *Nano Letters* **2008,** 8, 323-327.
7. Schmidt, H.; Flugge, H.; Winkler, T.; Bulow, T.; Riedl, T.; Kowalsky, W., Efficient semitransparent inverted organic solar cells with indium tin oxide top electrode. *Applied Physics Letters* **2009,** *94*, 243302-243302.

8. Vollmer, A.; Feng, X. L.; Wang, X.; Zhi, L. J.; Mullen, K.; Koch, N.; Rabe, J. P., Electronic and structural properties of graphene-based transparent and conductive thin film electrodes. *Applied Physics A-Materials Science & Processing* **2009,** 94, 1-4.

9. McCreery, R. L., Advanced carbon electrode materials for molecular electrochemistry. *Chemical Reviews* **2008,** 108, 2646-2687.

10. Daniel, D.; Gutz, I. G. R., Microfluidic cells with interdigitated array gold electrodes: Fabrication and electrochemical characterization. Talanta **2005,** 68, 429-436.

11. Iwasaki, Y.; Morita, M., Electrochemical measurements with interdigitated array microelectrodes. *Current Separations* **1995,** 14, 2-8.